# Applications of laser, optical and paramagnetic spectroscopy

**A thesis submitted for the degree of Doctor of Philosophy of the Australian National University**

**Samuel Alexander Margerison**

**August 2003**

The work described in this Thesis is my own except where otherwise stated. None of my own work described in this Thesis has been submitted for any other degree.

Samuel Alexander Margerison

# Acknowledgements

I would like to thank the Australian National University for providing me with a Graduate School Scholarship, and the Research School of Chemistry for an Alan Sargeson Merit Award, and the opportunity to do a PhD.

Thank you to my supervisor Professor Elmars Krausz for support, advice, the opportunity to use some powerful and unique spectroscopic instruments, and most importantly, for the chance to do a PhD in the field of laser and optical spectroscopy.

I would like to thank Dr Lucjan Dubicki for imparting an incredible amount of knowledge regarding the angular overlap model and ligand fields, and for all his assistance with the theoretical work.

Thank you to AMBRI Pty Ltd for the provision of a top-up scholarship for the first year of my PhD and the opportunity to work with the unique compounds used in the AMBRI biosensor. Particular thanks are due to Dr Lech Wieczorek and Dr Mohammed Isslam, formerly of AMBRI, and to Dr Ron Pace of the Department of Chemistry, for their technical assistance.

A special thanks to Keith Jackman for all his technical advice and the construction of numerous useful gadgets such as the sample holder, lens mount and viewing camera mount for the Triplemate spectrometer, and the gold electrodes used in chapter 3.

I would like to thank Dr Vincent Otieno-Alego, formerly of the Raman Microscopy Unit at the University of Canberra for access to the Raman microscope, and invaluable assistance with running spectra, and Dr Karin Ahrling of the Department of Chemistry, ANU for leading me through EPR spectroscopy by the hand.

Thank you to all the overlapping group members of the Krausz and White groups for the fun and laughs over the years, especially Robin, Derek, Marcus, Xueqin, Vanessa, Sindra, Elliot, Duncan, Gav and Jeremy.

I would like to thank my parents, my sister Jess, and Pam for all their support over the last four and half years.

And finally special thanks to Vanessa for her love and support during this endeavour, for her very useful proofreading and teaching me to use the single-beam absorption spectrometer.

# Abstract

This thesis consists of two distinct parts. The first part describes the construction of a new Raman spectrometer with the aim of studying self-assembled monolayers on gold films, particularly of molecules used to construct the bisensor designed by AMBRI Pty Ltd. The second part involved the study of trigonal ligand fields in some cobalt(II) and nickel(II) coordination complexes, which involved the use of low temperature absorption spectroscopy, electron paramagnetic resonance (EPR) and Raman spectroscopy.

For the first part of the research, a new Raman spectrometer based on a triple monochromator and a charge-coupled device (CCD) detector was constructed and compared with an existing spectrometer which employs photon counting detection. A number of attempts were made to collect Raman spectra of self-assembled monolayers using both instruments at the Research School of Chemistry and a Raman microscope at the University of Canberra. Both well-known thiol molecules, and a novel molecule synthesised by AMBRI for the biosensor were studied. These experiments enjoyed only limited success, mainly due to the high background signals. Anomalously intense spectra similar to those reported recently by an American research group (and assigned by them as transitions between electronic image states) were observed for particular excitation conditions. The overall result of this section of work was that a Raman spectrometer that was in several respects superior to the existing spectrometer at the Research School of Chemistry was constructed. However, it was found that Raman spectroscopy was not a suitable technique for the characterisation of the AMBRI biosensor.

Using electron paramagnetic resonance (EPR) spectroscopy, the anisotropy of the g-value for $[Co(H_2O)_6](BrO_3)_2$ was measured and related to the trigonal ligand field strength through the angular overlap model (AOM). Low temperature absorption spectra of $[Co(H_2O)_6](BrO_3)_2$ and $[Ni(H_2O)_6](BrO_3)_2$ were measured; these allowed the observation of the previously unmeasured $^3T_{2g} \leftarrow {}^3A_{2g}$ band in $[Ni(H_2O)_6](BrO_3)_2$. Modelling of the absorption and EPR spectra using ligand field and AOM techniques developed by Dr Lucjan Dubicki of the Research School of Chemistry confirmed the

existence of a substantial trigonal field in these complexes, which has been overlooked by a number of previous workers in the field.

EPR measurements for *bis*(*tris*(pyrazol-1-yl) methane) nickel(II) dinitrate ($[Ni(HCPz_3)_2](NO_3)_2$) and *bis*(hydro *tris*(pyrazol-1-yl)borate) nickel (II) ($[Ni(HBPz_3)_2]$) have allowed the determination of the zero-field splitting of the ground electronic state of these complexes. This has again been related to the trigonal ligand field strength through the angular overlap model. Results from these last two compounds have been compared with those measured for the monodentate complex *hexakis*(pyrazol-1-yl) nickel(II) dinitrate ($[Ni(Pz)_6](NO_3)_2$) to study the effect of the capping carbon or boron atom on the zero field splitting. High quality EPR spectra were also measured for the capped cobalt complexes $[Co(HCPz_3)_2](NO_3)_2$ and $[Co(HBPz_3)_2]$, particularly when frozen solutions of the compounds were studied.

A variety of single crystal absorption spectra have been measured for the pyrazolyl complexes. These include the capped complexes $[Co(HCPz_3)_2](NO_3)_2$, $[Ni(HCPz_3)_2](NO_3)_2$, $[Co(HBPz_3)_2]$, and $([Ni(HBPz_3)_2]$, where particularly clear trigonal splitting could be seen for the nickel complexes, and the uncapped complexes $[Co(Pz)_6](NO_3)_2$ and $[Ni(Pz)_6](NO_3)_2$. A clear ordering in the magnitude of the trigonal field strength could be observed for the three ligands ($HCPz_3$ > $HBPz_3$ > Pz). The ligand field and AOM calculations confirmed this ordering. Further, the theoretical work has shown that the in-plane tilting of the pyrazolyl rings is important even for the monodentate pyrazolyl complexes.

Raman spectroscopy was employed in the study of $[Co(H_2O)_6](BrO_3)_2$ and $[Co(HCPz_3)_2](NO_3)_2$ with the aim of observing the predicted electronic Raman peaks. High quality Raman spectra were measured for both $[Co(H_2O)_6](BrO_3)_2$ and $[Co(HCPz_3)_2](NO_3)_2$, with a good signal to noise ratio for the vibrational peaks. Unfortunately, no electronic Raman transitions could be identified for either compound. This is most likely to be due to peak broadening (as a result of short lifetimes), to the extent that the peaks can no longer be observed above the background noise.

# Table of contents

# List of figures

# List of tables

# Chapter 1: Spectroscopic methods, theory and literature history

This chapter presents an outline of the theory of various spectroscopic methods used in this thesis; namely absorption spectroscopy, electron paramagnetic resonance and Raman spectroscopy, including some discussion of the electronic Raman effect.

The discussion of each of the spectroscopic techniques is accompanied by a literature history relating to the use of the technique in some cobalt(II) and nickel(II) systems.

## 1.1 Polarised absorption spectroscopy

### 1.1.1 Theory

Polarised absorption spectroscopy using single crystals gives much more information than can be obtained when absorption spectra are measured using solutions. In a crystal, the chemical species of interest has a known orientation (or set of orientations) with respect to the crystal faces, provided the crystal structure is also known. By contrast, in a solution the chromophore has all possible orientations and the system is optically isotropic.

This knowledge of the orientation of the chromophore within the crystal allows in many cases for determination of the symmetry of electronic transitions through the Laporte (parity) and symmetry selection rules. Measurement of spectra for single crystals allows the distinction of electric- and magnetic-dipole transitions for uniaxial crystals. Species that are unstable or non-existent in solution can sometimes be studied spectroscopically within a crystal. Crystals are also easily studied at low temperature (down to a few kelvins). Measurement of spectra at low temperature offers several advantages. Often resolution is greatly improved as linewidths become narrower due to the depopulation of vibrationally excited levels. In some cases, complexes exist in a different spin state at low temperatures, and therefore exhibit completely different spectral properties than at room temperature. Inhomogeneous broadening of the

absorption bands is much reduced for crystals due to the reduced variation in the environments of the chromophores in crystals when compared with a glass or a solution. Finally, some species may be unstable in solution at room temperature.

Naturally, there are some disadvantages. One of these is that the technique is not universally useful for all crystal systems. Cubic crystals are optically isotropic, so the absorption spectra (like those of a solution or glass) do not show any polarisation behaviour for electric or magnetic dipole transitions. However, there will be other advantages to single crystal spectra, such as the reduced inhomogeneous broadening.

For crystal symmetries lower than cubic, the realities of crystal optics (i.e. birefringence)[1,2] can complicate or render impractical the measurement of spectra, particularly for triclinic crystals, or monoclinic crystals when light is propagated parallel to the unique axis. Finally of course, it may not be possible to grow crystals of sufficient optical quality.

The theory and previous work in polarised absorption spectroscopy of single crystals has been reviewed a number of times over the years[3-5], so a brief description of the theory will suffice.

The theoretical treatment of polarised absorption spectroscopy involves the use of quantum mechanics and group theory. Using the Schroedinger wave equation, a molecule is described using a mathematical function called the wavefunction $\Psi$. This wavefunction describes all the information about the molecule, such as geometry, vibrational frequencies, electronic energy levels etc. Observable properties of the molecule such as linear momentum, kinetic energy etc are obtained by applying the appropriate operator to the wavefunction.

A wavefunction can be written for each electronic energy level of a molecule. In absorption spectroscopy, a transition can in principle occur between a lower energy level $\psi_i$ and a higher energy level $\psi_f$ when the frequency of the incident light corresponds to the energy difference between the two levels. The rate of the transition can be determined theoretically from the matrix element:

$$\langle \psi_f | \hat{x} | \psi_i \rangle \quad (1.1)$$

where $\hat{x}$ is a quantum mechanical operator: usually $\hat{\mu}$ the electric dipole moment operator or $\hat{m}$ the magnetic dipole moment operator. A transition can also occur through higher order moments, such as through the electric quadrupole moment, however, these are much weaker and therefore not usually observed.

The matrix elements of the electric or magnetic dipole are isotropic, which has important group-theoretical implications. The group theoretical representation of a scalar in any point group is the totally symmetric representation. Therefore, for the overlap integral (and hence the intensity) to be non-zero, the direct product of the irreducible representations of the initial and final state wavefunctions, and the transition dipole moment operator must contain the totally symmetric representation of the point group of the molecule:

$$A_{1g} \in \Gamma_{\psi_f} \otimes \Gamma_{\hat{x}} \otimes \Gamma_{\psi_i} \quad (1.2)$$

The representations of the electric dipole operator are the same as those for the respective Cartesian x, y and z axes, while the representations of the magnetic dipole operator are the same as those for the rotations about the Cartesian axes ($R_x$, $R_y$, $R_z$). The appropriate representation can be obtained from a character table for the appropriate point group. If the condition of equation 1.2 is met, then a transition is allowed according to the symmetry selection rule. The intensity of such transitions varies, but is generally high. In many cases, the condition of equation 1.2 is not met and the transition is symmetry-forbidden. Transitions between electronic states formed from partially-filled d orbitals in octahedral transition metal complexes fall into this category, as all of these states have even parity, and transitions are only allowed between states of different parity according to the Laporte selection rule. However, a symmetry-forbidden transition can gain intensity through the vibronic coupling mechanism. In the case of transitions between electronic states of even parity, this involves the coupling of a single quantum of a molecular vibration of odd parity (and the appropriate symmetry) to give a vibronically-allowed transition.

The wavefunction of an electronic state consists of a spin part as well as the orbital part discussed above. By the spin selection rule, transitions are only allowed between electronic states of the same spin. Spin-forbidden transitions do occur in reality, through spin-orbit coupling. For example, a transition between a singlet ground state and a triplet excited state can gain intensity through mixing of nearby singlet excited states with the triplet state, giving the triplet excited state some singlet character, and results in a partially spin-allowed transition. The transition intensity depends on the size of the spin-orbit coupling. This increases with increasing atomic weight, resulting in spin-orbit coupling being larger than crystal field effects for the lanthanides for example. Spin-orbit coupling is strongest when the states in question lie close to one another, i.e. spin-forbidden transitions are more intense when they lie close in energy to spin-allowed ones. A similar mechanism can enhance the intensity of symmetry- and parity-forbidden transitions when a state of appropriate symmetry lies close in energy.

### 1.1.2 Instrumentation

A typical spectrometer used for low-temperature absorption spectroscopy of single crystals consists of a continuum light source (usually a tungsten filament lamp for spectra in the visible/near region and a deuterium or xenon lamp for the near-UV spectral region), a single-grating monochromator, a polariser, a sample compartment, and a detector. Detectors are usually photomultiplier (PM) tubes for visible or near UV work, and solid-state detectors for IR work.

The instrument employed to measure the absorption spectra for this thesis is a specialist single-beam spectrometer developed within the Krausz group[6,7] and optimised for measuring spectra of very small crystals. This incorporates a Spex 1704 one-metre single monochromator and a PM tube for the near-UV and visible region, a silicon photodiode for the visible-near IR region, or an indium antimonide detector for work further into the infrared. The light source is a 150 W quartz halogen lamp, while signals are processed through a Stanford Research SR510 lock-in amplifier and a PC running a QuickBasic program which also controls the monochromator.

The use of small crystals (even as small as 20 μm) has a number of advantages; lower optical density, which means that more light reaches the detector reducing the problem

of background noise, and the fact that smaller crystals generally have higher optical quality and are easier to grow. Single beam measurements have the advantage of more accurate baselines incorporating all effects such as those of the flow tube, plus construction of the instrument is simpler and more compact. A baseline is collected over the same wavelength range as the spectrum, and the absorbance values as a function of the wavelength (the absorption spectrum) are computed using the relation:

$$A = \log_{10} \frac{I_0}{I} \quad (1.3)$$

where A is the absorbance at wavelength $\lambda$, $I_0$ is the light intensity measured for the baseline at wavelength $\lambda$, and I is the light intensity measured for the spectrum at $\lambda$

In this thesis, the computation of absorbance data from the raw intensity data was achieved using Microsoft Excel spreadsheets. Spreadsheets were also used for in the calibration of the wavenumber values using neon lamp lines in the visible region, or water vibrational overtones in the near infrared region.

Sample cooling can be accomplished using either a cryostat, or a quartz flow tube cooled by a flow-through stream of cold nitrogen or helium[8].

### 1.1.3 Absorption spectroscopy in cobalt and nickel complexes

Divalent cobalt has the $d^7$ configuration, of which there are 120 possible microstates. Electron repulsion splits the microstates into terms, eight in the case of a free atom or ion with the $d^7$ configuration ($^2H$, $^2G$, $^4F$, $^2F$, two $^2D$ terms, $^4P$ and $^2P$). By Hund's rule, $^4F$ lies lowest in energy. Divalent nickel has the $d^8$ configuration of which there are 45 possible microstates. These are split into five terms by electron repulsion ($^3F$, $^3P$, $^1G$, $^1D$ and $^1S$), of which the $^3F$ lies lowest by Hund's rules.

For transition metals, the term energies are most commonly described using the Racah electron repulsion parameters A, B and C, as discussed in most texts on transition metal spectroscopy and ligand field theory. For example see the monographs by Figgis and Hitchman[9], Griffith[10], Kettle[11] or Schlaefer and Gliemann[12], or the work of Brorson and

Schaeffer[13]. The Racah parameters[14] are linear combinations of another set of parameters, the Condon-Shortley parameters $F_0$, $F_2$ and $F_4$:

$$A = F_0 - 49F_4$$
$$B = F_2 - 5F_4$$
$$C = 35F_4 \qquad (1.4\text{-}1.6)$$

In turn, the Condon-Shortley parameters[15] are fractions of the radial integrals $F_0$, $F_2$ and $F_4$ derived from the Coulomb and exchange operators of the many-electron Schroedinger equation by Slater[16].

The main advantage of the Racah parameters over the Condon-Shortley parameters are that separations between the ground term and excited terms with the same spin multiplicity depend on a single parameter, B.

For a $d^7$ configuration (e.g. $Co^{2+}$), the term energies using the Racah parameters are[10]:

$$E(^4F) = 3A - 15B$$
$$E(^4P) = 3A$$
$$E(^2H) = E(^2P) = 3A - 6B + 3C$$
$$E(^2G) = 3A - 11B + 3C$$
$$E(^2F) = 3A + 9B + 3C$$
$$E(^2D) = 3A + 5B + 5C \pm (193B^2 + 8BC + 4C^2)^{1/2} \qquad (1.7\text{-}1.12)$$

For a $d^8$ configuration (e.g. $Ni^{2+}$) the term energies are[10]:

$$E(^3F) = A - 8B$$
$$E(^3P) = A + 7B$$
$$E(^1G) = A + 4B + 2C$$
$$E(^1D) = A - 3B + 2C$$
$$E(^1S) = A + 14B + 7C \qquad (1.13\text{-}1.17)$$

As can be seen from the above expressions, the energy separations of the excited terms from the ground term do not depend on A. Therefore, in spectroscopic studies of transitions between terms of $d^N$ configurations, only the parameters B and C need to be

considered. From the above equations, for both $d^7$ and $d^8$ configurations, the excited term of the same multiplicity as the ground term is separated from the ground term by an amount 15B (see figures 1.1 and 1.2). The Racah parameters for free ions are tabulated in several references, for example, Figgis and Hitchman[9]. For $Co^{2+}$, B = 989 $cm^{-1}$, and for $Ni^{2+}$, B = 1042 $cm^{-1}$.

In a transition metal complex, the electron repulsion, and hence the Racah parameters are reduced from their free electron values, by an amount dependent on the identity of the metal ion, its charge and the identity of the ligand. This is known as the nephelauxetic effect, and the ratio $\beta = B_{complex}/B_{free\ ion}$ is the nephelauxetic ratio. There are two causes for the nephelauxetic effect, firstly, due to the presence of the ligand electrons, the effective nuclear charge of the metal in a complex is reduced compared with the free ion, and secondly, the electrons can be delocalised into the ligand orbitals. Ligands are arranged into a nephelauxetic series in order of their ability to reduce electron repulsion. Those which form bonds with a greater degree of covalency generally show a stronger nephelauxetic effect, for example iodide is higher in the nephelauxetic series than fluoride.

When a spherically symmetric free ion is complexed with six ligands, the symmetry is reduced to, at best, octahedral. The ion now experiences an additional field due to the ligands, and the free ion terms undergo further splitting. This splitting is described using ligand field theory, which is described in detail in many monographs such as those of Gerloch and Slade[17], Figgis and Hitchman[9], Schlaefer and Gliemann[12], and Ballhausen[18]. The separation of the terms in octahedral symmetry is a function of the octahedral ligand field splitting parameter $\Delta$. This parameter can be calculated from first principles, but is more usually derived from experiment. As with the nephelauxetic ratios, values of $\Delta$ depend on the ligand identity and the metal ion identity and oxidation state. Ligands are arranged in an analogous manner to the nephelauxetic series (the spectrochemical series). A ligand giving rise to a relatively high value of $\Delta$ is said to give a strong ligand field.

The $^4F$ and $^4P$ free ion terms of cobalt(II) split in an octahedral ligand field according to the pattern in figures 1.1 and 1.2. The $^4F$ term splits to give a $^4T_{1g}$ term lying lowest in octahedral symmetry, with $^4T_{2g}$ and $^4A_{2g}$ terms lying above, while the $^4P$ term yields a $^4T_{1g}$ term in an octahedral complex. Doublet states also lie in this region, mainly

originating from the $^2G$ free ion term. The observable spin-forbidden transitions usually give sharp peaks, while spin-allowed transitions give broader peaks (often a few thousand wavenumbers). In hexaquo cobalt complexes ($[Co(H_2O)_6]^{2+}$), the lowest energy transition ($^4T_{2g} \leftarrow {}^4T_{1g}$) is usually observed in the near IR at around 8000 $cm^{-1}$. The $^4T_{1g}(^4P) \leftarrow {}^4T_{1g}(^4F)$ transition is usually observed in the blue-violet region of the spectrum at around 21000 $cm^{-1}$. The $^4A_{2g} \leftarrow {}^4T_{1g}$ transition corresponds to a two-electron transition in the strong field limit, and is usually weak and difficult to detect. It is often obscured due to overlap with the nearby $^4T_{1g}(^4P) \leftarrow {}^4T_{1g}(^4F)$ transition. As a result of the absorption peak in the blue at around 21000 $cm^{-1}$, compounds containing the $[Co(H_2O)_6]^{2+}$ ion are pale red. The pyrazolyl ligands studied in this work are stronger field ligands than water, resulting in a blue shift of the absorption peaks, and giving compounds that are yellow or orange.

The octahedral terms are split further by two additional effects, which for first-row transition metal are of similar magnitude, namely spin-orbit coupling and low symmetry perturbations of the ligand field.

Spin-orbit coupling is a relativistic effect arising from the interaction of the magnetic moments of the electron arising from the orbital and spin angular momenta. The magnitude of the spin-orbit coupling of an electron within a configuration is described by the single-electron spin orbit coupling parameter $\zeta$, which is a property of the configuration. The spin-orbit coupling parameter $\lambda$ of the term (rather than a single electron) is related to $\zeta$ by the following equation:

$$\lambda = \frac{\pm\zeta}{2S} \quad (1.18)$$

where S is the total spin of the term. $\lambda$ is positive for d subshells less than half full, and negative when the d subshell is more than half full.

Spin-orbit coupling parameters can be calculated from fundamental atomic parameters[9,12], and free-ion values are tabulated, for example see Dunn[19]. Like the Racah parameters, the spin-orbit coupling parameters are reduced on the formation of a complex, and through similar mechanisms, i.e. reduction of the effective charge of the

metal ion, and delocalisation of electron density onto the ligands. The reduction in $\zeta$ is quantified using a parameter k, the orbital reduction factor:

$$\zeta_{complex} = k\zeta_{free\ ion} \quad (1.19)$$

The difference in k from 1 is a measure of the covalency of the metal-ligand bonding.

Spin-orbit coupling is dependent on the atomic number of the element, and becomes significantly larger for the heavier elements, for example for the $Fe^{2+}$ free ion, $\zeta = 400$ $cm^{-1}$, whereas for $Os^{2+}$, $\zeta \approx 3000$ $cm^{-1}$. As result, spin-orbit coupling is usually considered as a perturbation on the ligand-field split terms for the first-row transition metal complexes, whereas for third-row transition metals and the lanthanides, the splitting due to spin-orbit coupling can be comparable or larger than that of the ligand field.

Trigonal splitting is discussed in more detail in chapter 4.

The splitting pattern of the $^4T_{1g}$ ground octahedral term by trigonal ligand field perturbation and spin-orbit coupling is illustrated in figures 1.1 and 1.2 below, for octahedral complexes with symmetry reduced to $D_{3d}$. The approximate symmetry of the capped pyrazolyl complexes studied in this thesis is $D_{3d}$. The other complexes studied (the bromate hexahydrate and the monopyrazolyl complexes) have exact $S_6$ symmetry. Because cobalt(II) complexes are odd-electron systems, double group irrep symbols are employed to describe the states formed by trigonal splitting and spin-orbit coupling. Figures 1.1 and 1.2 are adapted from diagrams by Jesson[20] and Guha[21] respectively. The splitting patterns are different depending on the relative strengths of the trigonal field and the spin-orbit coupling. The excited states are similarly split by trigonal ligand fields, for example, the $^4T_{2g}$ first excited state splits into a $^4A_{1g}$ and $^4E_g$ states in a field with $D_{3d}$ symmetry. The trigonal states are further split by spin-orbit coupling.

Since the peaks in absorption spectra are usually fairly broad, the trigonal field strength is usually less than the peak width, so any splitting is usually only observed as a peak broadening, or the appearance of a shoulder.

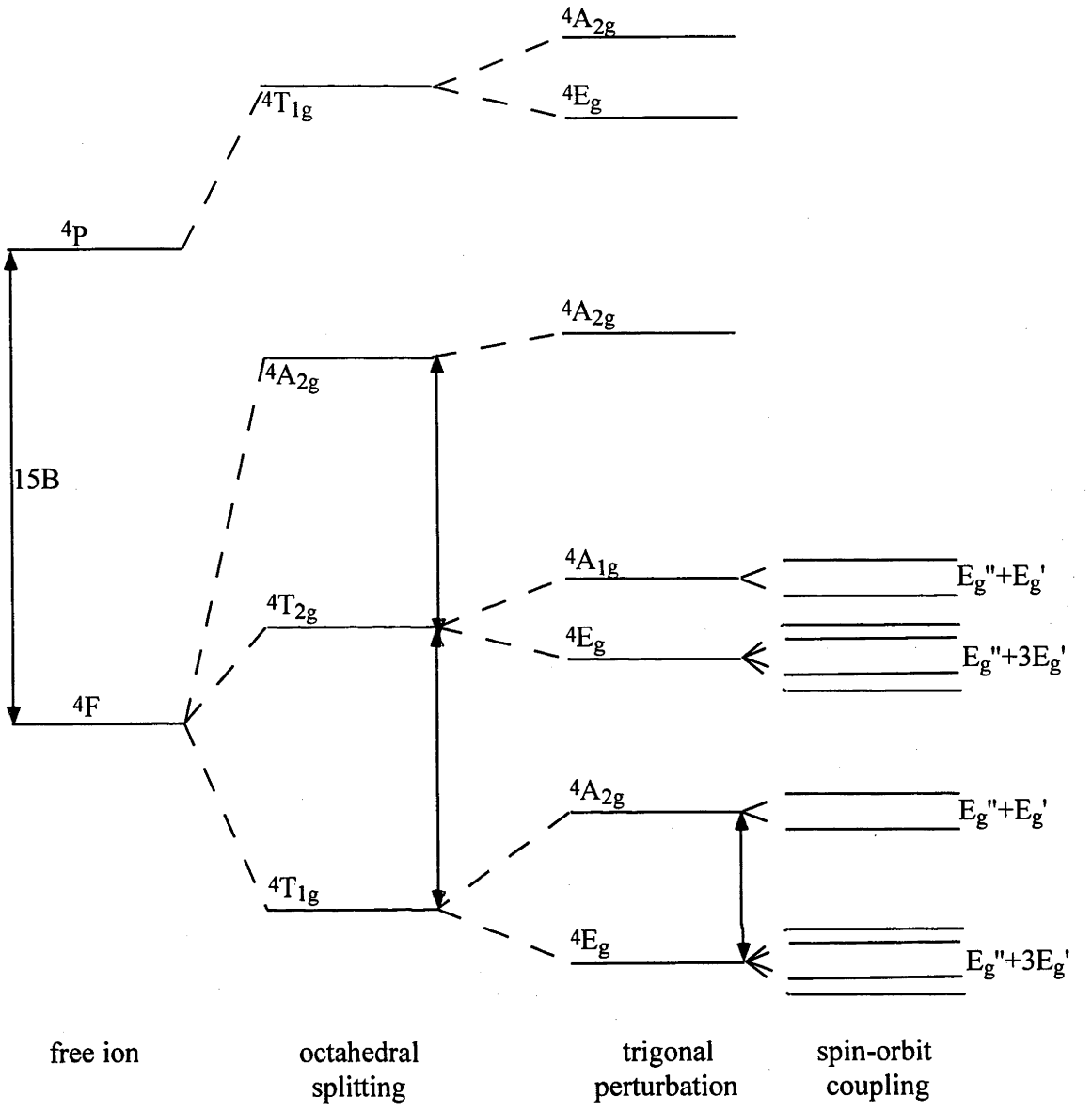


**Figure 1.1: Ground state trigonal splitting in high spin $d^7$ complexes: Spin-orbit coupling < trigonal splitting**

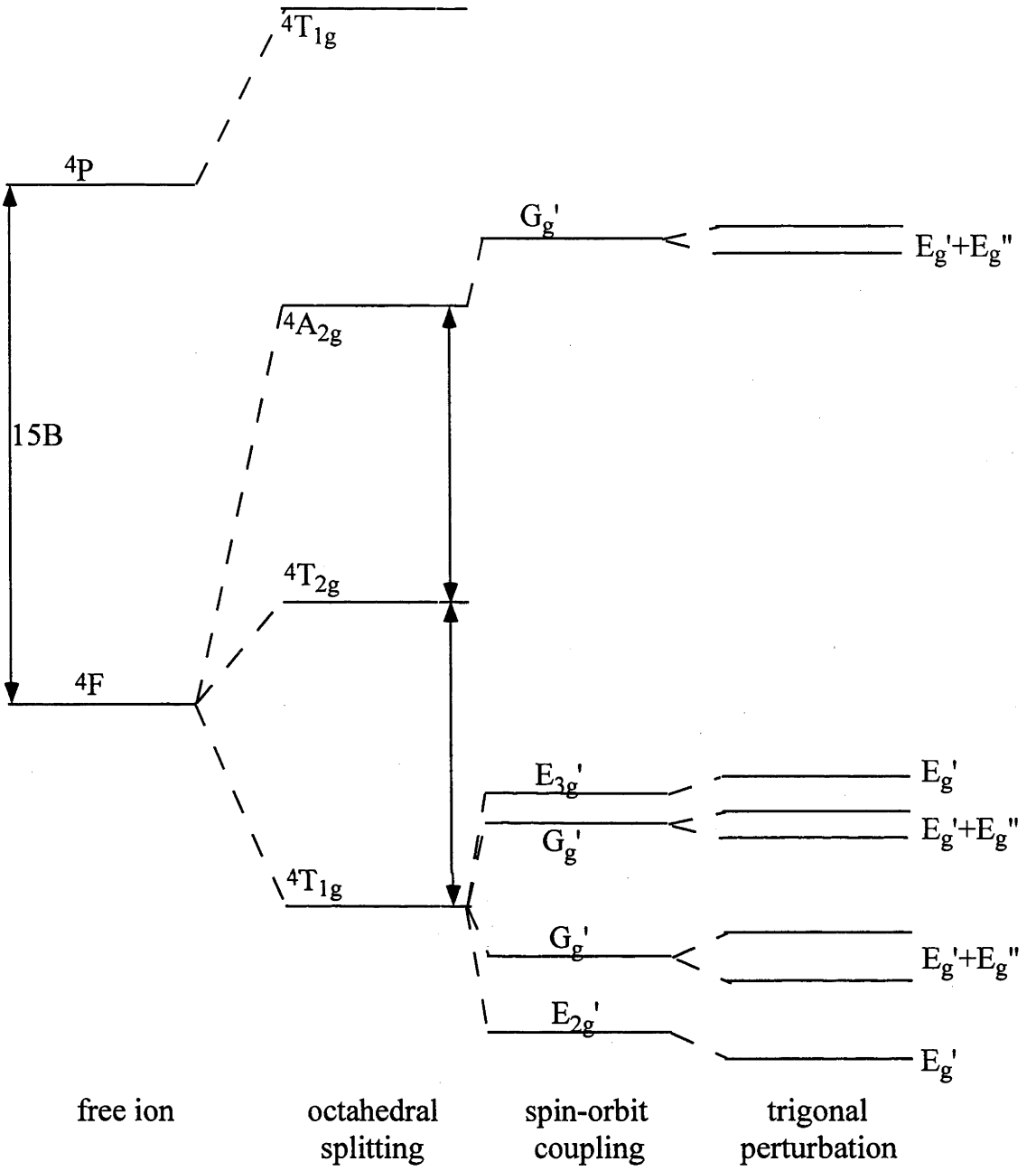


**Figure 1.2: Ground state trigonal splitting in high spin $d^7$ complexes: Spin-orbit coupling > trigonal splitting**

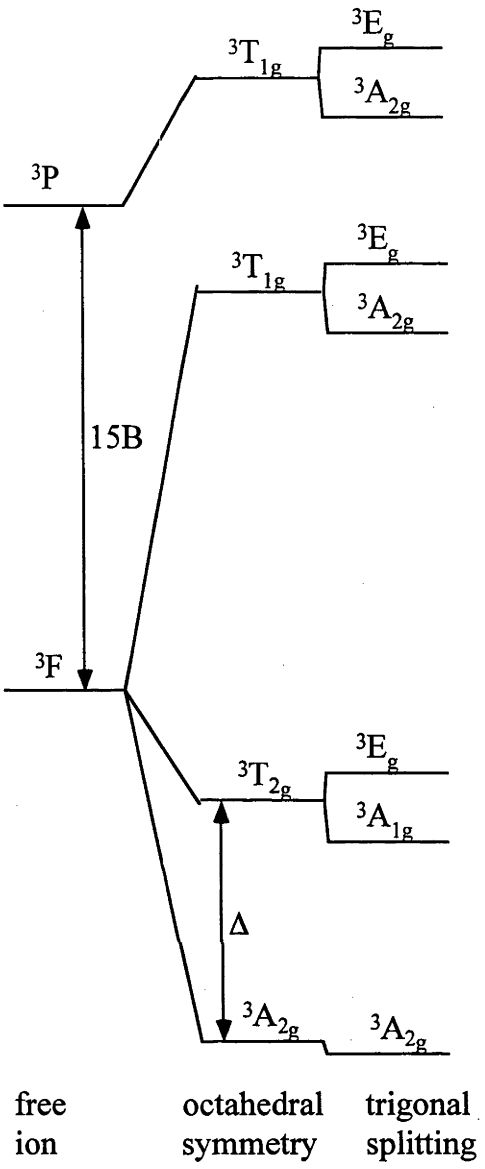


**Figure 1.3: A $d^8$ system in a trigonally-split cubic field**

The $^3F$ and $^3P$ free ion states of nickel(II) split in an octahedral ligand field according to the pattern in figure 1.3. The separation between the ground term $^3A_{2g}$ and the first excited term $^3T_{2g}$ is exactly equal to the octahedral ligand field splitting parameter Δ. Interspersed amongst these octahedral triplet states are two singlet states ($^1T_{2g}$ and $^1E_g$) arising from the $^1D$ free ion state, and the $^1A_{1g}$ from the $^1G$ free ion state. The $[Ni(H_2O)_6]^{2+}$ ion is green, resulting from peaks at 8700 $cm^{-1}$ ($^3T_{2g} \leftarrow {}^3A_{2g}$), 14500 $cm^{-1}$ ($^3T_{1g}(^3F) \leftarrow {}^3A_{2g}$) and 25300 $cm^{-1}$ ($^3T_{1g}(^3P) \leftarrow {}^3A_{2g}$). These values were measured in aqueous solution[9]. All of these transitions are due to one-electron jumps in the strong field limit. A shoulder at 14 000 $cm^{-1}$ is assigned to the spin-forbidden transition

$^1E_g \leftarrow {}^3A_{2g}$, which gains intensity through strong spin-orbit coupling with an $E_g$ spin-orbit component of the nearby triplet state $^3T_{1g}(^3F)$[22]. The stronger field pyrazolyl ligands used in this work give blue or purple nickel(II) complexes. The octahedral excited states of the nickel(II) ion are further split by a trigonal field (figure 1.3). The ground $^3A_{2g}$ state can be amenable to study by EPR spectroscopy, as a result of its splitting by second-order spin-orbit coupling, which is affected by the trigonal field, into two levels (see section 1.2.3 and figure 1.5 below).

## 1.2 Electron paramagnetic resonance (EPR) spectroscopy

EPR is a manifestation of the electronic Zeeman effect, although other effects such as spin-spin coupling (zero-field splitting), electron-nucleus hyperfine interaction, the nuclear Zeeman effect, and nuclear quadrupolar coupling can play a role and modify the spectra. Experimentally, EPR spectroscopy involves the measurement of microwave frequency transitions between molecular energy states formed when degenerate electronic energy levels are split by an applied magnetic field (the Zeeman effect). The technique was pioneered in 1944 by Zavoiski[23]. Several monographs describing the theory of the technique (and its application to transition metal compounds) exist, including those of Abragam and Bleaney[24], Pilbrow[25] and Mabbs and Collison[26]. Commonly studied systems include organic free radicals, transition metal, lanthanide and actinide compounds, metals, semiconductors, and solid state defects such as trapped electrons.

Many different effects can take place in a single EPR system, besides the electronic Zeeman effect. These include the nuclear Zeeman effect (responsible for NMR), hyperfine coupling between electron spin and nuclear spin and coupling between electron spins in systems with more than one unpaired electron (S>1/2). EPR is described phenomenologically using a formula known as the spin Hamiltonian (equation 1.20).

$$H = H_{FS} + \beta \hat{B} \cdot \tilde{g} \cdot \hat{S} + \hat{S} \cdot \tilde{D} \cdot \hat{S} + \hat{I} \cdot \tilde{A} \cdot \hat{S} + \hat{I} \cdot \tilde{P} \cdot \hat{I} - \tilde{g}_n \beta \hat{B} \cdot \hat{I} \quad (1.20)$$

where $H_{FS}$ is a fine-structure term; $\beta$ is the Bohr magneton; $\hat{B}$ is the magnetic field vector; $\tilde{g}$ is the electronic g-value tensor; $\hat{S}$ and $\hat{I}$ are the vectors representing electron and nuclear spin respectively; $\tilde{D}$, $\tilde{A}$ and $\tilde{P}$ are tensors representing the electron-electron coupling, electron-nuclear hyperfine coupling and nuclear quadrupolar coupling respectively; and $\tilde{g}_n$ is the nuclear g-value tensor. $\tilde{g}$, $\tilde{g}_n$, $\tilde{D}$, $\tilde{A}$ and $\tilde{P}$ are all second-rank tensors.

Transition energies in EPR spectra are generally of the order of 0.1-1 $cm^{-1}$ (in the microwave energy range) for the magnetic fields commonly employed.

### 1.2.1 Instrumentation

Continuous wave (CW) EPR systems require a microwave source (usually a klystron), waveguides and a sample cavity, a magnet, and detector. Most EPR systems have computer control of all these pieces of equipment. Water-cooled electromagnets are commonly used for magnetic fields up to approximately 1.4 tesla, while superconducting, liquid helium cooled magnets are required for higher fields. The magnetic field is usually modulated at a frequency of about 100 kHz, with the signal being detected using a lock-in amplifier and recorded as the first derivative. Nearly all CW-EPR systems operate with a fixed microwave frequency and scanned magnetic field. Several different frequencies are used, of which the two commonest are 9 GHz (X band) and 34 GHz (Q band). Higher frequency techniques (e.g. W-band, 95 GHz) employing superconducting magnets to give the necessary higher fields have extended the range of systems giving a measurable EPR spectrum. Most EPR spectrometers have some facility for sample cooling, in order to increase the spin-lattice relaxation time, thus reducing line broadening, which can often be a problem for transition metal containing samples. More recently, Fourier transform instruments (FT-EPR) have become more widely available, offering similar advantages to FT-NMR.

### 1.2.2 EPR spectroscopy of cobalt(II): theory and literature survey

Referring to figures 1.1 and 1.2 above, it can be seen that the ground level of an axially distorted high spin $d^7$ system (such as a cobalt(II) complex) is a Kramers doublet. The twofold degeneracy of this level is lifted when a magnetic field is applied to the system, as in an EPR experiment. Axially distorted high spin cobalt(II) therefore behaves as an effective S = 1/2 system in an EPR experiment even though in reality, it has S = 3/2, as well as non-zero orbital angular momentum. The mean g value differs markedly from the free electron value. Further, the g-value anisotropy (the difference between $g_{\|}$ and $g_{\perp}$, the g-values for transitions occurring when the magnetic field is, respectively, applied parallel or perpendicular to the molecular symmetry axis) of the system gives a very good measure of the degree of axial distortion in the system.

The second-rank $\tilde{g}$ tensor of a rhombic system is usually diagonalised to leave the principal tensor componenents (g-values) $g_{xx}$, $g_{yy}$ and $g_{zz}$. In a system with axial symmetry, $g_{\|} = g_{zz}$, and $g_{xx} = g_{yy} = g_{\perp}$.

It must be recognised that $g_{\|}$ and $g_{\perp}$ represent the maximum and minimum of the $\tilde{g}$ tensor components. If the magnetic field is at an angle $\theta$ to the molecular axis, then a transition with a g-value given by equation 1.21 will be observed:

$$g^2 = g_{\|}^2 \cos^2\theta + g_{\perp}^2 \sin^2\theta \quad (1.21)$$

This relationship is derived[24] from a more general relationship for complexes with rhombic symmetry that relates the g-value observed for a magnetic field in an arbitrary direction with respect to the principal directions to the principal g-values $g_{xx}$, $g_{yy}$ and $g_{zz}$:

$$g^2 = g_{xx}^2 l^2 + g_{yy}^2 m^2 + g_{zz}^2 n^2 \quad (1.22)$$

where l, m and n are the cosines of the angles between the magnetic field direction and the x-, y-, and z-axes (of the complex) respectively (the direction cosines).

In a powder EPR spectrum (all spectra measured for this thesis are powder spectra), provided there is no preferential alignment of the individual paramagnetic centres in the external magnetic field, all orientations of the molecular axis with respect to the direction of the external field are equally probable. Therefore, a spectrum with a continuum of g-values from $g_\perp$ to $g_\parallel$ will be observed. EPR spectra are nearly always recorded and plotted as the first derivative of the absorbance. For an S = 1/2 system (or a pseudo S' = 1/2 system, such as high spin Co(II)) with axial symmetry, this results in an 'absorption-like' Lorentzian (in the absence of inhomogeneous broadening) feature and a sigmoidal feature. These features correspond to the extrema of the g-values, i.e. $g_\parallel$ and $g_\perp$ respectively. If $g_\parallel > g_\perp$, then the $g_\parallel$ feature will be observed at low field, and the $g_\perp$ feature at high field, if $g_\perp > g_\parallel$, then the reverse will be observed. Given that there is a greater probability of a paramagnetic centre being aligned perpendicular to the external field (the field direction can lie anywhere in the xy plane) than parallel to the field, the intensity of the 'perpendicular' feature is greater than that of the 'parallel' feature.

The previous four paragraphs describe the spectral features resulting from the second term of the spin Hamiltonian (equation 1.20), the electronic Zeeman effect.

As the only stable isotope of cobalt ($^{59}Co$) has a non-zero nuclear spin (I = 7/2), the other important feature in the EPR spectra of high spin Co(II) systems is the hyperfine splitting, represented by the fourth term of equation 1.20. Hyperfine splitting results from coupling between the nuclear and electronic spins. In the zero- or weak-field region, the coupling is described using a coupling scheme analogous to spin-orbit coupling, where S and I are coupled to give the total spin F, and F = S + I, S + I – 1,...., |S – I|. These energy levels formed by the coupling of the electron and nuclear spin are then split by the magnetic field into states with magnetic quantum numbers $m_F$ ranging from –F to +F.

In the strong-field region, i.e. the energy level splittings due to the magnetic field are large compared with the splittings due to the spin-spin coupling, the electron and nuclear spins are uncoupled, and the nuclear spin interaction is considered as a perturbation on the electron states split by the magnetic field. This is the Back-Goudsmit region, which is an analogous to the Paschen-Back region where orbital and spin angular momenta uncouple in magnetic fields giving rise to larger splittings than

the spin-orbit coupling. It is the region of most interest for standard EPR experiments. In the Back-Goudsmit region, in classical terms, the nuclear spin moment is considered to precess about the field resulting from the combination of B (the external field) and $B_e$ (the steady-state component of the magnetic field resulting from the precessing electron spin moment, and which is parallel to B). Similarly, the electron spin moment is considered to precess about the resultant magnetic field $B + B_n$, where $B_n$ is the steady-state component of the magnetic field due to the precessing nuclear spin moment (which is parallel to B). In other word, in the Back-Goudsmit region, the two angular momenta are precessing independently about B, while in the weak-field (Zeeman) region, the two angular momenta are coupled.

Coupling of electron and nuclear spins results from two mechanisms:

- the Fermi contact interaction, which is due to the mixing of s-orbitals into the d-orbitals containing the unpaired electrons. In an s-orbital, there is a non-zero probability of an electron being at the nucleus.
- the through-space interaction of the electron and nuclear spins.

In an EPR spectrum of a high spin Co(II) system with axial symmetry, the hyperfine interaction splits each of the two main features arising from the transition between the electronic Zeeman states into eight peaks. The hyperfine splitting in high spin Co(II) is illustrated in figure 1.4 below. In the Back-Goudsmit region, the spin Hamiltonian for a high-spin $d^7$ system is:

$$H = \tilde{g}\beta_e \hat{B}^T \cdot \hat{S} + \hat{S} \cdot \tilde{A} \cdot \hat{I} \quad (1.23)$$

Like $\tilde{g}$, the hyperfine tensor $\tilde{A}$ is a second-rank tensor, and is often diagonalised to eliminate all but the principal hyperfine coupling parameters $A_{xx}$, $A_{yy}$, and $A_{zz}$ (in rhombic symmetry). In most systems, the principal axes of the hyperfine coupling tenstor coincide with the principal axes of the $\tilde{g}$ tensor. For an axially symmetric system, $A_{zz} = A_{\|}$, and $A_{xx} = A_{yy} = A_{\perp}$. Again, the values $A_{\|}$ and $A_{\perp}$ are the extrema of the hyperfine coupling parameters, and the value of A in an arbitrary direction with respect to the principal axes is determined by an equation analogous to equation 1.21.

$$g^2A^2 = g_{\|}^2A_{\|}^2\cos^2\theta + g_{\perp}^2A_{\perp}^2\sin^2\theta \quad (1.24)$$

Hyperfine coupling parameters have units of energy, and are usually of the order 0.01 $cm^{-1}$. Given that for X-band EPR spectra, the transition energy is about 0.3 $cm^{-1}$, the hyperfine coupling is observed as a splitting of the main peaks, as discussed above.

The state energies are given by:

$$E = g\beta_e BM_{S'} + AM_{S'}M_I \quad (1.25)$$

In the Back-Goudsmit region, the selection rules for the fully allowed tranistions are $\Delta M_S = \pm 1$ and $\Delta M_I = 0$. Given that $M_{S'} = 1/2$ for Co(II), the transition energies are therefore:

$$h\nu = g\beta B + AM_I \quad (1.26)$$

and given that for $^{59}Co$, $M_I = -7/2, -5/2, \ldots, +7/2$, each of the two principal features in an EPR spectrum of an axially symmetric system are split into eight peaks with an energy separation of A between each peak (see figure 1.4). As the hyperfine coupling parameters are of the order 0.01 $cm^{-1}$, even at the liquid helium temperatures usually employed for EPR spectroscopy of Co(II), the Boltzmann factor $e^{\frac{-h\nu}{kT}}$ is close to 1, i.e. the different states formed by the hyperfine splitting are nearly equally populated, and the peaks have near-equal intensity.

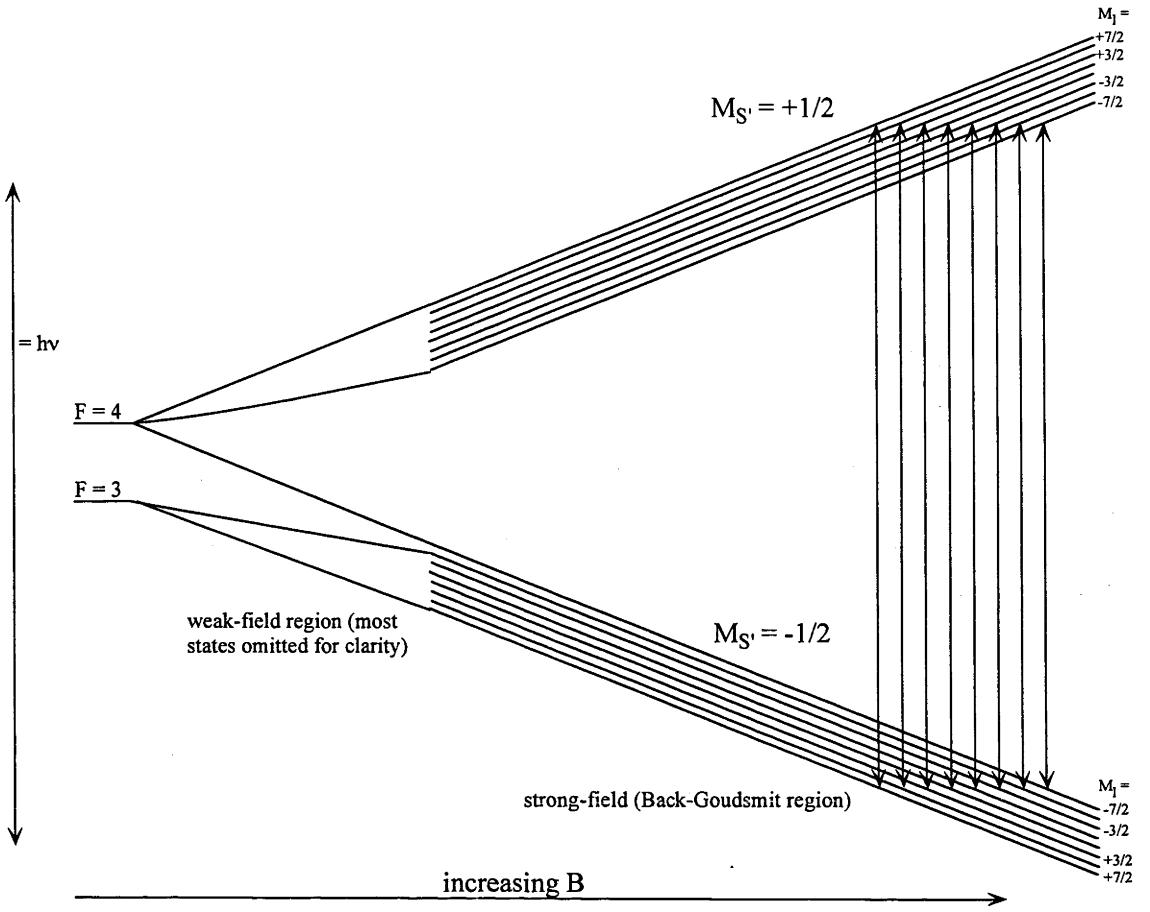


**Figure 1.4: Hyperfine splitting in the EPR spectra of high spin Co(II)**

EPR spectroscopy has been used a great deal since the early days of the technique to study both trigonally and tetragonally distorted octahedral high-spin cobalt(II) complexes[24-27]. A few representative examples of the use of EPR spectroscopy in the investigation of axial distortion in high spin cobalt(II) complexes will be discussed here.

The EPR spectra of cobalt in various halide lattices such as $CdCl_2$ and $CsCdCl_3$ have been studied by Edgar[28] and Christie et al[29]. Other authors have employed Zeeman Raman spectroscopic measurements to determine g-values for the five excited Kramers doublets[30,31]. Zeeman Raman spectroscopy involves measuring a Raman spectrum for a sample in a magnetic field to observe the Zeeman splitting of the excited Kramers doublets. In the lattices with the cadmium chloride structure, it was observed that $g_{\|}<g_{\perp}$, while for the double halides ($ABX_3$) type structures, $g_{\|}>g_{\perp}$. This is as expected, since all the structures are trigonally distorted, and cadmium chloride structures have $\theta>54.74°$ (trigonal compression), while for the double chloride $ABX_3$ structures,

$\theta<54.74°$ (trigonal elongation). $\theta$ is the trigonal cone angle, and 54.74° is the value for a perfect octahedron (see chapter 4 for a more detailed description).

The EPR spectra of the ammonium and potassium cobalt Tutton salts, $(NH_4)_2[Co(H_2O)_6](SO_4)_2$ and $K_2[Co(H_2O)_6](SO_4)_2$, were first measured in 1951[32]. These both crystallise in monoclinic space groups[33,34], with the $[Co(H_2O)_6]^{2+}$ ions lying on a centre of inversion, but having the approximate symmetry of a slightly tetragonally compressed octahedron. The EPR spectrum of $(NH_4)_2[Co(H_2O)_6](SO_4)_2$ showed a purely axial spectrum, while $K_2[Co(H_2O)_6](SO_4)_2$ had a significant rhombic component.

The hexahydrates of the first row transition metal hexafluorosilicates ($[M(H_2O)_6]SiF_6$) form an isomorphic series at room temperature, crystallising in the trigonal space group $R\bar{3}$. There is a single type of metal hexahydrate ion, with $S_6$ site symmetry. An axial EPR spectrum is therefore expected. Bleaney and Ingram reported EPR spectra of $Co^{2+}$ doped into $[Zn(H_2O)_6]SiF_6$, and determined $g_{\|} = 5.82$, $g_{\perp} = 3.44$[32]. Francis and Culvahouse measured the EPR spectrum of $Co^{2+}$ doped into $[Mg(H_2O)_6]SiF_6$ and found that the magnesium salt undergoes a phase transition at 25°C from the high temperature $R\bar{3}$ phase to a monoclinic structure with space group $P2_1/c$[35].

### 1.2.3 EPR spectroscopy of nickel(II): theory and literature survey

A $d^8$ ion such as nickel(II) has a $^3F$ term lowest, with $^3P$ as the next highest term. In an octahedral crystal field the ground term is split into a ground $^3A_{2g}$ term, and two excited triplets, $^3T_{2g}$ and $^3T_{1g}$ (see figure 1.3).

The ground $^3A_{2g}$ term is orbitally nondegenerate, however, the threefold spin degeneracy can be split by the combined effects of second-order spin-orbit coupling (which involves the mixing of excited terms such as $^3T_{2g}$ with the ground term) and an axial or rhombic ligand field (figure 1.5). The phenomenon, known as zero-field splitting, is described by the third term of equation 1.20. This splitting gives, for the case of the magnetic field being parallel to the z-axis, a non-degenerate ($M_S = 0$) level and a doubly degenerate ($M_S = \pm 1$) level in an axial field (in a rhombic field the degeneracy is fully lifted).

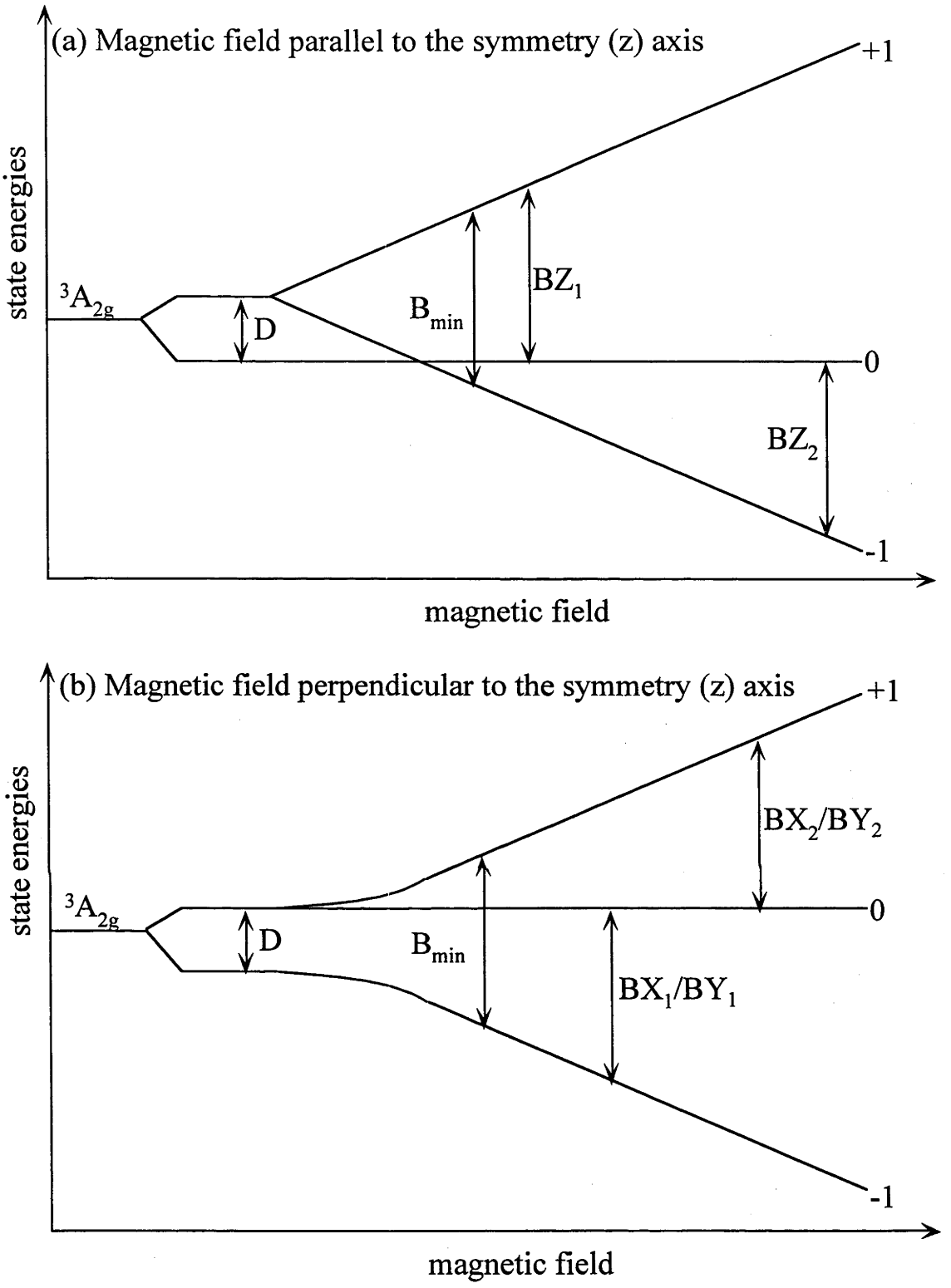


**Figure 1.5: The EPR experiment for the $^3A_{2g}$ ground term of $Ni^{2+}$ (an S = 1 system): a schematic of the Zeeman state energies as a function of magnetic field, showing the possible transitions. The diagram shows the case of positive D, i.e. the doubly degenerate level lies above the nondegenerate level at zero field. The size of D/hν in (a) and (b) is approximately 2.7, which is of the same order as the spectra of the systems studied in this thesis.**

The axial zero field splitting parameter (D) is usually of the order of a few tenths of wavenumbers to a few wavenumbers, and provides a useful indicator of the axial ligand field strength. By convention, D is positive if the doubly degenerate level lies higher, and negative if the nondegenerate level lies higher. A magnetic field (as in EPR spectroscopy) lifts the degeneracy of the doubly degenerate level as shown in figure 1.5.

The EPR selection rule ($\Delta M_S = \pm 1$) allows $-1 \leftrightarrow 0$ and $0 \leftrightarrow +1$ transitions to occur (the formally forbidden $-1 \leftrightarrow +1$ transition is also often observed, together with a transition corresponding to the absorption of two quanta of radiation: the double quantum transition). The double quantum transition is strictly only observable in systems with no zero-field splitting, as only in this case is it possible for two quanta of radiation with the same energy to be absorbed at a single value of the magnetic field. However, the transition can be observed in systems where the zero-field splitting does not differ too far from zero. Examples in the literature of the observance of the double quantum transition for Ni(II) systems with D (and in some cases, E) $\neq$ 0 included [Ni(5-methylpyrazole)$_6$]$X_2$ (where X = $ClO_4^-$ or $BF_4^-$)[36], and a large number of hexacoordinate nickel complexes with nitrogen-containing ligands such as acetonitrile, pyrazoles and imidazoles[37].

The magnitude of D may be sufficiently large to require a strong magnetic field (several tesla, necessitating a superconducting magnet), and a high frequency microwave source (e.g. W-band, which is commonly 95 GHz). Some high frequency EPR spectrometers employ a far infrared laser or a Gunn diode for frequencies greater than 100 GHz in place of a microwave source[36,38-42].

The EPR spectra of the S = 1 systems (i.e. the $Ni^{2+}$ complexes) studied in this thesis are described by the electronic Zeeman and zero-field splitting terms of the phenomenological spin Hamiltonian (equation 1.20). Hyperfine splitting, nuclear quadrupolar coupling and the nuclear Zeeman effect are neglected. For $Ni^{2+}$ complexes, the neglect of hyperfine splitting and the nuclear Zeeman effect are reasonable since, except for $^{61}$Ni, which exists in only 1.14% natural abundance and has I = 3/2, all stable nickel isotopes have zero nuclear spin (see the CRC Handbook of Chemistry and Physics[43]). A nucleus may only possess an electric quadrupole moment if both S and I

are at least one. Again, since this only applies to $^{61}Ni$, nuclear quadrupolar coupling can be neglected for $Ni^{2+}$ complexes.

The zero-field splitting tensor $\tilde{D}$ is a symmetric second-rank 3×3 tensor:

$$\tilde{D} = \begin{bmatrix} D_{XX} & D_{XY} & D_{XZ} \\ D_{XY} & D_{YY} & D_{YZ} \\ D_{XZ} & D_{YZ} & D_{ZZ} \end{bmatrix} \quad (1.27)$$

The tensor is traceless, i.e. $D_{ZZ} + D_{YY} + D_{XX} = 0$.

The zero-field splitting is parameterised from the diagonal tensor components in the form of two scalars, the axial zero field splitting parameter D, and the rhombic zero-field splitting parameter E:

$$D = \frac{3}{2}D_{ZZ} = -\frac{3}{2}(D_{XX} + D_{YY}) \quad (1.28)$$

$$E = \frac{1}{2}(D_{XX} - D_{YY}) \quad (1.29)$$

The quantitative spin Hamiltonian for systems with a zero field splitting is therefore given by equation 1.30.

$$H = g\beta_e \hat{B}^T \cdot \hat{S} + D\left(S_Z^2 - \frac{1}{3}S(S+1)\right) + E\left(S_X^2 - S_Y^2\right) \quad (1.30)$$

For axially symmetric systems (all $Ni^{2+}$ complexes studied in this thesis are strictly axial, or are treated as such), $D_{XX} = D_{YY}$, and E = 0 (equation 1.29). Therefore, the third term in equation 1.30 vanishes. In axial systems with S = 0 or S = 1/2, the second term of equation 1.30 is also zero. For S > 1, the axial zero-field splitting parameter, the second term of equation 1.30 is non-vanishing, and zero-field splitting will be observed in the spectra of axially symmetric systems.

Again, there are many studies in the literature concerning nickel(II). Here a few examples of axially symmetric $[NiL_6]$ complexes where L is a nitrogen-containing heterocycle are mentioned. This type of system is closely related to the three nickel

compounds studied in this thesis, $[Ni(HCPz_3)_2](NO_3)_2$, $[Ni(HBPz_3)_2]$ and $[Ni(Pz)_6](NO_3)_2$. Comparison between these and previously studied systems involving monocyclic ligands such as pyrazole will show the effect of the 'capping' boron or carbon atom on the zero field splitting.

Reedijk and Nieuwenhuijse[37] published a review of EPR spectra of various $[NiL_6][X]_2$ systems where L = pyrazole, acetonitrile, 5-methylpyrazole etc, X = $ClO_4^-$, $GaCl_4^-$, $BF_4^-$ amongst others. All systems exhibited isotropic g values between 2.17 and 2.20, and most showed axial zero field splittings (D values) ranging from 0.07 and 0.9 $cm^{-1}$. Strictly speaking,, complexes with lower than cubic symmetry cannot have isotropic g-values, however the anisotropy is usually too small to be resolved experimentally. Mabbs and Collison[26,36] have shown that:

$$D \approx -0.25\zeta[g_{\parallel} - g_{\perp}] \quad (1.31)$$

where $\zeta$ is the single-electron spin-orbit coupling constant for $Ni^{2+}$. Assuming the free ion value of $\zeta$ (630 $cm^{-1}$)[9], a value of $|D| = 0.9\ cm^{-1}$ will only result in $|g_{\parallel} - g_{\perp}| = 0.0057$, which at the typical X-band and Q-band frequencies (9.4 and 34 GHz respectively) and g-values in the range 2.17-2.20 will lead to peak separations of around 8 Gauss and 29 Gauss respectively. Given that the peaks in the spectra of the compounds studied by Reedijk and Nieuwenhuijse[37] have linewidths of the order of a few hundred Gauss, any splitting due to the g-value anisotropy will be very difficult to observe.

A few complexes also showed a rhombic field, with E ranging from 0.018 to 0.17 $cm^{-1}$. In this paper, Reedijk and Nieuwenhuijse also demonstrated a fitting method for the nickel spectra, based on methods previously employed for S = 1 free radicals.

Wilson et al.[44] studied the EPR spectra of $Ni^{2+}$ doped at levels of approximately 1% into $[Zn(en)_3](NO_3)_2$. The zinc host crystal was found to undergo a trigonal to monoclinic phase transition on lowering the temperature below 146 K. The high temperature spectrum was axial, with $D = -0.831 cm^{-1}$, and $g_{\parallel} = 2.181$, $g_{\perp} = 2.156$. On cooling below 146 K, the three line spectrum parallel to the symmetry axis became a spectrum containing three groups of six lines, each of the six corresponding to one of the six sites in the monoclinic unit cell. These sites are related by the $2C_3$ and $3C_2$ axes of the $D_3$ point group of the high temperature phase, and as a result, the spectrum was observed to

repeat itself every 60° of rotation of the crystal about the high temperature $C_3$ axis. The high temperature zero field splitting was found to arise mainly from changes in the bite angle (N-Ni-N) of the ethylenediamine ligands from 90° and changes in the trigonal cone angle from the octahedral value of 54.74° (figure 4.3). Later work incorporating high frequency EPR (150 GHz or D band) measurements[45] of the same system confirmed the earlier work, and provided better resolution.

Antonisamy et al.[46] reported room temperature Q-band EPR spectra of $Ni^{2+}$ doped $[Zn(pyrazole)_6](BF_4)_2$, which crystallises in the trigonal space group $P\bar{3}$. Again, an axial spectrum was observed, with an almost isotropic g value ($g_{||}$ = 2.1812, $g_{\perp}$ = 2.1851) and D = 0.1682 $cm^{-1}$. Only the $M_J=1 \leftrightarrow M_J=0$ and $M_J=-1 \leftrightarrow M_J=0$ allowed transitions could be observed.

Collison et al[36] published spectra of $[Ni(5\text{-methylpyrazole})_6]X_2$ (where X = $ClO_4^-$ or $BF_4^-$), along with the crystal structure of $[Ni(5\text{-methylpyrazole})_6](BF_4)_2$. This compound crystallises in the trigonal space group $P\bar{3}$, with the $Ni^{2+}$ ion lying on a site of $S_6$ symmetry at room temperature. On attempting to cool the crystal below 150 K, it was found to disintegrate. This phenomenon was ascribed to a significant structural change, and could be seen as a significant change in the EPR spectrum. The g-value was fully isotropic at 2.178 for both compounds, and the spectrum did not show a rhombic component at any studied temperature. The axial zero field splitting parameter D was observed to increase significantly (and irreversibly) on cooling. For the perchlorate salt, values of 0.41 $cm^{-1}$ (295 K) and 0.72 $cm^{-1}$ (100 K) were determined, while for the tetrafluoroborate salt, the values were 0.48 $cm^{-1}$ (295 K) and 0.54 $cm^{-1}$ (100 K).

## 1.3 Raman spectroscopy

### 1.3.1 Theory

Raman spectroscopy employs the Raman effect in the characterisation of chemical species. The effect was first discovered in 1928 by Raman and Krishnan[47]. Many excellent monographs on Raman spectroscopy exist[48-50].

The Raman effect is a phenomenon where light, incident upon a medium is inelastically scattered. The scattered light may have a lower energy than the incident exciting light (Stokes Raman scattering) or a higher energy than the incident light (anti-Stokes Raman scattering). The energy difference (commonly measured as a wavenumber shift from the exciting frequency; the Raman shift) is characteristic of the medium. The shift in energy of the radiation arises from a transition to a higher energy state for Stokes scattering, or to a lower energy state for anti-Stokes scattering. The transition may involve vibrations, rotations, phonons, electronic excitations, magnons, or a combination of two or more of the above. Vibrational transitions are most commonly studied with the Raman effect.

The Raman effect involves light coupling with the polarisability of a molecule, and inducing an electric dipole moment (equation 1.32). Only the first term is involved for the normal Raman effect. Higher order effects, (e.g. hyper Raman) also exist.

$$\hat{P} = \tilde{\alpha} \bullet \hat{E} + \frac{1}{2}\tilde{\beta} \bullet \hat{E}^2 + \frac{1}{6}\tilde{\gamma} \bullet \hat{E}^3 + \ldots \quad (1.32)$$

where $\hat{P} = (P_x, P_y, P_z)$, the induced electric dipole moment for the molecule, $\hat{E} = (E_x, E_y, E_z)$, the incident electric field, $\tilde{\alpha}$ is the molecular polarisability tensor, $\tilde{\beta}$ is the hyperpolarisability tensor and $\tilde{\gamma}$ is the second hyperpolarisability tensor.

The electric field of a light wave oscillates, inducing an oscillating electric dipole in the molecule. An oscillating electric dipole itself produces electromagnetic radiation; the scattered light. For elastic (Rayleigh) scattering only the static component of the polarisability is involved, so the induced dipole oscillates with the same frequency as the incident light, giving scattered light of the same frequency. Rayleigh scattered light is generally much more intense (of the order of $10^6$-fold) than Stokes Raman scattering. Stokes Raman scattering is itself more intense than anti-Stokes Raman scattering, as the latter involves a transition from an excited state to a lower level, rather than the other way around, and higher energy states have lower Boltzmann populations.

The molecular polarisability, $\tilde{\alpha}$, is a second-rank 3×3 tensor:

$$\tilde{\alpha} = \begin{pmatrix} \alpha_{xx} & \alpha_{xy} & \alpha_{xz} \\ \alpha_{yx} & \alpha_{yy} & \alpha_{yz} \\ \alpha_{zx} & \alpha_{zy} & \alpha_{zz} \end{pmatrix} \quad (1.33)$$

where, for example, $\alpha_{xy}$ is the polarisability tensor component responsible for the induced dipole in the x direction due to an incident electric field in the y direction.

The polarisability varies with changes in the molecule; rotational, vibrational or electronic. Rotation of a molecule changes its orientation, and hence its polarisability with respect to a set of fixed laboratory axes, provided the polarisability is anisotropic[#]. Vibration moves the nuclei with respect to one another, and hence distorts the electron cloud, which in turn changes the polarisability[*]. Electronic transitions move electrons to different states, changing the spatial distribution of the electrons and the polarisability. All of these changes cause the polarisability to oscillate with one of the natural frequencies of the molecule in a classical sense. In the classical picture, the molecular oscillations and the oscillation caused by the incident electric field interfere giving beat frequencies: $\nu_0 - \nu_k$ (Stokes Raman) and $\nu_0 + \nu_k$ (anti-Stokes Raman), where $\nu_0$ is the incident light frequency and $\nu_k$ are the molecular characteristic frequencies.

One quantum theoretical description for the Raman effect uses time-dependent perturbation theory[49,51]. Here, the molecule is given a full quantum mechanical treatment while the radiation is treated classically. This method explains the resonance Raman and electronic Raman effects and predicts the existence of different selection rules for the electronic and vibrational Raman effects. Two perturbations are involved, one caused by the incident light and one caused by the molecular vibrations.

[#] It is required for molecules to have an anisotropic polarisability for them to be rotationally Raman active. Isotropically polarisable species such as $CH_4$ and $SF_6$ do not have rotational Raman transitions.

[*] For a molecular vibration to be Raman active the polarisability of the molecule must change in the course of the vibration. This contrasts with infrared absorption where the vibration must give a change in dipole moment to be active. These two selection rules together result in the mutual exclusion principle, which states that a vibration in a molecule with an inversion centre cannot be both Raman and IR active, as it is impossible for one vibration to vary both polarisability and dipole moment in a centrosymmetric molecule.

The resulting equation for the transition polarisability tensor components $[\alpha_{\rho\sigma}]_{fi} = \langle\psi_f|\hat{\alpha}_{\rho\sigma}|\psi_i\rangle$ is given below.

$$[\alpha_{\rho\sigma}]_{fi} = \frac{1}{hc}\sum_r \left[\frac{\langle\psi_f|\hat{\mu}_\rho|\psi_r\rangle\langle\psi_r|\hat{\mu}_\sigma|\psi_i\rangle}{\nu_{ri} - \nu_0 + i\Gamma_r} + \frac{\langle\psi_f|\hat{\mu}_\sigma|\psi_r\rangle\langle\psi_r|\hat{\mu}_\rho|\psi_i\rangle}{\nu_{fr} + \nu_0 + i\Gamma_r}\right] \quad (1.34)$$

where $\hat{\mu}_\rho$, $\hat{\mu}_\sigma$ are dipole operators for a particular direction, e.g. x or y, $\psi_i$ is the initial state wavefunction, $\psi_r$ is the intermediate state wavefunction, $\psi_f$ is the final state wavefunction, $\nu_0$ is the exciting frequency (in wavenumbers), $\nu_{ri}$ is the frequency shift between states i and r, $\nu_{fr}$ is the frequency shift between states r and f, $\Gamma_r$ is the damping constant of state r. The summation is over all states.

The overall wavefunctions are separated into electronic and vibrational parts using the Born-Oppenheimer approximation.

$$[\alpha_{\rho\sigma}]_{an,gm} = \frac{1}{hc}\sum_{e,v} \left[\frac{\langle\phi_n|[\mu_\rho]_{ae}|\phi_v\rangle\langle\phi_v|[\mu_\sigma]_{eg}|\phi_m\rangle}{\nu_{ev,gm} - \nu_0 + i\Gamma_{ev}} + \frac{\langle\phi_n|[\mu_\sigma]_{ae}|\phi_v\rangle\langle\phi_v|[\mu_\rho]_{eg}|\phi_m\rangle}{\nu_{an,ev} + \nu_0 + i\Gamma_{ev}}\right] \quad (1.35)$$

where $[\mu_\rho]_{ae} = \langle\psi_a|\hat{\mu}_\rho|\psi_e\rangle$, a pure electronic transition dipole moment, $\phi_{n,\,v,\,m}$ are vibrational wavefunctions, $\psi_{a,\,e,\,g}$ are electronic wavefunctions.

The electronic transition dipole moments are expanded using the Herzberg–Teller expansion, a perturbation-theoretical approach where the perturbation is a molecular normal coordinate $Q_k$. The expanded transition dipole moments are substituted into the transition polarisability equation, to give a resultant equation with three types of terms. The integrals for the electronic and vibrational wavefunctions are separated and since the wavefunctions are orthonormal, terms such as $|\phi_v\rangle\langle\phi_v| = 1$, and are eliminated giving:

$[\alpha_{\rho\sigma}]_{an,gm} = A + B + C$, where:

$$A = \frac{1}{hc}\sum_{ev}\left[\frac{[\mu_\rho]^0_{ae}[\mu_\sigma]^0_{eg}}{\nu_{eg}-\nu_0+i\Gamma_e}+\frac{[\mu_\sigma]^0_{ae}[\mu_\rho]^0_{eg}}{\nu_{ae}+\nu_0+i\Gamma_e}\right]\langle\phi_n|\phi_m\rangle \quad (1.36)$$

$$B = \frac{1}{hc}\sum_{k}\sum_{ev}\left[\frac{[\mu_\rho]'_{ae}[\mu_\sigma]^0_{eg}+[\mu_\rho]^0_{ae}[\mu_\sigma]'_{eg}}{\nu_{eg}-\nu_0+i\Gamma_r}+\frac{[\mu_\sigma]'_{ae}[\mu_\rho]^0_{eg}+[\mu_\sigma]^0_{ae}[\mu_\rho]'_{eg}}{\nu_{eg}+\nu_0+i\Gamma_r}\right]\langle\phi_n|Q_k|\phi_m\rangle$$

(1.37)

$$C = \frac{1}{hc}\sum_{k}\sum_{l}\sum_{e,v}\left[\frac{[\mu_\rho]'_{ae}[\mu_\sigma]'_{eg}}{\nu_{eg}-\nu_0+i\Gamma_r}+\frac{[\mu_\sigma]'_{ae}[\mu_\rho]'_{eg}}{\nu_{eg}+\nu_0+i\Gamma_r}\right]\langle\phi_n|Q_kQ_l|\phi_m\rangle \quad (1.38)$$

where terms of type $[\mu_\rho]^0_{ae}$ are unperturbed transition dipole moments and terms of type $[\mu_\sigma]'_{eg}$ are perturbed transition dipole moments.

### 1.3.2 Comparison between vibrational and electronic Raman effects

If a = g in equations 1.36-1.38, i.e. the molecule returns to the ground electronic state, then the equations describe the vibrational Raman effect. A is zero unless n = m and so gives Rayleigh scattering. B is zero unless $n = m \pm 1$, and so gives Stokes and anti-Stokes fundamental Raman scattering. C is zero unless $n_k = m_k \pm 1$ and $n_l = m_l \pm 1$ and describes Raman scattering involving two vibrational quanta. If $k \neq l$, then these are binary combination bands, if k = l, then these are first overtone bands. Had the Herzberg-Teller expansion not been terminated at first order, there would also be equations for vibrational Raman transitions involving three and larger numbers of vibrational quanta. For the pure vibrational Raman effect, the selection rules for transitions are determined from group theoretical principles. If a transition between two vibrational states $\phi_i^{(0)}$ and $\phi_f^{(0)}$ is allowed, there must be at least one non-zero component of the transition polarisability tensor for that transition. For this to be the case, the direct product of the irreducible representations (irreps) for the molecular point group of

$\phi_i^{(0)}$, $\phi_f^{(0)}$ and at least one component of the polarisability tensor must contain the totally symmetric irrep of the point group, i.e.

$$\Gamma_f \otimes \Gamma_i \otimes \Gamma_{\rho\sigma} \supset A_1 \quad (1.39)$$

Irreps for the polarisability tensor components can be obtained from a character table of the appropriate point group, for example, see Cotton[52].

If $a \neq g$, then the molecule returns to a different electronic state and the equations describe Raman scattering involving both electronic and vibrational quanta.

The vibrational wavefunctions $\phi_n$ and $\phi_m$ now belong to different electronic states and can have non-zero overlap. The most effective mechanism for the overlap is displacement of the excited electronic state potential minimum along a normal coordinate of the molecule. An excited electronic state will always have its potential minimum displaced with respect to the ground electronic state potential minimum along any totally symmetric normal coordinate. Even so, this displacement is usually small for the small electronic energy differences seen in the electronic Raman effect; this results in small degrees of overlap when $\phi_n$ and $\phi_m$ have different quantum numbers.

Equation 1.36 now describes vibro-electronic Raman scattering involving progressions of totally symmetric vibrations superimposed on electronic Raman transitions (see figure 1.6a below). As a result of the small degree of displacement of the potential minima of the ground and excited electronic state potential minima with respect to each other, usually only the zero-phonon line is seen. 'Hot' bands (due to transitions from vibrational levels other than ground) may also be observed if the sample temperature is sufficient. Equation 1.37 describes progressions of totally symmetric vibrations superimposed upon combination transitions formed from an electronic transition and one quantum of a vibration of appropriate symmetry (figure 1.6b). Equation 1.38 gives for the electronic case progressions of totally symmetric vibrations superimposed upon combination transitions formed from an electronic transition and two vibrational quanta of appropriate overall symmetry (figure 1.6c).

Since the dipole operator is Hermitian and the transition moments in this case are real, by inspection of equations 1.36-1.38, for the vibration-only Raman effect (a = g), $[\alpha_{\rho\sigma}]_{fi} = [\alpha_{\sigma\rho}]_{fi}$ i.e. the transition polarisability tensor is symmetric for the vibrational Raman effect. If on the other hand, a ≠ g (electronic Raman), the polarisability tensor is asymmetric and terms such as $\alpha_{xy}$ will not necessarily be equal to $\alpha_{yx}$.

**Figure 1.6: Progression of a totally symmetric vibration on:**

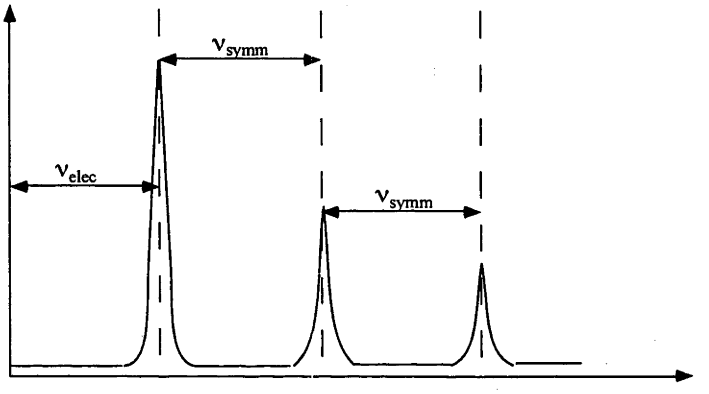


**(a) an electronic Raman transition (equation 1.36)**

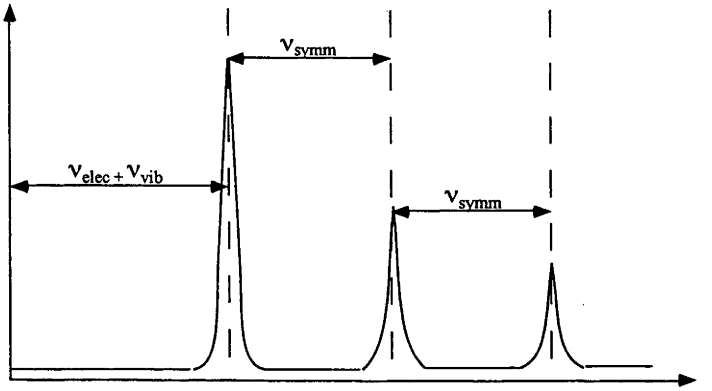


**(b) a combination of an electronic Raman transition and a non-totally symmetric vibration (equation 1.37)**

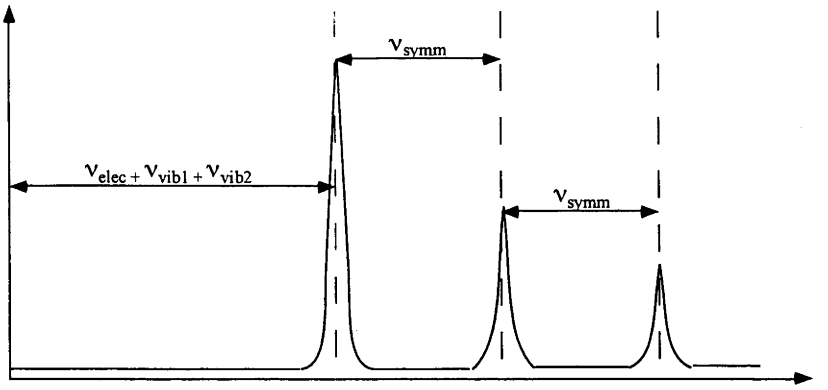


**(c) a combination of an electronic Raman transition and two non-totally symmetric vibrations (equation 1.38)**

This asymmetric nature of the polarisability tensor governing electronic Raman scattering means that the selection rules for vibro-electronic Raman scattering are less restrictive than those for pure vibrational Raman scattering. The requirement for the direct product $\Gamma_f \otimes \Gamma_i \otimes \Gamma_{\rho\sigma}$ to contain the totally symmetric irrep for the molecular point group remains. The polarisability tensor components now span the irreps of the Cartesian products, as well as those of the rotations $R_x$, $R_y$, $R_z$. The irreps can be obtained from character tables. Kiel and Porto have compiled a table of selection rules for the electronic Raman effect[53].

Measurement of polarised Raman spectra therefore allows the determination of symmetries of molecular vibrations and of low-lying (<~5000 $cm^{-1}$) excited electronic states. Transitions between states of particular symmetries will be stronger in some polarisations than in others, for example, a $T_{2g} \leftarrow A_{1g}$ transition in a complex with octahedral symmetry will be more prominent where the exciting light and scattered light are polarised perpendicular to one another than with parallel polarisations.

It is well known that Raman spectroscopy is a complimentary technique to infra red absorption, especially in the case of centrosymmetric molecules. Absorption spectroscopy involves the coupling of the incident light with molecular dipole moments (permanent or induced) rather than with the molecular polarisability. By the mutual exclusion rule, a molecular vibration will be active either in Raman spectroscopy, infra red spectroscopy or neither for a molecule with a centre of symmetry. Even in non-centrosymmetric molecules, vibrations which are strong in Raman spectra tend to be weak in infra red spectra and vice versa.

Different functional groups exhibit different characteristic vibrational frequencies. These are tabulated in many places. Vibrational Raman spectroscopy is therefore commonly employed as a technique for qualitative analysis, for example by police forces for detecting illicit substances for use as evidence[54,55], and by historical researchers for authentication of artefacts[56,57]. For example, six supposedly authentic Egyptian papyri were proved to be 20$^{th}$ century fakes as a result of the presence of copper phthalocyanine (first synthesised in 1935) and Prussian blue (first synthesised in 1704)[58]. Another application is in the authentication of extra virgin olive oils through the presence or absence of 'fingerprint' molecules[59,60] in the oil.

Electronic Raman spectroscopy is well suited for the study of transition metal and lanthanide coordination compounds. Many such compounds have low lying electronic excited states with energies suitable for study using Raman spectroscopy. An advantage of electronic Raman over absorption spectroscopy here lies in the fact that ligand field (d←d or f←f) transitions usually occur between states of the same parity, so are formally forbidden in absorption spectra but allowed in Raman spectra. A field which electronic Raman spectroscopy has been applied to in recent years is the characterisation of high temperature copper(II) superconductors[61]. For reviews on the electronic Raman effect, see Clark and Dines[51], Koningstein[62], or Schaack[63].

### 1.3.3 Instrumentation

Because of the inherent weakness of the Raman effect, Raman spectroscopy requires an intense and monochromatic excitation source, high rejection of stray light from the Raman scattered light and sensitive detection. The field was restricted in its development until the invention of the laser in 1960. Today, almost all Raman spectrometers use a laser as the excitation source. Being intense, highly monochromatic and coherent, laser light is the ideal source for Raman spectroscopy. Development of double- and triple-grating monochromators has provided orders-of-magnitude improvements in stray light rejection.

The original method of light detection for Raman and other types of spectroscopy was the photographic plate. Photomultiplier tubes (PMT) introduced from the 1960s

provided a sensitive and much more convenient detection system than photographic plates. However, the PMT is a single channel device and as such, requires a scanning monochromator with only one wavelength element able to be detected at one time. Charge-coupled device (CCD) detectors were introduced to Raman spectroscopy in the mid-1980s and provide high sensitivity, ease of use and like photographic plates, and the ability to detect a large wavelength range at one time. The high sensitivity of CCD detectors, along with their multi-channel detection ability means that a spectrum can be collected in a fraction of the time taken using a photomultiplier tube. A further development that has considerably facilitated the measurement of Raman spectra is Fourier transform (FT) Raman spectroscopy[64]. FT-Raman spectrometers employing 1064 nm Nd-YAG lasers are readily available commercially, and are as straightforward to use as Fourier transform infrared (FTIR) spectrometers; indeed, instruments which can operate as both FTIR and FT-Raman spectrometers are available.

A further important advantage of FT-Raman spectroscopy using a 1064 nm laser is that the problem of a stray fluorescence background is largely eliminated, since the excitation wavelength is not of sufficient energy to excite most fluorescence. However, the Raman intensity is reduced compared with visible excitation as a result of its being proportional to the excitation frequency raised to the power of 4. Finally, the coupling of a microscope with a Raman spectrometer using the microscope both to supply the exciting laser light and collect the 180° scattered Raman light has given rise to the versatile technique of Raman microscopy[65]. This technique is particularly well suited to collecting Raman spectra from solid samples or surfaces, and allows samples to be 'Raman mapped' in three dimensions, giving information about the spatial distribution of a particular component within a sample.

### 1.3.4 Electronic Raman spectroscopy of cobalt complexes: literature survey

In 1930, Rasetti[66] observed a band in the Raman spectrum of nitric oxide (NO) at 122 $cm^{-1}$ and correctly assigned it to the transition between the $^2\Pi_{1/2}$ and $^2\Pi_{3/2}$ levels. No further electronic Raman spectra were reported until 1963, when Hougen and Singh[67] measured the spectrum of praseodymium chloride. Transitions within the crystal field split $^3H_4$ ground level and between the ground level and the $^3H_5$ and $^3F_2$ excited levels

were identified. Spectra of other lanthanides have been published, including ytterbium, europium and neodymium in yttrium gallium garnet (YGG) matrices[68-70].

Well over half the published transition metal electronic Raman spectra involve high spin cobalt(II). Coordination complexes of cobalt(II) can display electronic Raman transitions between states formed by the combined effect of low symmetry and spin-orbit coupling on the ground multiplet.

An axial perturbation of an octahedral ligand field splits the $^4T_{1g}$ ground term into a $^4A_{2g}$ and a $^4E_g$ (for trigonal symmetry); the ordering depends on the sign of the trigonal field. Spin-orbit coupling splits the $^4T_{1g}$ term into 6 doubly-degenerate states known as Kramers doublets. By group theoretical and quantum mechanical rules, in the absence of a magnetic field, the degeneracy of any electronic state of an odd-electron compound cannot be less than two[52]. Odd electron species require the use of double groups.

If spin-orbit coupling is the stronger effect, the energy levels are constructed as trigonal perturbations of spin-orbit coupled octahedral levels. This is the approach used by virtually all the authors of papers concerning electronic Raman spectroscopy of $Co^{2+}$ in cadmium chloride- and caesium cadmium chloride-type structures[29-31,71-73]. An alternative approach used when the trigonal crystal field is the stronger effect considers the energy levels as spin-orbit split trigonal Russell-Saunders terms. The two approaches are compared in figures 1.1 and 1.2 (page 6).

Three groups reported electronic Raman spectra in 1970 for cobalt(II) in various matrices[71,74,75]. Spectra of $(NH_4)_2[Co(H_2O)_6](SO_4)_2$, were measured by Azima et al.[74] and transitions were observed between the ground and four excited Kramers doublets.

In cobalt(II) fluoride, which is antiferromagnetic below the Néel point (the temperature at which an antiferromagnetic material becomes paramagnetic) at 38 K and mixed $CoF_2/MgF_2$, cobalt(II) is in an orthorhombic environment. Macfarlane[75] in 1970 observed scattering from the lowest Kramers doublet in $CoF_2$ at 2 K. Transitions to the exchange-split first excited doublet at 169 $cm^{-1}$ and 194 $cm^{-1}$, as well as magnon and phonon peaks were identified. Hoff et al.[76] studied the electronic Raman spectra of $CoF_2$ above and below the Néel point, and observed transitions to four Kramers doublets with energy separations from the ground level ranging from 787 to 1393 $cm^{-1}$.

The band positions differed depending on whether spectra were measured above or below the Néel point. The spectra measured at 85 K gave energies in good agreement with fluorescence data for $MgF_2$ doped with 1% $Co^{2+}$ obtained by Johnson et al.[77]. Johnson et al. also determined the position of the lowest Kramers doublet at 152 $cm^{-1}$. Hoff et al.[76] observed broadening of the electronic Raman peaks on cooling $CoF_2$ below the Néel point. This broadening is due to exchange splitting of the Kramers doublets below the Néel point. The increase in electronic Raman peak width with *decreasing* temperature is peculiar to magnetically coupled materials. In materials that do not exhibit magnetic coupling, electronic Raman peaks broaden with *increasing* temperature due to more rapid relaxation of the excited state at higher temperatures.

Work has been done on electronic Raman spectra of $Co^{2+}$ doped in magnesium oxide, where the cobalt(II) is in an undistorted octahedral environment. Spin-orbit coupling splits to first order the $^4T_{1g}$ ground state of cobalt(II) into a ground doublet of $E_{2g}'$ symmetry (in the double group $O_h^*$), a quartet ($G_g'$) and a sextet. Second-order effects split the sextet into a quartet ($G_g'$) and a doublet ($E_{3g}'$). The convention of Cotton[52] is used for the term labels here. The spectrum was first reported by Guha[21], who assigned the peak at 936 $cm^{-1}$ to a $G_g' \leftarrow E_{2g}'$ transition on the basis of its relatively rapid (compared to the phonon transitions) broadening with increased temperature. Walsh et al.[78] located transitions to both quartets at 305 and 930 $cm^{-1}$ by electronic Raman spectroscopy; the transition to the $E_{3g}'$ doublet was hidden by phonon peaks. The peak at ~300 $cm^{-1}$ was also seen by Guha[21], but was not assigned as an electronic Raman peak due to incorrect interpretation of the temperature broadening,

Much work has been carried out for cobalt(II) in cadmium chloride-type lattices, which belong to the space group $D_{3d}^5/R\bar{3}m$. Systems studied include $CoCl_2$, $CoBr_2$ and $CoI_2$, as well as cobalt(II) doped into hosts like $MgCl_2$, $CdCl_2$, $CdBr_2$ and $MnCl_2$. Lockwood has reviewed the literature for electronic Raman spectroscopy of cobalt in halide lattices[79]. Christie and Lockwood[71] used temperature dependent measurements to identify electronic Raman transitions in spectra of cobalt(II) chloride from the ground level to all five excited Kramers doublets at 233, 551, 962, 984 and 1014 $cm^{-1}$. Lockwood et al.[72] studied $CoBr_2$ above and below the Néel temperature. Transitions to all five excited Kramers doublets were observed. Exchange splitting was evident for some peaks below the Néel temperature. The spectra and the EPR g-values for the six

Kramers levels were modelled using both a full crystal field calculation and a second-order effective Hamiltonian model. Spectra of cobalt iodide have also been measured[73].

Varying the percentage of the $Co^{2+}$ dopant in inert hosts allows observation of both single-ion and exchange-coupled cobalt(II) electronic Raman peaks. Lockwood and Christie[80] performed Raman measurements on $Co^{2+}$ doped, at levels from 1 to 50%, into $CdCl_2$, $CdBr_2$ and $MnCl_2$. Comparable electronic Raman peaks to those of pure $CoCl_2$[71] were observed, with considerable variations in Raman shifts between the chlorides and the bromide. Raising the $Co^{2+}$ concentration gave rise to exchange splitting in the spectra. Christie et al.[29] and Jones and Tomblin[30] have located transitions to all five excited Kramers doublets of the $^4T_{1g}$ manifold, as well as using Zeeman Raman scattering to provide experimental values for the magnetic splitting factors (EPR g values). A full crystal field calculation gave a good fit to the experimental single-ion $Co^{2+}$ electronic Raman spectra and the g values[30].

The compounds $ACoX_3$ (A = Rb, Cs; X = Cl, Br) belong to the hexagonal space group $D_{6h}^4$ ($P6_3/mmc$). The structure consists of chains of face-sharing $CoX_6^{4-}$ trigonally-distorted octahedra. Raman spectra of $CsCoBr_3$ were measured[81] between 8 to 100 K. Earlier studies[82] had found evidence for three magnetic phases in the material. Above the first Néel point ($T_N^1$) at 28.3 K, the compound is a one-dimensional antiferromagnet along the chain. Between $T_N^1$ and the second Néel point ($T_N^2$), postulated to lie between 10-14 K there is also some interchain antiferromagnetic coupling. Below $T_N^2$, there is full interchain coupling. Polarised Raman data[81] above $T_N^1$ showed strong evidence of intrachain antiferromagnetic coupling; a transition within the exchange-split ground Kramers doublet was seen at 96 $cm^{-1}$. Exchange-split peaks were seen for three of the five excited doublets. Cooling below $T_N^2$ resulted in further peaks due to interchain coupling being observed, particularly in the 100 $cm^{-1}$ region. Spectra of $CsCoCl_3$ were similar[83], the authors reporting all eleven intrachain exchange-split at 10 K. A comprehensive study by Lockwood et al.[84] of $RbCoCl_3$ showed behaviour similar to $CsCoBr_3$, with three different phases. The magnon peak was seen, as were transitions to the five exchange-split excited levels of the $^4T_{1g}$ manifold.

Kardontchik et al.[85] measured spectra for $Co^{2+}$:$CsMgCl_3$ at 2 K and compared the results with those obtained for $Co^{2+}$:$CdCl_2$[80]. The separation of the lowest and second-highest Kramers doublets was 1265 $cm^{-1}$ for $Co^{2+}$:$CsMgCl_3$, and 953 $cm^{-1}$ in

$Co^{2+}$:$CdCl_2$. In the second-order perturbation theory calculation used to model the spectra, the trigonal splitting parameter was almost twice as large for $Co^{2+}$:$CsMgCl_3$ than for $Co^{2+}$:$CdCl_2$. Jones and Kuok[31] performed Raman measurements (including some Zeeman Raman spectra) and crystal field calculations on both $Co^{2+}$:$CsMgCl_3$ and $Co^{2+}$:$CsCdCl_3$. Results for $Co^{2+}$:$CsMgCl_3$ single-ion electronic Raman peaks agreed with the earlier results of Kardontchik et al.[85], with the additional observation of transitions to the second and fifth excited Kramers doublet. The transition to the highest Kramers doublet was observed at 1380 $cm^{-1}$ (the largest trigonal splitting observed by electronic Raman spectroscopy in cobalt(II)) for $Co^{2+}$:$CsMgCl_3$ and 1070 $cm^{-1}$ for $Co^{2+}$:$CsCdCl_3$. The full $d^7$ configuration crystal-field calculation gave a very good fit to the Raman frequencies and g-values. The trigonal splitting parameters for $Co^{2+}$:$CsCdCl_3$ were smaller than those for $Co^{2+}$:$CsMgCl_3$. A similar effect is also shown for $Co^{2+}$:$CsMgBr_3$ and $Co^{2+}$:$CsCdBr_3$[86]. This paper[86] and another by Johnstone et al.[87] for $Co^{2+}$:$CsMgCl_3$ included results for higher $Co^{2+}$ concentrations, which showed substantial exchange splitting.

Electronic Raman studies have also been performed on cobalt germanate ($Co_2GeO_4$)[88,89], which has the cubic space group $Fd\bar{3}m$[89]. The $Co^{2+}$ ions are located on sites of $D_{3d}$ symmetry. Transitions to three of the five excited Kramers doublets were observed.

## 1.4 References


(1) Stoiber, R. E.; Morse, S. A. *Crystal Identification with the Polarising Microscope*; 1st ed.; Chapman and Hall: New York, 1994.

(2) Wahlstrom, E. E. *Optical Crystallography*; 5 ed.; John Wiley and Sons:, 1979.

(3) Day, P. *Angewandte Chemie International Edition* **1980**, *19*, 290-301.

(4) Ferguson, J. In *Electronic States of Inorganic Compounds: New Experimental Techniques*; 1st ed.; Day, P., Ed.; D. Reidel: Dordrecht, 1975.

(5) Hitchman, M. A.; Riley, M. J. In *Inorganic Electronic Structure and Spectroscopy*; 1st ed.; Solomon, E. I., Lever, A. B. P., Eds.; John Wiley and Sons: New York, 1999; Vol. 1.

(6) Krausz, E. *Australian Journal of Chemistry* **1993**, *46*, 1041-1054.

(7) Krausz, E. *Australian Optical Society News* **1998**, *12*, 21-24.

(8) Krausz, E.; Tomkins, C.; Adler, H. *Journal of Physics E: Scientific Instrumentation* **1982**, *15*, 1167-1168.

(9) Figgis, B. N.; Hitchman, M. A. *Ligand Field Theory and Its Applications*; 1st ed.; Wiley-VCH: New York, 2000; Vol. 1.

(10) Griffith, J. S. *The Theory of Transition Metal Ions*; 1st ed.; Cambridge University Press: Cambridge, 1961.

(11) Kettle, S. F. A. *Coordination Compounds*; 1st ed.; Thomas Nelson and Sons Ltd: London, 1969.

(12) Schlaefer, H. L.; Gliemann, G. *Basic Principles of Ligand Field Theory*; 1st ed.; John Wiley and Sons Ltd: London, 1969.

(13) Brorson, M.; Schaeffer, C. E. *Inorganic Chemistry* **1988**, *27*, 2522-2530.

(14) Racah, G. *Physical Review* **1942**, *62*, 438-462.

(15) Condon, E. U.; Shortley, G. H. *The Theory of Atomic Spectra*; 1st (6th printing) ed.; Cambridge University Press: Cambridge, 1935.

(16) Slater, J. C. *Physical Review* **1929**, *34*, 1293-1322.

(17) Gerloch, M.; Slade, R. C. *Ligand Field Parameters*; 1st ed.; Cambridge University Press: Cambridge, 1973.

(18) Ballhausen, C. J. *Introduction to Ligand Field Theory*; 1st ed.; McGraw-Hill Book Company: New York, 1962.

(19) Dunn, T. M. *Transactions of the Faraday Society* **1961**, *57*, 1441-1444.

(20) Jesson, J. P. *Journal of Chemical Physics* **1966**, *45*, 1049-1056.

(21) Guha, S. *Physical Review B* **1980**, *21*, 5808-5812.

(22) Bussiere, G.; Reber, C. *Journal of the American Chemical Society* **1998**, *120*, 6306-6315.

(23) Zavoiski, E. *Fizicheskii Zhurnal* **1944**, *9*, 211.

(24) Abragam, A.; Bleaney, B. *Electron Paramagnetic Resonance of Transition Ions*; 1st ed.; Oxford University Press: Oxford, 1970.

(25) Pilbrow, J. R. *Transition Ion Electron Paramagnetic Resonance*; 1st ed.; Oxford University Press: Oxford, 1990.

(26) Mabbs, F. E.; Collison, D. *Electron Paramagnetic Resonance of d Transition Metal Compounds*; 1st ed.; Elsevier: Amsterdam, 1992.

(27) Abragam, A.; Pryce, M. H. L. *Proceedings of the Royal Society A (London)* **1951**, *A206*, 173-191.

(28) Edgar, A. *Journal of Physics C: Solid State Physics* **1976**, *9*, 4303-4314.

(29) Christie, J. C.; Johnstone, I. W.; Jones, G. D.; Zdansky, K. *Physical Review B* **1975**, *12*, 4656-4665.

(30) Jones, G. D.; Tomblin, C. W. *Physical Review B* **1978**, *18*, 5990-5994.

(31) Jones, G. D.; Kuok, M. H. *Journal of Physics C: Solid State Physics* **1979**, *12*, 715-730.

(32) Bleaney, B.; Ingram, D. J. E. *Proceedings of the Royal Society A (London)* **1951**, *208*, 143-158.

(33) Cotton, F. A.; Daniels, L. M.; Murillo, C. A.; Queseda, J. F. *Inorganic Chemistry* **1993**, *32*, 4861-4867.

(34) Kirfel, A.; Klapper, H.; Schlaefer, W.; Schwabenlaender, F. *Zeitschrift fur Kristallographie* **1998**, *213*, 456-460.

(35) Francis, C. L.; Culvahouse, J. W. *Journal of Chemical Physics* **1977**, *66*, 1089-1097.

(36) Collison, D.; Helliwell, M.; Jones, V. M.; Mabbs, F. E.; McInnes, E. J. L.; Riedi, P. C.; Smith, G. M.; Pritchard, R. G.; Cross, W. I. *Journal of the Chemical Society Faraday Transactions* **1998**, *94*, 3019-3025.

(37) Reedijk, J.; Nieuwenhuijse, B. *Recueil* **1972**, *91*, 533-551.

(38) Bentum, P. J. M. v.; Horst, E. v. d.; Boonman, M. E. J.; Priem, A.; Hagen, W. R.; Reijerse, E. J.; Gross, M.; Goy, P.; Martinelli, M.; Colligiani, A. *Applied Magnetic Resonance* **2000**, *19*, 479-484.

(39) Eaton, G. R.; Eaton, S. S. *Applied Magnetic Resonance* **1999**, *16*, 161-166.

(40) Fuchs, M. R.; Prisner, T. F.; Moebius, K. *Review of Scientific Instruments* **1999**, *70*, 3681-3683.

(41) Gatteschi, D.; Sorace, L.; Sessoli, R.; Barra, A. L. *Applied Magnetic Resonance* **2001**, *21*, 299-310.

(42) Paschedag, L.; Tol, J. v.; Wyder, P. *Review of Scientific Instruments* **1995**, *66*, 5098-5099.

(43) *CRC Handbook of Chemistry and Physics*; 83rd ed.; Lide, D. R., Ed.; CRC Press: Boca Raton, Florida, 2002.

(44) Wilson, C. R.; Riley, M. J.; Wang, D.; Hanson, G. R. *Chemical Physics* **1997**, *217*, 63-70.

(45) Dam, P. J. v.; Klassen, A. A. K.; Reijerse, E. J.; Hagen, W. R. *Journal of Magnetic Resonance* **1998**, *130*, 140-144.

(46) Anthonisamy, V. S. X.; Padiyan, D. P.; Murugesan, R. *Molecular Physics* **1998**, *94*, 275-281.

(47) Raman, C. V.; Krishnan, K. S. *Nature* **1928**, *121*, 501.

(48) Gilson, T. R.; Hendra, P. J. *Laser Raman Spectroscopy*; 1 ed.; Wiley-Interscience:, 1970.

(49) Long, D. A. *Raman Spectroscopy*; 1 ed.; McGraw-Hill International Book Company:, 1977.

(50) Tobin, M. C. *Laser Raman Spectroscopy*; 1 ed.; Robert E. Krieger Publishing Company:, 1982; Vol. 35.

(51) Clark, R. J. H.; Dines, T. J. In *Advances in Infrared and Raman Spectroscopy*; Clark, R. J. H., Hester, R. E., Eds.; Heyden and Son Ltd: London, 1982; Vol. 9, p 282-360.

(52) Cotton, F. A. *Chemical Applications of Group Theory*; 3rd ed.; John Wiley and Sons: New York, 1990.

(53) Kiel, A.; Porto, S. P. S. *Journal of Molecular Spectroscopy* **1969**, *32*, 458-468.

(54) Bell, S. E. J.; Burns, D. T.; Dennis, A. C.; Speers, J. S. *Analyst* **2000**, *125*, 541-544.

(55) Carter, J. C.; Brewer, W. E.; Angel, S. M. *Applied Spectroscopy* **2000**, *54*, 1876-1881.

(56) Clark, R. J. H. *Journal of Molecular Structure* **1999**, *480-481*, 15-20.

(57) Burgio, L.; Clark, R. J. H. *Spectrochimica Acta Part A* **2001**, *57*, 1491-1521.

(58) Burgio, L.; Clark, R. J. H. *Journal of Raman Spectroscopy* **2000**, *31*, 395-401.

(59) Baeten, V.; Meurens, M.; Morales, M. T.; Aparicio, R. *Journal of Agricultural and Food Chemistry* **1996**, *44*, 2225-2230.

(60) Davies, A. N.; McIntyre, P.; Morgan, E. *Applied Spectroscopy* **2000**, *54*, 1864-1867.

(61) Cardona, M. *Physica C* **1999**, *317-318*, 30-54.

(62) Koningstein, J. A. In *Molecular Spectroscopy*; Barrow, R. F., Long, D. A., Sheridan, J., Eds.; Royal Society of Chemistry: London, 1976; Vol. 4, p 196-224.

(63) Schaack In *Light Scattering in Solids* 2000; Vol. VII, p 24-173.

(64) Chase, B. *Analytical Chemistry* **1987**, *59*, 881A-889A.

(65) Delhaye, M.; Dhamelincourt, P. *Journal of Raman Spectroscopy* **1975**, *3*, 33-43.

(66) Rasetti, F. *Zeitschrift fur Physik* **1930**, *66*, 646.

(67) Hougen, J. T.; Singh, S. *Physics Review Letters* **1963**, *10*, 406-407.

(68) Dabrowski, I.; Grunberg, P.; Koningstein, J. A. *Journal of Chemical Physics* **1972**, *56*, 1264-1268.

(69) Koningstein, J. A. *Journal of Chemical Physics* **1967**, *46*, 2811-2816.

(70) Koningstein, J. A.; Mace, G. *Chemical Physics Letters* **1969**, *3*, 443-444.

(71) Christie, J. H.; Lockwood, D. J. *Chemical Physics Letters* **1971**, *8*, 120-122.

(72) Lockwood, D. J.; Mischler, G.; Johnstone, I. W.; Schmidt, M. C. *Journal of Physics C: Solid State Physics* **1979**, *12*, 1955-1975.

(73) Mischler, G.; Lockwood, D. J.; Zwick, A. *Journal of Physics C: Solid State Physics* **1987**, *20*, 299-309.

(74) Azima, A.; Grunberg, P.; Hoff, J.; Koningstein, J. A.; Preudhomme, J. *Chemical Physics Letters* **1970**, *7*, 565-566.

(75) Macfarlane, R. M. *Physical Review Letters* **1970**, *25*, 1454-1457.

(76) Hoff, J. T.; Grunberg, P. A.; Koningstein, J. A. *Applied Physics Letters* **1972**, *20*, 358-359.

(77) Johnson, L. F.; Dietz, R. E.; Guggenheim, H. J. *Applied Physics Letters* **1964**, *5*, 21-22.

(78) Walsh, D.; Trudel, J.; Chase, L. L. *Solid State Communications* **1984**, *51*, 801-803.

(79) Lockwood, D. J. In *Light Scattering in Solids III*; Cardona, M., Guntherodt, G., Eds.; Springer-Verlag: Berlin, 1982; Vol. III, p 59-92.

(80) Lockwood, D. J.; Christie, J. H. *Chemical Physics Letters* **1971**, *9*, 559-563.

(81) Johnstone, I. W.; Dubicki, L. *Journal of Physics C: Solid State Physics* **1980**, *13*, 4531-4544.

(82) Yelon, W. B.; Cox, D. E.; Eibschutz, M. *Physical Review B* **1975**, *12*, 5007-5015.

(83) Breitling, W.; Lehmann, W.; Srinivasan, T. P.; Weber, R. *Journal of Magnetism and Magnetic Materials* **1977**, *6*, 116-119.

(84) Lockwood, D. J.; Johnstone, I. W.; Labbe, H. J.; Briat, B. *Journal of Physics C: Solid State Physics* **1983**, *16*, 6451-6474.

(85) Kardontchik, J. E.; Cohen, E.; Makovsky, J. *Physical Review B* **1976**, *13*, 2955-2961.

(86) Tomblin, C. W.; Jones, G. D.; Syme, R. W. G. *Journal of Physics C: Solid State Physics* **1984**, *17*, 4345-4368.

(87) Johnstone, I. W.; Jones, G. D.; Lockwood, D. J. *Journal of Physics C: Solid State Physics* **1982**, *15*, 2043-2058.

(88) Boal, D. H.; Hoff, J. T.; Grunberg, P.; Preudhomme, J.; Koningstein, J. A. *Journal of Raman Spectroscopy* **1973**, *1*, 489-498.

(89) Koningstein, J. A.; Grunberg, P. A.; Hoff, J. T.; Preudhomme, J. M. *Journal of Chemical Physics* **1972**, *56*, 354-357.

# Chapter 2: Building a CCD Raman spectroscopic system

## 2.1 Background

The current Raman/fluorescence spectrometer at the Research School of Chemistry is a lab-built system based on a Spex model 1401 0.75-metre double monochromator with a wavenumber drive. Detection is via a photomultiplier (PM) tube in conjunction with a Stanford Instruments SR400 photon counter. Two PM tubes are commonly used; the first, an RCA C31034A, has an extremely low dark current (2-10 counts per second at 10°C). The second tube (a Hamamatsu 943-02) has about fivefold better sensitivity, but much higher dark current and needs to be operated at –40°C in order to be useful. For the Hamamatsu tube, the dark charge is approximately 2200 counts per second (cps) at 10°C and 18 cps at –40°C. Cooling is achieved via a Peltier device in conjunction with a 10°C recirculated chilled water supply. The photon counter and monochromator are computer controlled. A Spectra Physics model 164/165 5-watt argon- or krypton-ion laser is used as the excitation source, providing excitation lines across the near UV-visible-near IR from approximately 350 nm to 800 nm. The sample compartment allows for the measurement of spectra of crystalline, powdered, pelleted, or solution spectra either at room temperature or at cryogenic temperatures using a cryostat or flow tube.

This system has a number of drawbacks. Firstly, the sensitivity of photomultiplier tubes is restricted, particularly in the red and near IR regions. Secondly, because PM tubes are single-channel detectors and require each wavelength element to be scanned individually, data collection times for a Raman spectrum covering a spectral region of, say, 1000 $cm^{-1}$ are of the order of several minutes to several hours. Thirdly, obtaining spatially-resolved spectral information for a sample is tedious at best.

A new Raman spectroscopy system, initially intended for the study of self-assembled monolayers on gold has been constructed using a Princeton Instruments CCD detector and a Spex model 1877 Triplemate triple spectrograph. The advantages of this system over the existing instrument include higher sensitivity, especially in the red region, data acquisition times of the order of several seconds as opposed to minutes or hours, and the

possibility of easily obtaining spatially-resolved spectral information. Finally, the use of a triple spectrometer as opposed to a double spectrometer gives an improvement in the stray light rejection ratio of around five orders of magnitude.

Systems of this type were first employed in the measurement of Raman spectra of thin organic films in the mid 1980s by Dierker and Murray et al.[1,2]. Raman spectrometers based on high quality monochromators and CCD detectors have been employed by a number of groups working on self-assembled monolayers, notably that of Pemberton[3-8].

## 2.2 Main system components

### 2.2.1 Princeton Instruments CCD detector

The CCD detector employed is a Princeton Instruments model 1340EB with liquid nitrogen cooling. Operating at liquid nitrogen temperatures dramatically reduces dark charge, giving reductions of both spectral background and background shot noise. The CCD chip is back-illuminated, deep depleted and has optimal sensitivity in the red and near IR spectral regions, with a quantum efficiency of 90% at 600 nm. Some instrumental parameters are given in table 2.1 below. Data are collected using the Winspec software supplied with the detector.

**Table 2.1: Some important parameters of the CCD detector**

| Parameter | Value |
|---|---|
| Thermostattable temperature range | –70 to –120 °C |
| Dark charge (at –120°C) | <1 electron per pixel per hour |
| Chip dimensions | 1340×400 pixels (26.8×8mm) |
| Pixel size | 20×20 μm |
| Readout noise | 2-4 electrons (50kHz), 6-9 electrons (1MHz) |

### 2.2.2 Spex Triplemate triple monochromator

The Spex Triplemate is a triple grating monochromator divided into two stages known as the filter stage and the spectrograph stage (see figure 2.2 below). The first (filter) stage selectively allows the passage of a section of the spectrum and consists of a dual Czerny-Turner monochromator with two subtractively-coupled gratings and an entrance focal length of 342 mm. The second grating of the filter stage cancels the dispersion of the first, so that undispersed light is delivered to the spectrograph stage entrance slit. The bandpass of the Triplemate is varied using the filter stage intermediate slit, which is between the first and second gratings. A toroidal mirror positioned between the filter stage gratings acts as a spatial filter. The second (spectrograph) stage of the Triplemate is a single Czerny-Turner monochromator with an exit focal length of 594.5 mm to disperse the light over the CCD chip. The grating equation describes the dispersion of light by a diffraction grating (equation 2.1).

$$\sin\alpha + \sin\beta = 2\sin\theta\cos\phi = nm\lambda \quad (2.1)$$

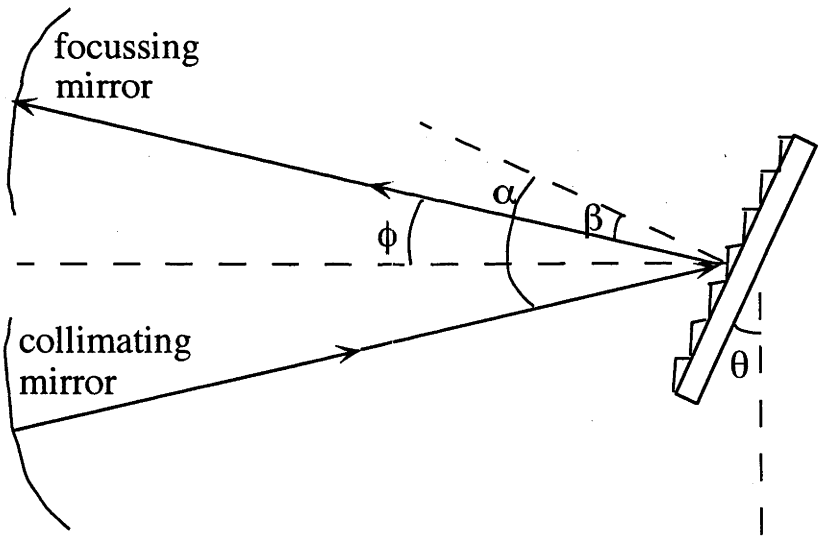


$\alpha$ = incident angle, $\beta$ = diffraction angle, $\phi$ = included angle (15° for the Triplemate), $\theta$ = angle of rotation, n = grating groove density, m = diffraction order, $\lambda$ = wavelength

**Figure 2.1: Reflecting diffraction grating in the Czerny-Turner configuration**

The maximum angle of rotation (θ) of the Triplemate stepper motors is 38.4°, which means that in first order, 500 nm is the maximum diffracted wavelength with 2400 lines/mm gratings, 1000 nm is the maximum with 1200 lines/mm gratings and so on. The Triplemate was supplied with holographic[#] 1800 lines per mm gratings, giving a maximum transmissible wavelength of 666.67 nm, and severely restricting the use of red laser lines for excitation.

For example, using the strongest red line of the krypton laser (647.1 nm), the maximum possible Stokes Raman shift from the excitation line is only 450 $cm^{-1}$, nowhere near, say, the 3000 $cm^{-1}$ shift needed for observation of carbon-hydrogen stretch peaks.

The longest excitation wavelength expected to be regularly used was the 752.5 nm (13289 $cm^{-1}$) krypton ion laser line, while the maximum Raman shift commonly considered is around 3200 $cm^{-1}$ (the carbon-hydrogen stretching region). It is sensible to use a spectrograph grating with the highest groove density possible, as this maximises spectral resolution at the CCD chip. So, in order to use the Triplemate to measure Stokes Raman spectra with a shift of up to 3200 $cm^{-1}$ from a 752.5 nm excitation wavelength the maximum groove density possible within the limit of the stepper motor is 1211 lines per mm. The closest readily commercially available grating is one of 1200 lines per mm. A 1200 lines per mm aluminium coated ruled grating manufactured by Richardson Grating Laboratory was therefore chosen for the spectrograph stage, and ordered to replace the supplied 1800 lines per mm grating. Use of a grating of lower groove density than 1200 lines per mm in order to allow the transmission of wavelengths longer than 1000 nm in first order would be of little value, since the CCD detector cut off wavelength is approximately 1100 nm (the silicon band gap) and sensitivity falls off rapidly above 1000 nm. A blaze wavelength of 500 nm was chosen for the new 1200 lines/mm grating. This blaze wavelength is useful throughout the visible region and into the near infrared. A recent survey of efficiency curves for Richardson Grating Laboratory 1200 lines/mm, 500 nm blaze master gratings revealed an average efficiency of 46% at 330 nm, 78% at 500 nm, and 35% at 1000 nm. All values are relative to the reflectance of aluminium and assume the use of unpolarised light.

[#] Grating generated optically by a laser interference pattern on a photosensitive template.

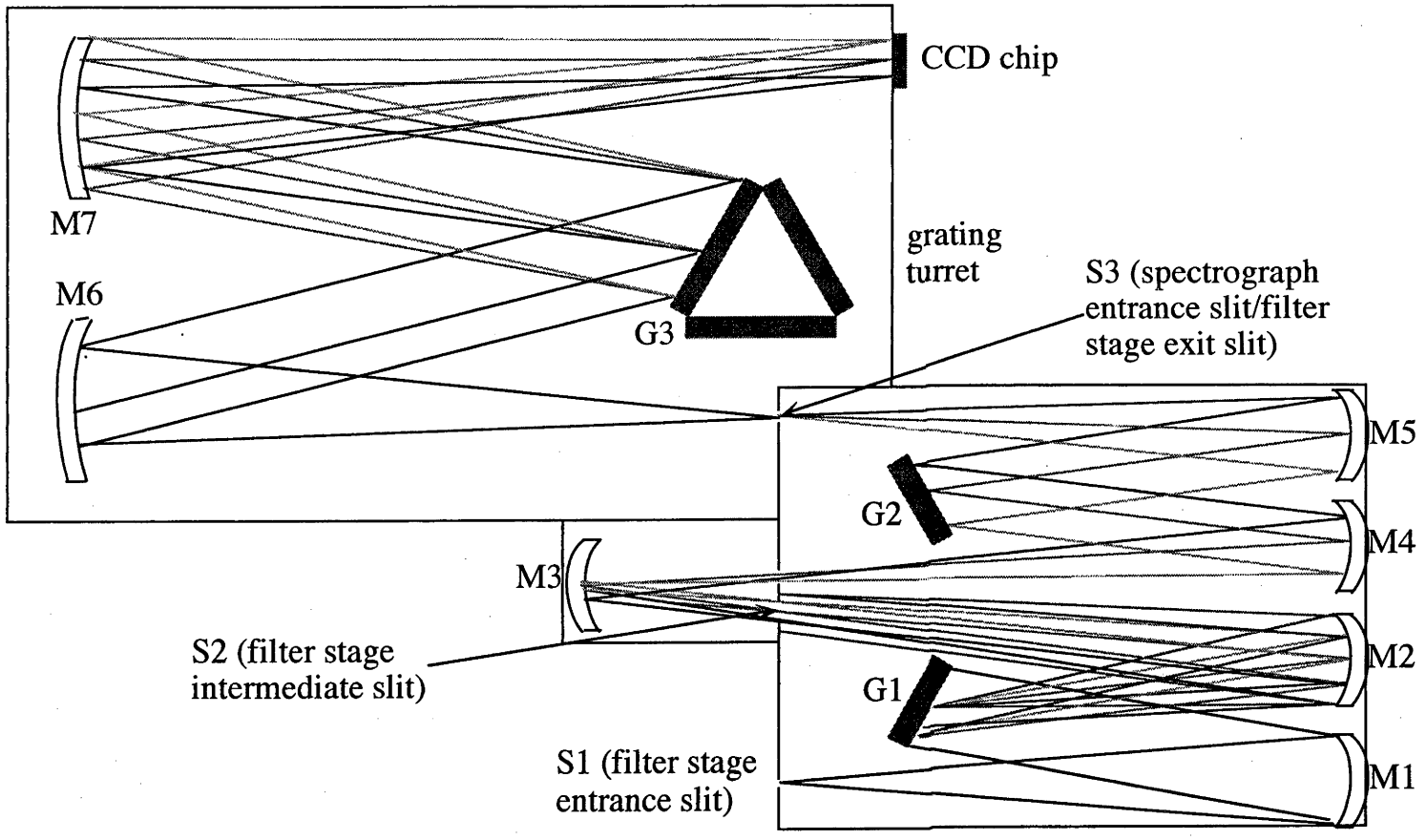


**Figure 2.2: Optical layout of the Spex Triplemate**

The bandpass and resolution of the system depends on a number of factors including the grating groove density, the exit focal length of both the first half of the filter stage and the spectrograph stage, the width of the filter stage entrance and intermediate slits, the dimensions of the CCD pixels and the overall CCD chip dimensions. The reciprocal linear dispersion R of a diffraction grating forming part of a monochromator is found by differentiating equation 2.1 to give $d\beta/d\lambda$, multiplying by the exit focal length and taking the inverse to give equation 2.2:

$$R = \frac{d\lambda}{dx} = \frac{\cos\beta}{nmL} \quad (2.2)$$

where $x$ = distance along the exit focal plane (the CCD detector), $\beta$ = diffraction angle, n = grating groove density, m = diffraction order, and L = exit focal length.

In the Triplemate, the filter stage intermediate slit width is always greater than the filter stage entrance slit width, so multiplication of the reciprocal linear dispersion of the first filter stage grating by the intermediate slit width gives the bandpass (full width at half maximum intensity) of the filter stage. Both the entrance and intermediate slits of the filter stage have widths adjustable from 0 to 8 mm, with 100 μm graduations. The height of the entrance slit is adjustable using a shutter. The spectrograph stage entrance slit width is adjustable from 0 to 3 mm with 2 μm graduations.

Figure 2.3 shows how the resolution of the Triplemate spectrograph stage (with a 1200 lines per mm grating installed) varies with wavelength across the visible and near infra red spectral regions, in two different units. The resolution per CCD pixel is the maximum attainable with a particular grating.

As can be seen from Figure 2.3, the resolution increases with increasing wavelength (a smaller number means an increased resolution). For the maximum attainable wavelength with a 1200 lines/mm grating in the spectrograph stage (1000 nm), a 34.5 nm bandpass is required to just fill the 26.8 mm width of the CCD chip. With the filter stage intermediate slit opened to its full width of 8 mm, this requires an angular dispersion of $8.93\times10^{-4}$ radians per nm after the first filter stage grating, which means that the ideal gratings for the filter stage are ones with a 532 lines/mm groove density.

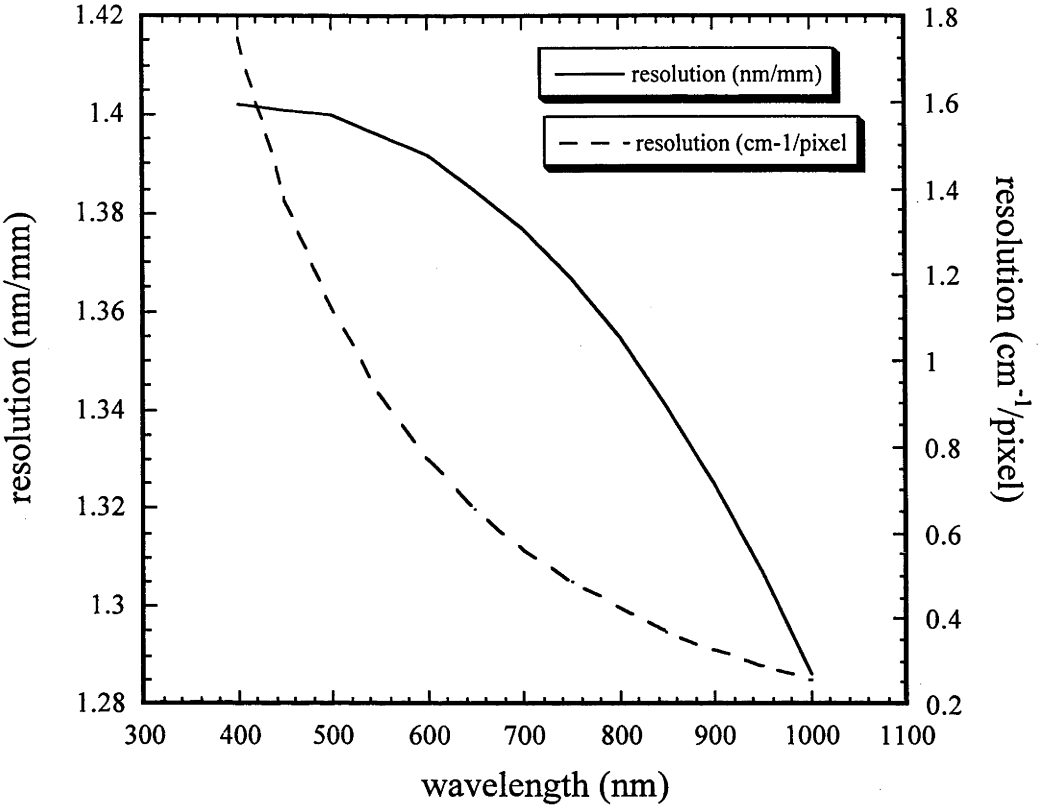


**Figure 2.3 Resolution of the Triplemate spectrograph stage when using a 1200 lines/mm grating**

As mentioned above, 1800 lines/mm holographic gratings were supplied with the Triplemate. A pair of ruled, 1200 lines per mm gratings of the correct size were also available. With the 1200 lines/mm gratings and the intermediate slit opened to its maximum of 8 mm, the CCD chip is approximately 60% filled at 400 nm, 50% filled at 800 nm, and 45% filled at 1000 nm. Clearly, this is not an ideal situation, as the full width of the CCD chip is not being used. Use of 600 lines/mm gratings (the closest to ideal gratings that are readily commercially available) doubles the bandpass of the Triplemate. Furthermore, it is then possible to fill at least 90% of the CCD chip width at all wavelengths accessible with a 1200 lines/mm spectrograph grating. In light of these facts, a pair of aluminium coated, ruled 600 lines/mm 50×50 mm gratings were obtained from Richardson Grating Laboratory for the filter stage. A blaze wavelength of 500 nm was chosen for the reasons outlined in the discussion of the spectrograph stage grating above.

## 2.3 Putting the system together

A plan of the layout of the Triplemate system is shown in figure 2.4 below. The laser, one of the plane mirrors, and the Littrow prism are located on a separate optical table from the other components to facilitate the use of the laser as an excitation source for other instruments.

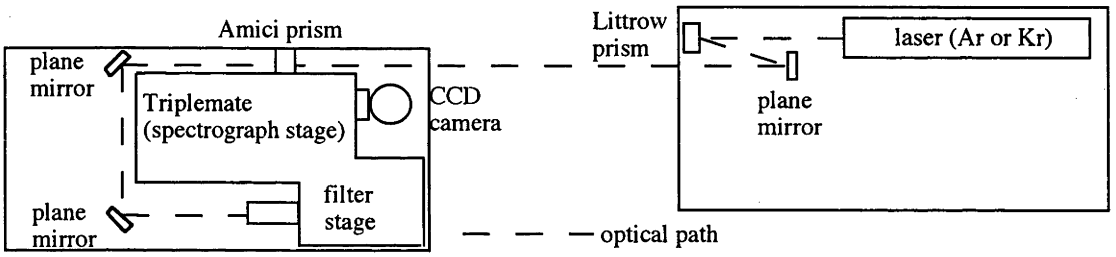


**Figure 2.4: Plan of the optical layout of the new Raman spectroscopic system**

### 2.3.1 Computer control of the Triplemate

A QuickBasic program for moving the spectrograph to the desired wavelength setting has been written (see appendix A). This program calculates the required number of steps, depending on the groove density of the grating. It is also capable of altering the stepping speed of the monochromator stages. ASCII commands from the program are sent to the Triplemate controller via one of the COM ports of the controlling PC.

### 2.3.2 Light collection optics

The system is set up for collection of scattered light at 90 degrees to the excitation light path. Two alternative light collection lenses are used. One is a f/1.2, 55 mm focal length Nikon camera lens while the other is a f/1.7, 50 mm focal length Minolta camera lens.

Due to the focal length, and the lens construction, the Nikon lens requires samples to be placed at a distance of approximately 10 mm in front of the lens, compared with approximately 35 mm for the Minolta. However, the Nikon lens collects between 3 and 4 times as much light from the same sample as the Minolta lens. The Nikon lens is therefore better suited to applications where it is important to collect as much light as possible from a weak signal. On the other hand, the Minolta lens is useful when a larger working distance between lens and sample is necessary, e.g. for flow tubes.

The lenses are attached to the Triplemate entrance slit by the means of a tubular aluminium housing constructed by Keith Jackman. This has provision for extra optical components such as a polariser, polarisation scrambler or holographic notch filter to be installed if required. The distance between lens and slit is adjustable to allow for lenses with different f/numbers to be matched to the f/number of the spectrometer. Matching the f/numbers of the spectrometer and the light collection optic allows the full light acceptance capacity of the spectrometer gratings to be used, while preventing the gratings from being overfilled. This would increase the background due to stray light.

The f/number of a circular optic is defined as:

$$\text{f/number} = \frac{\text{focal length}}{\text{diameter of optic}} \qquad (2.3)$$

However, diffraction gratings are commonly square or rectangular (as they are in the Triplemate). Different authors use two different conventions for the calculation of the f/numbers of spectrometers. Both are applicable when the grating is the limiting optic (as is usually the case). The convention used in the *Diffraction Grating Handbook*[9] uses the smaller of the two dimensions (height or width) of the grating in place of the diameter in equation 2.3. An alternative convention used in the publication 'The Optics of Spectroscopy' published by Jobin Yvon Horiba[10] computes the 'diameter' of a rectangle as the diameter of the circle with the same area as that rectangle:

$$\text{diameter} = 2\sqrt{\frac{\text{grating height} \times \text{grating width}}{\pi}} \qquad (2.4)$$

The first convention is the one used in this thesis. The main problem with the second convention is that a circle with an area given by equation 2.4 will not fully overlap the corresponding rectangle. Therefore, light filling a circle whose diameter is given by equation 2.4 will not be fully collected by the grating; some will be lost and will contribute to instrumental stray light. By using the first convention, light filling a circle whose diameter is equal to the smaller grating dimension will always be fully collected by the grating.

All three of the Triplemate gratings are square, however, rotation of the grating by the stepper motors to pass different wavelengths changes the apparent width of the grating when viewed from the entrance or exit slit (equation 2.5).

$$\begin{aligned} \text{apparent grating width} &= \text{actual width} \times \cos\alpha \text{ (from entrance slit)} \\ &= \text{actual width} \times \cos\beta \text{ (from exit slit)} \end{aligned} \quad (2.5)$$

where $\alpha$ = angle of incidence, $\beta$ = angle of diffraction

As the apparent width of the grating changes with wavelength, so do the input and output f/number of the grating.

The required distance between the lens and the slit was determined phenomenologically by back illumination of the Triplemate/camera lens combination using a tungsten lamp. The distance between the lens and the entrance slit was varied until the distance where the input f/number of the Triplemate is equal to the output f/number of the camera lens was found. If the lens is moved further away from the slit, the focussed image of the spectrograph grating (which is the limiting optic) begins to be cropped, i.e. the lens aperture is overfilled. If the lens is moved further back towards the slit, the lens aperture is underfilled. Another check was carried out by measuring the power of the light focussed by the camera lens for different separations between the lens and slit while the Triplemate was under back illumination[#]. The power after the lens was compared with the light power leaving the slit in order to obtain the percentage transmittance of the lens. Light power was measured using a photodiode. The

[#] Back illumination involves placing a light source at the exit focal length of a spectrometer, and monitoring the resultant light at the entrance focal point.

'matched f/numbers' point is the distance where moving the lens any further away from the Triplemate entrance slit results in a diminished percentage light transmittance. The two tests gave results, which were in reasonably good agreement. The results of the power test for the Nikon lens are shown in table 2.2 below.

The point at which the image appeared to be cropped was a lens-slit separation of between 245 and 250 mm. The reason for the discrepancy between the two methods is probably the greater sensitivity of the eye when compared with the photodiode; initially when the image begins to be truncated, only the corners are cropped, which may not result in enough of a power drop to register with the photodiode.

**Table 2.2 Matching the output f/number of the Nikon lens to the input f/number of the Triplemate by the transmitted power test**

| Lens-slit separation (mm) | Transmitted power (%) |
|---|---|
| 235 | 83±5 |
| 245 | 83±5 |
| 265 | 83±5 |
| 285 | 77±5 |
| 305 | 71±5 |
| 315 | 69±4 |

### 2.3.3 Excitation optics

In Raman spectroscopy, the excitation optics are designed to bring the excitation laser beam to and focus it on, the sample.

The laser beam is first incident upon a retroreflecting Littrow prism to remove plasma lines, before being folded in the horizontal plane by a series of three plane mirrors with coarse angular adjustment onto a final vertical-directing 45° plane mirror which has micrometer adjustment of elevation and azimuthal angles. To provide further rejection of laser plasma lines, an Amici prism is interspersed between the first and second of the plane mirrors.

### 2.3.4 Sample stage and final focussing optics

The sample stage (built by Keith Jackman) is constructed from anodised aluminium, and is structurally attached to the housing for the final plane mirror. The final focussing optic is a 30 mm diameter, 60 mm focal length biconvex lens fixed in a brass tube by a screw-in mount. The lens tube can be translated in the XY plane by micrometer adjustments, and can also be focussed using a knurled knob salvaged from a microscope. To hold the gold electrodes in place while measuring a spectrum, a plastic holder is used. This is attached to a manual stepper motor, allowing the adjustment of the angle of the electrode with respect to the beam path.

### 2.3.5 Sample alignment viewing camera

A viewing system based on a Toshiba security CCD camera and a TV monitor has been constructed to assist with aligning samples and the excitation laser beam.

The camera is attached to a brass tube by means of a screw thread. The brass tube has a simple planoconvex lens mounted at the end to focus the image onto the CCD chip. This focussing tube slides inside a second tube used for adjusting the position of the image on the monitor screen. The adjustment tube in turn sits in a brass flange mounted over an opening in the side wall of the Triplemate filter stage, so that the optical axis of the sample viewing system is at right angles to the Triplemate optical axis. A 45 degree plane mirror mounted on the end of the adjustment tube folds the light from the slit into the sample alignment tube. The apparatus used to connect the camera to the Triplemate was constructed by Keith Jackman.

## 2.4 Comparison of the performance of the new and existing Raman systems

To compare the sensitivity, stray light rejection, time efficiency etc of the existing PM tube Raman system and the new CCD camera system, a series of spectra of chloroform were run on both systems. Experimental parameters are given in table 2.3 below; parameters were identical between the spectrometers wherever possible.

As can be seen from table 2.3 and the spectra (figures 2.5 and 2.6), a spectrum of comparable quality can be obtained with the CCD camera system in a fraction of the time required for the PM tube system. Measurement of the 1-second accumulation spectrum in figure 2.5 took 7.5 seconds from the initiation of data collection to the appearance of the complete spectrum on screen. Allowing the same amount of time for the collection of a background (although usually a background would be used for a number of spectra, not just one), a total of 15 seconds is required. To measure the spectrum in figure 2.6, a total of 11 minutes 48 seconds is required, 47 times longer! Clearly, very significant time savings are possible with the CCD Raman system. Another advantage of the much shorter spectral acquisition time is that the CCD detector is less likely to be affected by cosmic rays which cause intense spikes such as the one around 500 $cm^{-1}$ in figure 2.6.

**Table 2.3: Parameters for the spectra (figures 2.5 and 2.6)**

| Parameter | CCD system | PM tube system |
|---|---|---|
| Excitation wavelength | 647.1 nm | 647.1 nm |
| Laser power supply current* | 25 A | 25 A |
| Resolution | 6 $cm^{-1}$ (at 700 $cm^{-1}$ from the laser, corresponds to 677.8 nm) | 2.3 $cm^{-1}$ (at 700 $cm^{-1}$) |
| Step size | 0.6 $cm^{-1}$ (at 700 $cm^{-1}$) | 0.5 $cm^{-1}$ |
| Spectral range | 300-1100 $cm^{-1}$ | 300-1100 $cm^{-1}$ |
| Time per step | Not applicable | 0.5 s |
| Accumulation time | 1 second | Not applicable |
| Total time required | 7.5 seconds | 11 minutes 48 seconds |

*The absolute value of the laser power was not a critical parameter for this experiment, provided the power was roughly the same for both spectra. Since the laser power is proportional to the applied current, the power was kept constant by using a constant current for both experiments. At the time of use, the maximum power obtainable on the 647.1 nm line of the krypton laser was approximately 100 mW. 25 A is around 60% of the maximum power, i.e. ~60 mW. The power at the sample would be less than this value as a result of losses due to the mirrors and lenses.

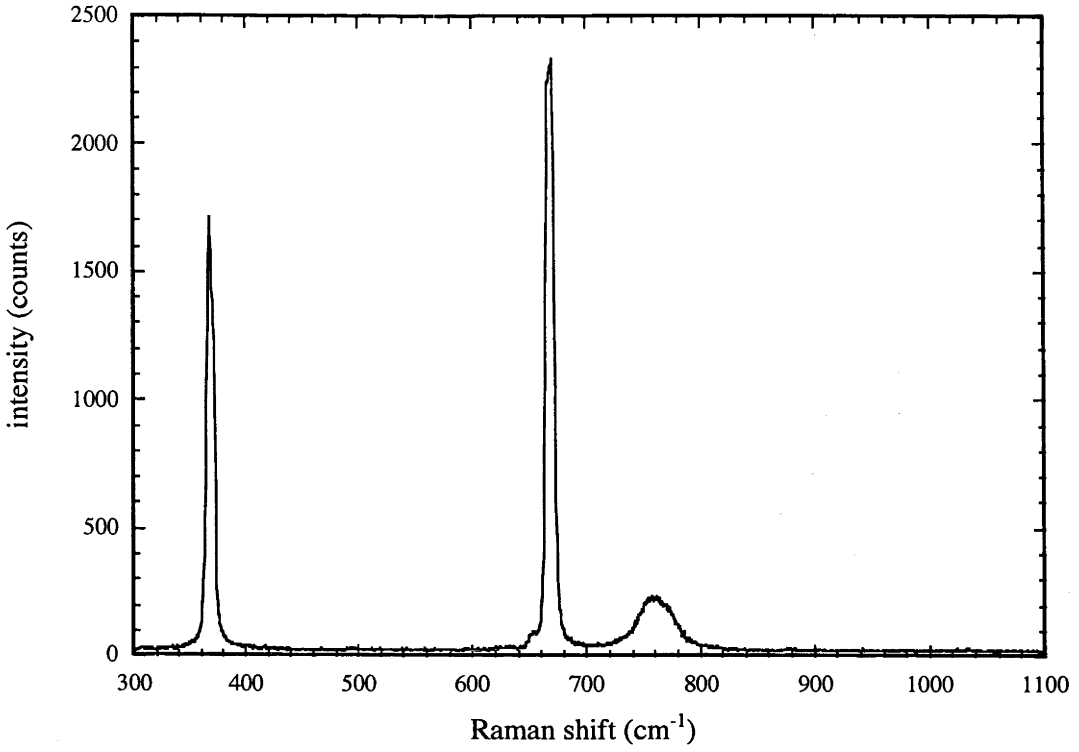


**Figure 2.5: Raman spectrum of liquid chloroform measured using the new CCD Raman spectrometer (accumulation time = 1 second)**

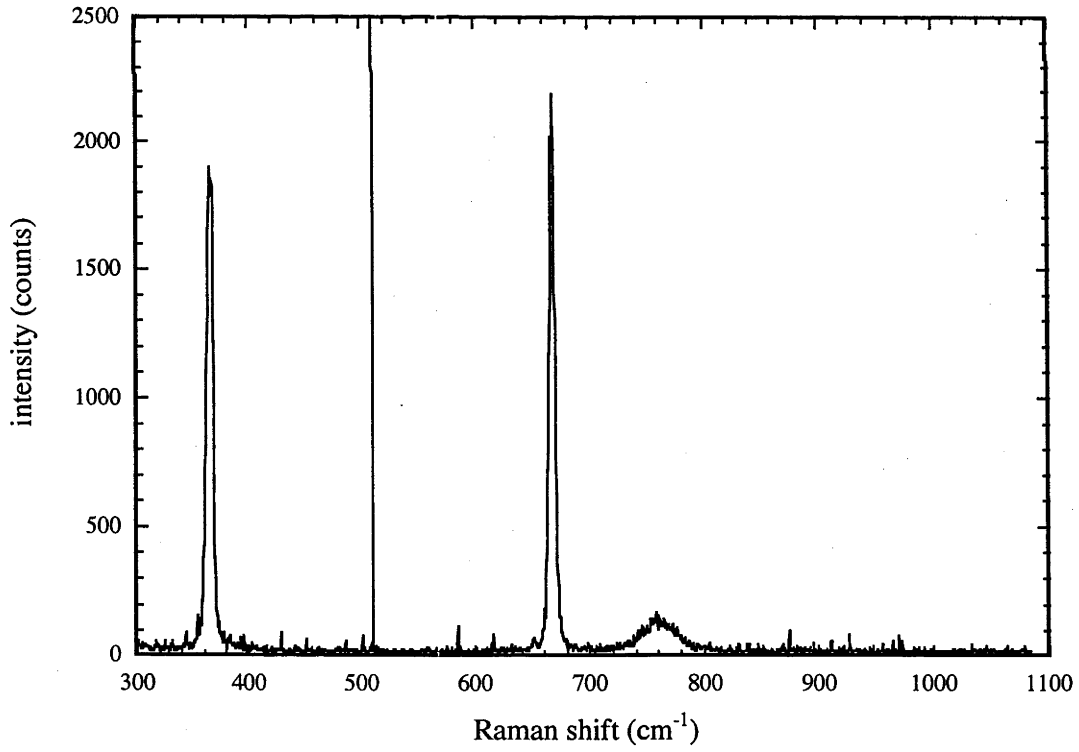


**Figure 2.6: Raman spectrum of liquid chloroform measured using the existing PM tube Raman spectrometer**

The PM tube spectrometer is capable of higher resolution than the CCD system, due to the longer focal length of the monochromator, and the fact that, in terms of dispersion, the Triplemate is a single rather than a double monochromator (the first two gratings are subtractively coupled and serve as a light filter). Since the spectrum in figure 2.5 was measured without horizontal binning (all 1340 columns were collected as data points), the 'step' size of 0.6 $cm^{-1}$ is the best resolution achievable at this wavelength with a 1200 lines per mm grating. Better resolution could only be achieved with a CCD chip with smaller pixels or a higher groove density grating, although, depending on the wavelength region, that might not be possible within the mechanical limit of the spectrometer (see section 2.2). The stepper motor of the double monochromator of the PM tube system has a ratio of 192 steps per wavenumber, so in theory a step size of ~0.005 $cm^{-1}$ is possible, however this is far in excess of the resolution achievable. Given that the minimum useful slit width is around 10 μm, the grating groove density was 1200 lines/mm, the angle $\phi$ is 6.858°, and the focal length is 0.75 m, the best resolution possible at 677.8 nm is 0.25 $cm^{-1}$ for each stage. This gives the double monochromator a theoretical maximum resolution of 0.125 $cm^{-1}$, about a five fold improvement on the Triplemate system.

In order to quantify the signal to noise ratio (SNR) for both systems, a method described in 'Raman Spectroscopy for Chemical Analysis'[11] was used. A series of repeated spectra were collected. For the CCD spectrometer, 32 consecutive 1-second accumulation time spectra were collected for the same Raman shift range of 300 to 1100 $cm^{-1}$. For the PM tube spectrometer, a series of 32 consecutive spectra was collected over the range 645-695 $cm^{-1}$. The SNR was calculated for both systems using the peak centred at around 667 $cm^{-1}$. This was done as follows (see equation 2.6): for the peak Raman shift and about 10 points either side, the mean intensity was calculated for each data point over the 32 spectra. The background value was subtracted from each mean intensity value to give the mean signal for each point. To obtain a value for the noise, the standard deviation (over the 32 spectra) was calculated for each point, and from that, the signal to noise ratio (SNR) was determined for that point.

$$SNR = \frac{\overline{S} - \overline{B}}{\sigma} \quad (2.6)$$

where $\bar{S}$ = the mean intensity for point X (averaged over the 32 spectra), $\bar{B}$ = mean background (measured between 400 and 600 $cm^{-1}$), $\sigma$ = standard deviation for the signal for point X (over the 32 spectra)

As the background is essentially flat in the regions considered, the background signal was calculated as the mean of all points between 400 and 600 $cm^{-1}$ where there are no peaks. The background noise is the standard deviation of those points. For the CCD system, the 32 consecutive spectra were used for background calculations, while for the PM tube system, two extra spectra were measured between 300 and 800 $cm^{-1}$. A dark spectrum (300-800 $cm^{-1}$) was also collected for both systems.

**Table 2.4: Measured values for the noise and SNR for the PM tube and CCD Raman systems**

| System | Dark noise | Background noise | SNR (667 $cm^{-1}$ peak) |
|---|---|---|---|
| PM tube | 26.2249 | 13.62567 | 22.55 |
| CCD | 15.93076 | 14.55918 | 19.721 |

To obtain a final value for the SNR of the 667 $cm^{-1}$ peak, the SNR values for the points at the top of the peak where S > 0.8Smax were averaged. Values for the SNR, the background noise and dark noise are given in table 2.4 above.

As can be seen from these data the signal to noise ratio of the two systems is very similar, even though the spectrum from the CCD system is obtainable in a fraction of the time required for the PM tube system. The maximum achievable signal to noise ratio is governed by Poisson statistics. The signal minus the background for the 667 $cm^{-1}$ peak is roughly 2200 in both spectra, giving a maximum SNR of 46.9. The values measured for the two Raman systems are roughly half this, so there is some scope for improvement.

If the accumulation time for the CCD spectrum was increased from 1 to 700 seconds, the SNR of the CCD spectrum would in theory increase approximately 26-fold ($\sqrt{700}$) to ~520! Together with the ~7 seconds required by the computer to process the spectrum, the CCD spectrum would then require the same amount of time as the PM tube spectrum in figure 2.6. In the measured spectra, although background noise is

similar between the CCD and PM tube systems, the dark noise is higher for the PM tube system as a result of spiking due to cosmic rays which occurred in those spectra.

In conclusion of this section of work, it can be seen that a spectrum of very similar quality can be obtained in a much shorter time for the CCD system when compared with the PM tube system. This is a very good illustration of the advantage of parallel as opposed to sequential detection and is the primary reason why CCD cameras have now become the detector of choice for Raman spectroscopy.

## 2.5 References


(1) Dierker, S. B.; Murray, C. A.; Legrange, J. D.; Schlotter, N. E. *Chemical Physics Letters* **1987**, *137*, 453-457.

(2) Murray, C. A.; Dierker, S. B. *Journal of the Optical Society of America A* **1986**, *3*, 2151.

(3) Bryant, M. A.; Pemberton, J. E. *Journal of the American Chemical Society* **1991**, *113*, 8284-8293.

(4) Bryant, M. A.; Pemberton, J. E. *Journal of the American Chemical Society* **1991**, *113*, 3629-3637.

(5) Schoenfisch, M. H.; Pemberton, J. E. *Langmuir* **1999**, *15*, 509-517.

(6) Schoenfisch, M. H.; Ross, A. M.; Pemberton, J. E. *Langmuir* **2000**, *16*, 2907-2914.

(7) Taylor, C. E.; Garvey, S. D.; Pemberton, J. E. *Analytical Chemistry* **1996**, *68*, 2401-2408.

(8) Taylor, C. E.; Schoenfisch, M. H.; Pemberton, J. E. *Langmuir* **2000**, *16*, 2902-2906.

(9) Palmer, C. *Diffraction Grating Handbook*; 4th ed.; Richardson Grating Laboratory: Rochester, New York, 2000.

(10) Lerner, J. M.; Thevenon, A. In;; Instruments SA Inc, 1988; Vol. 1999.

(11) McCreery, R. L. *Raman Spectroscopy for Chemical Analysis*; 1st ed.; Wiley Interscience: New York, 2000; Vol. 157.

# Chapter 3: Raman spectroscopy of monolayers on gold

## 3.1 Introduction

This chapter discusses work involving Raman spectroscopy of self-assembled monolayers (SAMs) of thiol molecules on gold. This work looked towards characterisation of the AMBRI biosensor, an analytical device based on synthetic ion channels 'floating' in an artificial lipid bilayer membrane tethered to a gold electrode via thiol linkages. As a prototype, SAMs of 1-dodecanethiol and benzyl mercaptan, and one of the AMBRI molecules (DLP) were studied. The spectra were measured using a Raman microscope.

## 3.2 Background

### 3.2.1 Raman spectroscopy of SAMs: history

A SAM is an ordered array of molecules chemisorbed to a solid surface. SAMs form spontaneously on immersion of the surface in a solution of the molecule and have been prepared for many systems; aromatic and aliphatic thiols and disulphides on gold and silver, carboxylic acids on alumina, alkyl groups on silicon, and organosilicon molecules on silicon dioxide or alumina[1].

The current interest in SAMs of sulphur-containing molecules on metal surfaces began with the synthesis of SAMs of dialkyl disulphides on gold by Nuzzo and Allara[2]. A comprehensive monograph partly concerning SAMs was written by Ulman[3], who has also authored a more recent review article[1].

Many techniques have been applied in the study of SAMs, including X-ray photoelectron spectroscopy (XPS), ellipsometry, contact-angle measurements, infra red spectroscopy, surface second harmonic generation (SSHG), electrochemistry, and Raman spectroscopy. To date, Raman spectroscopy has been used less than other

techniques. This perhaps results from the lack of suitable equipment in surface science research groups, and the higher availability of the alternatives.

The group of Jeanne Pemberton has used Raman spectroscopy extensively to characterise alkanethiol monolayers. In 1991 two papers were published in which a triple monochromator was used with a CCD detector to measure the Raman spectra of SAMs of aliphatic thiols on gold and silver electrodes[4,5]. SAMs were prepared using polished and electrochemically roughened electrodes. The spectra showed several important features. Firstly, the sulphur-hydrogen (S-H) stretch peak is absent in all spectra of 1-alkanethiols adsorbed on gold or silver. This agrees with earlier work[6-10] for alkanethiols on colloidal silver, and supports Whitesides and Laibinis[11] proposed structure for SAMs of 1-alkanethiols on gold or silver, where the molecule is attached to the surface by formation of a metal-sulphur bond after cleavage of the S-H bond. Secondly, the carbon-sulphur (C-S) stretch peak for molecules with the *trans* conformation about C1-C2[#] is more intense in the surface Raman spectrum than the corresponding peak for molecules with the *gauche* conformation. This spectral region resembles more closely the spectra of solid 1-alkanethiols than those of liquid 1-alkanethiols. This is indicative of the high degree of order present in SAMs of alkanethiols on gold and silver. In the carbon-carbon (C-C) stretching region the surface Raman spectrum of 1-octadecanethiol on gold or silver showed the C-C bonds to exist almost entirely in the *trans* conformation. 1-Dodecanethiol showed more *gauche* defects in the C-C bonds, i.e. the monolayer was less ordered than that of 1-octadecanethiol, but more ordered than liquid 1-dodecanethiol. 1-Butanethiol SAMs appeared to be highly ordered, consistent with the results of Joo et al.[7]. Finally, differences in the relative intensities of C-S and C-H stretch peaks, and C-C and C-H peaks, when interpreted in terms of surface selection rules[12], were consistent with molecular orientations predicted using molecular dynamics simulations and IR spectra.

Pemberton et al.[13] demonstrated the incorporation of pyrene into SAMs of alkanethiols, and that Raman peaks due to the pyrene correlated closely with impurity peaks in spectra of undoped alkanethiol SAMs, supporting the proposition that aromatic carbonaceous material is incorporated during formation of alkanethiol SAMs (probably during polishing). Methods of removing the contamination were published[14,15].

[#] C1 refers to the carbon atom immediately adjacent to the sulphur atom in a 1-alkanethiol molecule, while C2 refers to the carbon atom immediately adjacent to C1.

Another paper reporting the incorporation of contaminant molecules into SAMs is that of Kudelski and Krysinski[16], who showed using Raman spectroscopy that monolayers of octadecanethiol on gold assembled from acetonitrile solutions of the thiol contained trapped acetonitrile molecules.

Using a specially designed cell, Pemberton et al.[17] have measured through-solution Raman spectra of alkanethiol SAMs on silver electrodes. Apart from Sandroff et al.[18], who measured Raman spectra of 1-hexadecanethiol on silver island films immersed in both water and chloroform, this appears to be the only measurement of in-situ Raman spectra of alkanethiols on non-colloidal metal substrates. Sandroff et al. observed that water had little effect on the spectrum, with the thiol molecules remaining solid-like (predominantly all *trans* conformation). Chloroform produced a more liquid-like (*gauche* peaks were more evident) spectrum. Chloroform solvates the hydrophobic alkanethiol chains much more effectively than water, resulting in greater disorder than for an unsolvated SAM. Schoenfisch and Pemberton's results[17] confirmed that water had little effect on the structure of alkanethiol SAMs on silver.

The polished gold and silver electrodes used by the Pemberton group[19] were determined to give moderate surface-enhancement factors of $\leq 100$. This compares with the much larger enhancement factors ($10^6$ and more) seen in surface enhanced Raman spectroscopy (SERS). The SERS phenomenon was first observed in 1974[20] for pyridine on colloidal silver. A large number of papers on the subject have since been published, and SERS has been reviewed on a number of occasions[12,21-26]. The origin of the large enhancements was not initially clear, however it is now generally agreed that two factors are involved. The first (the 'electromagnetic enhancement') is optimised for surfaces with roughness features of the order of 10-100 nm; this can include roughened electrodes, metal colloids or vapour-deposited films for example. This factor arises from local enhancement of the incident and Raman-scattered light through excitation of surface plasmons. The second enhancement factor (the 'chemical enhancement') is thought to result from charge-transfer between the metal surface and the orbitals of the molecular adsorbate. The majority of SERS experiments have been performed using the so-called 'coinage metals' gold, silver and copper, as these metals show optimal enhancement of the Raman signal in the visible region.

Sandhayarani and Pradeep[27] studied the time dependence of monolayer formation. Increasing the adsorption time beyond 5 hours made little difference to the spectra, indicating that monolayer formation and ordering were essentially complete. Temperature-dependent experiments for octanethiol monolayers showed irreversible desorption beginning at 348 K. The monolayer also became less ordered as the temperature was increased.

The group of Robin Garrell at the University of California, Los Angeles has also been active in the use of Raman spectroscopy for characterisation of self-assembled monolayers. Papers have been published on several topics, including the use of Raman spectroscopy for characterising aromatic selenolate on gold monolayers[28], the study of oxidation of alkanethiol on gold SAMs[29] and Raman spectra of SAMs of aromatic thiols[30,31].

Evans and Ulman et al. have prepared monolayers on gold using alkanethiols containing mid-chain polar groups[32,33], such as sulfone, *p*-thiophenol and *p*-phenolsulfone. The effect of the mid-chain dipole strength, and of varying carbon chain length above and below the polar group on the monolayer order and formation was studied using contact angle measurement, ellipsometry, X-ray photoelectron spectroscopy, infrared spectroscopy and Raman spectroscopy.

Assembly kinetics are determined partly by optimisation of interchain van der Waals interactions, which relies on having well-ordered all-*trans* chains. In solution, the chains are disordered, and have to become ordered during the assembly process. Longer chains take longer to become ordered. Reducing the degrees of freedom by anchoring both ends of a chain slows ordering. The polar group has a preferred alignment to optimise dipole-dipole interactions, and this has an 'anchoring' effect on the chain. These factors result in slow formation kinetics (~5 days) for the monolayers with a 12-carbon chain between the anchoring polar group and the gold surface, and relatively fast kinetics (~1 hour) with a 4-carbon chain below the polar group. Contact-angle measurements showed shorter chains above the polar group having smaller contact angles for both water and hexadecane, consistent with a greater degree of dynamic disorder being present in monolayers formed from short-chain alkanethiols.

A paper by Clark et al.[34] presenting Raman spectra of alkanethiol SAMs on roughened gold electrodes, showed spectra very different from earlier results[4,27]. The peaks were sharper and more numerous, and the authors assigned the majority of them to transitions between image states[35]. These are thought to be hydrogen atom-like quantum states in which electrons sited within angstroms of a metal surface exist as a result of electrostatic interaction between the electron and the induced image charge in the metal. For most metal surfaces the image state electrons have energies corresponding to band gaps in the metal electronic structure, and cannot migrate into the metal bulk. The binding energies with respect to the vacuum energy are given by a Rydberg-type formula[35]:

$$E_B = \frac{-Rz_{eff}^{\ 2}}{16(n+a)^2} \quad (3.1)$$

where R = Rydberg constant, $z_{eff}$ = effective electron charge in electronic units, n = the principal quantum number, and a is a parameter between –0.5 and 0.5 accounting for screening of the electron and image charge by other electrons in the metal

Equation 3.1 shows that the image state energies with respect to the vacuum level do not depend on the metal properties, so are constant for different metals. Energies with respect to the Fermi energy and the band gap will vary between metals, as these quantities vary for different metals. Image states have been identified using inverse photoemission[36,37] and two-photon photoelectron spectroscopy[35]. Clark's work is the first to use Raman spectroscopy. Using equation 3.1, peaks were fitted to transitions from n = 1 to n = 2, 3, 4 and 5, with a = 0.23 and modifying $z_{eff}$ to include dielectric screening by the monolayer. The Raman transitions between image states appear to require resonance enhancement in order to be observed; Clark et al. reported that excitation wavelengths of 630 to 730 nm were necessary. This concurs with Sandhayarani and Pradeep[27], who used excitation at 1064 nm and did not observe the effect. However, Bryant and Pemberton[4,5] used an excitation wavelength of 720 nm for some of their spectra, and did not report the effect. The theoretical explanation was later expanded to include the postulated location of the electrons, and the crystallographic orientation of the gold[38-41]. It is not completely clear that the proposed explanation for the Raman peaks observed by Clark et al. is correct. Further work is needed to explain the requirement for excitation wavelengths between 630 and 730 nm,

to provide a more complete explanation of the screening of the image charge by other electrons and the monolayer, and to explain why the effect is only observed for thiol molecules of a certain length.

Surface Raman spectroscopy, like infra red spectroscopy, and unlike techniques such as ellipsometry and contact angle measurements, can provide molecular level information. Information can be obtained on the composition of mixed monolayers, the orientation and conformation of molecules with respect to the metal surface and the binding mode of molecules to the surface.

### 3.2.2 The AMBRI biosensor

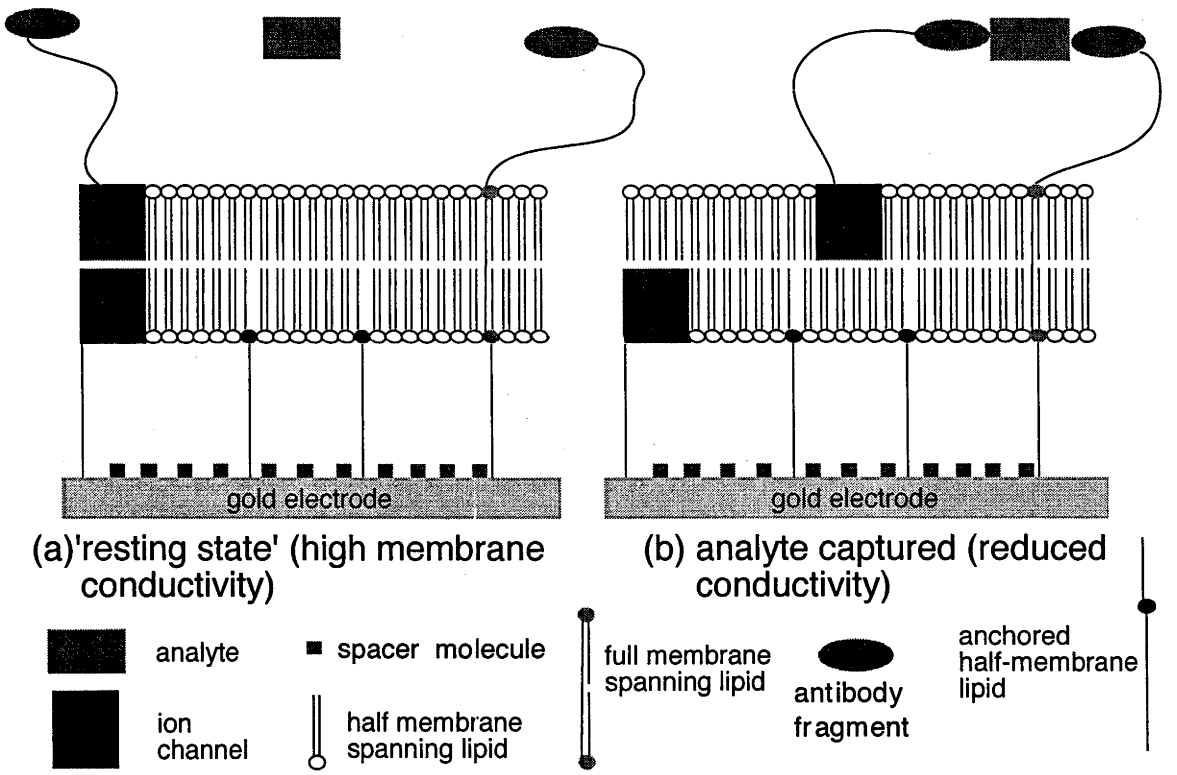


**Figure 3.1: Schematic of the AMBRI Biosensor (adapted from reference 43)**

Since 1988, AMBRI Pty Ltd (a subsidiary of Pacific Dunlop) has been developing a novel biosensor[42]. This biosensor is based around a lipid bilayer attached to a gold electrode via a thiol linkage. Detection of biologically active molecules occurs via target-specific antibody molecules attached to synthetic ion channels which 'float' in the membrane. Capture of a target molecule by an antibody fragment separates the two

halves of the ion channel, disrupting the ion flow and causing an abrupt change in the conductivity. The change in conductivity is detected at the electrode and is correlated with the concentration of the target biomolecule. A diagram of the biosensor membrane is shown in figure 3.1, while figure 3.2 shows three of the molecules used in the construction of the biosensor. The membrane is constructed in two stages using self-assembly techniques[43], and has been studied using ellipsometry, contact-angle measurements, conductivity measurements and scanning tunnelling microscopy.

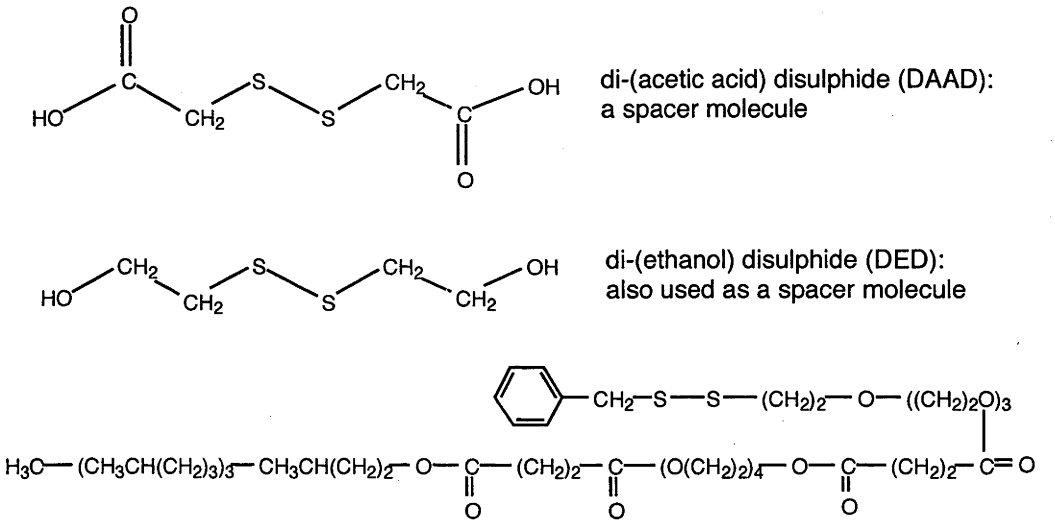


**Figure 3.2: Some molecules used in the AMBRI biosensor**

## 3.3 Experimental

Spectra have been measured for monolayers of three molecules on two different types of gold surfaces. The first surface type was a sputtered gold film of approximately 100 nm thickness on either glass or silicon wafer. The second surface type was an electrode manufactured from a gold disc of 6 mm diameter and 3 mm thickness soldered to a brass rod and encased in a Teflon® sheath. In the case of the gold electrodes, spectra were measured both on electrodes polished to a mirror finish using diamond pastes and alumina, and mirror-polished electrodes which were then electrochemically roughened by the method of Bryant and Pemberton[4].

Self-assembled monolayers were prepared by immersing the gold surfaces in ethanol solutions of the appropriate compound (concentration usually in the range of 1-5 mM) for periods ranging from 2 hours to a few weeks. On removal from the solution, the electrodes were rinsed with absolute ethanol and dried with a stream of dry nitrogen gas. The molecules 1-dodecanethiol, benzyl mercaptan and DLP were studied in order to consider an aliphatic thiol, an aromatic thiol and one of the AMBRI molecules.

Spectra were measured using a Renishaw 2000 Raman microscope (Renishaw plc, UK) at the University of Canberra. This employs a CCD detector, two alternative excitation lasers (632.8 nm helium-neon and 780 nm diode), a single-grating monochromator and a modified microscope to perform the roles of both excitation and collection optics. The Raman light is therefore collected at an angle of 180° to the incident light (backscattering geometry), compared with the 90° collection for the instruments described in chapter 2 and appendices B and C. A holographic notch filter appropriate for the excitation laser is incorporated in the system to reduce the amount of reflected laser light and Rayleigh scattered light reaching the detector. The sample stage is motorised and can be moved in three dimensions. Samples are aligned on the sample stage using the white light illumination mode of the microscope, viewing the sample on a monitor using a second CCD camera. Spectral resolution of 1 $cm^{-1}$ is achievable, while spatial resolution of 1 μm and depth of field of 2 μm is obtainable with the ×100 objective.

## 3.4 Results

It was not possible to measure Raman spectra of a monolayer on a thin gold film. All that was obtained was a high background, plus, for gold films on a silicon wafer, a characteristic Raman peak of silicon at 520 $cm^{-1}$ (the Si-O stretch).

The most likely reason for this absence of spectra for the SAMs on thin gold films is that the gold film is thin enough for substantial amounts of laser light to penetrate the gold and generate Raman scattering from the substrate. This scattered light from the substrate then swamps the Raman scattering from the monolayer. Indeed, on holding the gold-coated slides or silicon wafers to a bright light source, it was possible to see through them. On the other hand, spectra of self-assembled monolayers on the gold

electrodes (which had a gold layer of thickness ~3 mm as opposed to 100 μm) could be measured. Spectra have been measured for SAMs of 1-dodecanethiol, benzyl mercaptan and DLP, a molecule used to construct the AMBRI biosensor.

Spectra of DLP, benzyl mercaptan and 1-dodecanethiol are shown below (figures 3.3-3.10). In the case of 1-dodecanethiol, spectra are shown for different combinations of rough or smooth gold, and 632.8 nm or 780 nm excitation. The spectra are shown as measured.

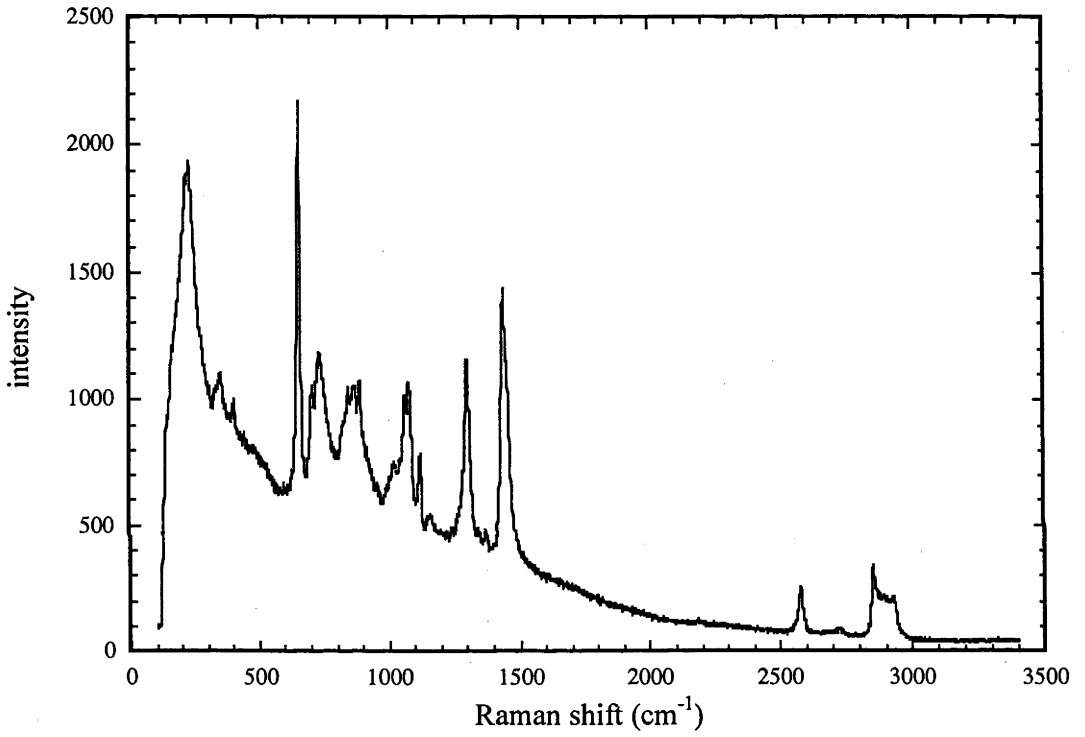


**Figure 3.3: Raman spectrum of liquid dodecanethiol (780 nm excitation)**

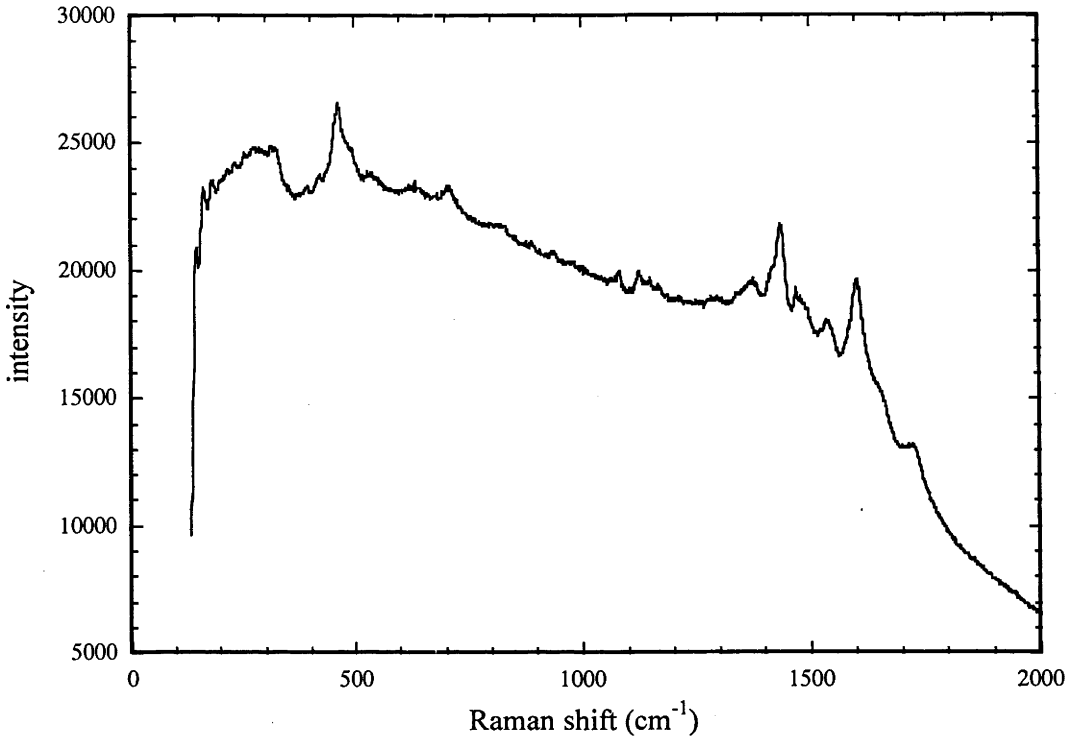


**Figure 3.4: 1-dodecanethiol on smooth gold (780 nm excitation)**

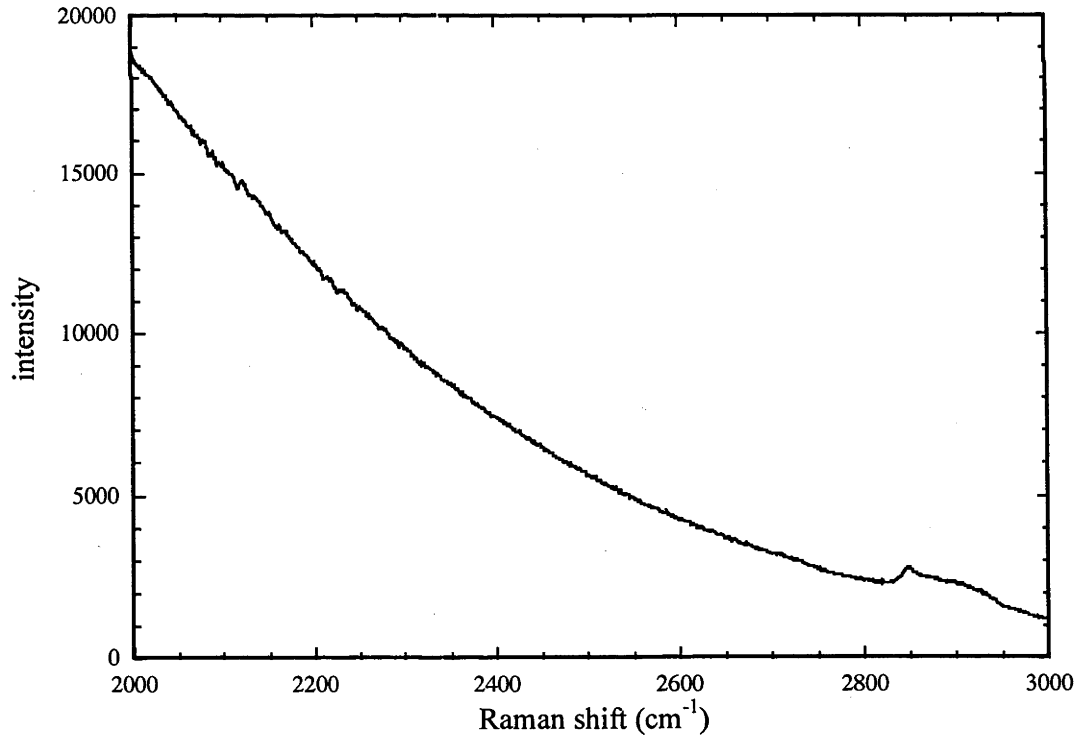


**Figure 3.5: 1-dodecanethiol on smooth gold (780 nm excitation)**

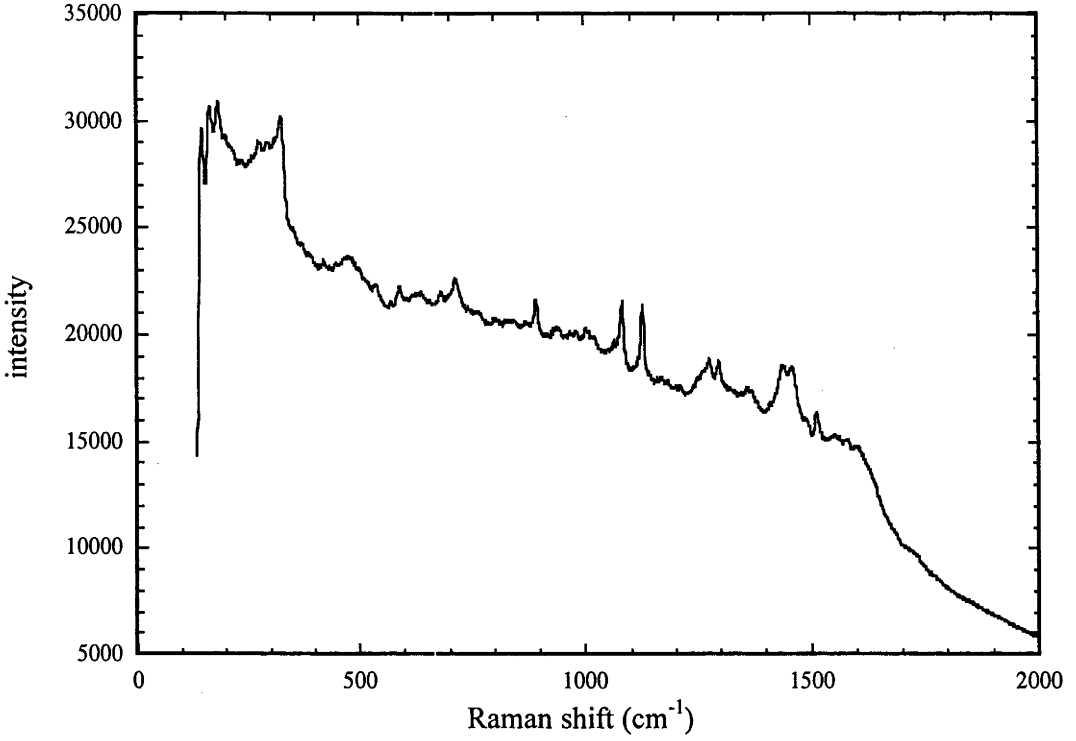


**Figure 3.6: 1-dodecanethiol on a roughened gold electrode (780 nm excitation)**

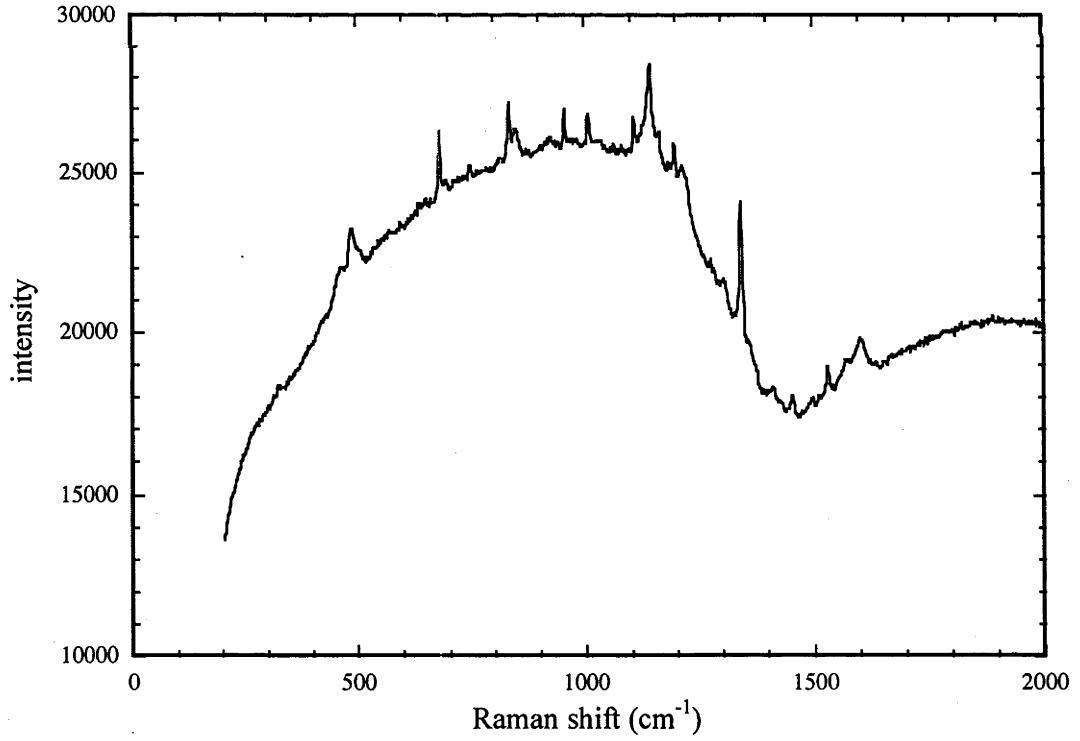


**Figure 3.7: 1-dodecanethiol on a smooth gold electrode (632.8 nm excitation)**

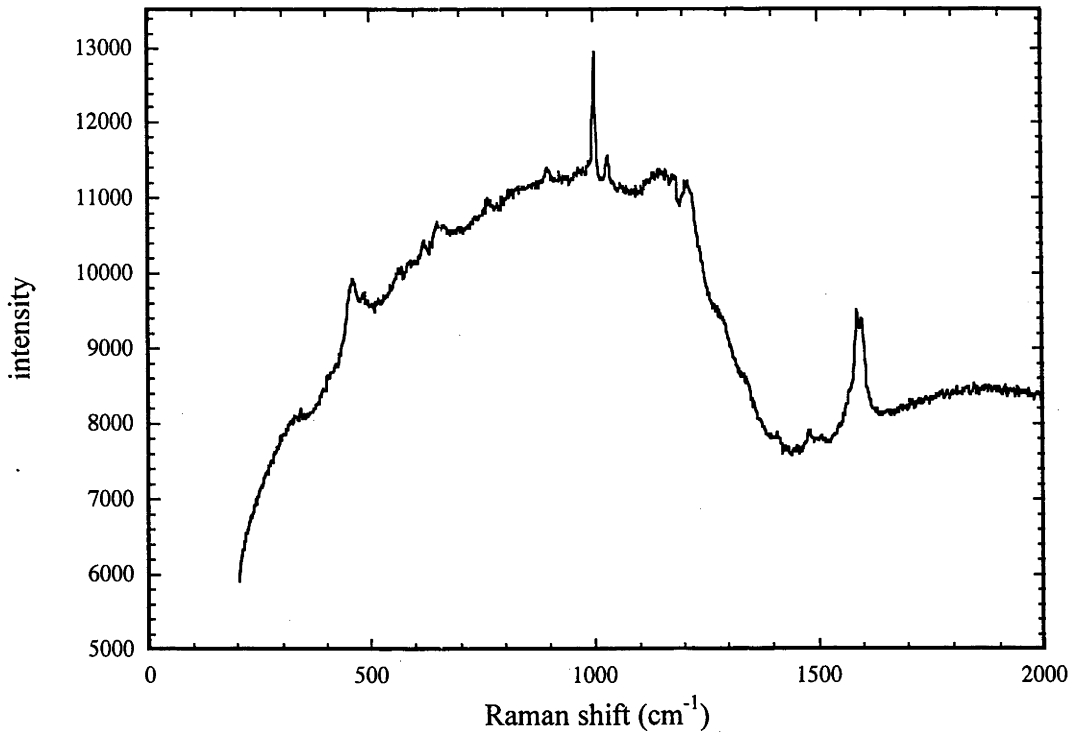


**Figure 3.8: Benzyl mercaptan on smooth gold (632.8 nm excitation)**

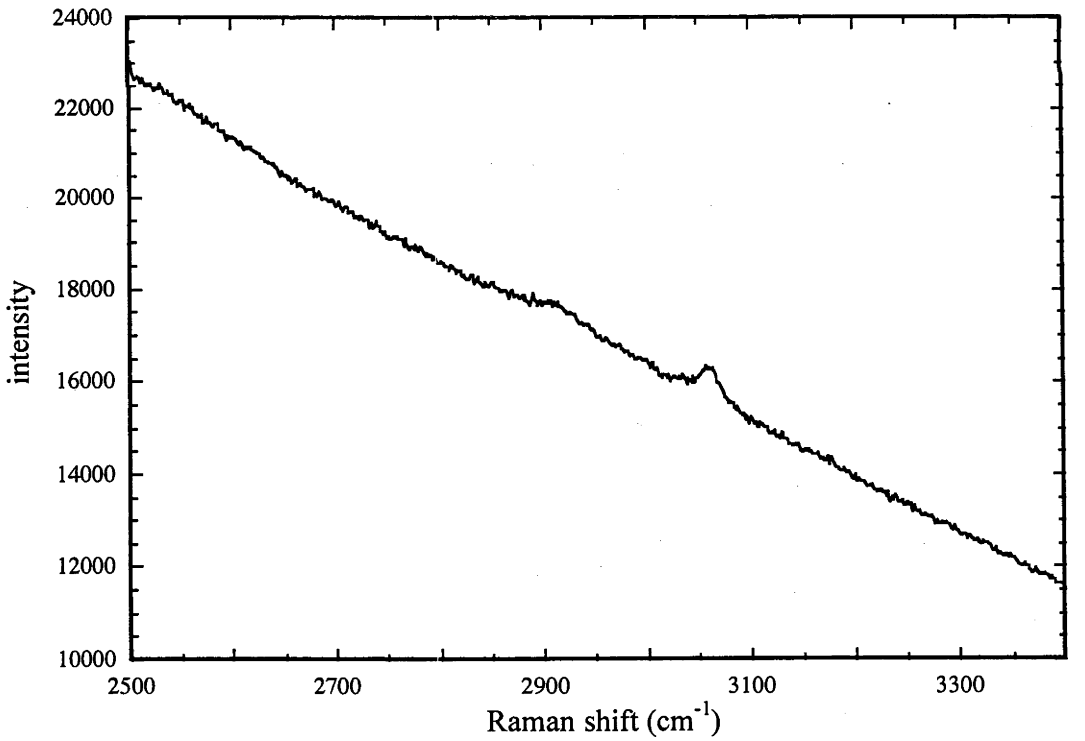


**Figure 3.9: Benzyl mercaptan on smooth gold (632.8 nm excitation)**

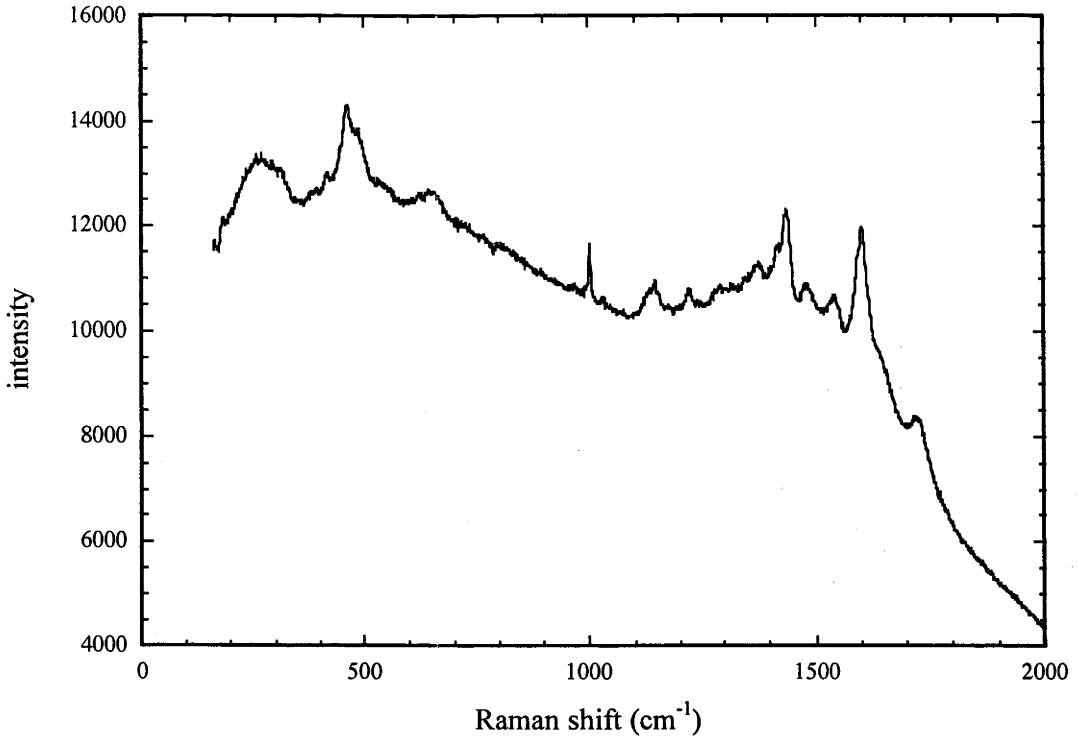


**Figure 3.10: DLP on smooth gold (780 nm excitation)**

## 3.5 Discussion

By examination of the spectra, from which a baseline has not been subtracted, it can be seen that there is a very high background (of the order of 10000-20000 counts for the surface spectra; figures 3.4-3.10). The surface spectra generated using 632.8 nm excitation show a 'double-humped' background with very broad peaks centred around 1000 $cm^{-1}$ and 1900 $cm^{-1}$ (see figures 3.7 and 3.8). By contrast, the surface spectra measured with 780 nm excitation show a 'single-humped' background which decreases steadily above ~500 $cm^{-1}$ and more rapidly above ~1700 $cm^{-1}$ (figures 3.4, 3.6 and 3.10). These patterns are most consistent with fluorescence from unidentified surface contaminants. The spectrum of liquid dodecanethiol (figure 3.3) has a much lower background (ranging from 100-1000) which shows a steady decrease below ~300 $cm^{-1}$. The large drop-off in intensity in all spectra below ~150 $cm^{-1}$ is due to the holographic notch filter incorporated in the system.

**Table 3.1: Peaks in the 1-dodecanethiol spectra (780 nm excitation)**

| Peak position ($cm^{-1}$) | | | Assignment[4,13,15,27,44] |
|---|---|---|---|
| Liquid | Figures 3.4 and 3.5 | Figure 3.6 | |
| 227 | | | ? |
| 349 | | | ? |
| 405 | | | ? |
| 655 | | | $\nu_{str}$(C-S) (gauche) |
| 706 | | | $CH_2$ rock |
| 737 | 708 | 712 | $\nu_{str}$(C-S) (trans) |
| 847 | | | ? |
| 868 | | | $CH_2$ rock (gauche) |
| 890 | | 891 | $CH_3$ rock (trans) |
| 1023 | | | $\nu_{str}$(C-C) |
| 1072 | 1083 | 1082 | $\nu_{str}$(C-C) (gauche) |
| 1124 | 1123 | 1126 | $\nu_{str}$(C-C) (trans) |
| | | 1275 | $CH_2$ twist |
| 1301 | | 1299 | $CH_2$ wag |
| | 1372 | 1365 | contaminant |
| 1438 | 1435 | 1439 | $CH_2$ scissor mode |
| | 1479 | | contaminant |
| | | 1513 | contaminant |
| | 1538 | | contaminant |
| | 1602 | | contaminant |
| | 1725 | | contaminant |
| 2576 | | | S-H stretch |
| 2851 | 2848 | | C-H stretch |
| ~2886 | ~2886 | | C-H stretch |

**Table 3.2: Peak locations in the 632.8 nm 1-dodecanethiol spectrum (figure 3.7)**

| Peak location ($cm^{-1}$) | Clark et al.[34] location ($cm^{-1}$) | Assignment |
|---|---|---|
| 484 | | ? |
| 679 | 680 | image state |
| 833 | 833 | image state |
| 848 | 848 | image state |
| 950 | 954 | image state |
| 1006 | | ? |
| 1105 | 1108 | image state |
| 1141 | | ? |
| 1196 | 1195 | image state |
| 1211 | | ? |
| 1339 | 1341 | image state |
| 1409 | | ? |
| 1453 | | ? |
| 1527 | 1529 | image state |
| 1570 | | ? |
| 1600 | | contaminant |

**Table 3.3: Peak locations in the benzyl mercaptan spectrum (figures 3.8 and 3.9)**

| Peak location ($cm^{-1}$) | Assignment[31,45,46] |
|---|---|
| 459 | contaminant |
| 657 | C-S stretch |
| 767 | $\nu_{11}$ (out of plane C-H bend) |
| 895 | $\nu_{7b}$ (out of plane C-H bend) |
| 1000 | aromatic ring breathing mode |
| 1031 | $\nu_{18a}$ (in-plane C-H bend) |
| 1152 | $\nu_{9b}$ (in-plane C-H bend) |
| 1182 | $\nu_{9a}$ (in-plane C-H bend) |
| 1479 | contaminant |
| 1593 | contaminant or ring deformation mode |
| ~2910 | aliphatic C-H stretch |
| 3060 | aromatic C-H stretch |

**Table 3.4: Peak locations in the DLP spectrum (figure 3.10)**

| Peak location ($cm^{-1}$) | Assignment |
|---|---|
| ~470 | contaminant |
| 650 | C-S stretch |
| 1002 | aromatic ring breathing mode |
| 1145 | ? |
| 1222 | ? |
| 1376 | ? |
| 1435 | $CH_2$ scissor mode |
| 1479 | contaminant |
| 1541 | contaminant |
| 1600 | contaminant |
| 1721 | contaminant |

Despite the poor quality of the data, peaks can be identified in all four spectra. In the case of 1-dodecanethiol using 780 nm excitation (figures 3.5 and 3.6), vibrational peaks due to C-S stretches (in the 600-800 $cm^{-1}$ region), C-C stretches (1000-1200 $cm^{-1}$ region) and C-H stretches (~2800 $cm^{-1}$) are observable. The observed peak positions correlate reasonably closely with those reported by Bryant and Pemberton[4] for 1-dodecanethiol on gold. Other peaks in the 800-1000 $cm^{-1}$ and 1200-1500 $cm^{-1}$ regions are assigned to $CH_2$ and $CH_3$ rock, twist and wag modes[15,27,44] (see table 3.1). The assignment of the peaks at 227, 349 and 405 $cm^{-1}$ in the liquid dodecanethiol spectrum is uncertain; these peaks are probably due to torsion modes. Further work with deuterated compounds and computations would be required to give more certainty to the assignments in table 3.1. A number of peaks commonly seen in the 1300-1600 $cm^{-1}$ region of monolayer Raman spectra have been proposed by Taylor et al.[13] to arise from polyaromatic hydrocarbon contaminants in the monolayer.

Peaks due to surface contamination can be seen in figure 3.4 at 462, 1372, 1479, 1538, 1602 and 1725 $cm^{-1}$. These prominent peaks are not visible in the spectrum of liquid dodecanethiol (figure 3.3), supporting the assignment to contaminants, possibly polyaromatic hydrocarbons. The contaminant peaks (e.g., 1479, 1538, 1602, 1725 $cm^{-1}$) have diminished in intensity in figure 3.6 when compared to figure 3.4,

suggesting that the electrochemical cycling has had a cleaning effect on the surface. Further support to the assignment of the peaks to surface contaminants is given by the fact that many of the same peaks are observed in the spectra of DLP and possibly benzyl mercaptan on smooth gold (figures 3.8 and 3.10 respectively).

Electrochemical roughening of the gold surface appears to have a moderate enhancement effect on the Raman spectrum of 1-dodecanethiol on gold. This is particularly noticeable for the C-C stretch peaks at ~1080 and ~1120 $cm^{-1}$ (about a 4-fold enhancement for these two peaks when comparing figures 3.4 and 3.6).

The S-H stretch peak, observed at 2576 $cm^{-1}$ in the spectrum of liquid 1-dodecanethiol (figure 3.3)[4,45], is absent in the spectra of benzyl mercaptan and 1-dodecanethiol on gold (figures 3.5 and 3.9). This supports the proposition that these molecules form monolayers through cleavage of the S-H bond and formation of a gold-sulphur bond.

The peaks in the spectrum of 1-dodecanethiol on smooth gold with 632.8 nm excitation (figure 3.7) mostly have frequencies which correspond closely to those of the peaks observed recently by Clark et al.[34] and assigned by them as image state transitions. The peak at 1600 $cm^{-1}$ is probably a carbonaceous surface contaminant (see the discussion of the 780 nm spectra above), while the assignment of the other seven peaks is uncertain. Clark et al. reported that observation of image states required excitation wavelengths in the 630-740 nm region, which agrees with the image state peaks being observed for 632.8 nm, but not 780 nm excitation. Clark et al.[34,38] observed that carbon chain lengths between nonanethiol and octadecanethiol were required to observe the image state transitions at room temperature. The fact that these peaks were observed for dodecanethiol, but not benzyl mercaptan, monolayers, even though 632.8 nm excitation was used for both spectra, agrees with the results of Clark et al.

In the benzyl mercaptan spectra (figures 3.8 and 3.9), the aromatic ring-breathing mode is prominent[45] at 1000 $cm^{-1}$. In the C-H stretching region, weak and broad peaks due to aromatic C-H stretch modes and the aliphatic $CH_2$ stretch modes are discernable. Raman spectra have been measured previously for benzyl mercaptan on gold electrodes (at various potentials)[31], on silver colloids and silver island films[47] and using the neat compound[48,49]. The most significant peak in figure 3.8 other than those already discussed is one at 1593 $cm^{-1}$. Based on the results of Joo et al.[46] and Szafranski et

al.[31], this peak could be due to an in-plane deformation mode ($\nu_{8a}$ in the Wilson system[50]). Alternatively, it could be one of the carbonaceous contaminant peaks observed for DLP and dodecanethiol. The absence of other contaminant peaks in the 1300-1600 $cm^{-1}$ region of figure 3.8 (these prominent peaks, which are evident in figures 3.4 and 3.10 are referred to as the 'cathedral peaks' by some authors) lends support to the assignment of the 1593 $cm^{-1}$ peak to the $\nu_{8a}$ vibration. Further work would be required to confirm this assignment. The remaining peaks are weaker. Based on the assignments of Szafranski et al.[31], the peak at 657 $cm^{-1}$ arises from the C-S stretch, while those at 767 and 895 $cm^{-1}$ are C-H out-of-plane bends, and those at 1031, 1152 and 1182 $cm^{-1}$ are due to C-H in-plane bends.

Only very limited observations can be made concerning the spectrum of DLP (figure 3.10). One strong peak seen at 1001 $cm^{-1}$ can be assigned as the ring breathing mode of the benzene ring which forms one 'half' of the disulphide bridge (see figure 3.2). This corresponds to the peak at 1000 $cm^{-1}$ in the benzyl mercaptan spectrum. It is unclear whether a sulfur-sulfur stretch peak[45] (expected between 450 and 550 $cm^{-1}$) is present. A peak is observed at roughly 470 $cm^{-1}$, however a similar peak is observed at 477 $cm^{-1}$ for dodecanethiol (figure 3.6). Although DLP contains carbonyl groups (see figure 3.2), the peak at 1725 $cm^{-1}$ is unlikely to be due to C=O stretches, as the same peak is observed for the spectra of dodecanethiol and benzyl mercaptan, neither of which contain carbonyl groups. Further, the carbonyl groups will be relatively distant from the gold surface and as a result will experience little enhancement. The peak at 1435 $cm^{-1}$ is tentatively assigned to the $CH_2$ scissor mode, based on the assignment of a peak at this position in the dodecanethiol spectra.

## 3.6 Conclusion

From this work, it was found that measurement of Raman spectra of self-assembled monolayers on metal surfaces is more straightforward using a Raman microscope (180° scattering instrument) than a 90° scattering instrument, mainly as a result of the sample alignment being fixed for a Raman microscope. This reduces the number of parameters to be adjusted, which has the advantage of reduced setting up time, but the disadvantage that the sample alignment cannot be optimised to improve the Raman signal. For a 90° scattering instrument such as those described in chapter 3, the orientation must be

optimised for each sample tested. It was unfortunate that spectra could not be obtained using either of the 90° scattering Raman spectrometers in the Krausz group, as these instruments have a number of advantages over the Raman microscope. These include a wider range of laser excitation wavelengths, better stray light rejection by virtue of the double and triple monochromators and a more sensitive detector in the shape of the Princeton Instruments CCD camera. The problem mentioned above relating to alignment could potentially be an advantage of 90° geometry: the fact that the sample alignment can be changed means that the alignment, and hence the spectrum obtained, can be optimised.

Other workers in the field of surface Raman spectroscopy[51-54] have calculated the effect of the angle of incidence on the magnitude of the incident electric field, and the effect of the angle of observation on the scattered light intensity using Fresnel's equations and considering the symmetry of the Raman mode (i.e. the polarisability tensor components involved). Mullins and Campion[54], for example, adapted the earlier calculations of Greenler and Slager[53] to determine the optimum angle of observation for the ring breathing mode of benzene lying flat on a silver (111) crystal surface. Very good agreement between theory and experiment was obtained.

Background was a severe problem in all the spectra shown here, and probably swamped many of the Raman peaks. Other workers have experienced similar problems, usually attributing it to fluorescence by surface contaminants such as polyaromatic hydrocarbons formed during the polishing process. These contaminants also gave rise to additional peaks in the spectra that could be confused with sample peaks. Possible means of circumventing the problem could include sputtering a gold overlayer on top of a gold electrode to provide a clean surface. The sputtered gold film would need to be of sufficient thickness to prevent the excitation laser penetrating the overlayer and producing Raman scattering from the contaminants on the electrode surface. The use of clean room facilities for monolayer preparation would also help in reducing the amount of surface contamination. Another factor working against the adoption of surface Raman spectroscopy is the necessity of surface roughening for signal enhancement. Substantial improvements and modifications would need to be made to this Raman spectroscopic method would be necessary before the technique could be used to perform routine measurements on AMBRI thin films.

## 3.7 References


(1) Ulman, A. *Chemical Reviews* **1996**, *96*, 1533-1554.

(2) Nuzzo, R. G.; Allara, D. L. *Journal of the American Chemical Society* **1983**, *105*, 4481-4483.

(3) Ulman, A. *An Introduction to Ultrathin Organic Films: From Langmuir-Blodgett to Self-Assembly*; Academic Press:, 1991.

(4) Bryant, M. A.; Pemberton, J. E. *Journal of the American Chemical Society* **1991**, *113*, 8284-8293.

(5) Bryant, M. A.; Pemberton, J. E. *Journal of the American Chemical Society* **1991**, *113*, 3629-3637.

(6) Joo, T. H.; Kim, K.; Kim, M. S. *Journal of Physical Chemistry* **1986**, *90*, 5816-5819.

(7) Joo, T. H.; Kim, K.; Kim, M. S. *Journal of Molecular Structure* **1987**, *158*, 265-274.

(8) Joo, T. H.; Kim, M. S.; Kim, K. *Journal of Molecular Structure* **1987**, *160*, 81-89.

(9) Kwon, C. K.; Kim, K.; Kim, M. S.; Lee, Y. S. *Journal of Molecular Structure* **1989**, *197*, 171-180.

(10) Lee, S. B.; Kim, K.; Kim, M. S.; Oh, W. S.; Lee, Y. S. *Journal of Molecular Structure* **1993**, *296*, 5-13.

(11) Whitesides, G. M.; Laibnis, P. E. *Langmuir* **1990**, *6*, 87-96.

(12) Moskovits, M. *Reviews of Modern Physics* **1985**, *57*, 783-826.

(13) Taylor, C. E.; Schoenfisch, M. H.; Pemberton, J. E. *Langmuir* **2000**, *16*, 2902-2906.

(14) Norrod, K. L.; Rowlen, K. L. *Analytical Chemistry* **1998**, *70*, 4218-4221.

(15) Schoenfisch, M. H.; Ross, A. M.; Pemberton, J. E. *Langmuir* **2000**, *16*, 2907-2914.

(16) Kudelski, A.; Krysinski, P. *Journal of Electroanalytical Chemistry and Interfacial Electrochemistry* **1998**, *443*, 5-7.

(17) Schoenfisch, M. H.; Pemberton, J. E. *Langmuir* **1999**, *15*, 509-517.

(18) Sandroff, C. J.; Garoff, S.; Leung, K. P. *Chemical Physics Letters* **1983**, *96*, 547-551.

(19) Sobocinski, R. L.; Bryant, M. A.; Pemberton, J. E. *Journal of the American Chemical Society* **1990**, *112*, 6177-6183.

(20) Fleischmann, M.; Hendra, P. J.; McQuillan, A. J. *Chemical Physics Letters* **1974**, *26*, 163-166.

(21) Aroca, R. *Journal of Molecular Structure* **1993**, *292*, 17-28.

(22) Campion, A.; Kambhampati, P. *Chemical Society Reviews* **1998**, *27*, 241-250.

(23) Creighton, J. A. In *Spectroscopy of Surfaces*; Clark, R. J. H., Hester, R. E., Eds.; John Wiley and Sons: Chichester, 1988; Vol. 16, p 37-89.

(24) Garrell, R. L. *Analytical Chemistry* **1989**, *61*, 401A-411A.

(25) Weaver, M. J.; Zou, S. In *Spectroscopy for Surface Science*; Clark, R. J. H., Hester, R. E., Eds.; John Wiley and Sons: Chichester, 1998; Vol. 26, p 219-272.

(26) Weaver, M. J.; Zou, S.; Chen, H. Y. H. *Analytical Chemistry* **2000**, *72*, 38A-47A.

(27) Sandhayarani, N.; Pradeep, T. *Vacuum* **1998**, *49*, 279-284.

(28) Huang, F. K.; Horton Jr, R. C.; Myles, D. C.; Garrell, R. L. *Langmuir* **1998**, *14*, 4802-4808.

(29) Garrell, R. L.; Chadwick, J. E.; Severance, D. L.; McDonald, N. A.; Myles, D. C. *Journal of the American Chemical Society* **1995**, *117*, 11563-11571.

(30) Szafranski, C. A.; Tanner, W.; Laibinis, P. E.; Garrell, R. L. *Langmuir* **1998**, *14*, 3580-3589.

(31) Szafranski, C. A.; Tanner, W.; Laibinis, P. E.; Garrell, R. L. *Langmuir* **1998**, *14*, 3570-3579.

(32) Evans, S. D.; Goppert-Berarducci, K. E.; Urankar, E.; Gerenser, L.; Ulman, A. *Langmuir* **1991**, *7*, 2700-2709.

(33) Evans, S. D.; Urankar, E.; Ulman, A.; Ferris, N. *Journal of the American Chemical Society* **1991**, *113*, 4121-4131.

(34) Clark, B. K.; Gregory, B. W.; Avila, A.; Cotton, T. M.; Standard, J. M. *Journal of Physical Chemistry B* **1999**, *103*, 8201-8204.

(35) Fauster, T. *Applied Physics A* **1994**, *59*, 479-486.

(36) Straub, D.; Himpsel, F. J. *Physical Review Letters* **1984**, *52*, 1922-1924.

(37) Straub, D.; Himpsel, F. J. *Physical Review B* **1986**, *33*, 2256-2262.

(38) Avila, A.; Gregory, B. W.; Clark, B. K.; Standard, J. M.; Cotton, T. M. *Langmuir* **2002**, *18*, 4709-4719.

(39) Clark, B. K.; Gregory, B. W.; Standard, J. M. *Physical Review B* **2000**, *62*, 17084-17088.

(40) Clark, B. K.; Standard, J. M.; Gregory, B. W.; Hall, A. D. *Surface Science* **2002**, *498*, 285-292.

(41) Gregory, B. W.; Clark, B. K.; Standard, J. M.; Avila, A. *Journal of Physical Chemistry B* **2001**, *105*, 4684-4689.

(42) Cornell, B. A.; Braach-Maksvytis, V. L. B.; King, L. G.; Osman, P. D. J.; Raguse, B.; Wieczorek, L.; Pace, R. J. *Nature* **1997**, *387*, 580-583.

(43) Raguse, B.; Braach-Maksvytis, V.; Cornell, B. A.; King, L. G.; Osman, P. D. J.; Pace, R. J.; Wieczorek, L. *Langmuir* **1998**, *14*, 648-659.

(44) Hayashi, M.; Shiro, Y.; Murata, H. *Bulletin of the Chemical Society of Japan* **1966**, *39*, 112-117.

(45) Freeman, S. K. *Applications of Laser Raman Spectroscopy*; 1st ed.; John Wiley and Sons: New York, 1974.

(46) Joo, T. H.; Yim, Y. H.; Kim, K.; Kim, M. S. *Journal of Physical Chemistry* **1989**, *93*, 1422-1425.

(47) Lee, T. G.; Kim, K.; Kim, M. S. *Journal of Raman Spectroscopy* **1991**, *22*, 339-344.

(48) Doerfell, K.; Adler, B. *Wissenschaftliche Zeitschrift der Technischen Hochschule fuer Chemie Carl Schorlemmer Leuna-Meuseburg* **1968**, *10*, 7-11.

(49) Mallick, P. K.; Chattopadhyay, S.; Banerjee, S. B. *Indian Journal of Pure and Applied Physics* **1973**, *11*, 609-611.

(50) Dollish, F. R.; Fateley, W. G.; Bentley, F. F. *Characteristic Raman Frequencies of Organic Compounds*; 1st ed.; John Wiley and Sons: New York, 1974.

(51) Campion, A. *Annual Reviews Physical Chemistry* **1985**, *36*, 549-572.

(52) Debe, M. K. *Progress in Surface Science* **1987**, *24*, 1-282.

(53) Greenler, R. G.; Slager, T. L. *Spectrochimica Acta* **1973**, *29A*, 193-201.

(54) Mullins, D. R.; Campion, A. *Journal of Physical Chemistry* **1984**, *88*, 8-10.

# Chapter 4: The angular overlap model and trigonal fields

The angular overlap model (AOM) was first proposed by Yamatera in 1957-8[1], for the restricted case of orthoaxial systems (complexes with octahedral geometry and linear ligators). Schäffer and Jorgensen improved the model and generalised it[2,3]. Several computer programs have been written to perform AOM calculations, notably CAMMAG by Gerloch et al.[4]. More recently, the model has been extended by the inclusion of such factors as s-d mixing, misdirected valency ('bent' bonds) and non-additive $\pi$ contributions[5].

The AOM introduces a set of bonding parameters that reflect the local charge distribution on the coordinating ligand atom. The charge distribution is reflected in the local geometry of the metal-ligand bond. The experimental ligand field parameters can then be related to the AOM and geometric parameters.

## 4.1 The 3d orbitals

Like all atomic orbitals, the five 3d orbitals are represented by functions, which can be real or imaginary. Different bases can be used to represent the orbitals, depending on the symmetry of the complex. For a complex with cubic symmetry, the real basis in terms of the cubic metal axes is:

$$
\begin{aligned}
u &= 2z^2 - x^2 - y^2 [d_{z^2}] \\
v &= \sqrt{3}(x^2 - y^2)[d_{x^2-y^2}] \\
\xi &= 2\sqrt{3}yz[d_{yz}] \qquad (4.1)-(4.5) \\
\eta &= 2\sqrt{3}xz[d_{xz}] \\
\varsigma &= 2\sqrt{3}xy[d_{xy}]
\end{aligned}
$$

For trigonal complexes it is convenient to introduce trigonal axes (X,Y,Z) in place of cubic axes (x,y,z). The standard definition is:

$$\begin{bmatrix} X \\ Y \\ Z \end{bmatrix} = \begin{bmatrix} -1/\sqrt{6} & -1/\sqrt{6} & 2/\sqrt{6} \\ 1/\sqrt{2} & -1/\sqrt{2} & 0 \\ 1/\sqrt{3} & 1/\sqrt{3} & 1/\sqrt{3} \end{bmatrix} \begin{bmatrix} x \\ y \\ z \end{bmatrix} \quad (4.6)$$

The functions for the $e_g$ orbitals, $u$ and $v$, remain the same as for the cubic basis. The $t_{2g}$ orbitals are represented in the trigonal basis as follows:

$$\rho = 1/\sqrt{6}(2\varsigma - \xi - \eta)$$
$$\sigma = 1/\sqrt{2}(\xi - \eta) \qquad (4.7) - (4.9)$$
$$\tau = 1/\sqrt{3}(\xi + \eta + \varsigma)$$

## 4.2 The standard configuration

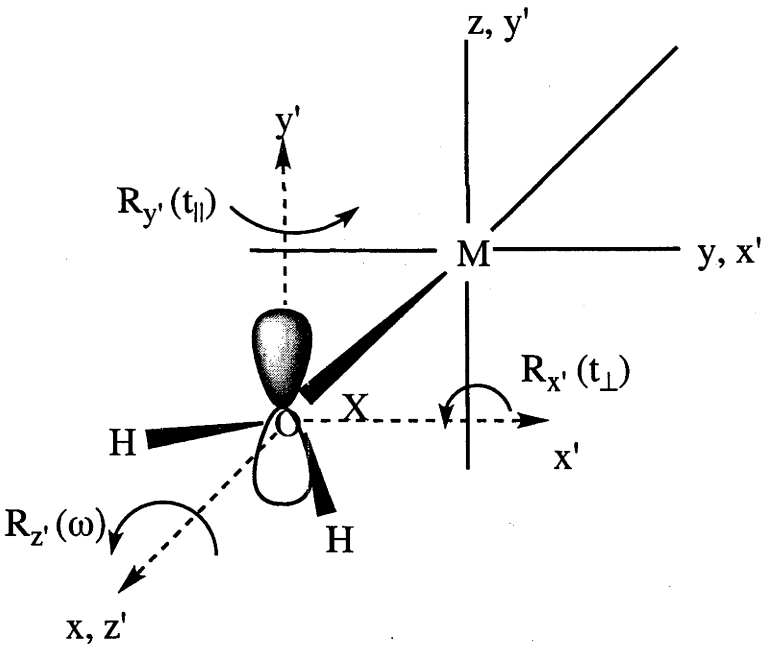


**Figure 4.1: Standard configuration for a water ligand in a transition metal hexahydrate complex, such as cobalt or nickel bromate hexahydrates (studied in this thesis). The axes (x, y, z) are the cubic metal axes, while the axes (x', y', z') are the ligand axes, or the metal axes rotated to match the ligand axes.**

The zero for each of the angles is arbitrary. For the purposes of this work, the standard configuration of a water ligand, is defined as the molecule lying in the x'z' plan, with the z'-axis being coincident with the metal-oxygen bond. The pπ orbital containing the lone pair of electrons is perpendicular to the molecular plane and coincident with the ligand y'-axis. Three angular parameters are needed to define the orientation of each ligand. The angles ω (rotation), $t_{||}$ (parallel tilt), $t_{\perp}$ (perpendicular tilt) are, respectively, the angles of anticlockwise rotation about the z', y' and x' axes; see figure 4.1. These angles are all zero in figure 4.1.

A similar definition of the standard configuration and the various rotation angles is given for the pyrazolyl ligands (see figure 4.2 below).

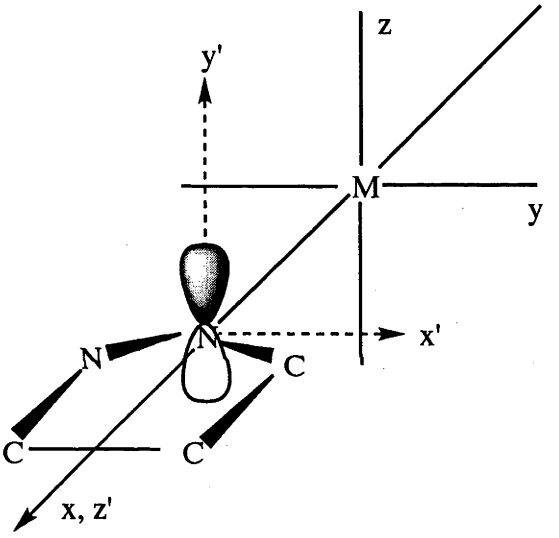


**Figure 4.2: Standard configuration for a pyrazolyl ligand in the monopyrazolyl and capped pyrazolyl complexes studied in this thesis**

The zero for the parallel tilt ($t_{||}$) angle is not defined for the pyrazolyl ligand as unlike water, pyrazole does not have a plane of symmetry in the y'z' plane. There will be an angle of $t_{||}$ that will give a symmetric charge distribution, and can therefore be regarded as $t_{||} = 0°$. However, this cannot be determined intuitively. This point is further discussed in section 4.3.2.

## 4.3 Distortion

An octahedral $ML_6$ complex can be distorted in a number of ways. This section discusses the various distortions, which in the right combination can result in trigonal symmetry.

While tetragonal distortion from octahedral symmetry results from elongation or compression of an axial pair of bonds, trigonal distortion arises from angular perturbations. Dubicki and Bramley[6] discussed the various angular changes that can result in overall trigonal symmetry.

### 4.3.1 Cone angle compression/elongation

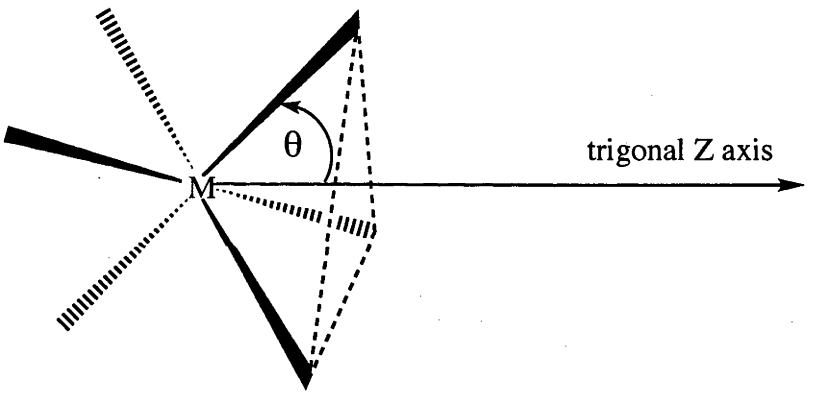


**Figure 4.3: Trigonal distortion of octahedral symmetry by cone angle changes. A complex with octahedral symmetry has θ = 54.736°, while for a trigonally elongated complex, θ < 54.736° and for a trigonally compressed complex, θ > 54.736°**

The simplest form of trigonal distortion is elongation or compression of an octahedral complex along the threefold rotational axes (see figure 4.3). This operation reduces the symmetry of the complex from $O_h$ to $D_{3d}$. The trigonal cone angle θ is defined as the acute angle between the remaining threefold rotational axis and a metal-ligand bond. In an undistorted octahedral complex, this angle is $\cos^{-1}(1/\sqrt{3})$ or 54.74° ($\theta_{oct}$); in a trigonally compressed complex, $\theta > \theta_{oct}$, while in a trigonally elongated complex, $\theta < \theta_{oct}$.

This form of trigonal distortion affects the ligand field produced by both σ- and π-bonds.

### 4.3.2 Tilt

Perpendicular tilt ($t_\perp$) often occurs in combination with rotation. Tilt affects both π and σ bonding, and is often found in complexes with polyatomic ligands. The sign of $t_\perp$ for a ligand on the cubic x axis is defined to be positive if the normal to the molecular plane of the ligand tilted away from the positive cubic z axis (i.e. anti-clockwise rotation about the ligand x' axis, see figure 4.1).

Parallel tilt ($t_\parallel$) involves the misalignment of the ligand σ-bonding orbital within the ligand plane (see figures 4.1 and 4.2). Any π bonding along the x' axis will also be affected, while π bonding along the y' axis will be unchanged by this distortion. In the undistorted case, there is no rotation of the ligand about the y' axis (see figures 4.1 and 4.2). For some special value of ∠MNN ($t_\parallel 0$), the AOM bonding parameter $e_{\sigma\pi}$ (x'z') is zero. Then $t_\parallel$ can be defined as $t_\parallel$ = ∠MNN – $t_\parallel 0$, although the value of $t_\parallel 0$ is not known.

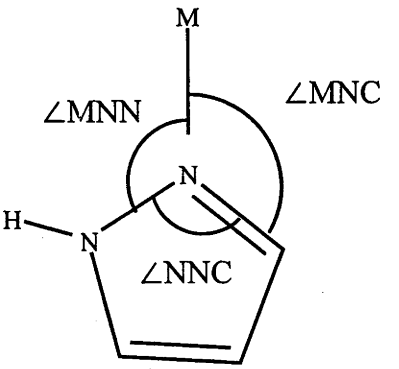


**Figure 4.4: The angles measured to quantify the parallel tilt for the pyrazolyl ligands**

### 4.3.3 Rotation (ω)

This form of trigonal distortion often occurs in combination with tilt. Unlike trigonal compression/elongation and tilt, rotation alone will only distort an octahedral ligand field if there is π bonding. Again considering the $[M(H_2O)_6]$ complex ion (see figure 4.1). In an undistorted $MO_6$ octahedron, the dihedral angle between the ligand plane normal and an adjacent metal-oxygen bond axis (ω) is 0°. The angle ω has positive sign if the rotation is anticlockwise.

### 4.3.4 Twist

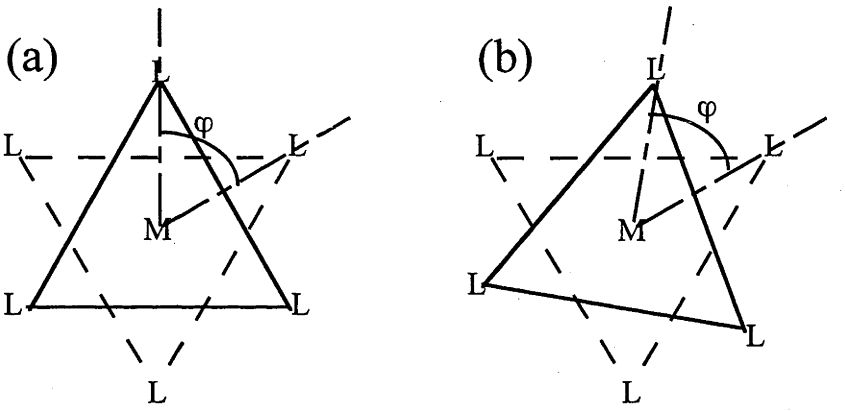


**Figure 4.5: Twisting of an octahedral $ML_6$ complex. Case (a) shows zero twist (φ = 60°), while case (b) shows a non-zero twist**

The $ML_6$ complexes represented in figure 4.5 are viewed along a threefold rotational axis. If the complex has perfect octahedral symmetry, the projection in the plane of the page of a bond from the metal to one of the lower group of three ligands will be at an angle of 60° to the corresponding projection of a bond from the metal to one of the ligands in the upper group of three (case (a) in figure 4.5). A complex may be distorted from octahedral geometry by twisting, i.e. rotation of the two groups of three ligands with respect to each other (case (b) in figure 4.5). The twist angle is the difference between the measured angles of the bond projections and the zero twist case (φ = 60°).

By symmetry, trigonally distorted complexes with $S_6$ or $D_{3d}$ symmetry must have zero twist. Introducing a twist to complexes with $D_{3d}$ or $S_6$ symmetry would destroy the centre of inversion, the three dihedral mirror planes and the sixfold rotation-inversion axes, reducing the symmetry to $D_3$ or $C_3$ respectively. The $[M(H_2O)_6](BrO_3)_2$, and the hexakis pyrazolyl complexes considered in this thesis, have precise $S_6$ symmetry, while the $[M(HCPz_3)_2](NO_3)_2$ and $[M(HBPz_3)_2]$ complexes have approximate $D_{3d}$ symmetry. Therefore, the twist is zero for the former group of complexes, and is very small and is ignored for the latter group.

### 4.3.5 Measurement of the geometric parameters

The parameters $t_\perp$ and $\omega$ can be simply measured using a Windows-based molecular graphics program such as Crystal Maker. Such programs will generate a pictorial representation of a chemical structure from crystallographic data entered as Cartesian or fractional coordinates. For the bromate complexes, the hydrogen atom positions in the X-ray structures are not sufficiently accurate for estimating $t_\perp$ and $\omega$. In these cases, the coordinates of the outer sphere oxygen atoms which form approximately linear hydrogen bonds are used (see table 4.1). As can be seen from this table, the differences between the values determined using the bromate oxygen positions and those determined using the hydrogens are substantial. Given that the bromate oxygen positions in the X-ray structures are more accurate than the hydrogen positions, the tilt and rotation angles determined using the bromate oxygens will be used in this thesis.

The tilt often occurs in combination with rotation and cone angle distortion. If the cone angle distortion is large, then the simple use of angles between bonds or dihedral angles between plane normals can lead to some error. These problems have been avoided by using a rigorous algebraic method[7] for deriving the $t_\perp$ and $\omega$ tabulated below. The relevant angles were calculated from published crystal structure data for the bromate hexahydrates, the monopyrazolyl compounds and the capped pyrazolyl compounds and are shown in the tables below.

**Table 4.1: Relevant angles and bond lengths in the bromate hexahydrates**

| Compound | Crystal structure reference | R (M-O) (Å, where M = Co, Ni or Cr) | Cone angle (θ) | Tilt ($t_\perp$) | | Rotation (ω) | |
|---|---|---|---|---|---|---|---|
| | | | | $t_{\perp O}$a | $t_{\perp H}$a | $\omega_O$a | $\omega_H$a |
| $[Co(H_2O)_6](BrO_3)_2$ | Blackburn et al. 1990[8] | 2.095 | 54.7° | –28.3° | –52.9° | 34.4° | 27.3° |
| $[Ni(H_2O)_6](BrO_3)_2$ | Blackburn et al. 1991[9] | 2.061 | 55.0° | –29.4° | –56.1° | 33.9° | 26.0° |

The calculated values of $t_\parallel$ are 2.2° and 2.4° for Ni(II) and Co(II) respectively. They are considered to be very small and the $t_\parallel$ distortion is neglected for the bromate complexes.

[a]The angles $t_{\perp O}$ and $\omega_O$ are determined using the hydrogen bonds (i.e. the bromate oxygens to which the 'strong' hydrogen bonds are formed), whereas the angles $t_{\perp H}$ and $\omega_H$ are determined using the hydrogen atom positions. The values used from this point on in thesis are $t_{\perp O}$ and $\omega_O$, and will be simply referred to as $t_\perp$ and ω.

**Table 4.2: Relevant angles and bond lengths for the nickel monopyrazolyl species**

| Compound | Crystal structure reference | R (Ni-N) (Å) | ∠MNC | ∠MNN | Tilt ($t_\perp$) | Rotation (ω) | Cone angle (θ) |
|---|---|---|---|---|---|---|---|
| $[Ni(Pz)_6](NO_3)_2$ | Reimann et al. 1970[10] | 2.125 | 129.2° | 126.0° | +3.5° | –14.5° | 55.3° |
| $[Ni(Pz)_6](BF_4)_2$ | ten Hoedt et al. 1983[11] | 2.098 | 131.2° | 126.2° | –5° | –11° | 55.1° |
| $[Mn(Pz)_6](ClO_4)_2$ | Lumme et al. 1988[12] | 2.261 | 130.9° | 124.6° | –6° | –10° | 55.1° |
| $[Ni(5MePz)_6](ClO_4)_2$ | Collison et al. 1998[13] | 2.099 | 130.6° | 125.1° | –4.4° | –2.3° | 54.7° |

**Table 4.3: Relevant angles and bond lengths for the capped pyrazolyl species (at 295 K except where indicated otherwise)[a]**

| Compound | Crystal structure reference | R (M-N) (Å) | ∠MNC | ∠MNN | Cone angle (θ) |
|---|---|---|---|---|---|
| $[Mn(HBPz_3)_2][Mn(H_2O)_6](ClO_4)_4$ | Chan and Armstrong 1989[14] | 1.955 | NA | NA | 53.8° |
| $[Fe(HCPz_3)_2](NO_3)_2$ (α form) | Anderson et al. 2000[15] | 1.968 | 137.1° | 117.9° | 53.1° |
| $[Co(HCPz_3)_2](NO_3)_2$ | Astley et al. 1993[16] | 2.115 | 137.4° | 117.4° | 50.9° |
| $[Co(HCPz_3)_2](NO_3)_2$ (173 K) | Keene and Tiekink 1994[17] | 2.086 | 137.5° | 117.4° | 51.1° |
| $[Ni(HCPz_3)_2](NO_3)_2$ | Astley et al. 1993[16] | 2.078 | 137.0° | 117.4° | 51.6° |
| $[Zn(HCPz_3)_2](NO_3)_2$ | Astley et al. 1993[16] | 2.142 | 137.8° | 117.0° | 50.8° |
| $[Co(HBPz_3)_2]$ | Churchill et al. 1970[18] | 2.129 | 134.7° | 119.1° | 51.6° |
| $[Ni(HBPz_3)_2]$ | Bandoli et al. 1979[19] | 2.093 | 135.0° | 118.4° | 52.5° |
| $[Zn(HBPz_3)_2]$ | Nakata et al. 1995[20] | 2.155 | 135.7° | 118.0° | 51.7° |

[a]For the capped pyrazolyl complexes, four of the pyrazole rings have essentially zero tilt perpendicular to the ring, while the other two are slightly tilted (t ~ 8°). This distortion produces a small rhombic field and is neglected. The averaged value of the rotation ω is close to the idealised value (135°) and is set to that value in the AOM calculations. NA = not available

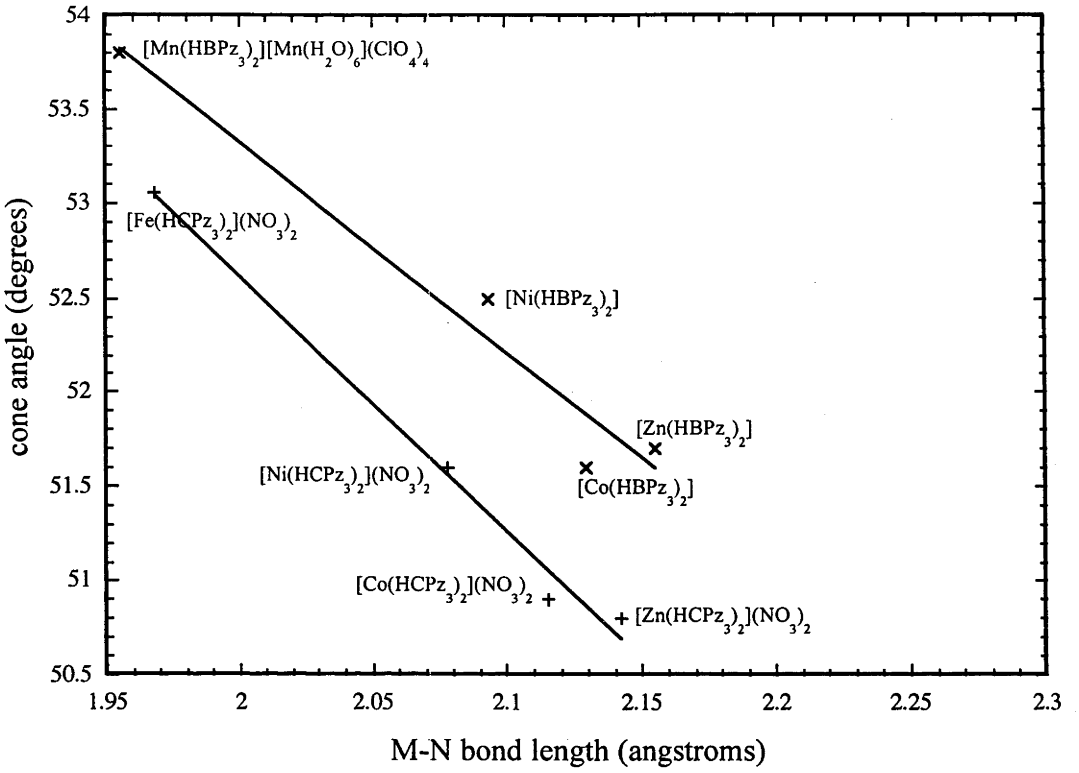


**Figure 4.6: Relationship between the cone angle and the average metal-ligand bond length for some capped pyrazolyl species**

The relationship between the cone angle and the metal-ligand bond length for the capped pyrazolyl complexes is represented graphically in figure 4.6, using the literature data from table 4.3. As can be seen from the figure, for each of the two series of capped pyrazolyl complexes (the pyrazolyl borates and the pyrazolyl methanes), the cone angle has an inverse relationship with the metal-ligand bond length.

## 4.4 Input energy matrices for the AOM

Using the real cubic basis for the 3d orbitals, the one-electron energies (in terms of angular overlap parameters for a single ligand) are given in the matrix below (4.10). The orbital symbols are now primed to indicate that the axis system is the matched ligand axes (see figure 4.1). This matrix applies to ligand molecules without planes of symmetry ($C_1$ microsymmetry) in or perpendicular to the molecular plane (i.e. the ligand has both a parallel and a perpendicular tilt).

$$\begin{array}{|c|cccccc|} & u' & v' & \xi' & \eta' & \zeta' \\ u' & e_\sigma & \times & e_{\sigma\pi}(y'z') & e_{\sigma\pi}(x'z') & * \\ v' & & \times & \times & * & * \\ \xi' & & & e_\pi(y'z') & * & * \\ \eta' & & & & e_\pi(x'z') & \times \\ \zeta' & & & & & \times \end{array} \qquad (4.10)$$

The matrix elements indicated by a × or a * are small because they involve a product of two misalignment geometric parameters and can be neglected.

When the ligand has only one symmetry plane ($C_s$ microsymmetry), as is the case with the water ligands in the $[M(H_2O)_6](BrO_3)_2$ complexes (the y'z' plane), the $e_{\sigma\pi}(x'z')$ term vanishes but the $e_{\sigma\pi}(y'z')$ term need not vanish. The small terms indicated with an asterisk in the above matrix also vanish within the basic approximations of the AOM.

$$\begin{array}{|c|cccccc|} & u' & v' & \xi' & \eta' & \zeta' \\ u' & e_\sigma & \times & e_{\sigma\pi}(y'z') & 0 & 0 \\ v' & & \times & \times & 0 & 0 \\ \xi' & & & e_\pi(y'z') & 0 & 0 \\ \eta' & & & & e_\pi(x'z') & \times \\ \zeta' & & & & & \times \end{array} \qquad (4.11)$$

If the ligand has a mirror plane both parallel and perpendicular to the plane of the metal-ligand pair ($C_{2v}$ microsymmetry), then both $e_{\sigma\pi}$ terms vanish, together with the remaining small terms (the parameters indicated with a ×).

$$\begin{array}{|c|cccccc|} & u' & v' & \xi' & \eta' & \zeta' \\ u' & e_\sigma & 0 & 0 & 0 & 0 \\ v' & & 0 & 0 & 0 & 0 \\ \xi' & & & e_\pi(y'z') & 0 & 0 \\ \eta' & & & & e_\pi(x'z') & 0 \\ \zeta' & & & & & 0 \end{array} \qquad (4.12)$$

Approximate analytical expressions for the AOM ligand field parameters can be derived in terms of the geometric parameters (the trigonal cone angle and the ligand rotation

angles) and the AOM bonding parameters. In the case of zero twist ($\varphi = 60°$, see figure 4.5 and section 4.3.4), the expressions for $\Delta$, $\nu$, $\nu'$, and $\nu''$ correct to first order are[6,7]:

$$\Delta = 3e_\sigma - 2e_\pi(y'z') - 2e_\pi(x'z')$$
$$\nu \approx -3\sin(2\omega)[e_\pi(y'z') - e_\pi(x'z')] - 3\sqrt{2}(d\theta)[e_\pi(y'z') + e_\pi(x'z')]$$
$$\nu' \approx 3d\theta e_\sigma - \frac{\sqrt{6}}{2}[\cos\omega - \sin\omega]e_{\sigma\pi}(y'z') - \frac{\sqrt{6}}{2}[\cos\omega + \sin\omega]e_{\sigma\pi}(x'z') \quad (4.13)-(4.16)$$
$$\nu'' \approx 3\frac{\sqrt{2}}{2}[\cos\omega + \sin\omega]e_{\sigma\pi}(y'z') - 3\frac{\sqrt{2}}{2}[\cos\omega - \sin\omega]e_{\sigma\pi}(x'z')$$

where $d\theta = (\theta - \theta_{Oh})$ (in radians). $\theta_{Oh}$ is the cone angle of a regular octahedron (54.736°)

The methods of the AOM can be used to derive the AOM ligand field matrix for d-orbitals with a real trigonal basis, and for a site of $S_6$ symmetry where $\nu''$ does not vanish[6,7]:

$$\begin{vmatrix} & u & v & \rho & \sigma & \tau \\ u & \Delta & 0 & \nu' & \nu'' & 0 \\ v & & \Delta & -\nu'' & \nu'' & 0 \\ \rho & & & -\nu/3 & 0 & 0 \\ \sigma & & & & -\nu/3 & 0 \\ \tau & & & & & 2\nu/3 \end{vmatrix} \quad (4.17)$$

This matrix involves the summation of the six individual ligand matrices to give the AOM matrix for the complex. Therefore, the axis system is now the metal axes, hence the disappearance of the primes from the orbital symbols. By rotation of the metal trigonal X and Y axes about the metal trigonal Z axis by an angle $\varphi$ where:

$$\varphi = 1/3\tan^{-1}\left\{-3\nu''/\left[\sqrt{2}(\Delta + \nu/3) + \nu'\right]\right\} \approx -\nu''/\sqrt{2}\Delta \quad (4.18)$$

the microscopic ligand field parameter $\nu''$ is incorporated into the other parameters, giving the following matrix[6,7]:

$$\begin{vmatrix} & u_s & v_s & \rho_s & \sigma_s & \tau_s \\ u_s & \Delta_s & 0 & \nu'_s & 0 & 0 \\ v_s & & \Delta_s & 0 & \nu'_s & 0 \\ \rho_s & & & -\nu_s/3 & 0 & 0 \\ \sigma_s & & & & -\nu_s/3 & 0 \\ \tau_s & & & & & 2\nu_s/3 \end{vmatrix} \qquad (4.19)$$

where:

$$\Delta_s = \Delta + \frac{5}{3}(\nu'')^2/\Delta$$
$$\nu_s = \nu + (\nu'')^2/\Delta \qquad (4.20) - (4.22)$$
$$\nu'_s = \nu' + \frac{1}{2\sqrt{2}}(\nu'')^2/\Delta$$

The parameters $\Delta_s$, $\nu_s$, and $\nu'_s$ are the microscopic or AOM ligand field parameters. They are to be compared with the spectroscopically determined parameters $\Delta$, $\nu$, and $\nu'$, thereby giving empirical estimates of the AOM symmetry parameters $e_\sigma$, $e_\pi$ and $e_{\sigma\pi}$.

The approximate expressions for the AOM ligand field parameters can be used as a guide in the analysis. The exact expressions are more cumbersome and are obtained using a computer program[6,7]. The 'exact' AOM calculations were used in the analysis described in chapters 5 and 6.

## 4.5 References


(1) Yamatera, H. *Bulletin of the Chemical Society of Japan* **1958**, *31*, 95-108.

(2) Schaeffer, C. E.; Jorgensen, C. K. *Molecular Physics* **1965**, *9*, 401-412.

(3) Schaeffer, C. E. *Pure and Applied Chemistry* **1970**, *24*, 361-392.

(4) Cruse, D. A.; Davies, J. E.; Gerloch, M.; Harding, J.; Mackey, D.; McMeeking, R. F. *CAMMAG, a FORTRAN computing package*; University of Cambridge:, 1979.

(5) Schoenherr, T. *Topics in Current Chemistry* **1997**, *191*, 87-152.

(6) Dubicki, L.; Bramley, R. *Chemical Physics Letters* **1997**, *272*, 55-60.

(7) Dubicki, L., private communication.

(8) Blackburn, A. C.; Galluci, J. C.; Gerkin, R. E. *Acta Crystallographica B* **1990**, *46*, 712-716.

(9) Blackburn, A. C.; Gallucci, J. C.; Gerkin, R. E. *Acta Crystallographica C* **1991**, *47*, 1786-1789.

(10) Reimann, C. W.; Santoro, A.; Mighell, A. D. *Acta Crystallographica B* **1970**, *B26*, 521-526.

(11) Hoedt, R. W. M. t.; Driessen, W. L.; Verschoor, G. C. *Acta Crystallographica C* **1983**, *C39*, 71-72.

(12) Lumme, P. O.; Lindell, E.; Mutikainen, I. *Acta Crystallographica C* **1988**, *C44*, 967-970.

(13) Collison, D.; Helliwell, M.; Jones, V. M.; Mabbs, F. E.; McInnes, E. J. L.; Riedi, P. C.; Smith, G. M.; Pritchard, R. G.; Cross, W. I. *Journal of the Chemical Society Faraday Transactions* **1998**, *94*, 3019-3025.

(14) Chan, M. K.; Armstrong, W. H. *Inorganic Chemistry* **1989**, *28*, 3777-3779.

(15) Anderson, P. A.; Astley, T.; Hitchman, M. A.; Keene, F. R.; Moubaraki, B.; Murray, K. S.; Skelton, B. W.; Tiekink, E. R. T.; Toftlund, H.; White, A. H. *Journal of the Chemical Society, Dalton Transactions* **2000**, 3505-3512.

(16) Astley, T.; Gulbis, J. M.; Hitchman, M. A.; Tiekink, E. R. T. *Journal of the Chemical Society Dalton Transactions* **1993**, 509-515.

(17) Keene, F. R.; Tiekink, E. R. T. *Zeitschrift fur Kristallographie* **1994**, *209*, 548-549.

(18) Churchill, M. R.; Gold, K.; Maw, C. E. *Inorganic Chemistry* **1970**, *9*, 1597-1604.

(19) Bandoli, G.; Clemento, D. A.; Paolucci, G.; Doretti, L. *Crystal Structure Communications* **1979**, *8*, 965-970.

(20) Nakata, K.; Kawabata, S.; Ichikawa, K. *Acta Crystallographica C* **1995**, *C51*, 1092-1094.

# Chapter 5: Spectroscopic Studies of Some Metal Bromate Hydrates

## 5.1 Introduction

This chapter presents the absorption, and electron paramagnetic resonance (EPR) spectra of two metal bromate hydrate compounds, $[M(H_2O)_6](BrO_3)_2$ (M = Co or Ni).

Interest in these complexes was stimulated by two factors. Their X-ray structures resemble those of the alums and hence the microscopic ligand field theory that has recently been applied to Cr(III) alums[1] can be readily extended to the trigonal $[M(H_2O)_6](BrO_3)_2$ complexes. Secondly, optical absorption studies conducted during the 1970s[2-6] have completely ignored the trigonal fields that must be present in these complexes. This fact was clearly indicated in an early EPR study of $[Ni(H_2O)_6](BrO_3)_2$ which measured a large ground state zero-field splitting (D = 1.93 $cm^{-1}$ at 290 K)[7].

Thus the absorption spectra have been re-examined and the EPR spectra extended to $[Co(H_2O)_6](BrO_3)_2$. As will be seen, the bromate complexes are indeed subjected to significant trigonal perturbations that can be accurately predicted by the microscopic ligand field model described in chapter 4.

## 5.2 History

The metal halate hydrates $M(YO_3)_2.xH_2O$ (where M = a divalent first row transition metal or alkaline earth ion, Y = Cl, Br or I and $0 \leq x \leq 10$) form a diverse class of compounds with a wide range of properties and structures. This diversity is illustrated by considering the water solubilities; most of the chlorates are deliquescent, the bromates tend to form stable, but highly water-soluble solids, while the iodates generally have a low level of water solubility.

The cobalt, nickel, copper, zinc and magnesium bromates are known to crystallise from room temperature solution as the hexahydrate. The solid compounds are stable at room

temperature, although damp crystals showed a tendency to slowly decompose over a period of days, giving off bromine. This was particularly noticeable for the cobalt compound. Decomposition could be slowed by storing the solid compounds in a refrigerator, or by dipping the crystals briefly in acetone (in which the compounds are only sparingly soluble) to remove excess water.

Differential scanning calorimetric measurements have been performed on $[Zn(H_2O)_6](BrO_3)_2$[8]. At 338 K and atmospheric pressure, the hexahydrate was observed to lose four water molecules, forming the dihydrate. Further heating to 378 K resulted in loss of the remaining two water molecules, giving the anhydrous compound. The identity of these compounds was confirmed with Raman and X-ray powder diffraction methods. No thermal studies have been performed for any other bromate hexahydrates, but given the isomorphicity with the zinc compound, the thermal behaviour would be expected to be similar.

### 5.2.1 Crystal structures

Early in the history of X-ray crystallography, Yue and Beevers determined the structure of zinc(II) bromate hexahydrate[9]. This has space group $Pa\bar{3}$, with the $[Zn(H_2O)]^{2+}$ ions lying on sites of $S_6$ symmetry, and the bromate ions on sites of $C_3$ symmetry.

In the 1930s, Belderbos carried out X-ray work on crystals of cobalt(II) and nickel(II) bromate hexahydrate[10], although this article appears to have been ignored by many later researchers. Both compounds were assigned to the cubic space group $Pa\bar{3}$, with unit cell edge lengths of 10.272Å (Ni) and 10.32Å (Co), and the metal atoms were located. Later work by Weigel[11] used X-ray powder diffraction to show that the cobalt(II), copper(II), and magnesium(II) bromate hexahydrates belonged to the $Pa\bar{3}$ space group.

Extensive X-ray crystallographic work was carried out at Ohio State University in the early 1990s for the bromate hexahydrates. High quality structures have been published for cobalt(II)[12], nickel(II)[13] and copper(II)[14], and also for nickel(II) chlorate hexahydrate[15]. The hydrogen atoms could now be located. The cubic space group $Pa\bar{3}$ was confirmed for all compounds, again with the metal hexahydrate ions lying on sites of $S_6$ symmetry (see figure 5.1 below), and the bromate ions on sites of $C_3$ symmetry.

The $MO_6$ inner coordination sphere is a near perfect octahedron with a single M-O bond length and O-M-O angles that differ from 90° by less than half a degree. The structure of $[Mg(H_2O)_6](BrO_3)_2$ was measured later by Peter et al.[16]; it is isomorphic with all the other bromate hexahydrates.

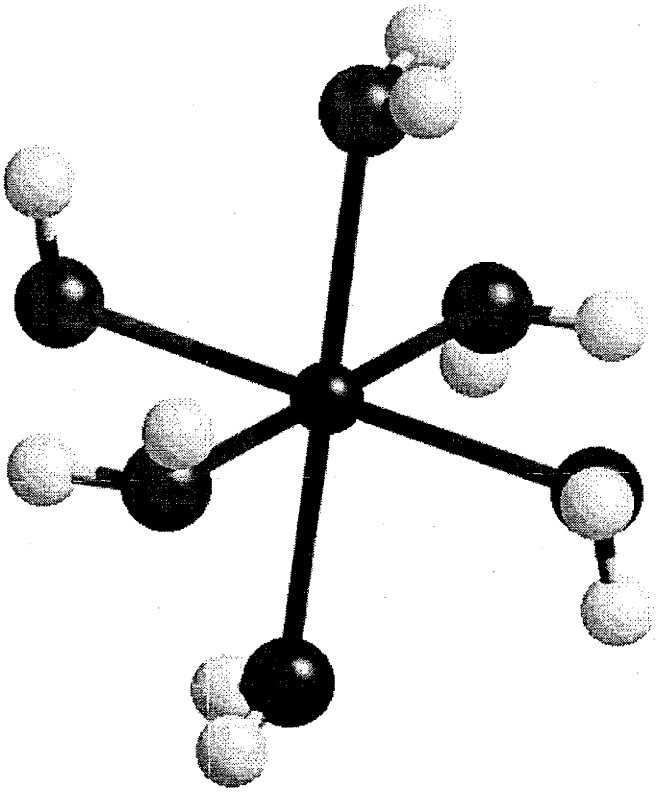

**Figure 5.1: The $M(H_2O)_6^{2+}$ complex ion in $[Co(H_2O)_6](BrO_3)_2$, viewed along the trigonal z-axis, and clearly showing the tilt and rotation of the ligands**

The water molecules possess two crystallographically inequivalent hydrogen atoms with O-H bond lengths in cobalt bromate hexahydrate of 0.86Å and 0.65Å (referred to here as H1 and H2 respectively)[12]. The structures possess an extensive network of hydrogen bonding between hydrogens and water oxygens on adjacent metal centres and between hydrogens and bromate oxygens. The hydrogen bonding is discussed in detail by the authors reporting the crystal structures. The most important of the hydrogen bonds are shown in figure 5.2. Briefly, each water hydrogen in $[Co(H_2O)_6](BrO_3)_2$ has a 'strong' hydrogen bond of length 1.96Å (atom H1, bond A1 in figure 5.2) or 2.18Å (atom H2, bond A2 in figure 5.2)[12] to an oxygen atom on a nearby bromate. The angle between the water oxygen, proton and bromate oxygen is approximately 160° for both these

bonds. In addition to these 'strong' hydrogen bonds, each proton has a weaker bond of length 2.65Å (H1) or 2.86Å (H2) to an oxygen on adjacent water molecule (the bonds denoted by the label B in figure 5.2). Finally, a bromate oxygen forms a 'bifurcated' bond of length 2.85-2.88Å to each of the two hydrogens (the 'C' bonds in figure 5.2). The angles of the strong hydrogen bonds are given below in table 5.1 and compared with those for some of the alums. It should be noted that these angles are only approximate due to the approximate locations of the hydrogen atoms. However, the differences of these angles from 180° are around 10-20°, an error of around 5-10%. A neutron structure would accurately locate the hydrogen atoms and thereby determine the accuracy of the assumption of hydrogen bond linearity.

Unfortunately, neutron structures are not available for any of the bromate hydrate compounds. Neutron structures would give more accurate positions for the hydrogen atoms, and enable more accurate determinations of the tilt and rotation angles of the water ligands. This problem was circumvented using the coordinates of the bromate oxygen atoms, which form roughly linear hydrogen bonds ($\angle$O–H···O ≈ 160°, the A1 and A2 bonds as discussed above and shown in figure 5.2) to determine the tilt and rotation angles, which are given in table 4.1. The atom coordinates were obtained from the published X-ray structures[12,13]. The hydrogen bond angles are listed below in table 5.1.

**Table 5.1: Hydrogen bond angles and distances for the bromates and some alums[17]**

| Compound | O2-O1A (Å) | O2-O1B (Å) | O2-H1-O1A | O2-H2-O1B |
|---|---|---|---|---|
| $[Co(H_2O)_6](BrO_3)_2$ | 2.77 | 2.80 | 156° | 159° |
| $[Ni(H_2O)_6](BrO_3)_2$ | 2.76 | 2.81 | 153° | 156° |
| $[K(H_2O)_6][Cr(H_2O)_6](SO_4)_2$ | 2.61 | 2.62 | 171° | 171° |
| $[K(H_2O)_6][Al(H_2O)_6](SO_4)_2$ | 2.63 | 2.60 | 170° | 169° |

O2 is the water oxygen. O2-H1 is the longer water O-H bond, while O2-H2 is the shorter. O1A is the bromate (or sulfate in the case of the alums) oxygen that is hydrogen bonded to H1, while O1B is the bromate oxygen that is hydrogen bonded to H2.

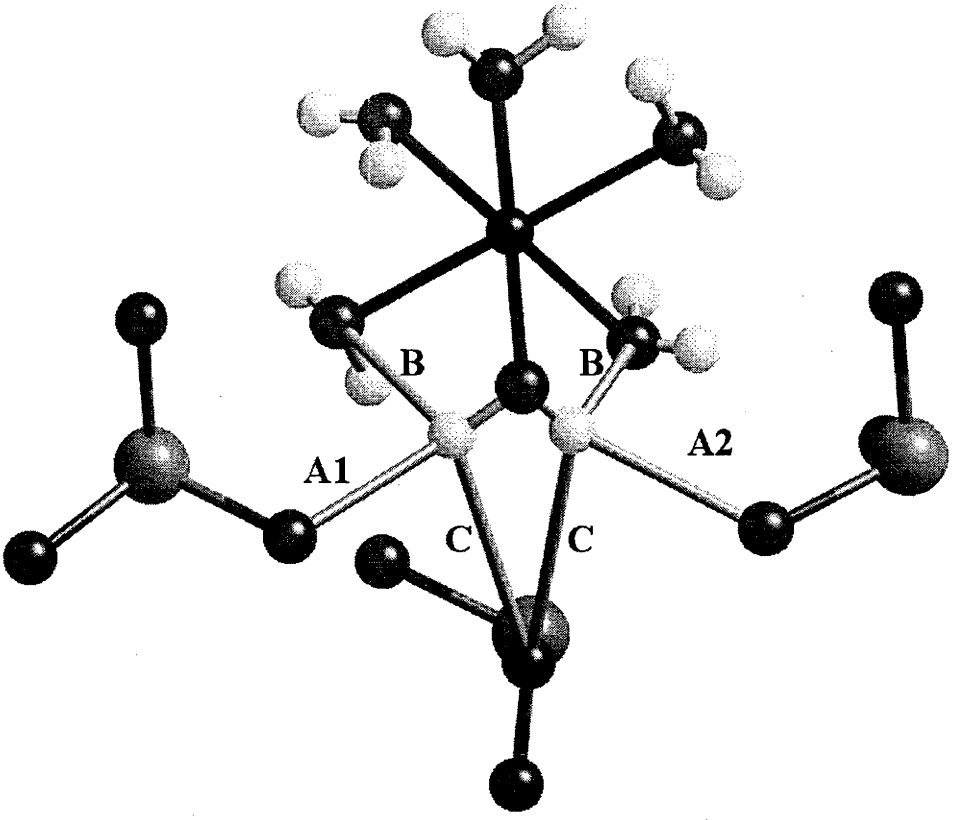


**Figure 5.2: The hydrogen bonding in the bromate hexahydrates. A1 and A2 are the shorter, 'strong' hydrogen bonds to oxygens on adjacent bromate ions, the B and C bonds are weaker and longer than A1 and A2.**

### 5.2.2 Previous spectroscopic studies

A number of studies has been carried out on the electronic (absorption and magnetic circular dichroism) spectroscopy of cobalt(II) and nickel(II) bromate hexahydrate. Harding and Briat measured the absorption and magnetic circular dichroism (MCD) spectra of the cobalt(II) compound in the visible and near UV regions[4] and later extended this to the infrared[5]. The former paper included extensive ligand field calculations of the transition energies, and the signs of the MCD B and C terms. Only semi-quantitative values for the MCD magnitudes could be obtained. The spin-allowed transitions $^4T_{2g} \leftarrow {}^4T_{1g}(^4F)$ in the near IR, and $^4A_{2g} \leftarrow {}^4T_{1g}(^4F)$ and $^4T_{1g}(^4P) \leftarrow {}^4T_{1g}(^4F)$ in the visible were identified. A large number of spin-forbidden transitions to doublet

excited states were located with in the MCD spectra. The trigonal ligand fields were not obvious in the spectra and were not considered in the ligand field analysis.

Harding et al. have also carried out studies of the absorption and MCD of the visible bands in nickel(II) bromate hexahydrate[3,18]. The visible absorption spectrum of the $[Ni(H_2O)_6]^{2+}$ complex ion consists of the 'red' band centred at ca 700 nm, and the 'blue' band centred at ca 400 nm. The 'blue' band has a simple Gaussian profile and is identified as the $^3T_{1g}(^3P) \leftarrow {}^3A_{2g}$ spin-allowed transition. The MCD was interpreted on the basis of a pure octahedral $^3T_{1g}$ ($^3P$) state subjected to spin-orbit splitting. Trigonal fields were not considered. This work shows that these complexes are subject to a significant trigonal field splitting $^3T_{1g}$ ($^3E_g$) > $^3T_{1g}$ ($^3A_{1g}$) for the $^3T_{1g}$ ($^3P$) state. The lineshape and the fine structure of the red band is complicated by the proximity of the $^1E_g$ and $^3T_{1g}$ ($^3F$) states. The interaction between the potential energy surfaces has been the subject of a detailed study[6]. Trigonal distortions in the $^3T_{1g}$ ($^3F$) state were also neglected.

The early EPR study of $[Ni(H_2O)_6](BrO_3)_2$[7] has been confirmed by Suassuna et al.[19]. They found that the spectrum had an isotropic g-value of 2.31±0.05, independent of temperature. Using the formally forbidden $\Delta m = +2$ transition (visible at liquid helium temperature), they determined the magnitude and sign of the zero-field splitting parameter D, which ranges from $-1.97$ cm$^{-1}$ at 300 K to $-1.77$ cm$^{-1}$ at 20 K (the minus sign indicates that the doubly degenerate level lies lower, see figure 1.3).

The EPR spectra of the copper-doped zinc salt exhibit a strong Jahn-Teller effect[20,21]. Although a tetragonal distortion lifts the orbital degeneracy of an octahedral $^2E_g$ ground state, a trigonal distortion does not. In 1955, Bleaney et al.[20] measured the EPR spectra of $Cu^{2+}$ doped into a number of lattices with trigonal site symmetry, including a single crystal of zinc(II) bromate hexahydrate. This spectrum at 90 K was nearly isotropic with a single g-value of 2.22. At liquid helium temperatures, the spectrum was observed to become anisotropic, with three separate axial spectra, each one corresponding to an elongation along one of the three mutually perpendicular O-Cu-O axes. The later work of Jesion et al.[21,22] measured the EPR spectrum at 4.2 K and 77 K, and employed isotopically pure $^{65}Cu$ to avoid complications in the nuclear quadrupole interaction. This confirmed the earlier work; the higher temperature spectra were essentially isotropic and the lower temperature spectra were fully anisotropic.

As discussed above, the following compounds are isomorphous: $[M(H_2O)_6](BrO_3)_2$ where M = Mg, Co, Ni and Zn, and $[Ni(H_2O)_6](ClO_3)_2$. As a result, the infrared and Raman spectra all have the same form[8,23,24]. The spectra have been measured for all compounds at room temperature and 90 K, for single crystals (Raman) and Nujol mulls (IR), in a comprehensive study by Lutz and Suchanek[23]. They were particularly interested in the halate ion modes, although water molecule modes were also briefly discussed. One result of interest was that the symmetric and asymmetric stretch modes of the bromate ions were accidentally degenerate. Matsuo et al. measured spectra of $[Co(H_2O)_6](BrO_3)_2$ at an unspecified temperature as part of a heat capacity determination[24]. IR and Raman peaks were tentatively identified using published data. Srinivasan and Devanathan measured the Raman spectrum of $[Zn(H_2O)_6](BrO_3)_2$ at room temperature and 90 K, the zinc bromate dihydrate at 338 K and the anhydrate at 378 K[8]. A few assignments were made, including the O-H stretches, bromate ion modes, and lattice modes. At this stage, no polarised Raman spectra have been published for any of these cubic hexahydrates. Further, no electronic Raman peaks were detected for $[Co(H_2O)_6](BrO_3)_2$.

## 5.3 Experimental

### 5.3.1 Synthesis

The $[M(H_2O)_6](BrO_3)_2$ complexes (M = Co, Ni or Zn) were synthesised by mixing an aqueous solution of the metal(II) sulphate with aqueous barium bromate.

e.g. $CoSO_{4(aq)} + Ba(BrO_3)_{2(aq)} \rightarrow Co(BrO_3)_{2(aq)} + BaSO_{4(s)}$

Since barium bromate is only sparingly soluble at room temperature, large volumes of hot water were required. The barium sulphate was removed from the metal bromate solution by decanting and filtration. The solutions were concentrated by rotary evaporation. The compounds were recrystallised from water and gave large crystals with well-developed [111] and smaller [100] faces. A simple and effective recrystallisation method was to place Petri dish of the solution saturated at room

temperature in a refrigerator. This gave crystals of high optical quality within a few hours.

The bromate compounds were checked for purity by microanalysis; this was performed by the Research School of Chemistry analytical unit. Hydrogen was determined by combustion analysis, while cobalt, nickel and zinc were determined using atomic absorption spectroscopy. Bromine was determined by reduction to the halide followed by titration with standard mercury(II) nitrate solution. Results are shown in table 5.2; the mass percentages all lie within ± 0.5% of theoretical values.

**Table 5.2: Purity check for the bromates**

| Compound | Calculated percentages | Found percentages |
|---|---|---|
| $[Co(H_2O)_6](BrO_3)_2$ | H: 2.86, Br: 37.79, Co: 13.94 | H: 2.88, Br: 37.96, Co: 13.86 |
| $[Ni(H_2O)_6](BrO_3)_2$ | H: 2.86, Br: 37.82, Ni: 13.89 | H: 2.54, Br: 37.82, Ni: 13.86 |
| $[Zn(H_2O)_6](BrO_3)_2$ | H: 2.82, Br: 37.23, Zn: 15.23 | H: 2.67, Br: 37.25, Zn: 15.52 |

### 5.3.2 Spectroscopic measurements

EPR spectra of $[Co(H_2O)_6](BrO_3)_2$ were measured at liquid helium temperatures for magnetically dilute powdered samples which were prepared by doping the cobalt complex into the corresponding zinc complex at levels of 1-5%. Spectra of the pure compound were also measured but the resonance lines were very broad and were not analysed.

Powdered samples were placed in quartz X-band EPR tubes flushed with nitrogen gas in order to exclude oxygen, which would interfere with the spectra. Spectra were measured using a Bruker EPR spectrometer equipped with a water-cooled electromagnet, and an Oxford Instruments ESR 900 model cryostat with cold helium flow for temperature control 4 K and above. Typical experimental parameters are shown in table 5.3.

**Table 5.3: Parameters used for EPR experiments on $[Co(H_2O)_6](BrO_3)_2$**

| Parameter | Figure 5.4 | Figure 5.5 |
|---|---|---|
| Microwave frequency (GHz) | 9.437 | 9.438 |
| Microwave power (mW) | 6.315 | 6.315 |
| Temperature (K) | 9.0 | 6.0 |
| Number of scans | 1 | 1 |
| Receiver gain | 80.0 | 63.0 |
| Modulation frequency (kHz) | 100 | 100 |
| Modulation amplitude (Gauss) | 20.181 | 20.181 |
| Resolution (Gauss) | 1.71 | 0.49 |

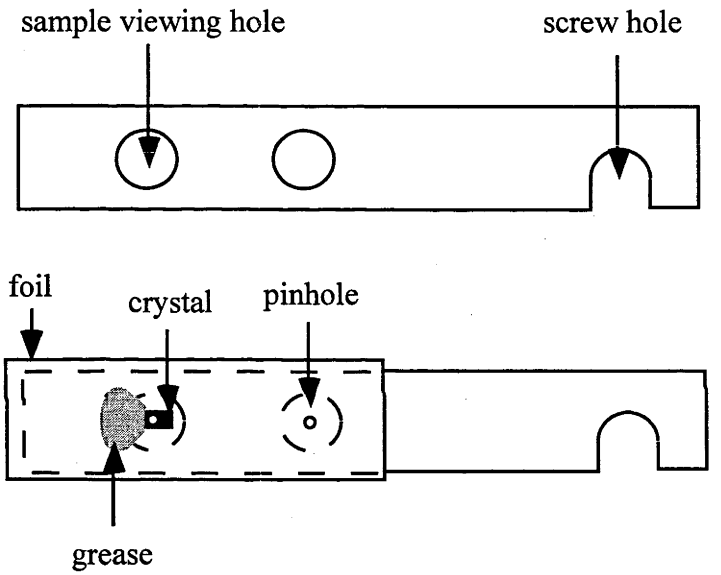


**Figure 5.3: Sample holder used for absorption spectroscopy**

Absorption spectra were measured for cobalt(II)- and nickel(II) bromate hexahydrate using the microcrystal spectrophotometer developed within the Krausz group[25,26]. The instrument is a single beam spectrometer with a tungsten filament lamp and a Spex model 1704 one-metre single monochromator. Various detectors were employed; a Hamamatsu S5 PM tube in the 300-600 nm region, a silicon photodiode in the 600-1000 nm region and an indium antimonide detector above 1000 nm. For spectra measured at low temperature, samples were cooled in a quartz flow tube with cold helium gas[27].

Crystals, typically of a size in the range 0.5-1 mm, were mounted over a pinhole in a strip of aluminium foil using Apiezon vacuum grease to attach the crystal. Small crystals were used for convenience; they are more numerous, so the chances of finding one with good optical quality is higher. Further, larger crystals have a greater absorbance (by the Beer-Lambert law), and the absorbance needs to be kept below ~2, otherwise the signal-to-noise ratio (SNR) becomes problematic. The foil strip was then fixed to a sample holder of brass or aluminium so that the crystal was positioned over one of the viewing holes (see figure 5.3).

The purpose of these spectra was to check earlier work with higher resolution, and to study the $^3T_{2g} \leftarrow {}^3A_{2g}$ transition for $[Ni(H_2O)_6](BrO_3)_2$, which has not been previously reported. Since the crystals are cubic and hence optically isotropic, no information can be gained from measuring polarised spectra, and no account was taken of crystal faces.

## 5.4 Results and discussion

### 5.4.1 Electron paramagnetic resonance

An EPR spectrum consistent with an axially symmetric complex was observed for cobalt bromate hexahydrate when measured at liquid helium temperatures (refer to the discussion in section 1.2.2). For the magnetically dilute sample, all eight hyperfine lines expected ($^{59}Co$ has nuclear spin I = 7/2) could be resolved in the $g_{\|}$ region, while seven of the eight hyperfine lines could be resolved in the $g_{\perp}$ region. The spectra are shown in figures 5.4-5.5. Peak positions are listed in table 5.4.

For a powder EPR spectrum of a S = 1/2 system, absorption-like peaks are observed in the $g_{\|}$ region, while first derivative peaks are seen in the $g_{\perp}$ region. Since high spin octahedral or pseudo-octahedral Co(II) is an odd-electron system, a Kramers doublet lies lowest. Such a system can be considered a pseudo S = 1/2 system[28,29], and as a result an EPR spectrum of high spin (distorted) octahedral cobalt (II) has the same form as a true S = 1/2 system. The values of the key parameters $g_{\|}$, $g_{\perp}$, and the hyperfine coupling constant A are given in table 5.5 below. Such a spectrum is clear evidence of the axial (in this case trigonal) symmetry of the $[Co(H_2O)_6]^{2+}$ complex ion.

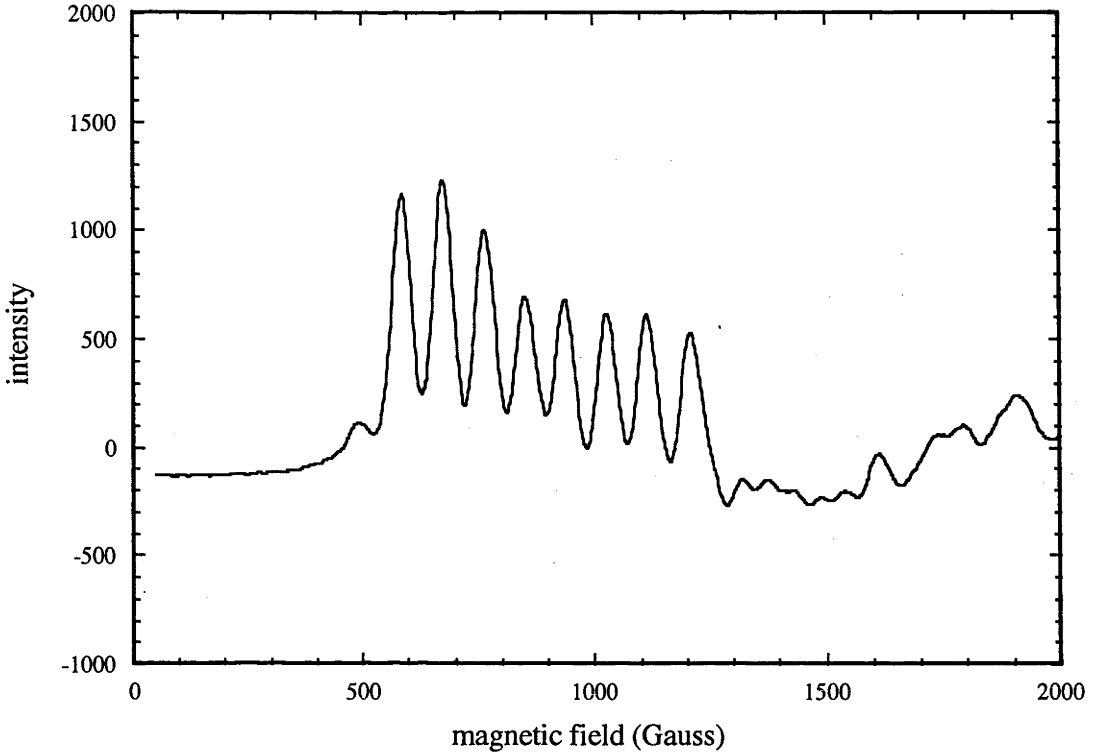


**Figure 5.4: EPR spectrum of $Co^{2+}$:$Zn(H_2O)_6(BrO_3)_2$ ($g_{||}$ region)**

**Table 5.4: Peak positions for the X-band EPR spectrum of magnetically dilute $[Co(H_2O)_6](BrO_3)_2$**

| Peak type | Magnetic field (Gauss) |
|---|---|
| $g_{||}$ region | 586, 673, 764, 849, 936, 1025, 1112, 1208 |
| $g_{\perp}$ region | 2811, 2929, ~3063, 3199, 3375, 3469 |

**Table 5.5: Values of $g_{||}$, $g_{\perp}$ and $A_{||}$ for $[Co(H_2O)_6](BrO_3)_2$**

| Parameter | Value |
|---|---|
| $g_{||}$ | 7.54 ± 0.03 |
| $g_{\perp}$ | 2.11 ± 0.01 |
| $A_{||}$ | 0.031 ± 0.01 $cm^{-1}$ |

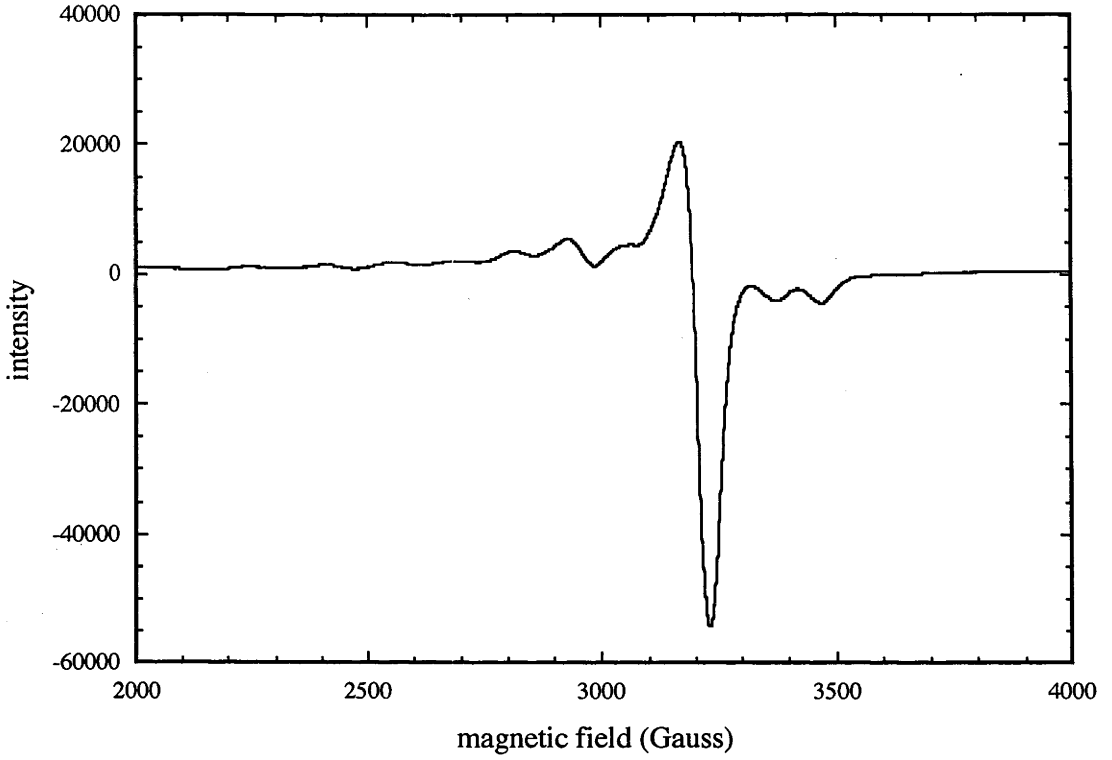


**Figure 5.5: EPR spectrum of $Co^{2+}$:$Zn(H_2O)_6(BrO_3)_2$ ($g_\perp$ region)**

### 5.4.2 Absorption spectroscopy

Absorption spectra with a large amount of fine structure were observed at low temperature for both $[Ni(H_2O)_6](BrO_3)_2$ and $[Co(H_2O)_6](BrO_3)_2$ (figures 5.6-5.11).

**Table 5.6 Experimental parameters for the absorption spectra below**

| Figure | T (K) | Resolution ($cm^{-1}$) | Step size (Å) | Time/step (s) |
|---|---|---|---|---|
| 5.6 | 11.5±1 | 4 at 22000 $cm^{-1}$ | 1 | 1 |
| 5.7/5.8 | 7.5±1.5 | 2.2 at 8500 $cm^{-1}$, 3 at 14000 $cm^{-1}$ | 5 | 1 (5500-10000 Å), 0.3 (10000-20000 Å) |
| 5.9/5.10 | 7.5±1.5 | 2.2 at 8500 $cm^{-1}$, 3 at 14000 $cm^{-1}$ | 5 | 1 (5500-10000 Å), 0.3 (10000-20000 Å) |
| 5.11 | 11.5±1.5 | 4 at 22000 $cm^{-1}$ | 1 | 1 |

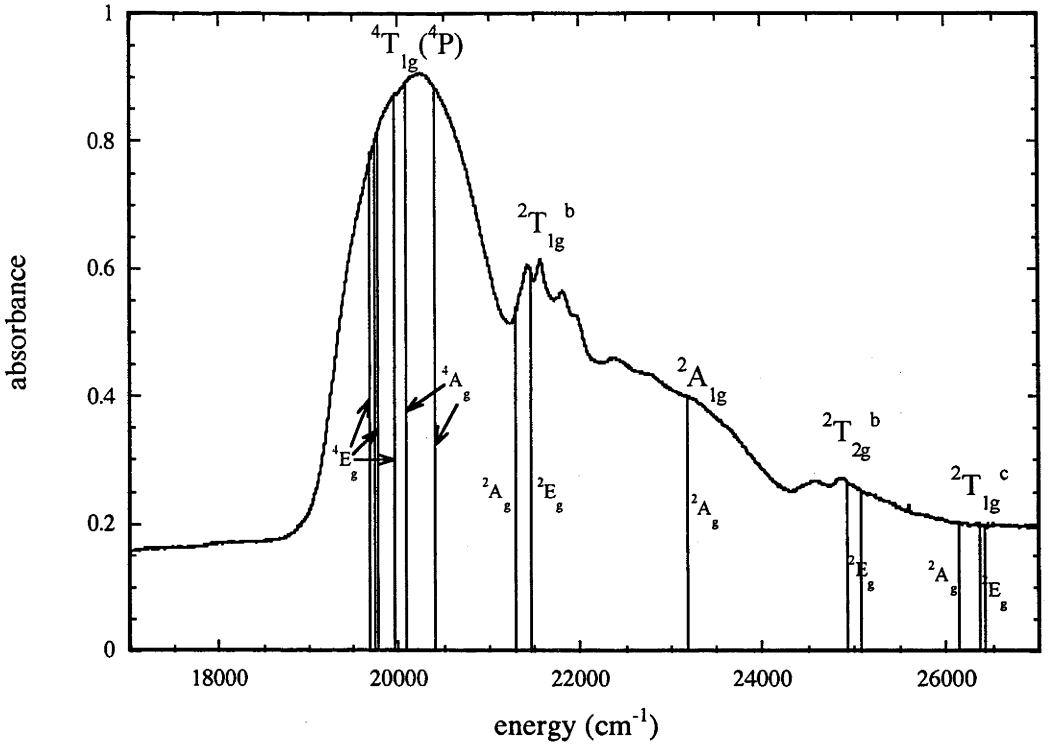


**Figure 5.6: Absorption spectrum showing the $^4T_{1g}$ ($^4P$) ← $^4T_{1g}$ ($^4F$) transition for $[Co(H_2O)_6](BrO_3)_2$**

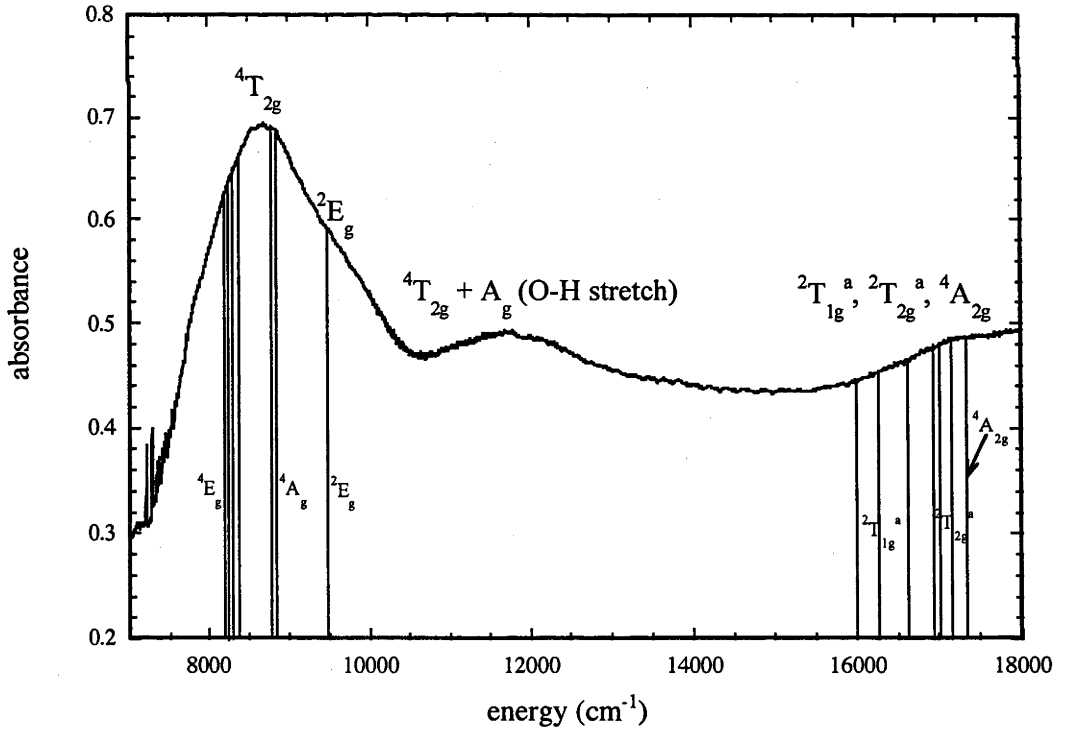


**Figure 5.7: Absorption spectrum ($^4T_{2g}$ ← $^4T_{1g}$($^4F$) transition) of $[Co(H_2O)_6](BrO_3)_2$**

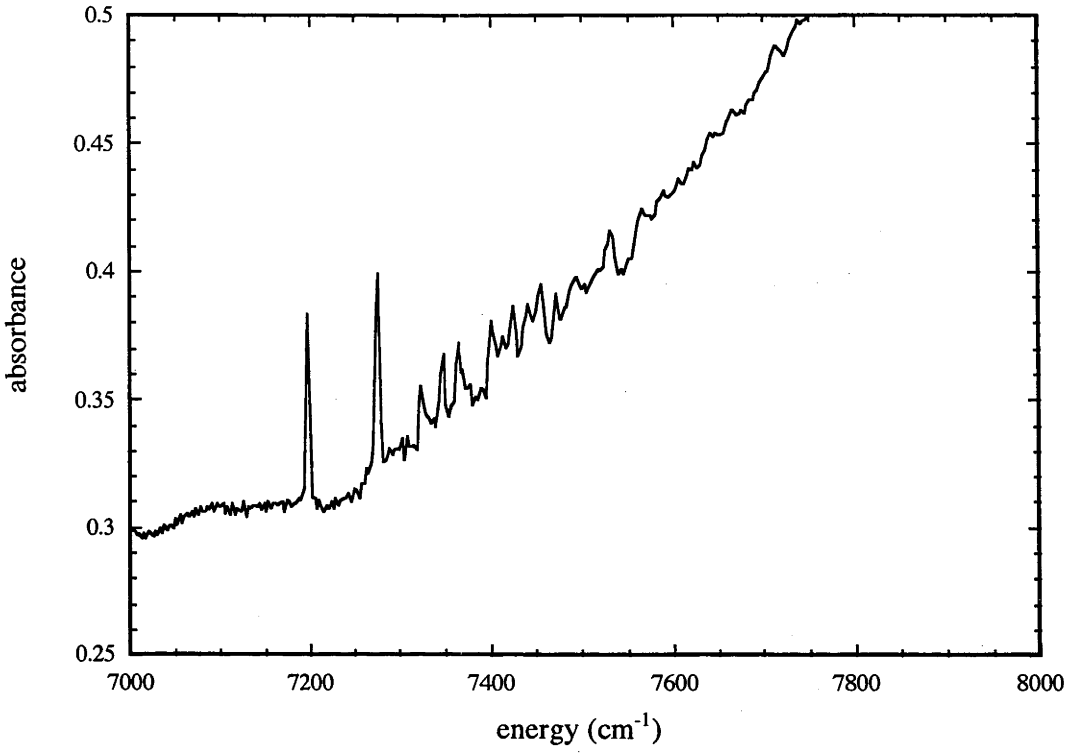


**Figure 5.8: Fine structure in the $^4T_{2g} \leftarrow {}^4T_{1g}$ band of $[Co(H_2O)_6](BrO_3)_2$**

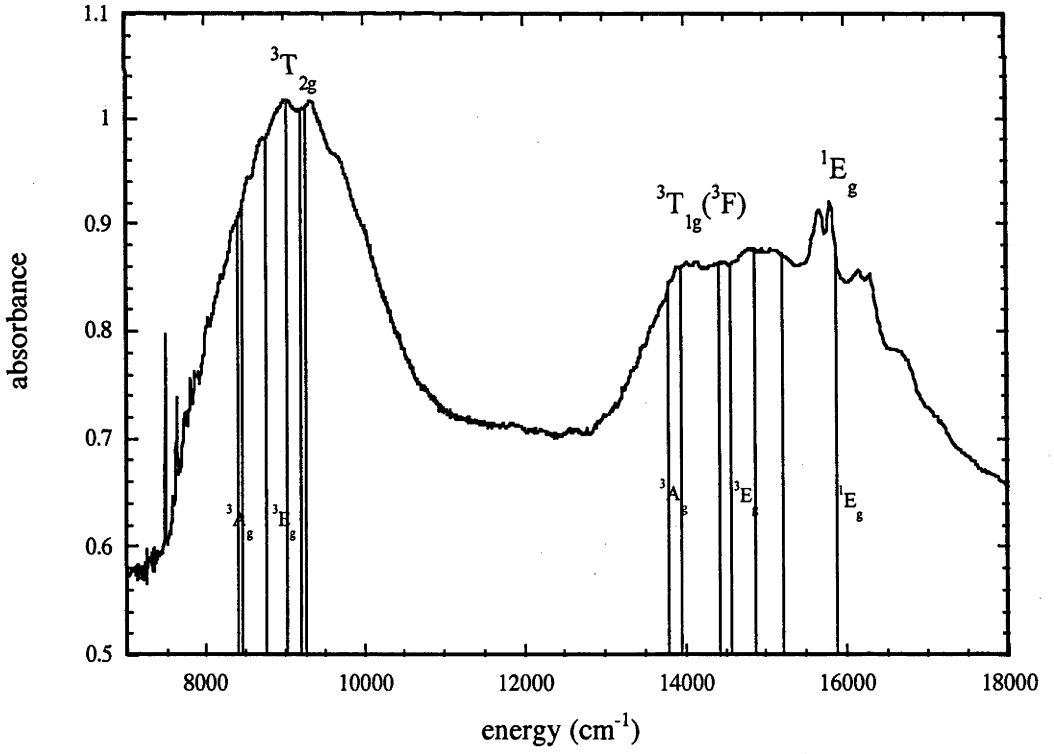


**Figure 5.9: $^3T_{2g} \leftarrow {}^3A_{2g}$ and $^3T_{1g}$ ($^3F$) $\leftarrow {}^3A_{2g}$ transitions in $[Ni(H_2O)_6](BrO_3)_2$**

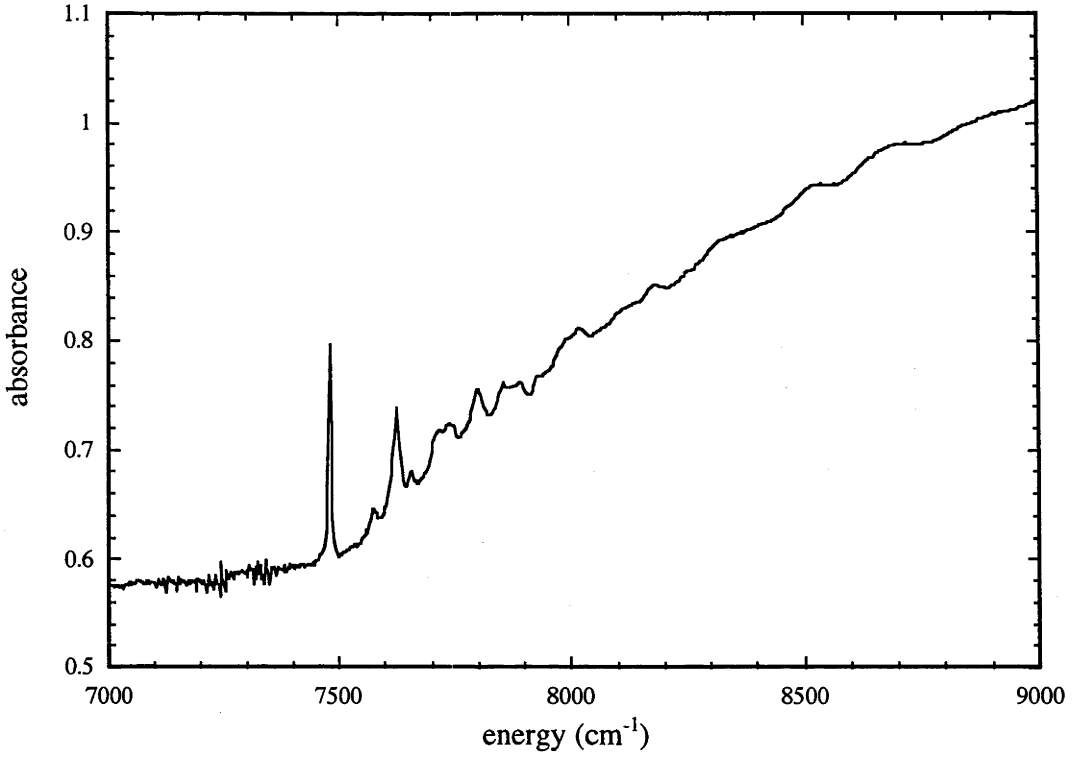


**Figure 5.10: Fine structure on the $^3T_{2g} \leftarrow {}^3A_{2g}$ band of $[Ni(H_2O)_6](BrO_3)_2$**

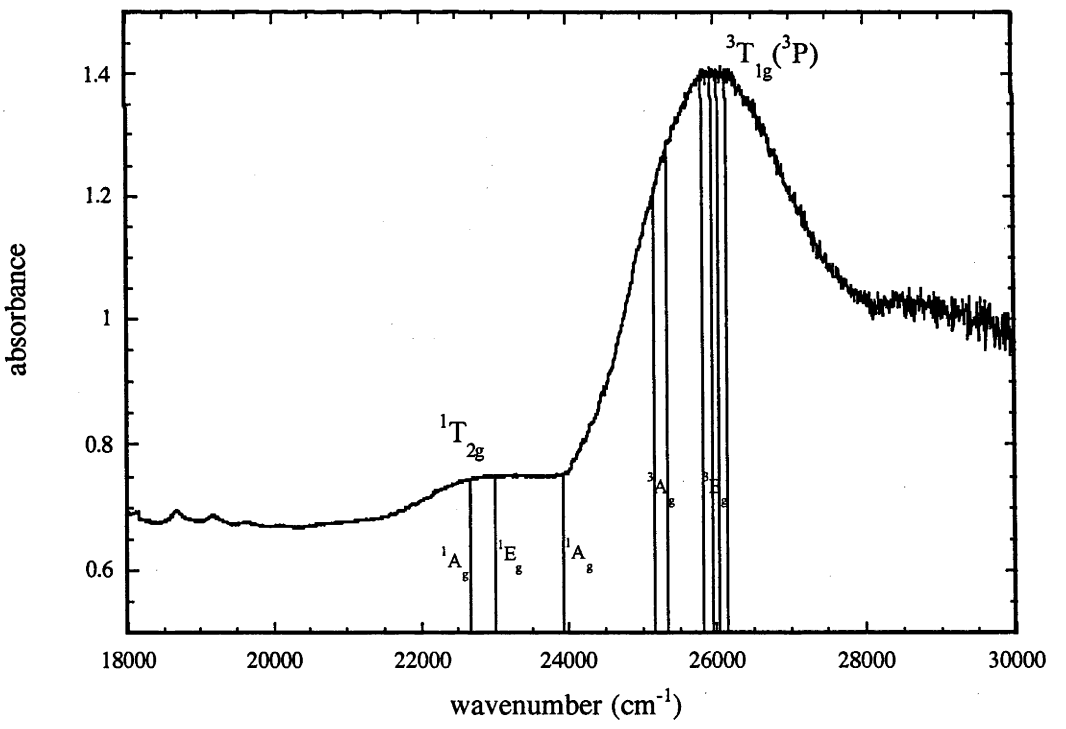


**Figure 5.11: Absorption spectrum ($^3T_{1g}$ ($^3P$) $\leftarrow$ $^3A_{2g}$ transition) of $[Ni(H_2O)_6](BrO_3)_2$ crystal**

For $[Ni(H_2O)_6](BrO_3)_2$ (figure 5.9), the $^3T_{2g}\leftarrow{}^3A_{2g}$ and $^3T_{1g}$ ($^3F$)$\leftarrow{}^3A_{2g}$ bands are clearly observable, with Franck-Condon maxima at roughly 9100 $cm^{-1}$ and 15000 $cm^{-1}$ respectively. The fine structure on the low energy side of the $^3T_{2g}$ band should be predominantly magnetic dipole origins and vibronically-induced false origins. A detailed analysis would require significant additional experimental work, such as a series of polarised Zeeman experiments, and magnetic circular dichroism (MCD) work. Further analysis on this fine structure was not pursued in this thesis. The resolution is much higher than that achieved by Harding et al.[2,3], but comparable to that achieved by Solomon and Ballhausen[6].

The $^3T_{1g}$ ($^3F$)$\leftarrow{}^3A_{2g}$ peak has a shoulder at 13915 $cm^{-1}$ that is assigned as one of the trigonally split components of the $^3T_{1g}$ state based on the calculations discussed in section 5.4.3 below. The two sharp peaks to the blue of the Franck-Condon maximum at 15688 and 15820 $cm^{-1}$ are assigned to false origins of the spin-forbidden $^1E_g\leftarrow{}^3A_{2g}$ transition. Progressions are visible for these two peaks.

The $^3T_{1g}$ ($^3P$)$\leftarrow{}^3A_{2g}$ transition (referred to as the 'blue' band by some authors) is located at 26010 $cm^{-1}$ (figure 5.11), with a shoulder to low energy that is assigned as a trigonally split state. As discussed in section 5.2.2, the opposite signed MCD associated with the shoulder was assigned by Harding et al.[2,3] as the result of spin-orbit splitting. The low intensity hump to the red of the main peak at ~22700 $cm^{-1}$ was assigned by Harding et al. as a spin-forbidden transition to the $^1T_{2g}$ state, the calculation discussed below agrees with this assignment.

Like nickel, better resolution was achieved for $[Co(H_2O)_6](BrO_3)_2$ when compared with the spectra of earlier workers[4,5], particularly for the near infrared band. Figure 5.7 shows the Franck-Condon maximum of the $^4T_{2g}\leftarrow{}^4T_{1g}$ ($^4F$) transition at 8680 $cm^{-1}$, with a much lower intensity peak at 11760 $cm^{-1}$ (~3080 $cm^{-1}$ to the blue) that probably incorporates one quantum of an O-H stretch vibration. Two sharp peaks to the red of the main peak can be observed at 7196 and 7275 $cm^{-1}$. A low energy shoulder can be discerned on the main $^4T_{2g}$ peak, this is probably a result of the trigonal splitting.

Figure 5.6 shows the main peak due to the $^4T_{1g}$ ($^4P$)$\leftarrow{}^4T_{1g}$ ($^4F$) transition with a maximum at 20250 $cm^{-1}$. A number of sharp peaks due to spin-forbidden transitions are also visible. Based on the calculations detailed in section 5.4.3, the sharp peaks

21426 and 21569 $cm^{-1}$ are likely to result from transitions to the $^2T_{1g}{}^b$ state, while those to higher energy at 24541, 24890 and 25606 $cm^{-1}$ result from transitions to the trigonally split $^2T_{2g}{}^b$ state. A shoulder to the red of the main $^4T_{1g}(^4P) \leftarrow {}^4T_{1g}(^4F)$ peak is due to trigonal splitting of the $^4T_{1g}(^4P)$ state. A weak, broad peak at around 17100 $cm^{-1}$ (most visible in figure 5.7), probably incorporates transitions to the $^2T_{1g}{}^a$, $^2T_{2g}{}^a$ and $^4A_{2g}$ states.

### 5.4.3 Ligand field calculations

The trigonal fields in $[Co(H_2O)_6](BrO_3)_2$ and $[Ni(H_2O)_6](BrO_3)_2$ can be estimated by direct comparison with the calculations performed on the Cr(III) alums[1,30] using the methods described in chapter 4. Within the angular overlap model (AOM), the $e_\sigma$, $e_\pi$ and $e_{\sigma\pi}$ parameters are independent of the angles $\omega$ and $\theta$ (chapter 4), but are sensitive to the oxidation state of the metal, and to a lesser extent, to the ligand tilt angles.

The effect of the metal ion and its oxidation state on the ligand field parameters is assumed as a first approximation to follow the spectrochemical series. For hexacoordinate Co(II) and Ni(II) complexes, the cubic ligand field $\Delta = 3e_\sigma - 2e_\pi(\|) - 2e_\pi(\perp)^*$, is half that of hexacoordinate Cr(III). The value of $\Delta = 18000$ $cm^{-1}$ for the Cr(III) $\alpha$ and $\beta$ alums is taken from Dubicki and Bramley[1]; therefore the $\Delta$ values for the Co(II) and Ni(II) bromates are in the region of 9000 $cm^{-1}$ to a first approximation. Given that the ligand is the same (ie..$H_2O$) for the chromium alum and the bromate hexahydrates, it is assumed that the magnitude of the $\sigma$- and $\pi$-bonding have the same ratio for both the alums and the bromates. , Therefore, as a first-order estimate it is assumed that the angular-overlap parameters ($e_\sigma$, $e_\pi$ and $e_{\sigma\pi}$) for the Co(II) and Ni(II) complexes are half the value of the corresponding parameters for the Cr(III) alums (for fixed values of $t_\perp$).

The value of $e_\pi(\|)$, the $\pi$-bonding within the molecular plane of the $H_2O$ ligand is difficult to determine. Most workers have assumed that $e_\pi(\|) \approx 0$. However, recent

* The angular-overlap parameters $e_\pi(\perp)$ and $e_\pi(\|)$ introduced here are alternatives to the notation introduced in chapter 4. The 'parallel' parameters denoted by $\|$ refer to the plane of the ligand (the x'z' plane), while the 'perpendicular parameters denoted by $\perp$ apply to the y'z' plane (see figure 4.1).

studies of the electronic fine structure of Cr(III) alums[1] indicate that $e_\pi(\|)$ may have a value of between 500 and 1000 $cm^{-1}$.

Dr Dubicki has shown[1,30] that the following analysis applies to both α- and β-alums to a first approximation. For Cr(III) alums, $e_\pi(\|) \approx 700$ $cm^{-1}$ was chosen[1], and therefore $e_\pi(\|) \approx 350$ $cm^{-1}$ is used for the Co(II) and Ni(II) bromates. The effect of $e_\pi(\|)$ on the AOM parameters increases as θ deviates from the octahedral value of 54.736°. The expected insensitivity of the microscopic ligand field parameters for the bromates is shown in table 5.6. The values employed for the Racah parameters B and C, the orbital reduction factor k, the one-electron spin-orbit coupling parameter ζ, the octahedral ligand field splitting parameter Δ, the π bonding angular-overlap parameter anisotropy, and the off-diagonal angular overlap parameter $e_{o\pi}(\perp)$, are given below the table. The values for the Racah parameters B and C used in the calculations were obtained using QuickBasic programs written by Dr Lucjan Dubicki. These programs use as inputs the experimentally observed energies for the ligand field transitions, and calculate the Racah parameters using similar mathematical equations to those used to construct Tanabe-Sugano diagrams. This is illustrated by the discussion below, which demonstrates how the Racah B parameters are obtained using Tanabe-Sugano diagrams.

From the nickel bromate experimental data (see table 5.11), the energy values of the Franck-Condon maxima of the three spin-allowed transitions give energy ratios of:

$$\frac{E(^3T_{1g}(^3F) \leftarrow {}^3A_{2g})}{E(^3T_{2g} \leftarrow {}^3A_{2g})} = 1.65 \quad (5.1)$$

$$\frac{E(^3T_{1g}(^3P) \leftarrow {}^3A_{2g})}{E(^3T_{2g} \leftarrow {}^3A_{2g})} = 2.86 \quad (5.2)$$

Fitting of these values to the Tanabe-Sugano diagram for $d^8$ configurations results in E/B values of 10, 16.6 and 28.7 for the $^3T_{2g} \leftarrow {}^3A_{2g}$, $^3T_{1g}(^3F) \leftarrow {}^3A_{2g}$ and $^3T_{1g}(^3P) \leftarrow {}^3A_{2g}$ transitions respectively. Based, on the experimental data, B is therefore chosen as 910 $cm^{-1}$, representing a reduction to 87% of the free-ion value (1042 $cm^{-1}$)[31].

For $[Co(H_2O)_6](BrO_3)_2$, the observed experimental values (table 5.11) of the $^4T_{2g} \leftarrow {}^4T_{1g}(^4F)$ and $^4T_{1g}(^4P) \leftarrow {}^4T_{1g}(^4F)$ transitions have an energy ratio of 2.33. Fitting this

value to the Tanabe-Sugano diagram for $d^7$ configurations results in E/B values of 10.2 and 24.1 for the transitions. Based on this data, the value of B is therefore chosen, representing a reduction to 86% of the free-ion value (989 $cm^{-1}$)[31]. This value is very similar to that used by Harding and Briat[4].

The value of the one-electron spin-orbit coupling parameter for the $[Ni(H_2O)_6](BrO_3)_2$ complex can be calculated from the EPR g-value and Δ using the following relations[31,32]:

$$g = 2.0023 + \frac{4k^2\zeta_0}{\Delta} \quad (5.3-5.4)$$
$$\zeta \approx k\zeta_0$$

using the measured EPR g-value. Unfortunately, the uncertainty in the $[Ni(H_2O)_6](BrO_3)_2$ g-value (2.31±0.05) measured by Suassuna et al.[19] is too great, so a literature value of the g-value for nickel Tutton salt, a complex with a very similar structure to the bromates was employed for the calculation.

The value for the free-ion spin-orbit coupling parameter $\zeta_0$ for $Ni^{2+}$ was obtained from a tabulation by Bendix, Brorson and Schaeffer[33].

**Table 5.7 Dependence of the microscopic ligand field parameters on $e_\pi(\|)$ in $[Ni(H_2O)_6](BrO_3)_2$[a] All parameters are in the table are in $cm^{-1}$**

| $e_\pi(\|)$ | $e_\sigma$ | $\nu_s$ | $\nu_s'$ | $D(^3A_2)$ |
|---|---|---|---|---|
| 0 | 3143 | –969 | –20 | –1.75 |
| 350 | 3610 | –982 | –14 | –1.81 |
| 500 | 3810 | –987 | –12 | –1.83 |

[a] $\Delta_s$ = 8800 $cm^{-1}$, $e_\pi(\perp) - e_\pi(\|)$ = 379 $cm^{-1}$, $e_{\sigma\pi}(\perp)$ =277 $cm^{-1}$, B = 910 $cm^{-1}$, C = 3997 $cm^{-1}$, ζ = 590 $cm^{-1}$, k = 0.88. $D(^3A_2)$ experimental = –1.97 $cm^{-1}$ (300 K)[7], –1.77 $cm^{-1}$ (20 K)[19]

Given that the ligands, and the metal-oxygen bond lengths and angles are almost identical for the nickel and cobalt complexes, the orbital reduction factor k is assumed to be the same. The one-electron spin-orbit coupling parameter ζ for the cobalt

complex was then calculated using the free-ion value ($\zeta_0$) for $Co^{2+}$, also obtained from Bendix, Brorson and Schaeffer.

The bonding parameter $e_\sigma$ should be fairly independent of tilt angles since it represents the total σ perturbation energy. The parameters $e_\pi(||)$ should be sensitive to $t_{||}$ (not $t_\perp$) but since $t_{||} \leq 2°$ for M(II) bromates and Cr(III) alums, the tilting within the $H_2O$ molecular plane (rock) is neglected. The effect of tilt on the remaining bonding parameters is described by the following empirical estimates, based on crystallographic data for the alums[30]:

$$e_\pi(\perp) - e_\pi(||) \approx 1000\cos^2 t_\perp \quad (5.5)$$

$$e_{\sigma\pi}(\perp) \approx \sin 2t_\perp \quad (5.6)$$

From Cr(III) α and β alums the following values are obtained:

$\Delta = 17500\ cm^{-1}$;
$e_\pi(\perp) - e_\pi(||) = 1000\ cm^{-1}$ for $t_\perp = 0°$;
$e_{\sigma\pi}(t_\perp) = -380\ cm^{-1}$ for $t_\perp = 18°$; and
$e_\pi(||) \approx 700\ cm^{-1}$.

The above parameters are those from Dubicki and Bramley[1], with the exception of the Δ and $e_\pi(||)$ parameters which are based on more recent work[30]. The π bonding parameters used in Dubicki and Bramley are related to $e_\pi$ as follows:

$e_\pi(\perp) - e_\pi(||) = \pi^o$
$e_\pi(||) = \pi^e$

Hence for Co(II) and Ni(II) bromates $\Delta \approx 8750\ cm^{-1}$ and for convenience a value of $\Delta_s = 8800\ cm^{-1}$ is chosen as the standard cubic ligand field that should be experimentally observable. Inspection of the $^3T_{2g} \leftarrow {}^3A_{2g}$ transition in $[Ni(H_2O_6](BrO_3)_2$ (figure 5.9) shows that the observed Franck-Condon maximum is approximately $9000\ cm^{-1}$. Furthermore, these complexes have a centre of inversion and the absorption intensity will be dominated by the false origin of a vibronic transition. This mechanism will shift the transition to higher energy. Ideally, one should measure the Franck-Condon

maximum for a pure static electric dipole transition. Consequently the value $\Delta_s$ is a first approximation and is likely to be an overestimate.

The values of the bonding parameters $e_{\sigma\pi}$ and $e_\pi(\perp) - e_\pi(\|)$ are estimated using equations 5.5 and 5.6 and the spectrochemical reduction factor:

$$e_{\sigma\pi}(-29.5) = 0.5(-380) \times \sin(-59)/\sin(36) = 277\ cm^{-1}$$

$$e_\pi(\perp) - e_\pi(\|) = 0.5(1000) \times \cos^2(-29.5) = 379\ cm^{-1}$$

The exact expressions connecting the AOM bonding and microscopic ligand field parameters are obtained from a computer program written by Dr Lucjan Dubicki (see table 5.8). Similar results can be obtained from the approximate analytical expressions given in chapter 4 (equations 4.13-4.16).

**Table 5.8: The calculated coefficients for the microscopic ligand field parameters and the AOM bonding parameters (nickel bromate)**

| $[Ni(H_2O)_6](BrO_3)_2$[a] | | | | |
|---|---|---|---|---|
| | $e_\sigma$ | $e_\pi(\perp) - e_\pi(\|)$ | $e_\pi(\perp) + e_\pi(\|)$ | $e_{\sigma\pi}(\perp)$ |
| $\Delta$ | 2.9997 | 0 | –1.9998 | 0 |
| $\nu$ | 0.0002 | –2.5793 | –0.0197 | 0.0034 |
| $\nu'$ | 0.0139 | 0.0129 | 0 | –0.3356 |
| $\nu''$ | 0 | 0.0060 | 0 | 2.9437 |

[a] $\theta = 55.0°$, $\omega = 33.9°$, $t_\perp = -29.5°$

**Table 5.9: The calculated coefficients for the microscopic ligand field parameters and the AOM bonding parameters (cobalt bromate)**

| $[Co(H_2O)_6](BrO_3)_2$[b] | | | | |
|---|---|---|---|---|
| | $e_\sigma$ | $e_\pi(\perp) - e_\pi(\|)$ | $e_\pi(\perp) + e_\pi(\|)$ | $e_{\sigma\pi}(\perp)$ |
| $\Delta$ | 3.0000 | 0 | –2.0000 | 0 |
| $\nu$ | 0 | –2.7994 | 0.0026 | –0.0004 |
| $\nu'$ | –0.0019 | –0.0017 | 0 | –0.3183 |
| $\nu''$ | 0 | –0.0008 | 0 | 2.9488 |

[b] $\theta = 54.7°$, $\omega = 34.4°$, $t_\perp = -28.2°$

From table 5.8, $\nu'' = 0.0060(379) + 2.9437(277)$

$= 818\ cm^{-1}$ (for $[Ni(H_2O)_6](BrO_3)_2$)

From equation 4.20 (chapter 4), $\Delta \approx 8671\ cm^{-1}$, where $\Delta = 3e_\sigma - 2e_\pi(\perp) - 2e_\pi(\|)$

Given that $e_\pi(\|) = 350\ cm^{-1}$, $e_\sigma$ then has the value $3610\ cm^{-1}$. Hence $\nu$ and $\nu'$ can be computed and corrected for the rotatory ligand field $\nu''$ (see equations 4.13-4.16 and 4.18). Similar calculations were performed for $[Co(H_2O)_6](BrO_3)_2$. The final set of standard microscopic ligand field parameters is given in table 5.10. The small difference in $\nu_s'$ for Co(II) and Ni(II) is due to the small difference in the cone angle ($\theta$).

**Table 5.10: Microscopic ligand field and bonding parameters for $[M(H_2O)_6](BrO_3)_2$[a]**

| Parameter | Ni(II) | Co(II) |
|---|---|---|
| $t_\perp$ | –29.5° | –28.2° |
| $e_{\sigma\pi}(t_\perp)$ | $277\ cm^{-1}$ | $269\ cm^{-1}$ |
| $e_\pi(\perp) - e_\pi(\|)$ | $379\ cm^{-1}$ | $388\ cm^{-1}$ |
| $e_\pi(\perp)$ | $729\ cm^{-1}$ | $738\ cm^{-1}$ |
| $e_\sigma$ | $3610\ cm^{-1}$ | $3618\ cm^{-1}$ |
| $\nu''$ | $818\ cm^{-1}$ | $793\ cm^{-1}$ |
| $\Delta$ | $8671\ cm^{-1}$ | $8679\ cm^{-1}$ |
| $\Delta_s$ | $8800\ cm^{-1}$ | $8800\ cm^{-1}$ |
| $\nu_s$ | $-982\ cm^{-1}$ | $-986\ cm^{-1}$ |
| $\nu_s'$ | $-14\ cm^{-1}$ | $-60\ cm^{-1}$ |

[a] $e_\pi(\|)$ is set at $350\ cm^{-1}$ for both complexes.

The results of the full ligand field calculations on $[Co(H_2O)_6](BrO_3)_2$ and $[Ni(H_2O)_6](BrO_3)_2$ are presented in tables 5.11 and 5.12 below, and compared with the results obtained from the absorption data. The values of the Racah parameters B and C, the one-electron spin-orbit coupling parameter and the orbital reduction factor k used in the calculation are given below the tables.

**Table 5.11: Results of the full calculation on $[Ni(H_2O)_6](BrO_3)_2$**

| $O_h$ term | $S_6$ term | Observed values ($cm^{-1}$) | Calculated values ($cm^{-1}$)[a] |
|---|---|---|---|
| $^3A_{2g}$ | $^3A_g$ | | 0 (2) |
| | | | 1.813 |
| $^3T_{2g}$ | $^3A_g$ | ~9100 $cm^{-1}$ ($^3T_{2g} \leftarrow {}^3A_{2g}$ Franck-Condon maximum) | 8391 (2) |
| | | | 8463 |
| | $^3E_g$ | | 8751 (2) |
| | | | 9027 (2) |
| | | | 9199 |
| | | | 9250 |
| $^3T_{1g}$ ($^3F$) | $^3A_g$ | 13915 | 13775 |
| | | | 13941 (2) |
| | $^3E_g$ | 14970 | 14419 (2) |
| | | | 14560 |
| | | | 14878 |
| | | | 15223 (2) |
| $^1E_g$ | $^1E_g$ | 15688/15820 (see discussion in section 5.4.2 | 15839 (2) |
| $^1T_{2g}$ | $^1A_g$ | ~22600-22800 | 22663 |
| | $^1E_g$ | | 22993(2) |
| $^1A_{1g}$ | $^1A_g$ | | 23929 |
| $^3T_{1g}$ ($^3P$) | $^3A_g$ | ~24950 (shoulder) | 25145 (2) |
| | | | 25324 |
| | $^3E_g$ | 26010 | 25824 (2) |
| | | | 25955 (2) |
| | | | 26034 |
| | | | 26140 |

[a] B= 910 $cm^{-1}$, C = 3997 $cm^{-1}$, $\Delta_s$ = 8800 $cm^{-1}$, $\zeta$ = 590 $cm^{-1}$, k = 0.88, $v_s$ = –982 $cm^{-1}$, $v_s'$ = –14 $cm^{-1}$

(2) denotes a doubly degenerate spin-orbit state

**Table 5.12 Full ligand field calculations for $[Co(H_2O)_6](BrO_3)_2$**

| $O_h$ term | $S_6$ term | Observed values ($cm^{-1}$) | Calculated values ($cm^{-1}$)[a] |
|---|---|---|---|
| $^4T_{1g}$ ($^4F$) | $^4E_g$ | Raman spectra were measured in an attempt to observe electronic Raman transitions to these states. Unfortunately the transitions were not observed (see section 5.5 and appendix B) | 0 |
| | | | 207 |
| | | | 421 |
| | | | 721 |
| | $^4A_g$ | | 1437 |
| | | | 1534 |
| $^4T_{2g}$ | $^4E_g$ | Franck-Condon maximum at 8685 $cm^{-1}$, shoulders on both sides at (very approximately) 7800-8000 $cm^{-1}$ and 9400-9600 $cm^{-1}$ | 8185 |
| | | | 8240 |
| | | | 8296 |
| | | | 8367 |
| | $^4A_g$ | | 8776 |
| | | | 8840 |
| $^2E_g$ | $^2E_g$ | | 9482 |
| | | | 9491 |
| $^2T_{1g}$[a] | $^2E_g$ | Weak, broad peak centred around 17100 $cm^{-1}$ | 16001 |
| | | | 16276 |
| | $^2A_g$ | | 16619 |
| $^2T_{2g}$[a] | $^2E_g$ | | 16930 |
| | | | 17002 |
| | $^2A_g$ | | 17158 |
| $^4A_{2g}$ | $^4A_g$ | | 17336 |
| | | | 17340 |
| $^4T_{1g}$ ($^4P$) | $^4E_g$ | Franck-Condon maximum at 20240 $cm^{-1}$ | 19676 |
| | | | 19738 |
| | | | 19767 |
| | | | 19951 |
| | $^4A_g$ | | 20091 |
| | | | 20389 |
| $^2T_{1g}$[b] | $^2A_g$ | 21420, 21570 $cm^{-1}$ | 21294 |
| | $^2E_g$ | | 21459 |
| | | | 21459 |

**Table 5.12 (continued)**

| $O_h$ term | $S_6$ term | Observed values ($cm^{-1}$) | Calculated values ($cm^{-1}$)[a] |
|---|---|---|---|
| $^2A_{1g}$ | $^2A_g$ | | 23193 |
| $^2T_{2g}$[b] | $^2E_g$ | 24870 $cm^{-1}$ | 24929 |
| | | | 25067 |
| | $^2A_g$ | | 25672 |
| $^2T_{1g}$[c] | $^2A_g$ | | 26136 |
| | $^2E_g$ | | 26366 |
| | | | 26410 |

[a] $B = 850\ cm^{-1}$, $C = 3750\ cm^{-1}$, $\Delta_s = 8800\ cm^{-1}$, $\zeta = 470\ cm^{-1}$, $k = 0.88$, $\nu_s = -986\ cm^{-1}$, $\nu_s' = -60\ cm^{-1}$

Given that Co(II) is an odd-electron species, all levels will remain at least doubly degenerate (Kramers doublets) in the absence of external perturbations such as magnetic fields.

**Table 5.13: Computed and experimental g-values for the ground state of $[Co(H_2O)_6](BrO_3)_2$**

| Value | $g_{\|}$ | $g_{\perp}$ |
|---|---|---|
| Experimental | 7.54 | 2.11 |
| Using ligand field parameters in table 5.8 | 7.66 | 1.99 |
| Neglecting the rotatory trigonal field $\nu''$ | 7.81 | 1.83 |

## 5.5 Conclusion

It can be seen from the above experimental work and calculations that the trigonal fields in $[Co(H_2O)_6](BrO_3)_2$ and $[Ni(H_2O)_6](BrO_3)_2$ are significant. This is particularly evident in the EPR spectra of both compounds, in the large g-value anisotropy in the cobalt spectra presented here, and in the significant zero-field splitting in the nickel spectra measured by Bowers[7] and later re-measured by Suassuna et al.[19]. The absorption data presented by earlier workers[2-6] for both compounds were analysed without reference to the trigonal fields; the complexes were assumed to possess octahedral symmetry. The evidence of trigonal splitting in the absorption spectra is certainly much less spectacular, however, Bowers' EPR measurements of

$[Ni(H_2O)_6](BrO_3)_2$ were published a full fifteen years prior to the absorption spectra of Harding et al. and Solomon and Ballhausen, and it showed a large zero-field splitting, strong evidence of an axial field. The crystal structure of $[Zn(H_2O)_6](BrO_3)_2$, published in 1936 by Yue and Beevers[9] showed that the complex ion lies on a site of trigonal (in this case $S_6$) symmetry. The structures published later for the cobalt and nickel compounds[12,13] confirmed the trigonal site symmetry.

Raman spectra were also measured for the cobalt and nickel bromates with the intention of locating the electronic Raman transitions predicted to occur at energies below 1500 $cm^{-1}$ (see table 5.11 above). This would have provided further evidence of the trigonal fields present in these compounds. Unfortunately, although Raman spectra were obtained, no electronic Raman peaks could be seen. The Raman spectra are presented in appendix B.

## 5.6 References


(1) Dubicki, L.; Bramley, R. *Chemical Physics Letters* **1997**, *272*, 55-60.

(2) Harding, M. J.; Mason, S. F.; Robbins, D. J.; Thomson, A. J. *Chemical Physics Letters* **1970**, *7*, 70-72.

(3) Harding, M. J.; Mason, S. F.; Robbins, D. J.; Thomson, A. J. *Journal of the Chemical Society A* **1971**, 3047-3058.

(4) Harding, M. J.; Briat, B. *Molecular Physics* **1973**, *25*, 745-776.

(5) Harding, M. J.; Billardon, M.; Kramer, A. *Molecular Physics* **1974**, *27*, 457-466.

(6) Solomon, E. I.; Ballhausen, C. J. *Molecular Physics* **1975**, *29*, 279-299.

(7) Bowers, K. D.; Owen, J. *Reports on Progress in Physics* **1955**, *18*, 304-373.

(8) Srinivasan, T. K. K.; Devanathan, T. *Journal of Raman Spectroscopy* **1990**, *21*, 91-98.

(9) Yue, S. H.; Beevers, C. A. *Zeitschrift fur Kristallographie* **1936**, 426-434.

(10) Belderbos, C. *Natuurwetenschappelijk Tijdschrift* **1937**, *19*, 189-196.

(11) Weigel, D. *Bulletin de la Societe Chimique France* **1963**, 2087-2090.

(12) Blackburn, A. C.; Galluci, J. C.; Gerkin, R. E. *Acta Crystallographica B* **1990**, *46*, 712-716.

(13) Blackburn, A. C.; Gallucci, J. C.; Gerkin, R. E. *Acta Crystallographica C* **1991**, *47*, 1786-1789.

(14) Blackburn, A. C.; Gallucci, J. C.; Gerkin, R. E. *Acta Crystallographica C* **1991**, *C47*, 2019-2023.

(15) Gallucci, J. C.; Gerkin, R. E. *Acta Crystallographica C* **1990**, *C46*, 350-354.

(16) Peter, S.; Suchanek, E.; Esser, D.; Lutz, H. D. *Zeitschrift fur Naturforschung* **1996**, *51B*, 1072-1078.

(17) Nyburg, S. C.; Steed, J. W.; Aleksovska, S.; Petrusevski, V. M. *Acta Crystallographica B* **2000**, *B56*, 204-209.

(18) Harding, M. J.; Mason, S. F.; Robbins, D. J.; Thomson, A. J. *Journal of the Chemical Society A* **1971**, 3058-3062.

(19) Suassuna, J. F.; Rettori, C.; Vargas, H.; Barberis, G. E.; Hennies, C. E.; Oliveira, N. F. *Journal of the Chemistry of Solids* **1977**, *38*, 1075-1077.

(20) Bleaney, B.; Bowers, K. D.; Trenam, R. S. *Proceedings of the Royal Society A* **1955**, *228*, 157-166.

(21) Jesion, A.; Shing, Y. H.; Walsh, D.; Donnay, J. D. H. *Journal of Physics C: Solid State Physics* **1976**, *9*, L219-L222.

(22) Jesion, A.; Shang, Y. H.; Walsh, D. *Physical Review B* **1977**, *16*, 3012-3015.

(23) Lutz, H. D.; Suchanek, E. *Spectrochimica Acta Part A* **2000**, *56*, 2707-2713.

(24) Matsuo, T.; Kinami, N.; Suga, H. *Thermochimica Acta* **1995**, *267*, 421-434.

(25) Krausz, E. *Australian Journal of Chemistry* **1993**, *46*, 1041-1054.

(26) Krausz, E. *Australian Optical Society News* **1998**, *12*, 21-24.

(27) Krausz, E.; Tomkins, C.; Adler, H. *Journal of Physics E: Scientific Instrumentation* **1982**, *15*, 1167-1168.

(28) Mabbs, F. E.; Collison, D. *Electron Paramagnetic Resonance of d Transition Metal Compounds*; 1st ed.; Elsevier: Amsterdam, 1992.

(29) Pilbrow, J. R. *Transition Ion Electron Paramagnetic Resonance*; 1st ed.; Oxford University Press: Oxford, 1990.

(30) Dubicki, L., private communication.

(31) Figgis, B. N.; Hitchman, M. A. *Ligand Field Theory and Its Applications*; 1st ed.; Wiley-VCH: New York, 2000; Vol. 1.

(32) Ballhausen, C. J. *Introduction to Ligand Field Theory*; 1st ed.; McGraw-Hill Book Company: New York, 1962.

(33) Bendix, J.; Brorson, M.; Schaeffer, C. E. *Inorganic Chemistry* **1993**, *32*, 2838-2849.

# Chapter 6: Spectroscopic Studies of Some Metal Pyrazolyl Complexes

## 6.1 Introduction

This chapter presents the absorption and electron paramagnetic resonance (EPR) spectra of a number of the metal pyrazolyl complexes mentioned in chapter 4, together with the results of angular-overlap model calculations. Examples of both monopyrazolyl and capped tris pyrazolyl complexes were considered.

The capping of the pyrazolyl ligands in the complexes $[M(HCPz_3)_2](NO_3)_2$ and $[M(HBPz_3)_2]$[#] with a carbon or boron atom not only rotates the pyrazole ligands so as to maximise the $\nu$ trigonal field, but also produces a large tilting within the pyrazole plane. The former distortion is well known, but the latter has been neglected in all previous ligand field calculations.

The aim of this work was to determine the dependence of the trigonal ligand fields on the in-plane tilting ($t_{||}$) and whether it is reflected in the electronic fine structure.

To achieve this, the EPR and absorption spectra of a number of capped and uncapped complexes were measured. These results were analysed together with previously published work on closely related complexes. Surprisingly, even in the uncapped $[Ni(Pz)_6]^{2+}$ complexes, there is a significant in-plane distortion that is characterised by the $e_{\sigma\pi}(||)$ parameter, whose sign is reversed for the capped geometry.

## 6.2 History

The capped pyrazolyl compounds, form an important class of ligands in inorganic chemistry. The pyrazolyl borate ligands $H_nBPz_{4-n}^-$ where n = 0, 1 or 2 were first

[#] Given the cumbersome systematic names of the capped pyrazolyl complexes, e.g. $[Co(HCPz_3)_2](NO_3)_2$ is *bis*(*tris*(pyrazol-1-yl)methane) cobalt(II) dinitrate, and $[Co(HBPz_3)_2]$ is *bis*(hydrotris(pyrazol-1-yl)borate)cobalt(II), the abbreviations will be used from this point forward.

prepared in the 1960s by Trofimenko[1]. Complexes of the divalent cations of Mg, Ca, Mn, Fe, Co, Ni, Cu, Zn, Cd, Pb, Sr, Ba, and Hg were reported and characterised soon after[2]. The chemistry of poly-pyrazolyl borates has been extensively and regularly reviewed by Trofimenko[3-5], culminating in a monograph published in 1999[6]. Only the complexes of $HBPz_3^-$ will be considered further in this thesis. Hydrotris(pyrazol-1-yl) borate forms stable, water-insoluble complexes, melting at approximately 280°C, with many divalent transition metals, and Group 2 and Group 14 divalent ions. Trofimenko has coined the term 'scorpionate' to describe the family of polypyrazolylborate ligands ($RBPz_2R'$, where R' may be a third pyrazolyl group, or another coordinating functional group)[5,6]. The term arises from the resemblance of the ligand coordinated with a metal ion to a scorpion catching prey; the 'claws' (the two pyrazolyl ligands) grasp the 'prey' (the metal ion), and the 'tail'(the R' group) reaches round to sting the prey. This term can also apply to the polypyrazolyl methanes.

The chemistry of pyrazolyl methanes is considerably older than that of pyrazolyl borates, but has been much less widely studied. Only the *tris*(pyrazol-1-yl) methane ($HCPz_3$) ligand will be considered further. The synthesis of $HCPz_3$ was first reported in 1937 by Hückel and Bretschneider[7], and it was recognised by Trofimenko in 1970 that this and other poly pyrazolyl methanes could act as ligands for transition metals in a manner analogous to poly pyrazolyl borates[8]. $HCPz_3$ reacts with simple salts (e.g. chlorides, nitrates and sulfates) of divalent transition metals to form stable complexes with very similar properties to those of the corresponding pyrazolyl borate complex.

Like other nitrogen-containing heterocycles, pyrazole itself can form complexes with a number of transition metal ions[9-11], although only cobalt(II) and nickel(II) form *hexakis* pyrazolyl nitrates. Cobalt(II) and nickel(II) can form complexes of type $[M(Pz)_4(NO_3)_2]$ where the nitrates are also coordinated to the metal ion.

### 6.2.1 Crystal structures and molecular geometry

The crystal structures of the complexes $[M(HCPz_3)_2](NO_3)_2$ where M = Co, Ni, Cu, or Zn were determined by Astley et al.[12]. All are isostructural, with the monoclinic space group $P2_1/n$. The metal ion is located on a crystallographic inversion centre, with the $[M(HCPz_3)_2]^{2+}$ complex having approximate $D_{3d}$ symmetry (see figure 6.1). The

complex ions are slightly trigonally elongated. Relevant angles are tabulated in chapter 4 (table 4.3).

The $[M(HBPz_3)_2]$ complexes (M = Co, Ni or Zn) are isostructural, with the monoclinic space group $P2_1/n$[13-15]. The unit cell contains two pairs of crystallographically equivalent molecules. Unlike the $[M(HCPz_3)_2]^{2+}$ complex ions, the metal ions do not lie on inversion centres. The complexes again have distorted $D_{3d}$ symmetry. Relevant angles are given in table 4.3 (chapter 4).

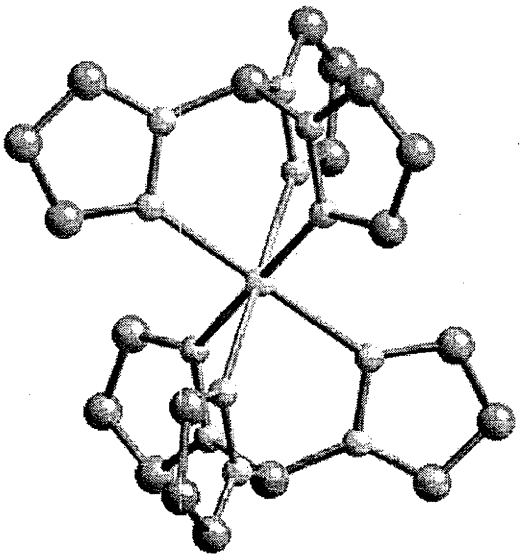

**Figure 6.1: The complex ion in $[Co(HCPz_3)_2](NO_3)_2$, the other pyrazolyl methane complexes, and the pyrazolyl borates, are similar**

The crystal structures of a number of hexakis pyrazolyl complexes of divalent metal ions have been determined, including $[Ni(5MePz)_6](ClO_4)_2$[16], $[Ni(Pz)_6](BF_4)_2$[17], $[Mn(Pz)_6](ClO_4)_2$[18] and $[Ni(Pz)_6](NO_3)_2$[19]. All have the trigonal space group $P\bar{3}$ and the M(II) ion has $S_6$ site symmetry. The important geometric parameters are summarised in table 4.2. The zinc analogues are all isostructural, except in the case of the nitrate salt where the tetrakis pyrazolyl compound $[Zn(Pz)_4](NO_3)_2$ is formed. The geometry of the complex ion in $[Ni(Pz)_6](NO_3)_2$ is shown in figure 6.2.

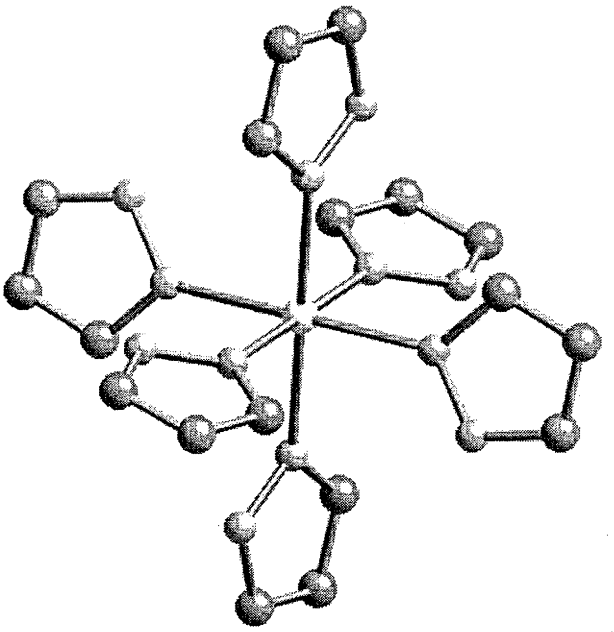

**Figure 6.2: The $[Ni(Pz)_6]^{2+}$ ion in $[Ni(Pz)_6](NO_3)_2$, viewed along the trigonal axis**

### 6.2.2 Previous spectroscopic studies

The optical absorption and electron paramagnetic resonance (EPR) spectra for $[Co(HBPz_3)_2]$ and the nitrate, chloride and sulfate salts of *bis*(*tris*(pyrazol-1-yl) cobalt(II), were measured in 1966 by Jesson[20]. The measured axial and equatorial g-values are tabulated below. These are the largest anisotropies observed for trigonally distorted cobalt(II).

**Table 6.1: Axial ($g_{\|}$) and equatorial ($g_{\perp}$) g-values observed by Jesson[20]**

| Compound | $g_{\|}$ | $g_{\perp}$ |
|---|---|---|
| $[Co(HBPz_3)_2]$ | 8.46±0.01 | 0.98±0.01 |
| $[Co(HCPz_3)_2](NO_3)_2$ | 8.53±0.01 | 0.83±0.01 |
| $[Co(HCPz_3)_2]Cl_2$ | 8.53±0.01 | 0.78±0.01 |
| $[Co(HCPz_3)_2](SO_4)$ | 8.06±0.01 | 1.30±0.01 |

**Table 6.2: Predicted separations between the six Kramers doublets of the ground manifold of two trigonally distorted cobalt(II) pyrazolyl complexes (in $cm^{-1}$)**

| $[Co(HCPz_3)_2](NO_3)_2$ | $[Co(HBPz_3)_2]$ |
|---|---|
| 0 | 0 |
| 206 | 206 |
| 417 | 417 |
| 656 | 659 |
| 2510 | 2278 |
| 2539 | 2310 |

Jesson used the effective Hamiltonian model of Abragam and Pryce[21] to fit the ground state g-values and calculate the g-values for the other five Kramers doublets of the $^4T_{1g}$ ground state, and their energy separations (table 6.2). These are the largest trigonal field splittings calulated for a cobalt(II) complex, a fact in line with these complexes having the largest observed g-value anisotropy for axially-distorted cobalt(II).

Raman studies of these two complexes (appendix C) have unfortunately not revealed any electronic transitions within the ground $^4T_{1g}$ multiplet.

Astley et al. measured the absorption spectra of $[M(HCPz_3)_2](NO_3)_2$ where M = Co, Ni, or Cu for both KBr discs and single crystals at room temperature and 15 K[12]. The single crystal spectra were polarised, although the crystal faces used are not specified in the paper. For cobalt, a broad, slightly asymmetric peak due to the $^4T_{2g} \leftarrow {}^4T_{1g}(^4F)$ transition could be clearly seen, centred at ca 12500 $cm^{-1}$. Sharp peaks assigned to spin-forbidden transitions were seen just above 20000 $cm^{-1}$, and a broad peak with a low-energy shoulder was seen at ca 23000 $cm^{-1}$. This last peak was assigned to a combination of the $^4A_{2g} \leftarrow {}^4T_{1g}(^4F)$ and $^4T_{1g}(^4P) \leftarrow {}^4T_{1g}(^4F)$ transitions. For nickel, a broad, highly asymmetric peak could be seen at ca 12000 $cm^{-1}$, and was assigned to the trigonally-split $^3T_{2g} \leftarrow {}^3A_{2g}$ transition. A doublet at ca 20000 $cm^{-1}$ was assigned to the trigonal components of the $^3T_{1g}(^3F) \leftarrow {}^3A_{2g}$ transition. The $^3T_{1g}(^3P) \leftarrow {}^3A_{2g}$ transition was at too high an energy to be observed. Two sharp peaks assigned to spin-forbidden transitions to the $^1E_g$ and $^1A_{1g}$ states were also observed.

Astley et al. applied the AOM to account for the broad peaks in the electronic spectra, in particular the large trigonal splitting observed for the $^3T_{1g}(^3F)$ state of the nickel

complex. The analysis did not independently determine the trigonal ligand field parameters $\nu$ and $\nu'$. Their calculations do not account for the zero-field splitting of the $^3A_{2g}$ ground state of the nickel complex. This failure is not surprising given that the effect of the $t_{||}$ distortion was neglected. Their work provided the motivation for the EPR and absorption measurements, and theoretical analysis described in this chapter.

## 6.3 Experimental

### 6.3.1 Synthesis

The *tris*(pyrazol-1-yl)methane ($HCPz_3$) ligand was prepared by two different methods. The first was the solid-liquid phase transfer method of Juliá et al.[22] involving refluxing pyrazole (Aldrich) in chloroform (Univar) with potassium carbonate (Univar) for twelve hours. Tetrabutylammonium hydrogen sulfate (Aldrich) was used as the phase transfer catalyst to remove HCl liberated by the reaction from the organic layer to the potassium carbonate. The dark brown solid product was either used without further purification, or purified by column chromatography using the method of Juliá et al.[22].

The second synthetic method was the liquid-liquid phase transfer method of Reger et al.[23]. This method involved the gentle refluxing over three days of pyrazole, chloroform, water and sodium carbonate. Tetrabutylammonium bromide was used as the phase transfer agent in this case. This gave a much purer product with an off-white colour. Further purification was not required.

$[Co(HCPz_3)_2](NO_3)_2$, $[Ni(HCPz_3)_2](NO_3)_2$ and $[Zn(HCPz_3)_2](NO_3)_2$ were prepared by mixing acetone solutions of the appropriate metal nitrate salt and $HCPz_3$ in a 1:2 molar ratio, with stirring. The resulting $[M(HCPz_3)_2](NO_3)_2$ solids were filtered, washed with acetone and air-dried. The products were recrystallised by evaporation from water to give well-formed yellow (cobalt), violet (nickel) or colourless (zinc) inclined non-regular hexagonal prisms. Purity and identity of the complexes was checked by microanalyses performed by the analytical unit of the Research School of Chemistry. Carbon, hydrogen and nitrogen were determined by combustion analysis, while cobalt,

nickel and zinc were determined using atomic absorption spectroscopy. Typical results are shown in table 6.3; the mass percentages all lie within ± 0.5% of theoretical values.

**Table 6.3: Purity checks for the pyrazolyl compounds (performed by the Research School of Chemistry microanalytical unit)**

| Compound | Calculated percentage | Found percentage |
|---|---|---|
| $[Co(HCPz_3)_2](NO_3)_2$ | C:39.29, H:3.30, N:32.07, Co:9.64 | C:39.19, H: 3.36, N: 32.31, Co: 9.88 |
| $[Ni(HCPz_3)_2](NO_3)_2$ | C:39.31, H:3.30, N:32.09, Ni:9.60 | C:39.39, H:3.37, N:32.42, Ni: 9.53 |
| $[Zn(HCPz_3)_2](NO_3)_2$ | C:38.88, H:3.26, N:31.74, Zn:10.58 | C:38.86, H:3.27, N:31.84, Zn:10.74 |
| $[Co(HBPz_3)_2]$ | C:44.58, H:4.16, N:34.66, Co:12.15 | C:44.56, H:4.05, N:34.62, Co:12.51 |
| $[Ni(HBPz_3)_2]$ | C:44.60, H:4.16, N:34.67, Ni:12.11 | C:44.64, H:4.31, N:35.00, Ni:11.84 |
| $[Zn(HBPz_3)_2]$ | C:43.99, H:4.10, N:34.20, Zn:13.30 | C:44.24, H:4.21, N:34.57, Zn:13.55 |
| $[Co(Pz)_6](NO_3)_2$ | C: 36.56, H: 4.09, N: 33.16, Co: 9.96 | C: 36.38, H: 4.16, N: 33.20, Co: 9.99 |
| $[Ni(Pz)_6](NO_3)_2$ | C: 36.57, H: 4.09, N: 33.17, Ni: 9.93 | C: 36.22, H: 4.12, N: 32.97, Ni: 9.91 |

The metal pyrazolyl borate complexes ($[M(HBPz_3)_2]$, where M = Co, Ni or Zn) were synthesised by the method of Jesson et al.[24]. Although Jesson et al. report (hydrotris(pyrazol-1-yl) borate) potassium ($KHBPz_3$) to be air stable, literature from the manufacturer suggested that the compound is air-sensitive. Therefore, as a precaution, the synthesis was carried out in a glove box under a flow of nitrogen, using water degassed with nitrogen. $KHBPz_3$ (Strem Chemicals) was dissolved in water and added, with stirring, to an aqueous solution of the appropriate metal nitrate in a 2:1 molar ratio. A precipitate formed almost immediately but stirring was continued for about five minutes to ensure complete reaction. The resulting precipitate was filtered, washed with water, and dried on a low heat (approx. 40°C) in an oven.

The compounds were recrystallised by evaporation from toluene solutions to give yellow (cobalt), violet (nickel) or colourless (zinc) crystals. Purity was checked by microanalysis (analytical unit, Research School of Chemistry), using the same methods as for the pyrazolyl methane compounds. The results are shown in table 6.3; the mass percentages all lie within ± 0.5% of theoretical values.

The complexes $[M((Pz)_6](NO_3)_2$ where M = Co or Ni were prepared by mixing stoichiometric amounts of the metal nitrate salt and pyrazole in aqueous solution, followed by recrystallisation by solvent evaporation from a Petri dish[25]. The cobalt complex formed orange crystals while the nickel complex formed blue crystals. The purity of the products was again checked by microanalysis (table 6.3).

### 6.3.2 Spectroscopic measurements

A Bruker spectrometer was employed to measure the EPR spectra. Data were obtained at both room and liquid helium temperatures, using both X- and Q-band microwave frequencies. Spectra were measured at both frequencies for powdered samples of both $[Ni(HCPz_3)_2](NO_3)_2$ and $[Ni(HBPz_3)_2]$, both for the pure compounds and for magnetically dilute samples, where the nickel compound was doped into the corresponding zinc compound at levels of ca 3%. For $[Ni(Pz)_6](NO_3)_2$, only spectra of the pure compound were measured as there is no isostructural nonmagnetic host compound. X-band spectra were also measured for magnetically dilute $[Co(HBPz_3)_2]$ and $[Co(HCPz_3)_2](NO_3)_2$, and pure $[Co(Pz)_6](NO_3)_2$. To remove any peaks due to rhombic splitting, spectra were also measured using frozen toluene solutions of $[Co(HBPz_3)_2]$ in the concentration range 0.01-0.05 mol $L^{-1}$. This gave substantially 'cleaner' spectra. For $[Co(HCPz_3)_2](NO_3)_2$, frozen methanol solutions were used. Experimental parameters for the EPR spectra are given in tables 6.4-6.8.

**Table 6.4: Experimental parameters for the EPR spectra of $[Ni(Pz)_6](NO_3)_2$**

| Parameter | Figure 6.10 | Figure 6.11 |
|---|---|---|
| Microwave frequency (GHz) | 9.438541 | 9.438815 |
| Microwave power (mW) | 0.63 | 0.63 |
| Temperature (K) | 9 | 295 |
| Receiver gain | 32 | 8000 |
| Resolution (Gauss) | 2.93 | 6.84 |

**Table 6.5: Experimental parameters for the EPR spectra of the capped nickel pyrazolyl compounds**

| Parameter | Figure 6.12 | Figure 6.13 | Figure 6.14 | Figure 6.15 |
|---|---|---|---|---|
| Microwave frequency (GHz) | 33.95 | 33.965 | 9.439 | 9.438 |
| Microwave power (mW) | 50.16 | 50.16 | 6.315 | 6.315 |
| Temperature (K) | 295 | 295 | 7.5 | 7.5 |
| Number of scans | 1 | 1 | 1 | 1 |
| Receiver gain | 10000 | 10000 | 5000 | 50000 |
| Modulation frequency (kHz) | 50 | 50 | 100 | 100 |
| Modulation amplitude (Gauss) | 20.751 | 20.751 | 20.181 | 20.181 |
| Resolution (Gauss) | 3.42 | 3.42 | 2.44 | 3.17 |

**Table 6.6: Experimental parameters for the EPR spectrum of $[Co(Pz)_6](NO_3)_2$**

| Parameter | Figure 6.16 |
|---|---|
| Microwave frequency (GHz) | 9.437 |
| Microwave power (mW) | 6.315 |
| Temperature (K) | 7.5 |
| Number of scans | 1 |
| Receiver gain | 32 |
| Modulation frequency (kHz) | 100 |
| Modulation amplitude (Gauss) | 2.264 |
| Resolution (Gauss) | 0.88 |

**Table 6.7: Experimental parameters for the EPR spectra of $[Co(HBPz_3)_2]$**

| Parameter | Figure 6.17 | Figure 6.18 | Figure 6.19 | Figure 6.20 |
|---|---|---|---|---|
| Microwave frequency (GHz) | 9.437 | 9.438 | 9.439 | 9.439 |
| Microwave power (mW) | 6.315 | 6.315 | 6.315 | 6.315 |
| Temperature (K) | 7.5 | 7.5 | 7.5 | 7.5 |
| Number of scans | 1 | 1 | 1 | 1 |
| Receiver gain | 1250 | 5000 | 630 | 10000 |
| Modulation frequency (kHz) | 100 | 100 | 100 | 100 |
| Modulation amplitude (Gauss) | 20.181 | 2.264 | 20.181 | 2.264 |
| Resolution (Gauss) | 2.93 | 0.88 | 3.42 | 0.88 |

**Table 6.8: Experimental parameters for the EPR spectra of $[Co(HCPz_3)_2](NO_3)_2$**

| Parameter | Figure 6.21 | Figure 6.22 | Figure 6.23 | Figure 6.24 |
|---|---|---|---|---|
| Microwave frequency (GHz) | 9.436 | 9.436 | 9.439 | 9.439 |
| Microwave power (mW) | 6.315 | 6.315 | 6.315 | 6.315 |
| Temperature (K) | 7.5 | 7.5 | 7.5 | 7.5 |
| Number of scans | 1 | 2 | 2 | 3 |
| Receiver gain | 630 | 10000 | 6300 | 10000 |
| Modulation frequency (kHz) | 100 | 100 | 100 | 100 |
| Modulation amplitude (Gauss) | 20.181 | 2.264 | 20.181 | 2.264 |
| Resolution (Gauss) | 3.42 | 0.88 | 3.42 | 0.88 |

Absorption spectra were measured for $[Co(HCPz_3)_2](NO_3)_2$, $[Ni(HCPz_3)_2](NO_3)_2$, $[Co(HBPz_3)_2]$, $[Ni(HBPz_3)_2]$, $[Co(Pz)_6](NO_3)_2$, and $[Ni(Pz)_6](NO_3)_2$ using the microcrystal spectrophotometer developed within the Krausz group[26,27]. For a description of the instrument and the sample mounting method, see section 5.3.2.

The two pyrazolyl methane complexes formed crystals with faces which were readily identifiable using X-ray reflection methods in conjunction with optical microscopy, so spectra were measured with the incident light polarised parallel with the two extinction directions of a known crystal face. For the other compounds, spectra were measured with the incident light polarised parallel with the extinction directions of an arbitrary crystal face. Spectra were measured at 10 K for all six compounds, together with a room temperature spectrum of $[Ni(HCPz_3)_2](NO_3)_2$.

## 6.4 Results and discussion

### 6.4.1 Absorption spectroscopy

The spectra are shown in figures 6.3-6.9, and transition energies are listed in tables 6.9-6.14, which also give the calculated transition energies, based on the analysis described in section 6.5.4. The calculated values are marked on the spectra with 'sticks'.

The absorption spectrum of $[Ni(Pz)_6](NO_3)_2$ (figure 6.3) has two broad peaks at 11000 $cm^{-1}$ and 17500 $cm^{-1}$. These are transitions to the $^3T_{2g}$ and $^3T_{1g}$ ($^3F$) excited states respectively. The $^3T_{2g}$ peak has a slight asymmetry, which takes the form of a low energy shoulder. Another broad peak, off the scale of the spectrum at ~30000 $cm^{-1}$, corresponds to the $^3T_{1g}$ ($^3P$)←$^3A_{2g}$ transition. Two sharp peaks are also noted at 13500 $cm^{-1}$ ($^1E_g$) and 22500 $cm^{-1}$ ($^1A_{1g}$).

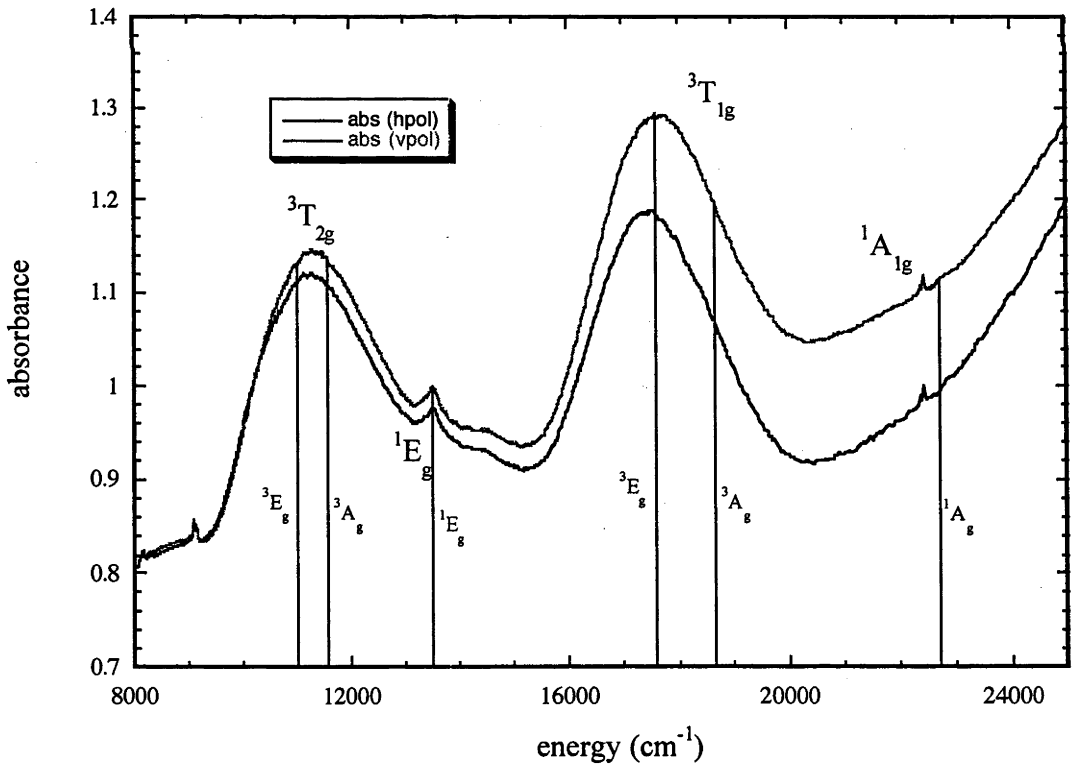


**Figure 6.3: Absorption spectrum of $[Ni(Pz)_6](NO_3)_2$ (arbitrary face, 10K)**

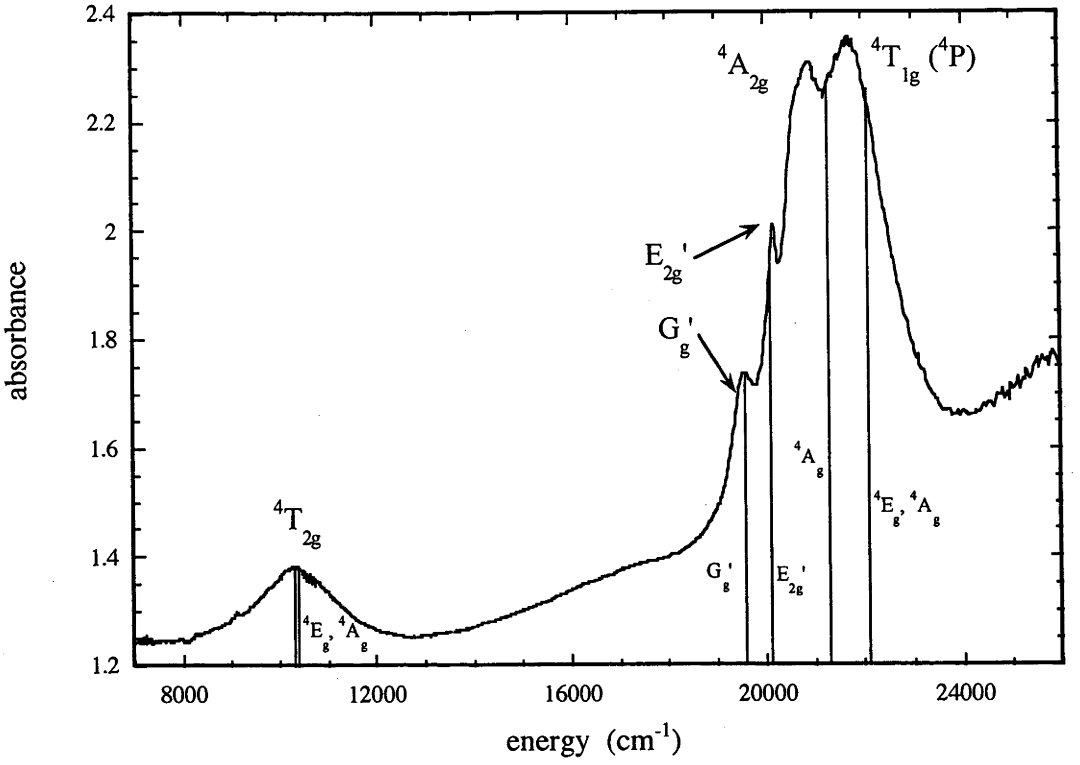


**Figure 6.4: Absorption spectrum of $[Co(Pz)_6](NO_3)_2$ (arbitrary face, 10 K)**

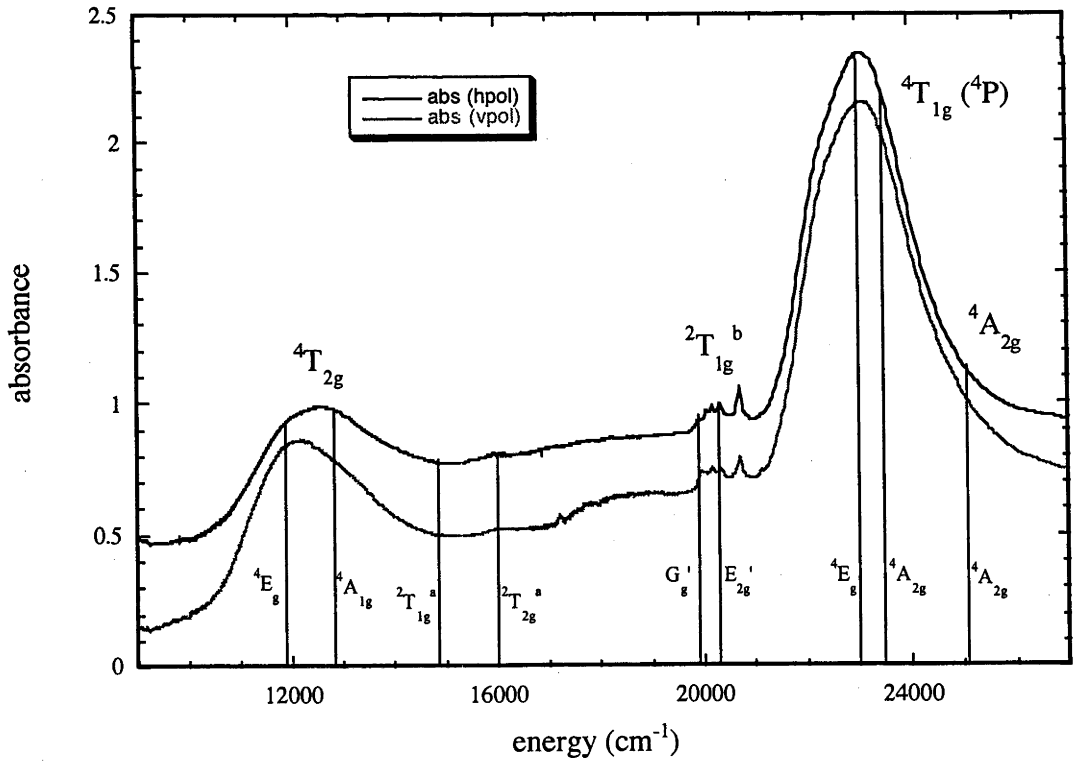


**Figure 6.5: Absorption spectrum of $[Co(HCPz_3)_2](NO_3)_2$, (001 face, 10 K)**

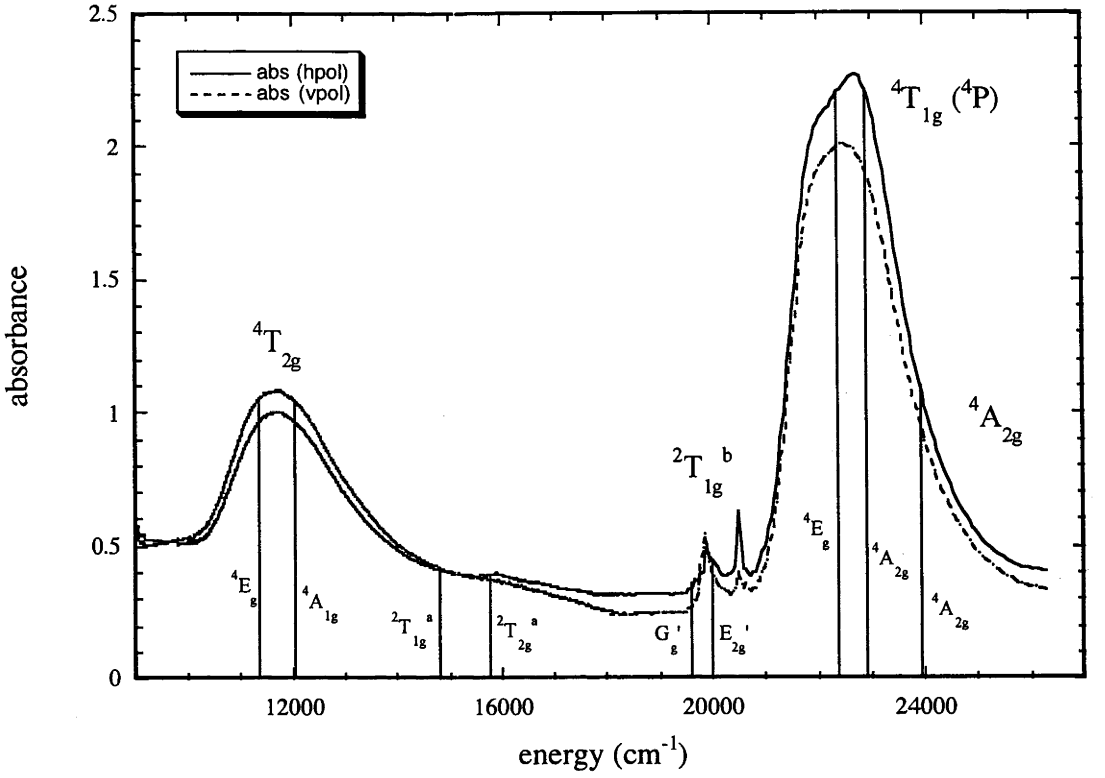


**Figure 6.6 Absorption spectrum of $[Co(HBPz_3)_2]$ (arbitrary face, 10K)**

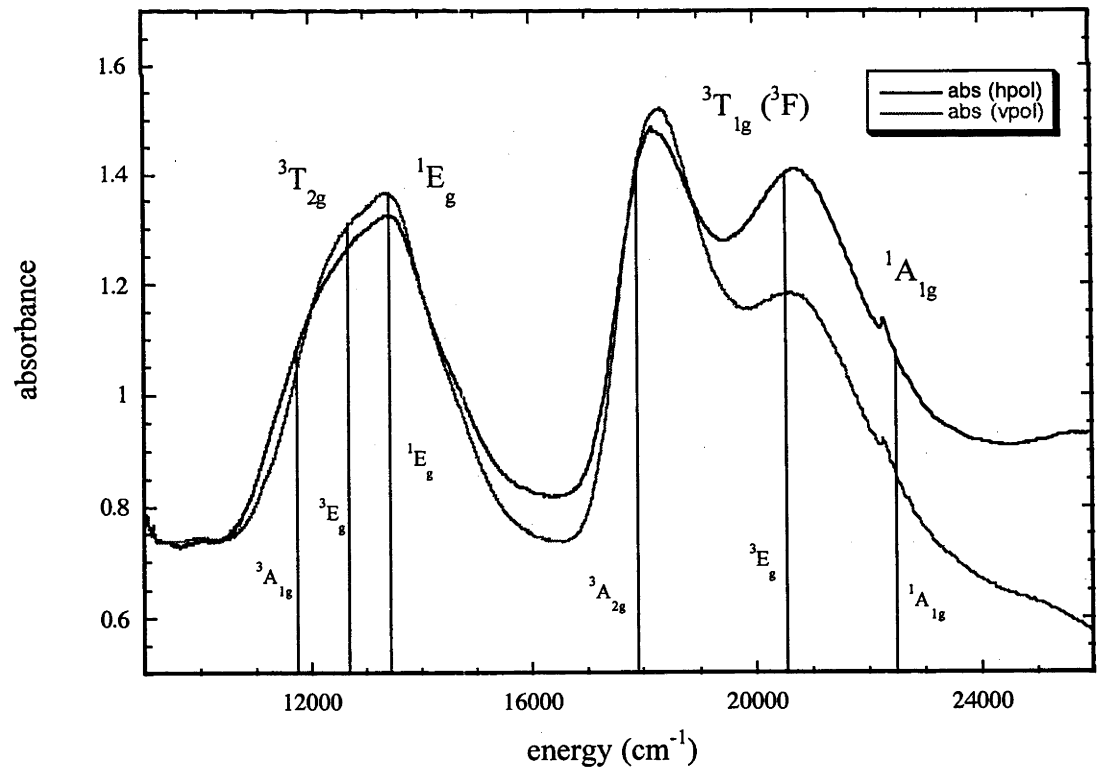


**Figure 6.7 Absorption spectrum of $[Ni(HCPz_3)_2](NO_3)_2$ (001 face, 10 K)**

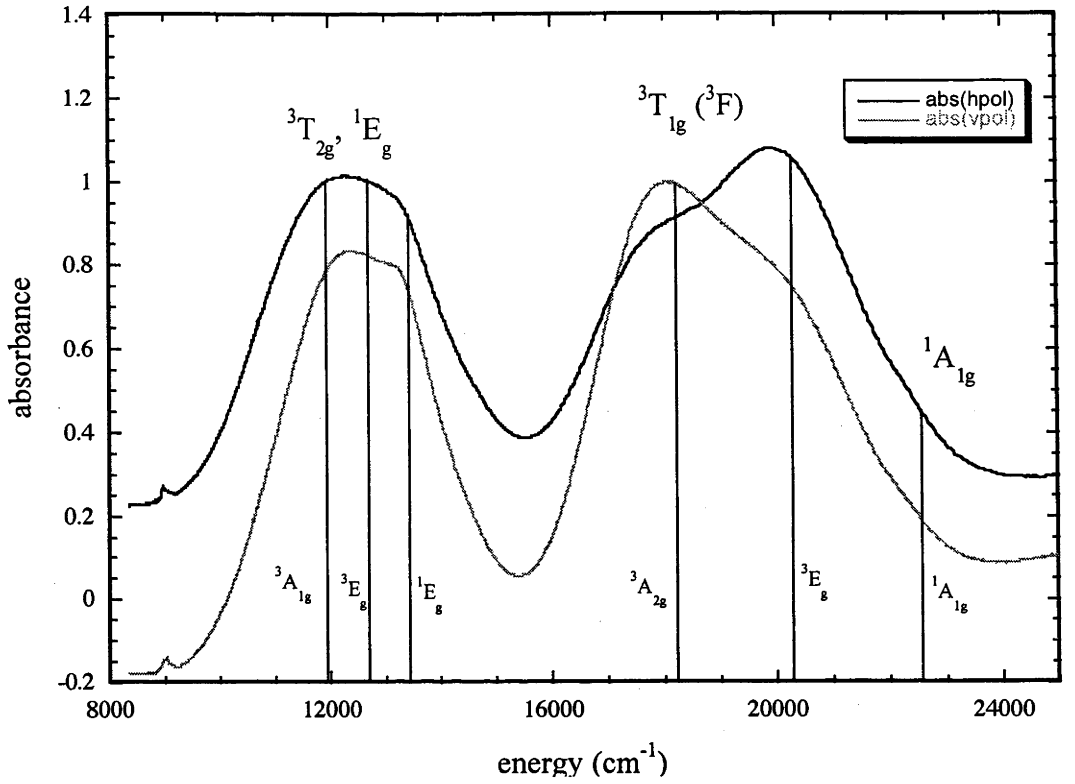


**Figure 6.8 Absorption spectrum of $[Ni(HCPz_3)_2](NO_3)_2$ (001 face, 295 K)**

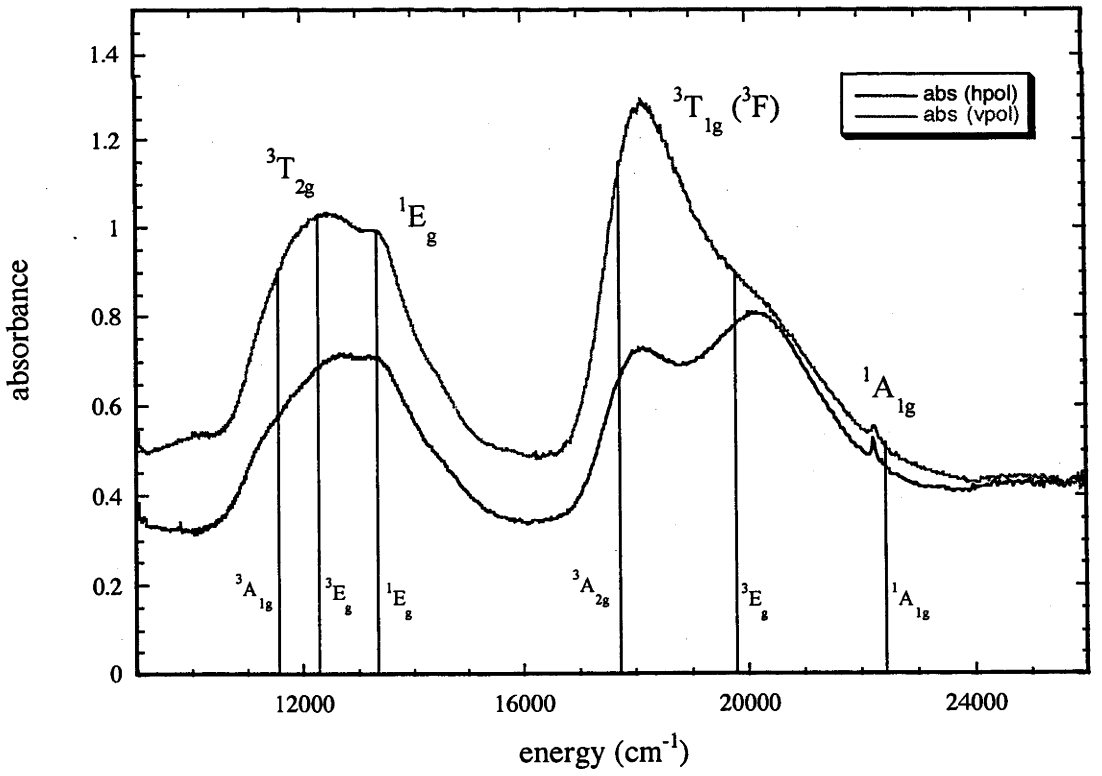


**Figure 6.9 Absorption spectrum of $[Ni(HBPz_3)_2]$ (arbitrary face, 10 K)**

The value of Δ is smaller than the measured $^3T_{2g}$ band maximum because the vibronic electric dipole mechanism raises the band maximum to higher energy. For convenience, Δ = 11200 $cm^{-1}$ is chosen. It is recognised that this value is probably a slight overestimate of the true value. Similar problems are encountered for the remaining spectra.

The spectrum of $[Co(Pz)_6](NO_3)_2$ (figure 6.4) shows a broad peak around 10300 $cm^{-1}$ ($^4T_{2g}$) as well as a composite peak centred around 21500 $cm^{-1}$. The full ligand-field calculation in table 6.10 shows that the structure between 19000 and 22000 $cm^{-1}$ originates from the three octahedral states $^2T_{1g}$[b], $^4A_{2g}$ and $^4T_{1g}(^4P)$.

**Table 6.9: Observed and calculated energies for $[Ni(Pz)_6](NO_3)_2$**

| Parameter | | Observed value[a] | Calculated value[b] |
|---|---|---|---|
| Ground state zero-field splitting, $D(^3A_{2g})$ | | \|0.12\| | –0.123 |
| **Term energy** | | | |
| **$O_h$** | **$S_6$** | | |
| $^3T_{2g}$ | $^3E_g$ | ~11200 | 11005 |
| | $^3A_{1g}$ | | 11549 |
| $^1E_g$ | | 13515 | 13476 |
| $^3T_{1g}$[a] | $^3E_g$ | 17540 | 17573 |
| | $^3A_{2g}$ | | 18679 |
| $^1A_{1g}$ | | 22450 | 22713 |

[a] All values measured at 10 K

[b] B = 860, C = 3440 (4B), Δ = 11200, ζ = 584, k = 0.87 ν = 580 and ν' = 270 are the trigonal ligand field parameters estimated for the low temperature structure and for a negative sign of $D(^3A_{2g})$. All parameters have units of $cm^{-1}$, except k, which is dimensionless.

The first two sharp lines at 19570 and 20180 $cm^{-1}$ in the spectrum of $[Co(Pz)_6](NO_3)_2$ (table 6.10) occur in both capped and uncapped Co(II) complexes. The lower energy line is usually broader and sometimes displays more vibration fine structure. The calculations show that $^2T_{1g}$[b] has a large spin-orbit splitting of ~500 $cm^{-1}$ in the octahedral limit, with $G_g'$ lying below $E_{2g}'$. This multiplet is largely resistant to trigonal fields and the main result is a small splitting of $G_g'$, which is often not resolved, but

produces a broadening in the lineshape. Hence in the tables, these sharp lines are labelled using their representation in the octahedral double group.

The values of Δ, the Racah parameters B and C, the one-electron spin-orbit coupling parameter ζ and the orbital reduction factor k used in the calculations are given below tables 6.9-6.14. The methods used to determine these parameters are discussed in section 5.4.3.

The ligand field calculations show that for ζ = 0 (this enables the octahedral parentage of the Kramers doublets to be followed), the $^4A_{2g}$ state lies below the $^4T_{1g}(^4P)$ for $[Co(Pz)_6](NO_3)_2$. The order is reversed for the capped complexes, where the ratio Δ/B has increased from ~13 to ~15.

**Table 6.10: Observed and calculated energies for $[Co(Pz)_6](NO_3)_2$**

| Term energy | | Observed values[a] | Calculated values[b] |
|---|---|---|---|
| $O_h$ | $S_6$ | | |
| $^4T_{1g}$ ($^4F$) | | | 0, 106, 782, 1045, 1157, 1329 |
| $^2E_g$ | | | 6044 |
| $^4T_{2g}$ | $^4A_{1g}$ | 10310 | 10304 |
| | $^4E_g$ | | 10364 |
| $^2T_{1g}$[a] | | | 15099 |
| $^2T_{2g}$[a] | | | 15817 |
| $^2T_{1g}$[b] | $G_g'$ | 19570 | 19597 |
| | $E_{2g}'$ | 20180 | 20096 |
| $^4A_{2g}$ | | 20910 | 21298 |
| $^4T_{1g}(^4P)$ | $^4E_g$, $^4A_{2g}$ | 21710 | 22080 |
| **EPR g-values** | | | |
| $g_{\|\|}$ | | 2.25-2.50 | 2.30 |
| $g_\perp$ | | ~5.2 | 4.90 |

[a] All values measured at 10 K

[b] B = 840, C = 3360 (4B), Δ = 11000, ζ = 480, k = 0.90, ν = 580 and ν' = 270 (all values in $cm^{-1}$ except k)

The spectra of the capped metal complexes show two notable features (figures 6.5-6.9). Firstly, the cubic fields of the carbon-capped complexes are some 1300 $cm^{-1}$ larger than

those of the corresponding $[M(Pz)_6]^{2+}$ complexes, and approximately 400 $cm^{-1}$ larger than those of the boron-capped complexes (tables 6.11 and 6.12). These observations are consistent with the change in M-N bond length, e.g. $R_{M-N}$ = 2.125 Å for $[Ni(Pz)_6](NO_3)_2$, 2.093 Å for $[Ni(HBPz_3)_2]$ and 2.078 Å for $[Ni(HCPz_3)_2](NO_3)_2$.

**Table 6.11: Observed and calculated energies for $[Ni(HCPz_3)_2](NO_3)_2$**

| Parameter | | Observed | | Calculated[a] | Calculated[b] | Calculated[c] |
|---|---|---|---|---|---|---|
| | | 10 K | 295 K | | | |
| $D(^3A_{2g})$ | | Not measured | <\|0.66\| | +0.66 | +1.27 | +0.66 |
| $^3T_{2g}$ | $^3A_{1g}$ | ~11700 | ~11500 | 11754 | 12010 | 11936 |
| | $^3E_g$ | ~12600 | ~12300 | 12683 | 12845 | 12665 |
| $^1E_g$ | | ~13500 | ~13300 | 13432 | 13475 | 13431 |
| $^3T_{1g}$ | $^3A_{2g}$ | 18200 | 18050 | 17885 | 17869 | 18239 |
| | $^3E_g$ | 20700 | 19930 | 20538 | 20629 | 20281 |
| $^1A_{1g}$ | | 22290 | Not measured | 22506 | 22382 | 22555 |

[a]B= 840, C = 3360 (4B), Δ = 12500, ζ = 567, k = 0.85, ν = –1875 and ν' = –691 (all values are in $cm^{-1}$ except for the orbital reduction factor k)

[b]The calculation of Astley et al.[12] can be accurately reproduced with Δ = 12666, B = 800, C = 3500, ζ = 0, ν = –1735 and ν' = –848 $cm^{-1}$. Their calculation is extended by including ζ = 567 $cm^{-1}$ and k = 0.85.

[c]Ligand field parameters are the same as for calculation a except that ν = –1300 $cm^{-1}$, and ν' = –580 $cm^{-1}$. Calculation c reproduces the observed trigonal splitting $D(^3T_{1g}(^3F)) \approx 2000$ $cm^{-1}$ for 298 K.

Secondly, the trigonal fields are evident in the spectra of the capped complexes. The splitting of the $^3T_{1g}(^3F)$ band in the capped nickel complexes is clearly resolved and changes from ~2000 $cm^{-1}$ in $[Ni(HBPz_3)_2]$ (figure 6.9) to ~2500 $cm^{-1}$ in $[Ni(HCPz_3)_2](NO_3)_2$ (figure 6.7), when measured at low temperature. On warming to room temperature, the spectrum of $[Ni(HCPz_3)_2](NO_3)_2$ (figure 6.8) shows a moderate reduction in the splitting of the $^3T_{1g}(^3F)$ band. The peaks have also broadened with the increase in temperature. The spin-forbidden transition to the $^1A_{1g}(^1G)$ state is clearly resolved in the low temperature nickel spectra on the blue side of the $^3T_{1g}(^3F)$ peak. The transition to the $^1E_g$ state is observed in the form of a 'bump' at the high energy end of the band centred around 12500 $cm^{-1}$.

## Table 6.12: Observed and calculated energies for $[Ni(HBPz_3)_2]$

| Parameter | | Observed[a] | Calculated[b] |
|---|---|---|---|
| $D(^3A_{2g})$ | | <\|0.59\| | +0.59 |
| $^3T_{2g}$ | $^3A_{1g}$ | ~11500 | 11551 |
| | $^3E_g$ | ~12500 | 12278 |
| $^1E_g$ | | ~13400 | 13330 |
| $^3T_{1g}$ | $^3A_{2g}$ | 18130 | 17706 |
| | $^3E_g$ | 20170 | 19790 |
| $^1A_{1g}$ | | 22240 | 22431 |

[a]The value of $D(^3A_{2g})$ is measured from EPR spectrum at 295 K, whereas the excited state energies were taken from the absorption spectra measured at 10 K

[b]B= 840, C = 3360 (4B), $\Delta$ = 12100, $\zeta$ = 567, k = 0.85, $\nu$ = –1370 and $\nu'$ = –560 (all values are in $cm^{-1}$ except for k)

## Table 6.13: Observed and calculated energies for $[Co(HCPz_3)_2](NO_3)_2$

| Parameter | | Observed[a] | Calculated[c] | Calculated[d] |
|---|---|---|---|---|
| $^4T_{1g}(^4F)$ | $^4E_g$ | | 0, 192, 418, 675 | 0, 203, 436, 700 |
| | $^4A_{2g}$ | | 2768, 2878 | 2777, 2867 |
| $^2E_g$ | | | 4846 | 5793 |
| $^4T_{2g}$ | $^4E_g$ | ~12000 | 11884 | 11879 |
| | $^4A_{1g}$ | ~12700 | 12820 | 12623 |
| $^2T_{1g}$[a] | | | 14854 | 15674 |
| $^2T_{2g}$[a] | | | 15989 | 16786 |
| $^2T_{1g}$[b] | $\Gamma_8$ | 19950 | 19911 | 20700 |
| | $\Gamma_6$ | 20700 | 20303 | 21124 |
| $^4T_{1g}(^4P)$ | $^4E_g$ | ~22400 | 23003 | 23004 |
| | $^4A_{2g}$ | 23060 | 23482 | 23829 |
| $^4A_{2g}$ | | | 25041 | 25273 |
| $g_{\|\|}$ | | 8.52[b] | 8.53 | 8.60 |
| $g_\perp$ | | 0.79[b] | 0.71 | 0.68 |

[a]All values measured at 10 K

[b]From the EPR spectrum measured for a frozen methanol solution (see table 6.19 below).

[c]B = 820, C= 3280 (4B), $\Delta$ = 12300, $\zeta$ = 460, k = 0.863, $\nu$ = –1875 and $\nu'$ = –691 $cm^{-1}$

[d]The calculation of Astley et al.[12] can be accurately reproduced with B = 845, C = 3500, $\Delta$ = 12165, $\nu$ = –1556 and $\nu'$ = –971 and $\zeta$ = 0. Their calculation is extended by including $\zeta$ = 460 and k = 0.86.

The splitting of the spin-allowed bands in the capped cobalt compounds is smaller than for the nickel compounds (see tables 6.13 and 6.14). Comparing the $^4T_{2g} \leftarrow {}^4T_{1g}$ peaks of $[Co(HCPz_3)_2](NO_3)_2$ and $[Co(HBPz_3)_2]$, the trigonal splitting is more evident in the former spectrum. There is a difference of approximately 1100 $cm^{-1}$ between the main peak and its shoulder for $[Co(HCPz_3)_2](NO_3)_2$.

For the spectra of $[Co(HBPz_3)_2]$, the shoulder is barely visible. The shoulder is visible on the $^4T_{1g} \leftarrow {}^4T_{1g}$ peak for both spectra, although the symmetry of the peak is visibly greater for $[Co(HCPz_3)_2](NO_3)_2$ than for $[Co(HBPz_3)_2]$. In both of the capped cobalt complexes, the peak due to $\Gamma_8$ component of the transition to the $^2T_{1g}{}^b$ state shows splitting as a result of vibrations; this is particularly noticeable in the spectra of $[Co(HCPz_3)_2](NO_3)_2$.

**Table 6.14: Observed and calculated energies for $[Co(HBPz_3)_2]$**

| Parameter | | Observed[a] | Calculated[b] |
|---|---|---|---|
| $^4T_{1g}(^4F)$ | $^4E_g$ | | 0, 192, 414, 675 |
| | $^4A_{2g}$ | | 2195, 2295 |
| $^2E_g$ | | | 5072 |
| $^4T_{2g}$ | $^4E_g$ | 11670 | 11344 |
| | $^4A_{1g}$ | | 12035 |
| $^2T_{1g}{}^a$ | | | 14793 |
| $^2T_{2g}{}^a$ | | | 15756 |
| $^2T_{1g}{}^b$ | $\Gamma_8$ | 19880 | 19594 |
| | $\Gamma_6$ | 20510 | 20015 |
| $^4T_{1g}(^4P)$ | $^4E_g$ | 21950 | 22381 |
| | $^4A_{2g}$ | 22710 | 22885 |
| $^4A_{2g}$ | | | 23944 |
| $g_{\|\|}$ | | 8.35[a] | 8.38 |
| $g_\perp$ | | 1.00[a] | 1.01 |

[a]From the EPR spectrum measured for a frozen toluene solution (see table 6.19 below).

[b]B = 820, C= 3280 (4B), $\Delta$ = 11850, $\zeta$ = 460, k = 0.86, $\nu$ = –1370 and $\nu'$ = –560 $cm^{-1}$

### 6.4.2 EPR spectroscopy (nickel compounds)

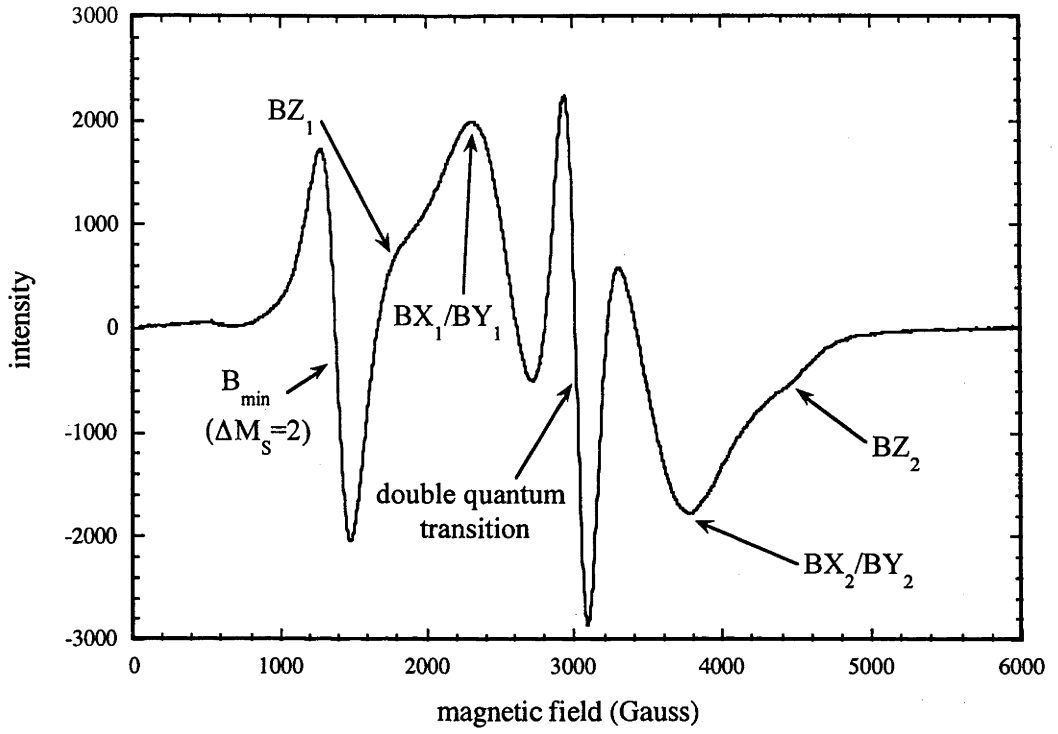


**Figure 6.10 Low temperature X-band EPR spectrum of pure $[Ni(Pz)_6](NO_3)_2$ powder**

At liquid helium temperatures, pure $[Ni(Pz)_6](NO_3)_2$ showed a good quality X-band EPR spectrum with all peaks observed between 0 and 5000 Gauss (figure 6.10), evidence of a small zero field splitting (ZFS). Most peaks were well resolved, with the exception of two (the $BZ_1$ and $BZ_2$) that are only seen as shoulders. The room temperature spectrum (figure 6.11) showed shifts in the peak positions, as well as some broadening. The double quantum transition is no longer visible. The measured and calculated peak positions are listed in table 6.15.

The peak positions were measured using the methods of Reedijk[28]. The $B_{min}$ and double quantum peaks were measured as the mean value of maximum and minimum. In principle, the $BX_1/BY_1$ and $BX_2/BY_2$ peaks are measured as the maxima of the derivative curve, however, when the derivative curve passes through the zero line a correction is necessary[29]. The correction is made in the direction of the band maximum (the zero point in the derivative curve) such that the cut-off from the top of the

derivative lines is as tall as the negative part of these curves. This was the convention used in this thesis. Table 6.15 shows the measured values for the peaks, as well as the values calculated using the method and parameters described below.

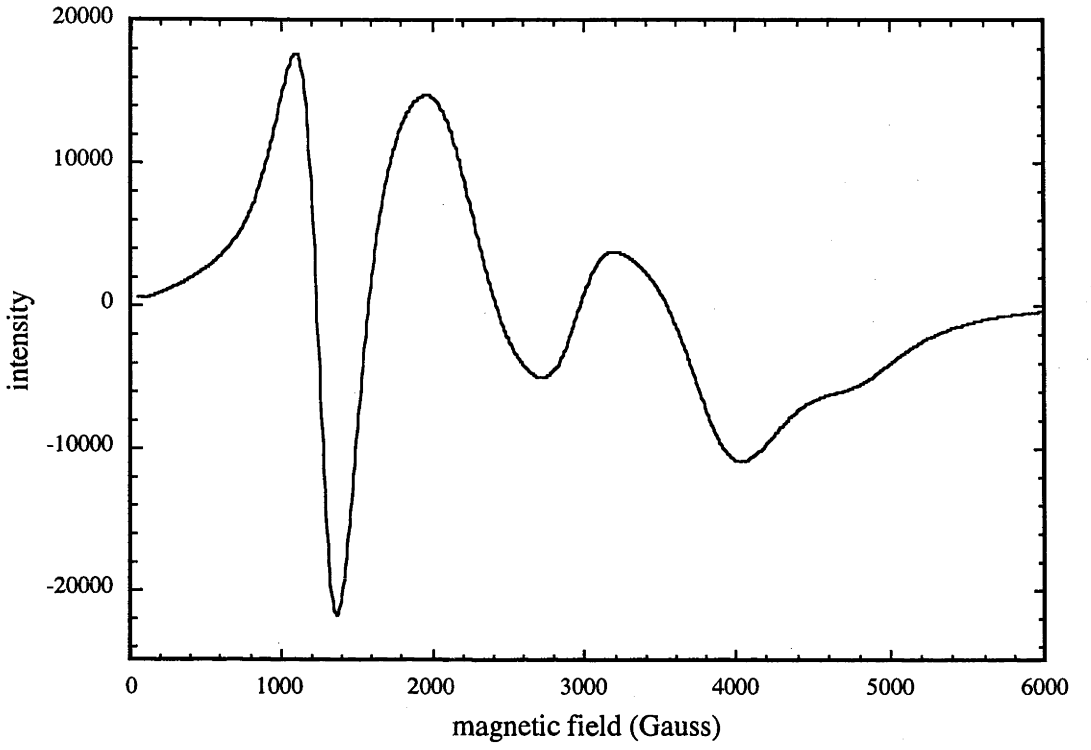


**Figure 6.11 Room temperature X-band EPR spectrum of $[Ni(Pz)_6](NO_3)_2$ powder**

**Table 6.15: Peak positions in the EPR spectra of $[Ni(Pz)_6](NO_3)_2$ (values in Gauss)**

| Peak | Figure 6.10 | | Figure 6.11 | |
|---|---|---|---|---|
| | Measured | Calculated | Measured | Calculated |
| $B_{min}$ | 1379 | 1389 | 1231 | 1252 |
| $BZ_1$ | ~1871 | 1914 | | 1521 |
| $BX_1/BY_1$ | 2454 | 2434 | 2184 | 2169 |
| double quantum | 3017 | 3018 | | 2957 |
| $BX_2/BY_2$ | 3581 | 3635 | 3799 | 3799 |
| $BZ_2$ | ~4485 | 4272 | ~4844 | 4665 |

The peaks located at a 'g-value' of 5.90 and 2.27/2.29 in the Q-band spectra of the two capped nickel compounds (figures 6.12 and 6.13) are assigned to the $B_{min}$ and double quantum transitions respectively. In all four spectra (figures 6.12-6.15) the peaks located at g = 2.02/2.05 and 0.57 are due to impurities. Test spectra of pure powdered $[Zn(HBPz_3)_2]$ and $[Zn(HCPz_3)_2](NO_3)_2$ were run to determine whether these peaks are of ligand origin. No peaks were seen in the spectra of the pure zinc compounds, indicating that the extraneous peaks do not result from the ligand. Peaks were observed at the same g-values in the X-band EPR spectra of $[Co(HCPz_3)_2](NO_3)_2$, particularly for the powder spectrum (figure 6.23). This suggests that the peaks are due to a metal ion impurity in the cobalt and nickel nitrate salts used to prepare the compounds.

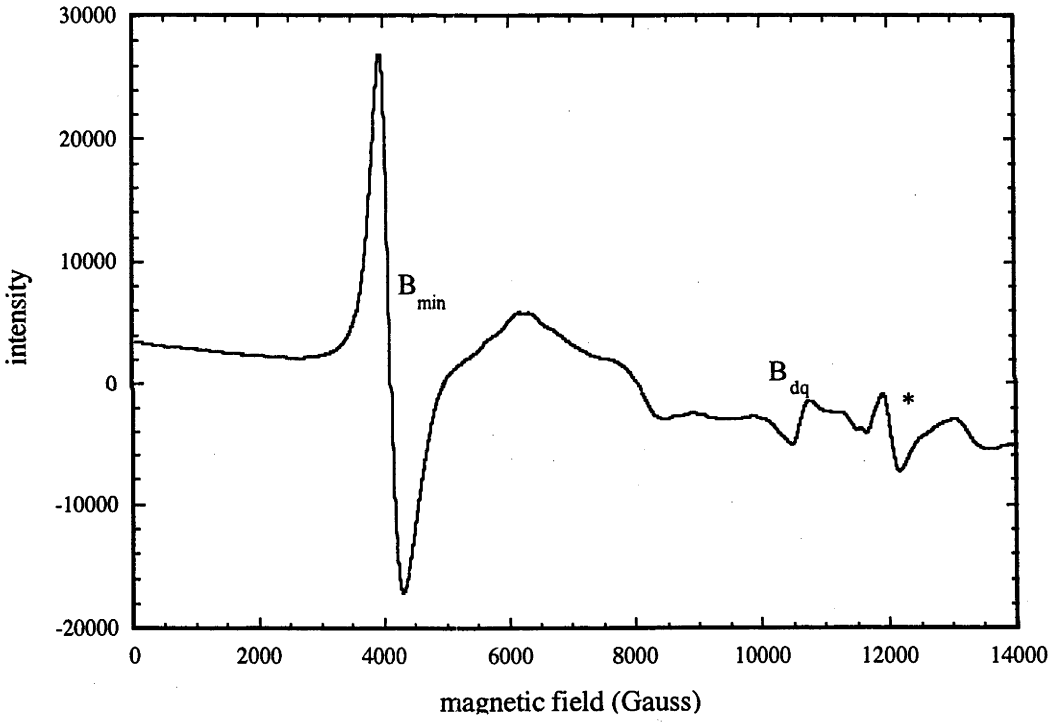


**Figure 6.12: Room temperature Q-band EPR spectrum of magnetically dilute $[Ni(HCPz_3)_2](NO_3)_2$ powder. The asterisk indicates an impurity peak.**

**Table 6.16: Peak positions in the EPR spectra of the capped pyrazolyl nickel compounds**

| Compound/spectrum | Peak positions (Gauss) | Peak positions (g-value) |
|---|---|---|
| $[Ni(HCPz_3)_2](NO_3)_2$, X-band | 3292±25*, 11903±25* | 2.05, 0.57 |
| $[Ni(HCPz_3)_2](NO_3)_2$, Q-band | 4110±25, 10609±25, 12037±25* | 5.90, 2.29, 2.02 |
| $[Ni(HBPz_3)_2]$, X-band | 3284±20* | 2.05 |
| $[Ni(HBPz_3)_2]$, Q-band | 4118±25, 10712±25 | 5.90, 2.27 |

*indicates an impurity peak

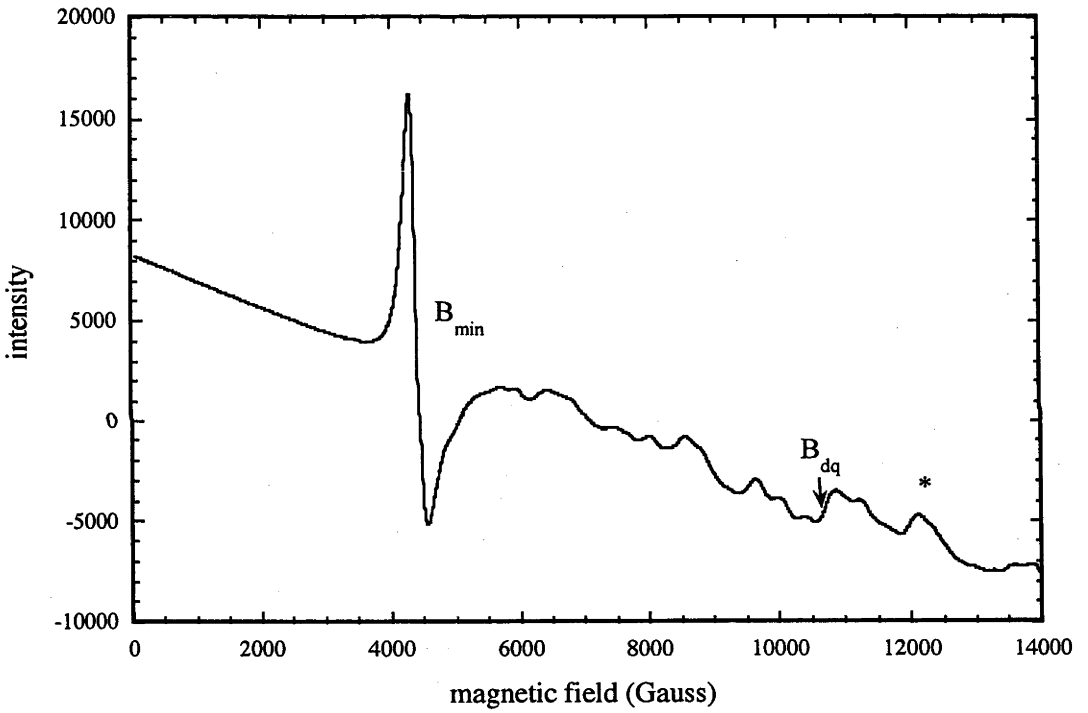


**Figure 6.13: Room temperature Q-band EPR spectrum of magnetically dilute $[Ni(HBPz_3)_2]$ powder. The asterisk indicates an impurity peak.**

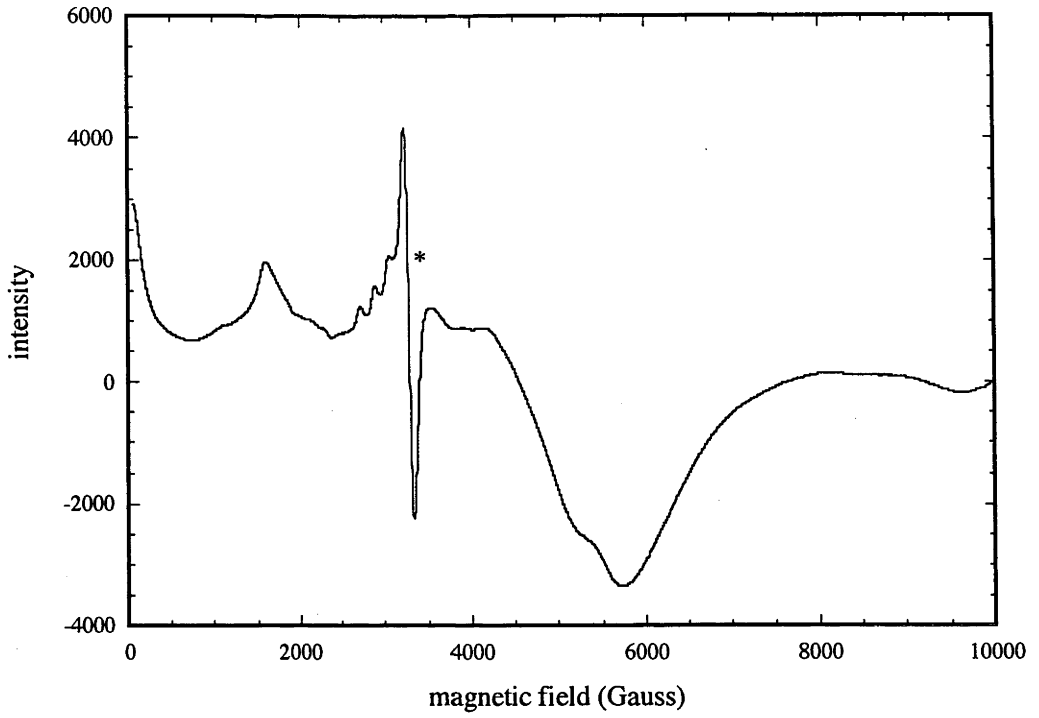


**Figure 6.14: X-band EPR spectrum of magnetically dilute $[Ni(HBPz_3)_2]$ powder (7.5 K). The asterisk indicates an impurity peak.**

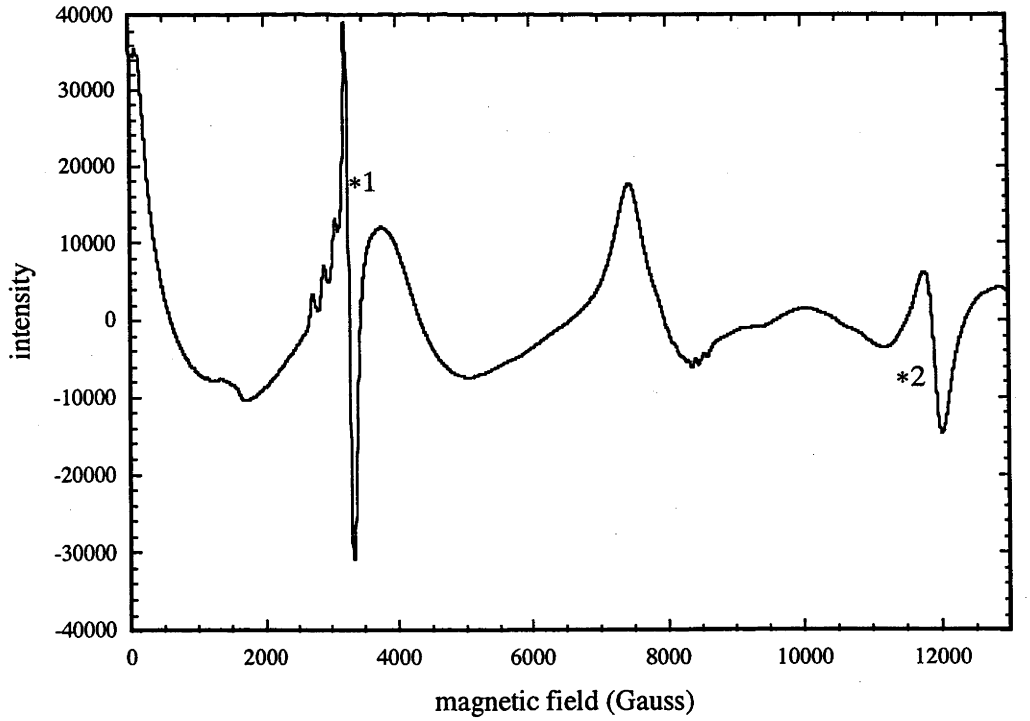


**Figure 6.15: X-band EPR spectrum of magnetically dilute $[Ni(HCPz_3)_2](NO_3)_2$ powder (7.5 K). The asterisks indicate impurity peaks.**

The methods of Reedijk for analysing powder nickel EPR spectra are employed in the analysis[28]. Reedijk's theories are adapted from methods used for analysing EPR spectra of randomly-oriented biradicals, which are also S = 1. These methods are applicable when the axes of the g tensor and the zero-field splitting tensor D are coincident. Up to eight transitions can be observed, six of which are $\Delta M_S = 1$ transitions. The final two are the $\Delta M_S = 2$ line ($B_{min}$) and the double quantum transition. The equations for these transitions are given below (6.1)-(6.8):

$$BX_1 = \frac{2.0023}{g_x}\sqrt{[(B_0 - D + E)(B_0 + 2E)]} \qquad BY_1 = \frac{2.0023}{g_y}\sqrt{[(B_0 - D - E)(B_0 - 2E)]}$$

$$BZ_1 = \frac{2.0023}{g_z}\sqrt{[(B_0 - D)^2 - E^2]} \qquad BX_2 = \frac{2.0023}{g_x}\sqrt{[(B_0 + D - E)(B_0 - 2E)]}$$

$$BY_2 = \frac{2.0023}{g_y}\sqrt{[(B_0 + D + E)(B_0 + 2E)]} \qquad BZ_2 = \frac{2.0023}{g_z}\sqrt{[(B_0 + D)^2 - E^2]}$$

$$B_{min} = \frac{2.0023}{g_{min}}\sqrt{[B_0^2/4 - D^2/3 - E^2]} \qquad B_{dq} = \frac{2.0023}{g_{av}}\sqrt{[B_0^2 - D^2/3 - E^2]}$$

(6.1)-(6.8)

where $g_x$, $g_y$, $g_z$ are the Cartesian g-values, $B_0$ is the magnetic field in Gauss corresponding to the transition of a free electron (g = 2.0023) at the frequency used, D is the axial zero field splitting parameter in Gauss, E is the rhombic zero field splitting parameter in Gauss.

**Table 6.17: Zero-field splitting parameters for the nickel compounds studied**

| Compound | D ($cm^{-1}$) | $g_{av}$ |
|---|---|---|
| $[Ni(Pz)_6](NO_3)_2$ (7 K)[a] | \|0.12\| | 2.18 |
| $[Ni(Pz)_6](NO_3)_2$ (295 K)[a] | \|0.16\| | 2.18 |
| $[Ni(HBPz_3)_2]$ (295 K)[a] | <\|0.60\| | 2.15 |
| $[Ni(HCPz_3)_2](NO_3)_2$ (295 K)[a] | <\|0.67\| | 2.15 |
| $[Ni(5MePz)_6](ClO_4)_2$ (295 K)[b] | \|0.41\| | 2.178 |
| $[Ni(Pz)_6](BF_4)_2$:$Zn^{2+}$ (295 K)[c] | \|0.168\| | 2.185 |
| $[Mn(Pz)_6](BF_4)_2$:$Zn^{2+}$ (295 K)[c] | +0.0284 | 2.00 |

[a]This work. [b]Collison et al.[16]. [c]Anthonisamy et al.[30]

The $[Ni(Pz)_6]^{2+}$ cation in $[Ni(Pz)_6](NO_3)_2$ has $S_6$ site symmetry, so is axially symmetric. As a result, $g_x = g_y = g_\perp$, $g_z = g_\parallel$ and $E = 0$. Therefore, $BX_1 = BY_1$ and $BX_2 = BY_2$, and we expect a maximum of six peaks. All six peaks are observed, however the $BZ_1$ peak is a poorly resolved shoulder on the $BX_1/BY_1$ and $BZ_2$ is a shoulder on $BX_2/BY_2$.

By inspection of the spectra, all peaks are located below 5000 Gauss. Comparison with powder spectra observed by Reedijk and Nieuwenhuijse[28] for other axially symmetric $NiN_6$ compounds suggests that $D < 0.25$ $cm^{-1}$. This would result in g-value anistropy ($|g_\parallel - g_\perp|$) of less than 0.0016 (see equation 1.4). At the X-band frequency used, and the g-value subsequently determined, this anisotropy would result in peak separations of less than 2.3 Gauss, which would be unresolvable given the linewidths observed (several hundred Gauss). Therefore, within experimental error, $g_\parallel = g_\perp = g$ (and $g_{min} = g_{av} = g$). As a result, there are only two variables to be determined from the spectra and equations 6.1-6.8, g and D. Using, equations 6.4 and 6.8. values for g and D were determined from the observed values of the minimum-field and double quantum transitions for both temperatures studied. As a confirmation, SigmaPlot, a commercial mathematical modelling and graphing software package (SPSS Inc, Chicago, Illinois), was used to calculate the expected energies for all the EPR transitions from equations 6.1-6.8, based on a number of different values of g and D, i.e. a fitting procedure was employed. The calculated values are given in table 6.15 above.

The observed zero field splitting parameter for $[Ni(Pz)_6](NO_3)_2$ is small (table 6.17). A temperature dependence is observed, with the zero field splitting parameter decreasing as the temperature is decreased, suggesting that the complex is less trigonally-distorted at low temperature. Unfortunately, there is no low temperature crystal structure to verify this. By way of comparison, in the crystal structure of $[Co(HCPz_3)_2](NO_3)_2$ at room temperature and 173 K (see table 4.3), a slight increase in the trigonal cone angle from 50.9° to 51.1° is observed as the crystal is cooled, showing that the structure becomes a little less trigonally distorted at low temperature (the errors in the crystal structures are of the order of 0.1°).

The spectra of the capped pyrazolyl nickel compounds $[Ni(HBPz_3)_2]$ and $[Ni(HCPz_3)_2](NO_3)_2$ are of lower quality than those of $[Ni(Pz)_6](NO_3)_2$. For both $[NiHCPz_3)_2](NO_3)_2$ and $[Ni(HBPz_3)_2]$, the $B_{min}$ and double quantum transitions are visible in the room temperature Q-band. Using equations 6.4 and 6.8, values for g and

D were calculated (see table 6.17) using the procedures discussed above for $[Ni(Pz)_6](NO_3)_2$. Again, by the arguments discussed for $[Ni(Pz)_6](NO_3)_2$ above, at the D values determined, g-value anisotropy will be around 0.004. At the subsequently determined g-value of 2.15, for a Q-band spectrum peaks shifts due to this anisotropy will be of the order of 20 Gauss, much less than the observed linewidths. Therefore, the assumption of isotropic g-values within experimental error can again be made. Literature values for three other hexakis pyrazolyl complexes are also presented (table 6.17).

As the $Ni^{2+}$ ion in the capped pyrazolyl compounds lies on a site of $C_1$ or $C_i$ symmetry, the rhombic splitting parameter E will be non-zero. However, insufficient information is available to determine E. Therefore, the D′ values in table 6.17 will include a rhombic as well as an axial component, i.e. $D' = (D^2 + 3E^2)^{1/2}$, which represents an upper limit for D. Further, the sign of D′ cannot be determined, since only the double quantum and $B_{min}$ peaks were observed, and the position of these peaks does not depend on the sign of D′. As can be seen, the D′ parameter for $[Ni(HCPz_3)_2](NO_3)_2$ is about 10% larger than that for $[Ni(HBPz_3)_2]$. This is expected, as $[Ni(HCPz_3)_2](NO_3)_2$ shows a greater degree of trigonal distortion than $[Ni(HBPz_3)_2]$, with the trigonal cone angle being 52.47° for the borate, compared with 51.55° for the carbon-capped compound. It should be noted however that since E has not been quantified for either complex, differences in this parameter may account for some of the difference between the two values of D′.

### 6.4.3 EPR spectroscopy (cobalt compounds)

Pure $[Co(Pz)_6](NO_3)_2$ shows an axial high spin $Co^{2+}$ spectrum (figure 6.16) , with $g_{\|} < g_{\perp}$. The peaks are broad, and difficult to measure accurately. Large linewidths of $g_{\|}$ and $g_{\perp}$ indicate a broad inhomogeneous distribution of trigonal species, which may include rhombically-distorted species. The crystal structure of $[Co(Pz)_6](NO_3)_2$ is unknown. Although it might be expected to be isostructural with $[Ni(Pz)_6](NO_3)_2$ at room temperature, it is quite possible that a phase transition to lower symmetry occurs on cooling. Unfortunately, no diamagnetic host (e.g. $[Zn(Pz)_6](NO_3)_2$) is available to dope the compound into to sharpen the spectrum.

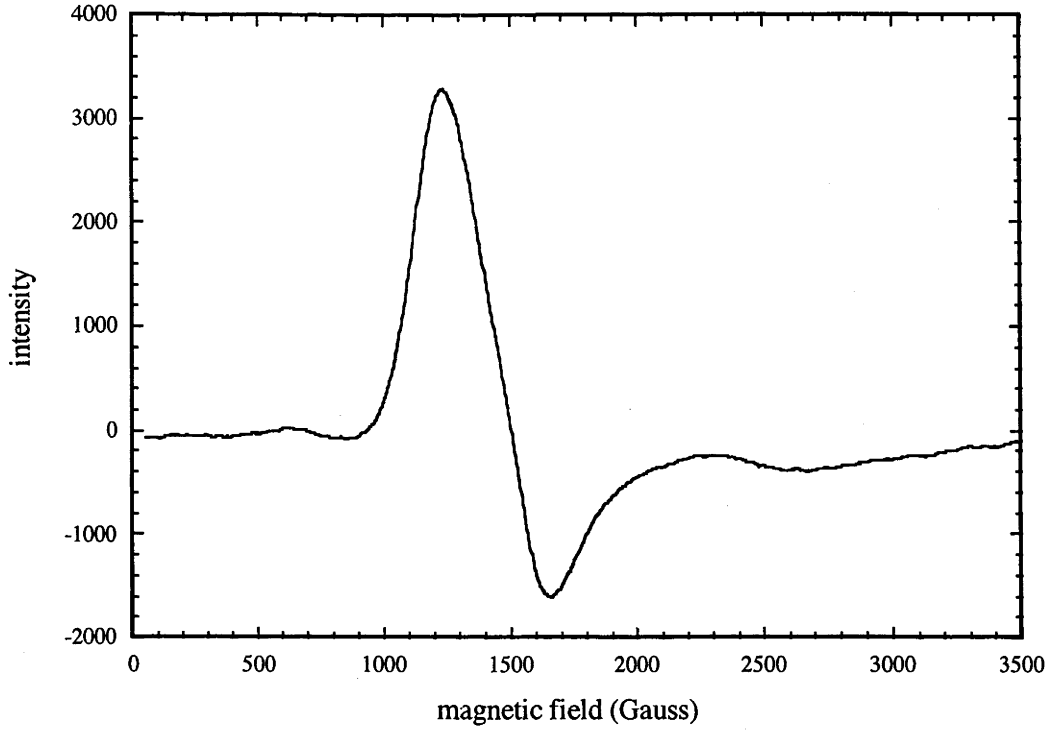


**Figure 6.16: Low temperature X-band EPR spectrum of pure $[Co(Pz)_6](NO_3)_2$ powder**

The spectrum of the monopyrazolyl compound $[Co(Pz)_6](NO_3)_2$ shows an axial EPR signal with $g_{\|} < g_{\perp}$, which is as expected for a trigonally distorted octahedron where the main distortion is trigonal *compression* (increase of the cone angle). The peak positions can only be determined approximately due to the broadness and asymmetry of the spectral features. Unfortunately, there appears to be no isomorphic diamagnetic host (e.g. $[Zn(Pz)_6](NO_3)_2$) to dope this compound into and give sharper peaks. The EPR spectrum was measured for ~3%$Co^{2+}$ in $[Ni(Pz)_6](NO_3)_2$. Unfortunately, all the cobalt peaks were obliterated by those due to nickel.

The EPR spectra of magnetically dilute $[Co(HCPz_3)_2](NO_3)_2$ and $[Co(HBPz_3)_2]$ powders showed a highly axial spectrum with strong g-value anisotropy, consistent with the spectra observed by Jesson[20]. Hyperfine splitting is well resolved for the $g_{\|}$ band. Rhombic distortion is evident, especially for the $g_{\|}$ band. The spectra of the frozen solutions showed essentially the same g-values as the magnetically dilute powders, without the rhombic distortion. This is expected, as the solution environment allows the complex to take up its 'natural' configuration unconstrained by the crystal lattice.

**Table 6.18 Peak positions in the cobalt EPR spectra**

| Sample | Peak positions (Gauss) |
|---|---|
| pure $[Co(Pz)_6](NO_3)_2$ powder | ~1300 ($g_\perp$), ~2700 ($g_\parallel$) |
| frozen toluene solution of $[Co(HBPz_3)_2]$ | 481, 572, 665, 758, 850, 943, 1036, 1129, 6650 ($g_\perp$) |
| magnetically dilute $[Co(HBPz_3)_2]$ powder | 494, 531, 580, 652, 758, 855, 952, 1055, 1148, 1262, 6695 ($g_\perp$) |
| frozen methanol solution of $[Co(HCPz_3)_2](NO_3)_2$ | 460*, 482, 517, 554*, 585, 610, 649*, 677, 706, 743*, 772, 803, 839*, 870, 895, 933*, 964, 992, 1028*, 1060, 1086, 1124*, 1152, 3288#, 8540 ($g_\perp$), 11861# |
| magnetically dilute $[Co(HCPz_3)_2](NO_3)_2$ powder | 482, 580, 678, 775, 883, 1006, 1119 3287#, 8150 ($g_\perp$), 11828# |

* indicates the main peak

# indicates an impurity peak

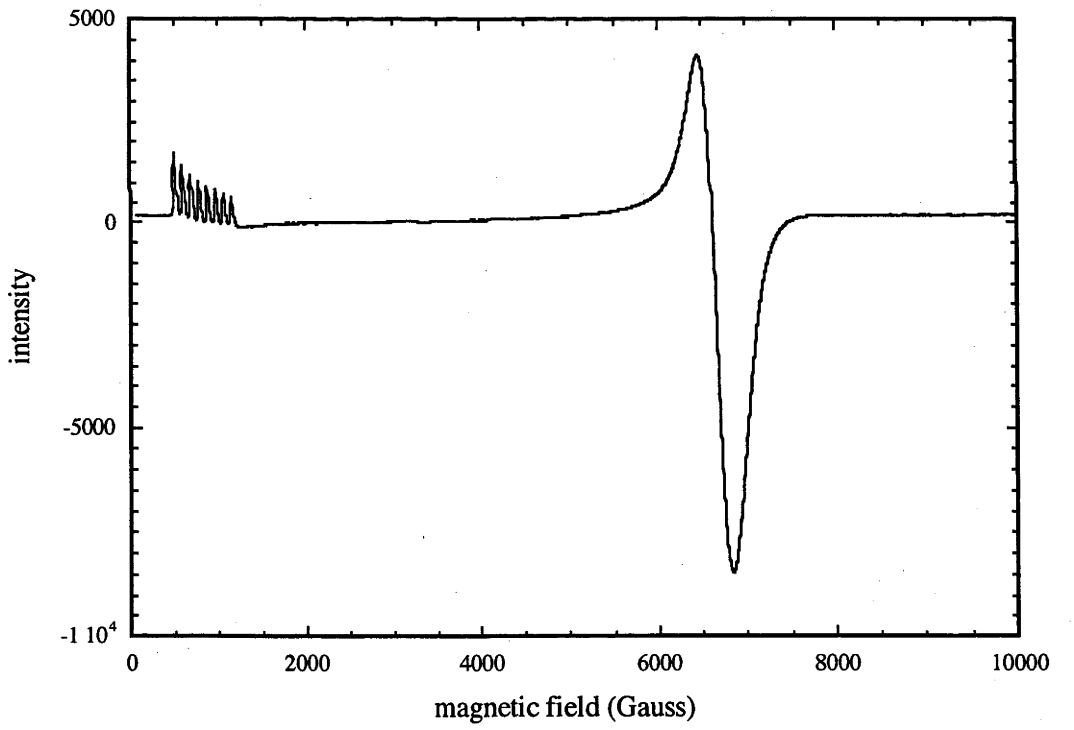


**Figure 6.17: EPR spectrum of a frozen 0.01 M toluene solution of $[Co(HBPz_3)_2]$**

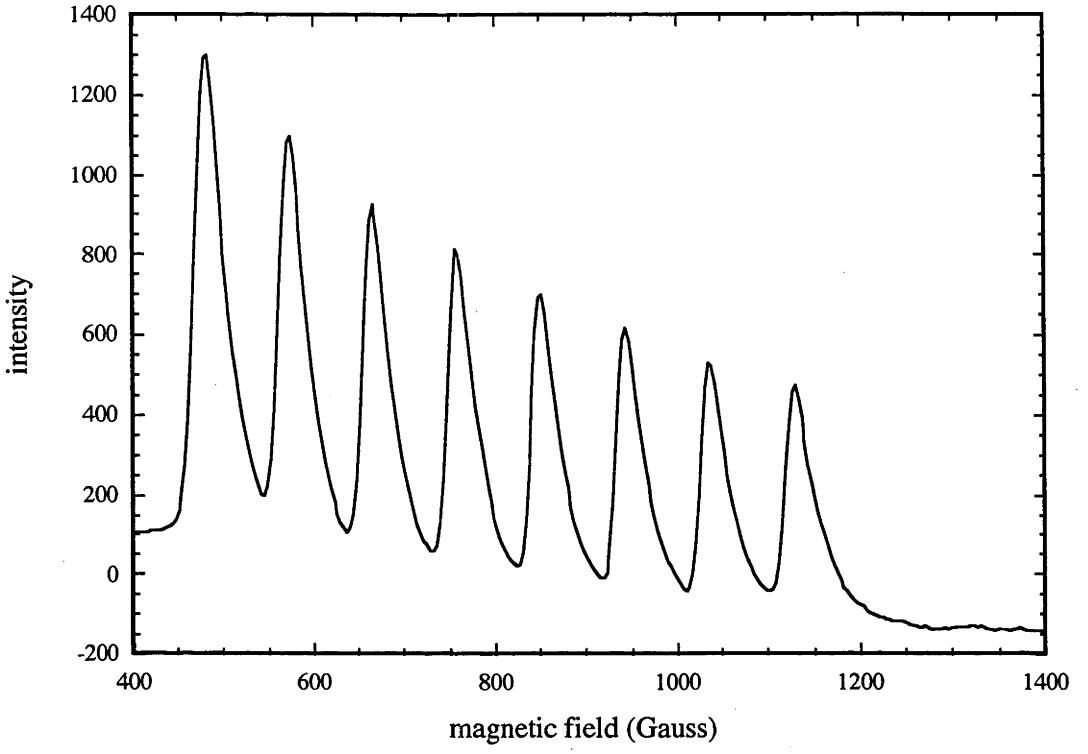


**Figure 6.18: EPR spectrum of a frozen toluene solution of $[Co(HBPz_3)_2]$ ($g_{||}$ region)**

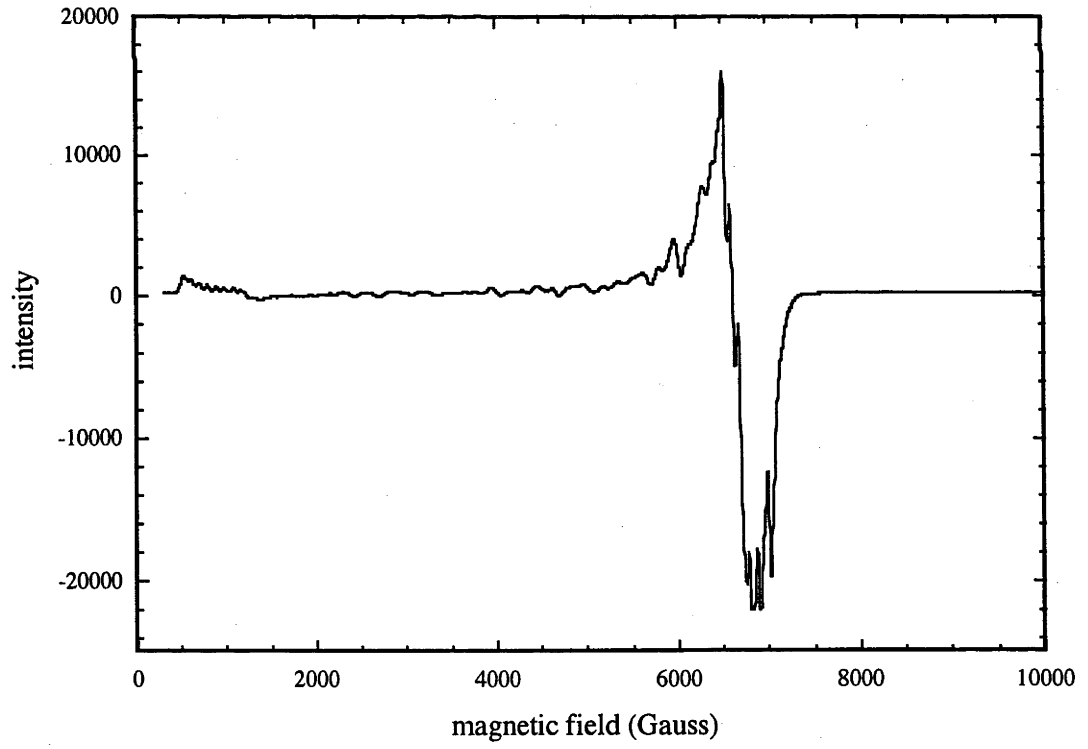


**Figure 6.19: X-band EPR spectrum of magnetically dilute $[Co(HBPz_3)_2]$ powder**

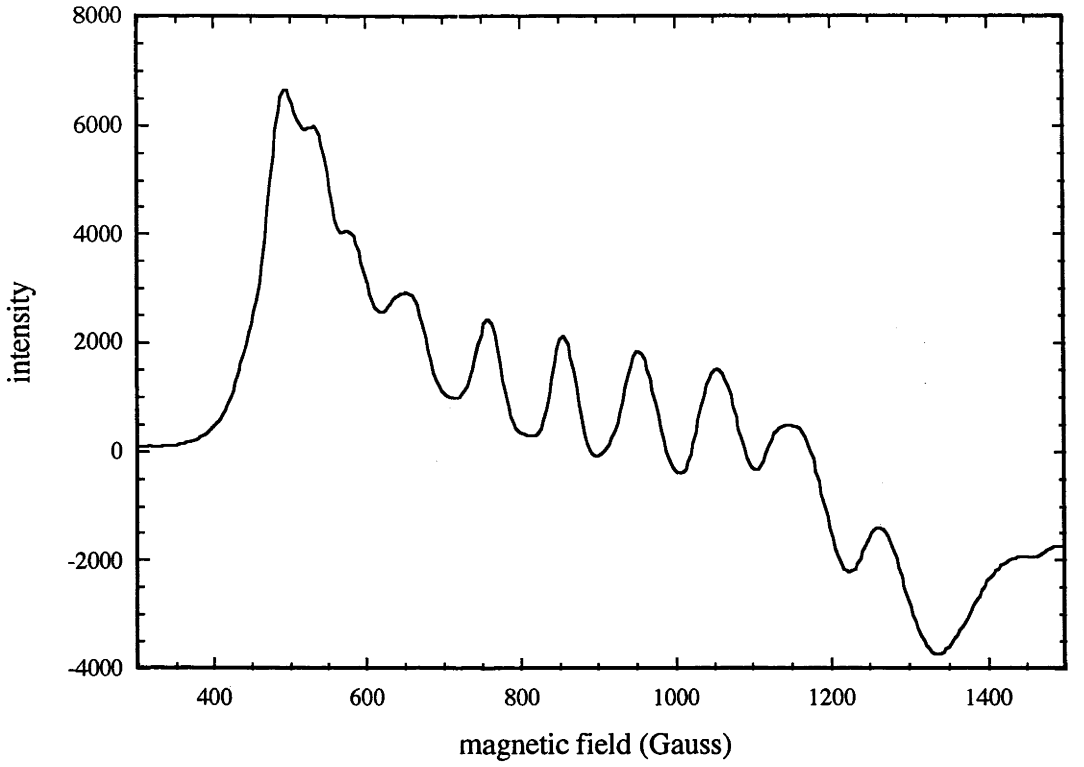


**Figure 6.20: EPR spectrum of magnetically dilute $[Co(HBPz_3)_2]$ powder ($g_{||}$ region)**

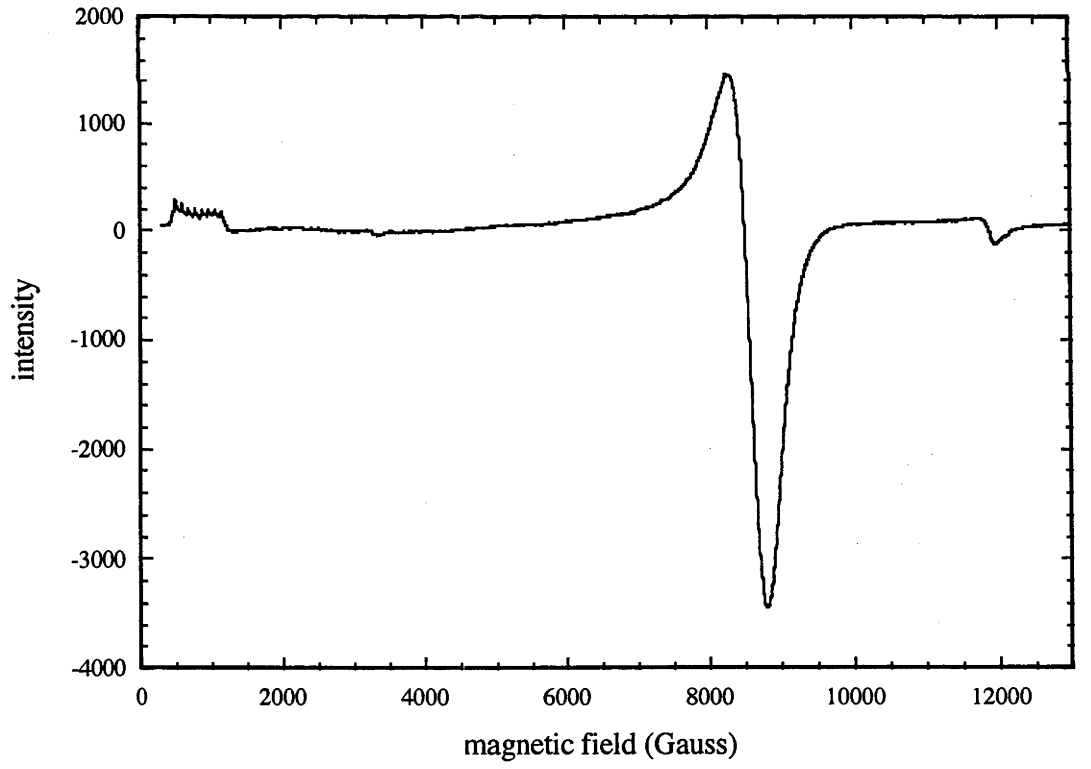


**Figure 6.21: EPR spectrum of frozen methanol solution of $[Co(HCPz_3)_2](NO_3)_2$**

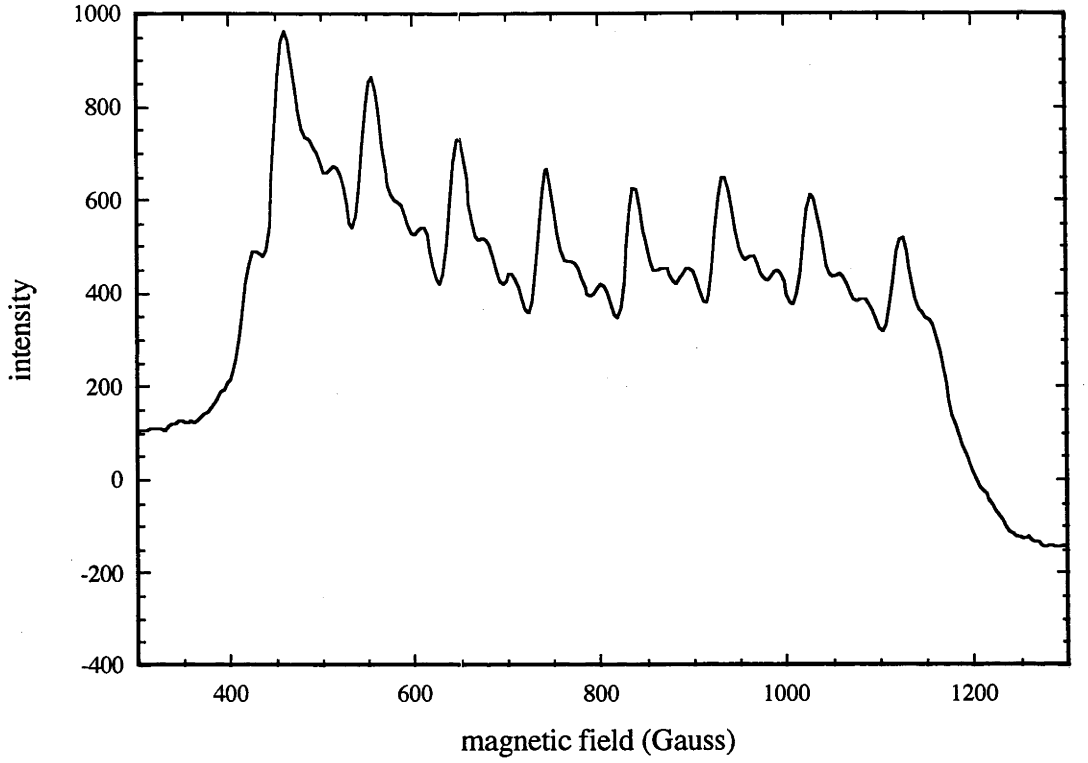


**Figure 6.22: EPR spectrum of $[Co(HCPz_3)_2](NO_3)_2$ solution ($g_{||}$ region)**

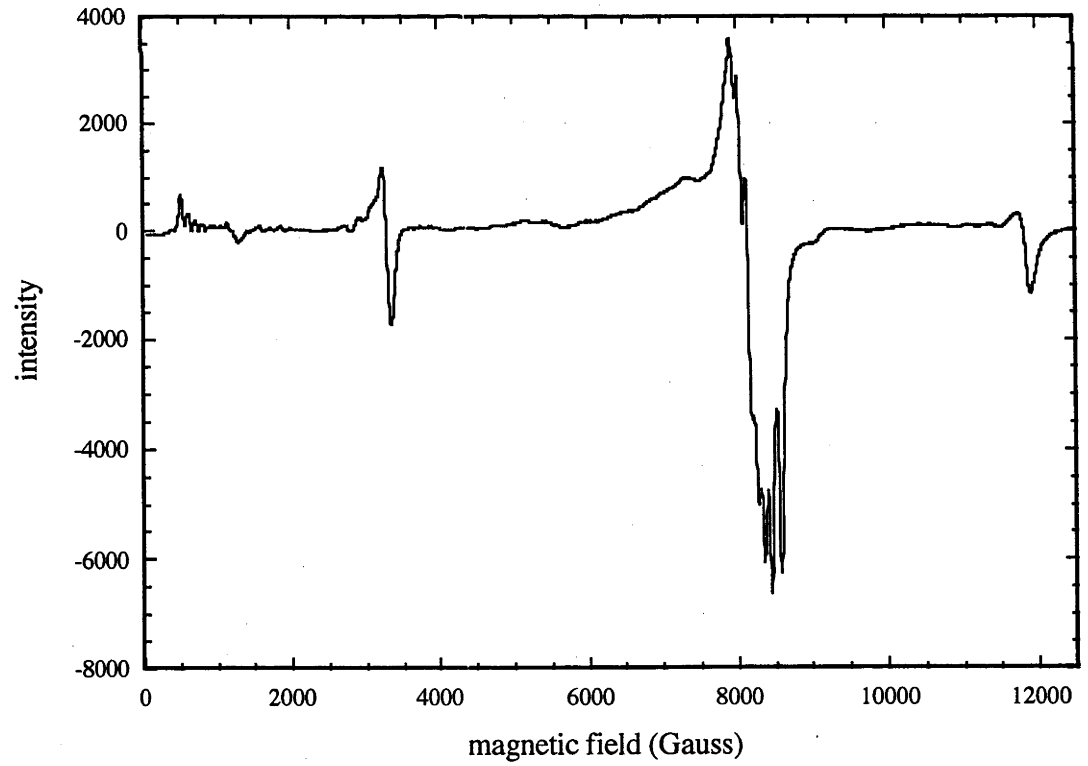


**Figure 6.23: EPR spectrum of magnetically dilute $[Co(HCPz_3)_2](NO_3)_2$ powder**

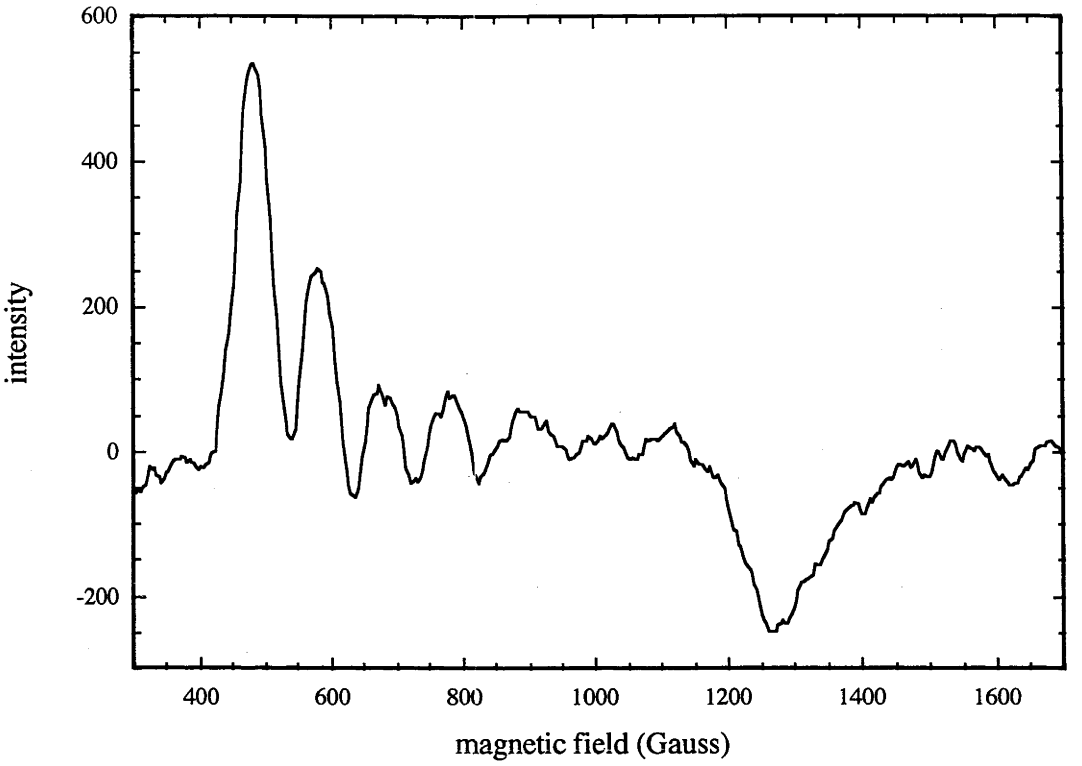


**Figure 6.24: EPR spectrum of magnetically dilute $[Co(HCPz_3)_2](NO_3)_2$ powder ($g_{||}$ region)**

**Table 6.19 Key g-values ($g_{||}$ and $g_{\perp}$), and axial hyperfine splitting parameters ($A_{||}$) for the cobalt pyrazolyl compounds**

| Sample | $g_{\|\|}$ | $g_{\perp}$ | $A_{\|\|}$ ($cm^{-1}$) |
|---|---|---|---|
| pure $[Co(Pz)_6](NO_3)_2$ powder | ~2.52 | ~4.66 | - |
| magnetically dilute $[Co(HBPz_3)_2]$ powder | 8.31±0.04 | 1.01 | 0.036±0.08 |
| frozen toluene solution of $[Co(HBPz_3)_2]$ | 8.38±0.04 | 1.01 | 0.0363±0.005 |
| frozen methanol solution of $[Co(HCPz_3)_2](NO_3)_2$ | 8.52±0.04 | 0.79 | 0.0378±0.005 |
| magnetically dilute $[Co(HCPz_3)_2](NO_3)_2$ powder | 8.14±0.04 | 0.83 | 0.040±0.06 |

All spectra of the scorpionate pyrazolyl complexes, $[Co(HBPz_3)_2]$ and $[Co(HCPz_3)_2](NO_3)_2$, both magnetically dilute powders and the frozen solutions, are

highly anisotropic with the $g_{\|}$ and $g_{\perp}$ values differing significantly, indicative of the strong trigonal field. In these compounds, $g_{\|} > g_{\perp}$, as expected for trigonally elongated octahedral complexes. The observed g-values are consistent with those observed previously for magnetically dilute powders of these two compounds[20]. Changing from magnetically dilute powder to frozen solution does not result in a great change in the g-values. The main difference observed is that the $g_{\perp}$ peak is much smoother in the frozen solution spectra, without all the side peaks and shoulders observed for magnetically dilute powders. The side peaks are due to hyperfine splitting and rhombic distortion (recall that the $CoN_6$ coordination sphere does not have perfect trigonal $D_{3d}$ symmetry). In the frozen solution, the complexes will not be subject to lattice forces and will be free to adopt their preferred conformation. It is noticeable, however, that the frozen solution spectrum of $[Co(HCPz_3)_2](NO_3)_2$ in particular shows two series of less intense subsidiary peaks in the hyperfine ($g_{\|}$) region. Each of these two series shows a hyperfine splitting very close in magnitude to that of the main series (see table 6.19 above). This suggests the presence of different sites for the metal complexes in the frozen solution.

Once again, the different values observed for $[Co(HBPz_3)_2]$ and $[Co(HCPz_3)_2](NO_3)_2$ can be compared and discussed in terms of the difference in trigonal field strength. For the frozen solutions, the values of $g_{\|}$ and $g_{\perp}$ were 8.38 and 1.01 for $[Co(HBPz_3)_2]$ and 8.52 and 0.79 for $[Co(HCPz_3)_2](NO_3)_2$, i.e. there is a greater difference in the g-values for the pyrazolyl methane compound than for the pyrazolyl borate, consistent with a stronger trigonal field. The powder spectra of $[Co(HBPz_3)_2]$ gave very similar g-values to the frozen solution spectra of the same compound. For $[Co(HCPz_3)_2](NO_3)_2$, the $g_{\|}$ value is significantly lower for the powder spectrum than for the frozen solution spectrum. Further, the value measured here is significantly lower than that measured by Jesson (see table 6.1). This suggests a measurement error, perhaps as a result of insufficient cobalt concentration in the magnetically dilute powder. The impurity peaks seen in the EPR spectra of the capped nickel compounds are also seen for $[Co(HCPz_3)_2](NO_3)_2$, particularly in the powder spectrum.

By contrast, the EPR spectrum of the monopyrazolyl cobalt compound $[Co(Pz)_6](NO_3)_2$, though the peaks are broad, shows the reverse order for the g-values, i.e. $g_{\|} < g_{\perp}$. Although the structure of $[Co(Pz)_6](NO_3)_2$ is not known at any temperature, the structure of $[Ni(Pz)_6](NO_3)_2$ is known[19] to show trigonal compression rather than

elongation. The reverse ordering of the g-values when compared with the capped pyrazolyl complexes suggests a trigonal field of opposite sense to those in the capped complexes, which would be consistent with a trigonally-compressed structure rather than an elongated one. As mentioned above, a crystal structure of $[Co(Pz)_6](NO_3)_2$, preferably at low temperature as well as room temperature, is necessary to make further progress on this compound.

### 6.4.4 Angular overlap model calculations

In the initial application of the AOM to $[M(Pz)_6]^{2+}$ ions, it was assumed that there is no tilting within the plane of the pyrazolyl ligand, and hence $e_{\sigma\pi}(\|) = 0$. The analysis failed when it was extended to three hexakis pyrazolyl nickel ($[Ni(Pz)_6]^{2+}$) complexes. The complexes are $[Ni(Pz)_6](NO_3)_2$, which was studied spectroscopically in this thesis, and $[Ni(5MePz)_6](ClO_4)_2$ and $[Ni(Pz)_6](BF_4)_2$, for which the EPR spectra were measured by Collison et al.[16] and Anthonisamy et al.[30] respectively.

Evidently, the assumption that there is an effective local symmetry plane perpendicular to the plane of the pyrazolyl ligands is incorrect. Removal of this assumption requires the introduction of extra bonding parameters (see chapter 4) and the AOM energy matrix for pyrazole in trigonal $[M(Pz)_6]^{2+}$ ions contains five bonding parameters, $e_\sigma$, $e_\pi(\perp)$, $e_\pi(\|)$, $e_{\sigma\pi}(\perp)$ and $e_{\sigma\pi}(\|)$*. It is assumed that for fixed values of $t_{\|}$ and $t_\perp$, the parameters for $e_\sigma$, $e_\pi$, and $e_{\sigma\pi}$ are the same for all three monodentate pyrazolyl complexes. This assumption ignores the small differences (<1.5%) in the Ni-N bond lengths (see table 4.2) amongst the three nickel monopyrazolyl complexes considered.

For the $[Ni(Pz)_6]^{2+}$ complex ions, the parameters $\Delta = 11300$, $B = 870$, $C = 4B$, $\zeta = 584$ $cm^{-1}$ and $k = 0.87$ were employed. The spin-orbit coupling constant $\zeta$ and the orbital reduction factor k were determined from the ground state g-value (2.18) using the equation of Ballhausen[31,32] (equation 6.9), and the approximation $\zeta \approx k\zeta_0$ where $\zeta_0$ (668 $cm^{-1}$ for $Ni^{2+}$, obtained from Bendix, Brorson and Schaeffer[33]) is the free ion value. .The remaining parameters were obtained from the measured spectrum of

* The angular-overlap parameters $e_\pi(\perp)$ and $e_\pi(\|)$ used here are alternatives to the notation introduced in chapter 4. The 'parallel' parameters denoted by $\|$ refer to the plane of the ligand (the x'z' plane), while the 'perpendicular parameters denoted by $\perp$ apply to the y'z' plane (see figure 4.1).

$[Ni(Pz)_6](NO_3)_2$ (figure 6.3). The values of the Racah parameters B and C were calculated from the experimental transition energies using QuickBasic programs written by Dr Lucjan Dubicki (see discussion in section 5.4.3).

$$g = 2.0023 + \frac{4\zeta_0 k^2}{\Delta} \quad (6.9)$$

The signs of the zero-field splitting parameters (D) are not known for any of the $[Ni(Pz)_6]^{2+}$ complexes. In these cases, the observed value of D can be fitted using two series of solutions, corresponding to the two possible signs of D. Each series is a function of $\nu$ and $\nu'$. In the case of $[Ni(Pz)_6](BF_4)_2$, additional information is obtained from the EPR study of $Mn^{2+}$ doped in $[Zn(Pz)_6](BF_4)_2$, where the sign and magnitude of $D(^6A_{1g})$ has been determined[30] (see table 6.17). By applying ligand field theory to the Mn(II) complex and applying a small spectrochemical correction, a constraint on the value of $\nu$ and $\nu'$ is obtained, viz. $\nu + 2\nu' \approx 1100$ cm$^{-1}$ for $[Ni(Pz)_6](BF_4)_2$, since $D(^6A_{1g}) \propto \nu + 2\nu'$[34]. The trigonal field solutions for $[Ni(Pz)_6](BF_4)_2$ are thereby restricted to $\nu$ = 690 cm$^{-1}$, $\nu'$ = 205 cm$^{-1}$ (D = +0.168 cm$^{-1}$) and $\nu$ = 550 cm$^{-1}$, $\nu'$ = 275 cm$^{-1}$ (D = -0.168 cm$^{-1}$). For $[Ni(5MePz)_6](ClO_4)_2$, there is no additional information, but the constraints on the solutions can be obtained by using the microscopic ligand field model (table 6.22) which gives:

$$\nu\ ([Ni(Pz)_6](BF_4)_2) = 1.12[e_\pi(\perp) - e_\pi(\parallel)] - 0.024[e_\pi(\perp) + e_\pi(\parallel)] \quad (6.9)$$

$$\nu'\ ([Ni(Pz)_6](BF_4)_2) = 0.017e_\sigma + 1.44e_{\sigma\pi}(+5°, \perp) - 0.98e_{\sigma\pi}(\parallel) \quad (6.10)$$

$$\nu\ ([Ni(5MePz)_6](ClO_4)_2) = 0.24[e_\pi(\perp) - e_\pi(\parallel)] \quad (6.11)$$

$$\nu'\ ([Ni(5MePz)_6](ClO_4)_2) = 1.12e_{\sigma\pi}(+5°, \perp) - 1.12e_{\sigma\pi}(\parallel) \quad (6.12)$$

All $e_{\sigma\pi}(\perp)$ values have been expressed in terms of $e_{\sigma\pi}(+5°)$ by using the exact equation $e_{\sigma\pi}(-t) = (-)\, e_{\sigma\pi}(t)$ and the approximate empirical relationship $e_{\sigma\pi}(t) \propto \sin(2t)$.

The terms involving $e_{\sigma\pi}(\perp)$ and $e_{\sigma\pi}(\parallel)$ in the $\nu'$ expressions for $[Ni(Pz)_6](BF_4)_2$ and $[Ni(5MePz)_6](ClO_4)_2$ have the same signs and similar coefficients for both complexes, and can be approximated by a common expression:

$$1.3e_{\sigma\pi}(+5°, \perp) - e_{\sigma\pi}(\parallel)$$

Hence the microscopic model predicts

$$\nu ([Ni(5MePz)_6](ClO_4)_2) \approx (0.241/1.115)\nu ([Ni(Pz)_6](BF_4)_2) \quad (6.13)$$

$$\nu' ([Ni(5MePz)_6](ClO_4)_2) \approx \nu' ([Ni(Pz)_6](BF_4)_2) - 0.017e_\sigma \quad (6.14)$$

where $e_\sigma = 1/3[\Delta + 2e_\pi(\perp) + 2e_\pi(\|)]$ and as a first approximation, $e_\sigma \approx 4500$ cm$^{-1}$.

At this stage, the choice of the values for $e_\pi(\|)$ and $e_\pi(\perp)$ are not critical for deriving $e_\sigma$. The above choice for $e_\sigma$ is a first approximation, which is refined during the calculations.

From equations (6.9)-(6.14) two possible values are predicted for $[Ni(5MePz)_6](ClO_4)_2$:

$\nu \approx 150$ cm$^{-1}$ and $\nu' = 128$ cm$^{-1}$ derived from $D([Ni(Pz)_6](BF_4)_2) = +0.168$ cm$^{-1}$
and $\nu \approx 120$ cm$^{-1}$ and $\nu' = 198$ cm$^{-1}$ derived from $D([Ni(Pz)_6](BF_4)_2) = -0.168$ cm$^{-1}$

These predicted solutions are now compared with the more accurate double series of solutions that are obtained by fitting ligand theory to $D([Ni(5MePz)_6](ClO_4)_2) = |0.408|$ cm$^{-1}$ (value from Collison et. al.[16]. These calculations were similar to those performed for $[Ni(Pz)_6](BF_4)_2$ and employed the same ligand field parameters $\Delta = 11300$ cm$^{-1}$, B = 870 cm$^{-1}$, C = 4B, $\zeta = 584$ cm$^{-1}$ and k = 0.87. Agreement is obtained only for D = –0.408 cm$^{-1}$, $\nu = 130$ cm$^{-1}$ and $\nu' = 188$ cm$^{-1}$, that is, one solution of the more accurate calculations.

Hence, $D([Ni(Pz)_6](BF_4)_2) = -0.168$ cm$^{-1}$, and the more accurate trigonal ligand field parameters for $[Ni(Pz)_6](BF_4)_2$ that are derived from the full ligand field calculations are $\nu = 550$ cm$^{-1}$ and $\nu' = 275$ cm$^{-1}$.

These more accurate trigonal field parameters and equations 6.9-6.12 then give the approximate expressions:

$$e_\pi(\perp) - e_\pi(\|) \approx 520 \text{ cm}^{-1} \quad (6.15)$$

$$1.3e_{\sigma\pi}(5°, \perp) - e_{\sigma\pi}(\|) \approx 198 \text{ cm}^{-1} \quad (6.16)$$

As with the bromate complexes, it is not possible to estimate $e_\pi(\|)$ with any precision. A value of $e_\pi(\|) > 0$ gives better agreement for the value of $e_\pi(\perp) - e_\pi(\|)$ that is derived from the parameters $\nu$ = 550 $cm^{-1}$ and 130 $cm^{-1}$ and equations 6.9 and 6.10 respectively. To resolve the values of $e_{\sigma\pi}(\perp)$ and $e_{\sigma\pi}(\|)$ it is necessary to study an additional trigonal complex, $[Ni(Pz)_6](NO_3)_2$, for which the crystal structure is known[19]. The EPR study of $[Ni(Pz)_6](NO_3)_2$ (see section 6.4.2) did not establish the sign of D ($|D|$ = 0.16 $cm^{-1}$ at 295 K, as determined in this thesis) and so the application of ligand field theory generates two series of solutions for $\nu$ and $\nu'$ (one series for D = +0.16 $cm^{-1}$ and the other for D = –0.16 $cm^{-1}$).

The microscopic model and equation 6.15 leads to the prediction of $\nu([Ni(Pz)_6](NO_3)_2) \approx 700$ $cm^{-1}$. The value of $\nu'$ cannot be estimated since the $e_{\sigma\pi}$ parameters now have different coefficients:

$$\nu'([Ni(Pz)_6](NO_3)_2) = 0.0303e_\sigma - 1.06e_{\sigma\pi}(5°,\perp) - 0.89e_{\sigma\pi}(\|) \quad (6.17)$$

The values of $e_{\sigma\pi}(\|)$ are assumed to be the same for the three Ni complexes, since the ∠NiNN angles are similar for all three compounds (see table 4.2). The application of the predicted value $\nu([Ni(Pz)_6](NO_3)_2) \approx 700$ $cm^{-1}$ to the two series of solutions leads to two possible values for the trigonal ligand fields and the $e_{\sigma\pi}$ parameters for the three complexes (see table 6.20).

It was not possible to resolve the ambiguity in the values of the off-diagonal angular-overlap-model (AOM) trigonal field parameter $\nu'$ for $[Ni(Pz)_6](NO_3$. The EPR spectrum of $[Co(Pz)_6](NO_3)_2$ (see section 6.4.3) was not sufficiently accurate to provide useful data about the trigonal field through the g-value anisotropy. Additional data would be required to resolve this ambiguity, for example, the zero-field splitting parameter ($D(^6A_{1g})$) for $[Mn(Pz)_6](NO_3)_2$ at 298 K, which could be obtained from an EPR spectrum. Therefore, the best estimates for the angular overlap and ligand field parameters for $[Ni(Pz)_6](NO_3)_2$ are: $\Delta \leq 11300$ $cm^{-1}$, $e_\sigma \approx 4700$ $cm^{-1}$, $e_\pi(\perp) - e_\pi(\|) \approx 500$ $cm^{-1}$ and $e_\pi(\|) \approx$ 340-450 $cm^{-1}$.

**Table 6.20: Microscopic ligand field parameters for $[Ni(Pz)_6](NO_3)_2$, with $e_\pi(\|) = 360$ $cm^{-1}$ (all parameters are in $cm^{-1}$)**

| | D = +0.16 | D = –0.16 |
|---|---|---|
| ν ($[Ni(Pz)_6](NO_3)_2$) | 700 | 700 |
| ν' ($[Ni(Pz)_6](NO_3)_2$) | 211 | 344 |
| $e_{\sigma\pi}(5°, \perp)$ | 50 | –10 |
| $e_{\sigma\pi}(\|)$ | –130 | –210 |
| ν'' ($[Ni(5MePz)_6](ClO_4)_2$) | 196 | 480 |
| ν'' ($[Ni(Pz)_6](BF_4)_2$) | 240 | 540 |
| ν'' ($[Ni(Pz)_6](NO_3)_2$) | 388 | 560 |

The analysis was repeated and corrections to the ν'' field were included. These corrections were negligible for the parameters derived from D($[Ni(Pz)_6](NO_3)_2$) = +0.16. For the other set of parameters based on from D($[Ni(Pz)_6](NO_3)_2$) = –0.16, the corrections to $e_\pi$ and $e_\sigma$ were small and in view of the uncertainty in the value of $e_\pi(\|)$ they were neglected. Table 6.21 gives the current estimates of the bonding parameters for the $[Ni(Pz)_6]^{2+}$ complex ion. Note that the values of $e_{\sigma\pi}(\|)$ are not very sensitive to the value of $e_\pi(\|)$.

**Table 6.21: Bonding parameters for the $[Ni(Pz)_6]^{2+}$ ion[a]**

| | $e_\pi(\|) = 360$ | $e_\pi(\|) = 0$ |
|---|---|---|
| $e_\pi(\perp) - e_\pi(\|)$ | 520 | 520 |
| $e_\pi(\perp) + e_\pi(\|)$ | 1240 | 520 |
| $e_\sigma$ | 4590 | 4100 |
| $e_{\sigma\pi}(5°,\perp)$ | +50(–10) | +37(–24) |
| $e_{\sigma\pi}(\|)$ | –130(–210) | –150(–230) |

[a] The values of $e_{\sigma\pi}$ were obtained using both the positive sign for D ($[Ni(Pz)_6](NO_3)_2$), and the negative sign (value in brackets)

The ambiguity is sign for $e_{\sigma\pi}(\perp)$ is unfortunate. The sign of $e_{\sigma\pi}(\|)$ is negative irrespective of the sign of D($[Ni(Pz)_6](NO_3)_2$). If the origin of $e_{\sigma\pi}(\|)$ is assumed to be

the misalignment of the σ-bonding orbital on the coordinating nitrogen atom away from the Ni-N bond direction then for the standard configuration (see figure 4.2) the orientation shown in figure 6.25 is deduced.

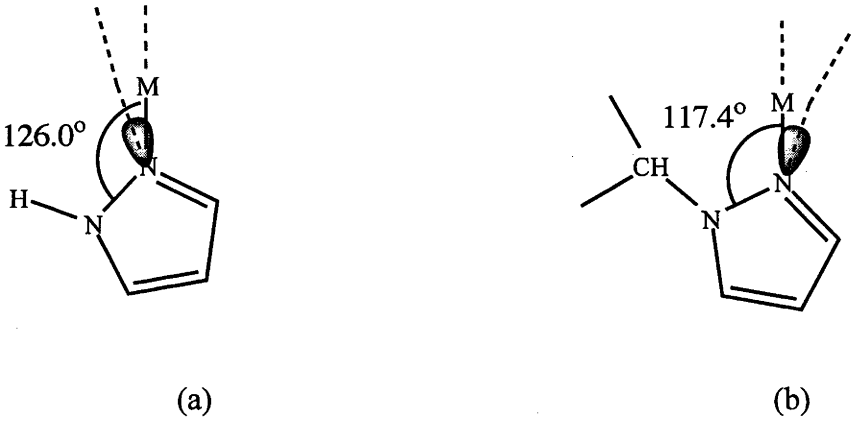


(a) (b)

**Figure 6.25: Differences in the in-plane tilt of the pyrazolyl rings between the uncapped (a) and capped (b) complexes**

The $t_{\|}$ value in the expression for $e_{\sigma\pi}(\|)$ is expected to be only a few degrees. Since the capping of the pyrazolyl ligands changes the ∠NiNN from ~126° to ~117.5°, it is very likely that for the capped complexes the nitrogen σ-bonding orbital lies in the opposite quadrant (figure 6.25). The simple covalency model of misalignment then predicts that $e_{\sigma\pi}(\|)$ will have a positive sign.

According to the microscopic model (table 6.22) a positive sign for $e_{\sigma\pi}(\|)$ will reduce the large negative contribution to ν' that comes from the small cone angles ($\theta < \theta_{Oh}$) for the capped complexes of the divalent metal ions. This is dramatically revealed in table 6.9-6.11, where the repetitions of the calculations of Astley et al.[12] predict D = +1.27 $cm^{-1}$ for $[Ni(HCPz_3)_2](NO_3)_2$, whereas the experimental value is D < |0.66| $cm^{-1}$.

**Table 6.22 The calculated expressions for the microscopic ligand field parameters and the AOM bonding parameters[a]**

| $[Ni(5MePz)_6](ClO_4)_2$ $\theta = 54.7°$, $\omega = -2.3°$ ($t_\perp = -4.4°$) | | | | | |
|---|---|---|---|---|---|
| | $e_\sigma$ | $e_\pi(\perp) - e_\pi(\parallel)$ | $e_\pi(\perp) + e_\pi(\parallel)$ | $e_{\sigma\pi}(\perp)$ | $e_{\sigma\pi}(\parallel)$ |
| $\Delta$ | 3.000 | | –2.00 | | |
| $\nu$ | | 0.24 | | | |
| $\nu'$ | –0.001 | | | –1.27 | –1.17 |
| $\nu''$ | | | | 2.03 | –2.20 |
| $[Ni(Pz)_6](BF_4)_2$ $\theta = 55.1°$, $\omega = -11°$ ($t_\perp = -5°$) | | | | | |
| | $e_\sigma$ | $e_\pi(\perp) - e_\pi(\parallel)$ | $e_\pi(\perp) + e_\pi(\parallel)$ | $e_{\sigma\pi}(\perp)$ | $e_{\sigma\pi}(\parallel)$ |
| $\Delta$ | 3.000 | | –2.00 | | |
| $\nu$ | | 1.11 | –0.024 | 0.02 | 0.01 |
| $\nu'$ | 0.017 | –0.01 | | –1.45 | –0.98 |
| $\nu''$ | | 0.02 | | 1.68 | –2.49 |
| $[Ni(Pz)_6](NO_3)_2$ $\theta = 55.3°$, $\omega = -14.5°$ ($t_\perp = +3.5°$) | | | | | |
| | $e_\sigma$ | $e_\pi(\perp) - e_\pi(\parallel)$ | $e_\pi(\perp) + e_\pi(\parallel)$ | $e_{\sigma\pi}(\perp)$ | $e_{\sigma\pi}(\parallel)$ |
| $\Delta$ | 3.000 | | –2.00 | | |
| $\nu$ | 0.001 | 1.43 | –0.04 | 0.03 | 0.02 |
| $\nu'$ | 0.030 | –0.01 | | –1.51 | –0.89 |
| $\nu''$ | | 0.03 | | 1.52 | –2.58 |
| $[Co(HCPz_3)_2](NO_3)_2$ $\theta = 50.9°$, $\omega = -135°$ ($t_\perp \sim 0°$) | | | | | |
| | $e_\sigma$ | $e_\pi(\perp) - e_\pi(\parallel)$ | $e_\pi(\perp) + e_\pi(\parallel)$ | $e_{\sigma\pi}(\perp)$ | $e_{\sigma\pi}(\parallel)$ |
| $\Delta$ | 2.934 | –0.02 | –1.96 | | |
| $\nu$ | 0.043 | –3.25 | 0.26 | 0.06 | 0.25 |
| $\nu'$ | –0.188 | –0.19 | –0.01 | | 1.52 |
| $[Co(HBPz_3)_2]$ $\theta = 51.6°$, $\omega = -135°$ ($t_\perp \sim 0°$) | | | | | |
| | $e_\sigma$ | $e_\pi(\perp) - e_\pi(\parallel)$ | $e_\pi(\perp) + e_\pi(\parallel)$ | $e_{\sigma\pi}(\perp)$ | $e_{\sigma\pi}(\parallel)$ |
| $\Delta$ | 2.956 | –0.01 | –1.97 | | |
| $\nu$ | 0.029 | –3.21 | 0.22 | 0.04 | 0.20 |
| $\nu'$ | –0.156 | –0.16 | –0.01 | | 1.57 |

**Table 6.22 (continued)**

| $[Ni(HCPz_3)_2](NO_3)_2$ $\theta = 51.6°$, $\omega = -135°$ ($t_\perp \sim 0°$) | | | | | |
|---|---|---|---|---|---|
| | $e_\sigma$ | $e_\pi(\perp) - e_\pi(\|\|)$ | $e_\pi(\perp) + e_\pi(\|\|)$ | $e_{\sigma\pi}(\perp)$ | $e_{\sigma\pi}(\|\|)$ |
| $\Delta$ | 2.954 | –0.02 | –1.97 | | |
| $\nu$ | 0.030 | –3.21 | 0.22 | 0.04 | 0.13 |
| $\nu'$ | –0.158 | –0.16 | –0.01 | | 1.56 |
| $[Ni(HBPz_3)_2]$ $\theta = 52.5°$, $\omega = -135°$ ($t_\perp \sim 0°$) | | | | | |
| | $e_\sigma$ | $e_\pi(\perp) - e_\pi(\|\|)$ | $e_\pi(\perp) + e_\pi(\|\|)$ | $e_{\sigma\pi}(\perp)$ | $e_{\sigma\pi}(\|\|)$ |
| $\Delta$ | 2.977 | –0.01 | –1.98 | | |
| $\nu$ | 0.015 | –3.15 | 0.16 | 0.02 | 0.11 |
| $\nu'$ | –0.114 | –0.11 | | | 1.62 |

[a]See tables 4.2 and 4.3 for a detailed listing of the geometric parameters of these complexes.

**Table 6.23: Trigonal ligand fields and the microscopic bonding parameters for the limiting case $e_\pi(\|) = 0$ for $[Ni(HCPz_3)_2](NO_3)_2$**

| $D(^3T_{1g}(^3F))$ | $\nu$ | $\nu'$ | $e_\pi(\perp)$ | $e_\sigma$ | $e_{\sigma\pi}(\|\|)$ |
|---|---|---|---|---|---|
| 2500 | –1743 | –669 | 630 | 4652 | +106 |
| 2347 | –1600 | –640 | 581 | 4619 | +117 |
| 2235 | –1500 | –620 | 547 | 4596 | +124 |
| 2000 | –1320 | –570 | 586 | 4556 | +146 |

The trigonal fields were obtained by fitting ligand field theory to the observed $D(^3T_{1g}(^3F))$, $D(^3A_{2g}) = 0.66$, $B = 840$, $C = 3360$, $\zeta = 567$, $k = 0.85$, $\Delta = 12500$ $cm^{-1}$

In the following discussion only $[Ni(HCPz_3)_2](NO_3)_2$ will be examined in detail. The trigonal ligand fields, in general, are sensitive to temperature and, ideally, the optical, EPR and structural data should be measured at the same temperature.

The large splitting of the $^3T_{1g}(^3F)$ band and the ground state zero-field splitting are sufficient for the determination of $\nu$ and $\nu'$. However the measured value of $D(^3T_{1g}(^3F)) \approx 2000$ $cm^{-1}$ at 295 K is probably smaller than the true value as a result of the strong overlap between the two trigonal components.

**Table 6.24: Trigonal ligand fields and the microscopic bonding parameters for $[Ni(HCPz_3)_2](NO_3)_2$ with the constraint $e_\pi(||) > 0$ and $e_\pi(\perp) - e_\pi(||) \approx 560\text{-}580\ cm^{-1}$**

| $D(^3T_{1g}(^3F))$ | $e_\pi(\perp) - e_\pi(\|\|)$ | $e_\sigma$ | $e_\pi(\|\|)$ | $e_{\sigma\pi}(\|\|)$ |
|---|---|---|---|---|
| 2500 | No solution, $e_\pi(\|\|) < 0$ | | | |
| 2347 | 581 | 4619 | 0 | +117 |
| 2235 | 560 | 4698 | 71 | +137 |
| | 580 | 4898 | 210 | +158 |
| 2000 | 560 | 5232 | 469 | +222 |

At 10 K, $D(^3T_{1g}(^3F)) \approx 2500\ cm^{-1}$ is significantly greater not only as a result of reduced overlap between the trigonal components but because the $\nu$ and $\nu'$ parameters may be temperature-dependent. The value of $D(^3T_{1g}(^3F))$ at 295 K is expected to be a little greater than 2000 $cm^{-1}$ and hence the $\nu$ and $\nu'$ parameters are determined for a range of values of $D(^3T_{1g}(^3F))$ between 2000 and 2500 $cm^{-1}$. These results are displayed above in table 6.23, where the results of a microscopic analysis are given for the limiting case ($e_\pi(||) = 0$).

The bond length Ni-N in $[Ni(HCPz_3)_2](NO_3)_2$ (2.078 Å) is significantly shorter than that for $[Ni(Pz)_6](NO_3)_2$ (2.125 Å). The distance dependence of the bonding parameters is assumed to follow the $1/r^5$ approximation.

Hence the expected values for the primary bonding parameters for the capped complex are:

$e_\pi(\perp) - e_\pi(||) \approx 560\text{-}580\ cm^{-1}$

$e_\sigma \approx 4600\ cm^{-1}$ (for $e_\pi(||) = 0$)

$e_\sigma \approx 5100\text{-}5200\ cm^{-1}$ (for $e_\pi(||) \approx 400\ cm^{-1}$)

In table 6.23 the microscopic analysis for $e_\pi(||) = 0$ gives physically reasonable values for $e_\pi(\perp)$ and $e_\sigma$ for $D(^3T_{1g}(^3F)) \approx 2230\text{-}2350\ cm^{-1}$. Furthermore, $e_{\sigma\pi}(||)$ is relatively insensitive to the uncertainty in $D(^3T_{1g}(^3F))$ and its sign is unambiguous.

The analysis based on the assumption that $e_\pi(||) > 0$ (table 6.24) gives similar results and if $e_\pi(||) \geq 360\ cm^{-1}$, it tends to favour a value of $D(^3T_{1g}(^3F))$ closer to 2000 $cm^{-1}$.

In both cases $e_{\sigma\pi}(\|)$ is found to have a positive sign that is opposite to that observed in the uncapped complexes. Thus the primary objective of this chapter has been achieved. The capping of the pyrazolyl ligands produces a tilt within the plane of the pyrazolyl rings of $t_{\|} \approx 8°$ and changes the value of $e_{\sigma\pi}(\|)$ from –130/–210 $cm^{-1}$ to +130/+200 $cm^{-1}$. This distortion is reflected in the magnitude of the off-diagonal trigonal field $v'$.

For the $[Ni(HBPz_3)_2]$ complex, a room temperature spectrum is unfortunately not available over the relevant spectral region, and so a detailed angular overlap model analysis was not attempted.

## 6.5 Conclusion

The low temperature microcrystal absorption spectra of $[M(Pz)_6](NO_3)_2$ and $[M(HCPz_3)_2](NO_3)_2$ were re-measured, while the spectra of $[M(HBPz_3)_2]$ (M = Co and Ni) were measured for the first time. The trigonal splitting of the $^3T_{1g}(^3F)$ state was clearly visible in the spectra of the capped nickel compounds, being noticeable smaller for $[Ni(HBPz_3)_2]$ than for $[Ni(HCPz_3)_2](NO_3)_2$. The splitting decreased slightly for $[Ni(HCPz_3)_2](NO_3)_2$ on warming to room temperature. Transitions to the spin-orbit split $^2T_{1g}{}^b$ state were clearly visible in the spectra of all three cobalt compounds, with the separation of these peaks from the $^4T_{1g}(^4P)$ peak increasing with increasing trigonal field strength.

The different ligand field strengths are evident from the absorption spectra, and the corresponding values of the crystal field splitting parameter $\Delta$; the observed order is $HCPz_3 > HBPz_3^- > Pz$. This correlates with the increasing metal-ligand bond length on moving along this series. The difference between $HBPz_3^-$ and Pz is greater than that between $HCPz_3$ and $HBPz_3^-$. The greater difference in ligand field strengths between the former pair is evident in the colours of the complexes; both capped cobalt complexes are yellow, while the monodentate complex is orange, and both capped nickel complexes are purple, while the monodentate complex is blue.

From the EPR data, the absolute value of the axial zero-field splitting parameter D of $[Ni(Pz)_6](NO_3)_2$ was determined to be 0.12 $cm^{-1}$ at 10 K and 0.16 $cm^{-1}$ at 295 K. Upper

limits were determined for $[Ni(HBPz_3)_2]$ and $[Ni(HCPz_3)_2](NO_3)_2$ at 295 K (0.59 and 0.66 respectively, in keeping with the smaller trigonal field in the former compound). For these two compounds, the quoted |D| value incorporates the rhombic splitting parameter E.

The g-values of the ground Kramers doublet in $[Co(HBPz_3)_2]$ and $[Co(HCPz_3)_2](NO_3)_2$ determined here for frozen solutions of the compounds were very close to literature values for magnetically dilute powders. Strong peaks due to an impurity were present in the spectra of $[Co(HCPz_3)_2](NO_3)_2$ and the two capped nickel compounds.

The calculations using the angular overlap model, for the nickel monopyrazolyl compound studied in this chapter ($[Ni(Pz)_6](NO_3)_2$), plus three examples from the literature showed that there is a significant contribution from in-plane tilting, requiring the introduction of the additional AOM parameter $e_{\sigma\pi}(||)$. This parameter is determined to be negative for the monodentate pyrazolyl nickel compounds, and positive for the capped compounds, in line with the significant shift change in the in-plane tilt angles between these two groups of complexes (see figure 6.25). It was unfortunately not possible to resolve the sign of the D parameter for $[Ni(Pz)_6](NO_3)_2$ by calculation; additional data for a compound such as $[Mn(Pz)_6](NO_3)_2$ would be required. For the two literature examples ($[Ni(5MePz)_6](ClO_4)_2$ and $[Ni(Pz)_6](BF_4)_2$, the sign could be determined as EPR data for $[Mn(Pz)_6](BF_4)_2$, was also available, which provided an additional constraint for the calculations.

It is clear from the above results that the in-plane AOM parameters $e_\pi(||)$ and $e_{\sigma\pi}(||)$ cannot simply be neglected for coordination complexes of nitrogen-containing heterocycles such as pyrazole. For the capped nickel compounds $[Ni(HCPz_3)_2](NO_3)_2$ and $[Ni(HBPz_3)_2]$, the EPR data determined in this work provided an additional experimental parameter in form of the axial zero-field splitting parameters. This put an additional constraint on the AOM calculation, and showed that the $\nu$ trigonal field was slightly larger than that predicted by Astley et al.[12], while the off-diagonal trigonal field $\nu'$ is significantly smaller.

There are several potential avenues for future work. The first is a measurement of the absorption spectrum of $[Ni(HBPz_3)_2]$ between 300 and 550 nm. This will provide an experimental value for the trigonal field splitting of the $^3T_{1g}(^3F)$ state at room

temperature, and would mean that absorption, EPR and crystal data would be available for both capped nickel pyrazolyl complexes at one temperature, allowing a valid comparison.

Further, the determination of crystal structures at low temperature (~10 K) for $[Ni(HBPz_3)_2]$, $[Ni(HCPz_3)_2](NO_3)_2$ and $[Ni(Pz)_6](NO_3)_2$ would ascertain whether any significant structural changes occur for these compounds on cooling. It is already known that $[Co(HCPz_3)_2](NO_3)_2$ retains the same basic structure on cooling from room temperature to 173 K[35], however structural changes could occur on further cooling. To complete the picture, the Q-band EPR spectra of magnetically dilute $[Ni(HBPz_3)_2]$ and $[Ni(HCPz_3)_2](NO_3)_2$ should be measured, giving a full set of structural, EPR and optical data for both compounds at two temperatures. Finally, since the EPR spectra of the monodentate compound $[Ni(Pz)_6](NO_3)_2$ were measured using the pure compound, Q-band spectra of the capped compounds could be measured to study the effect of dilution on the EPR spectra of these two compounds.

As with the bromate compound ($[Co(H_2O)_6](BrO_3)_2$), Raman spectra were measured for $[Co(HCPz_3)_2](NO_3)_2$ in an attempt to locate electronic Raman transitions to the Kramers doublets (generated as a result of spin-orbit coupling and trigonal splitting) of the $^4T_{1g}$ ground state. This would have provided another experimental measure of the trigonal field. Unfortunately, although good quality Raman spectra were measured, no electronic peaks could be identified by comparison with the spectra of $[Zn(HCPz_3)_2](NO_3)_2$. The Raman spectra are presented in appendix C.

## 6.6 References


(1) Trofimenko, S. *Journal of the American Chemical Society* **1966**, *88*, 1842-1844.

(2) Trofimenko, S. *Journal of the American Chemical Society* **1967**, *89*, 3170-3177.

(3) Trofimenko, S. *Chemical Reviews* **1972**, *72*, 497-508.

(4) Trofimenko, S. In *Progress in Inorganic Chemistry*; Lippard, S. J., Ed.; John Wiley and Sons: New York, 1986; Vol. 34, p 115-209.

(5) Trofimenko, S. *Chemical Reviews* **1993**, *93*, 943-980.

(6) Trofimenko, S. *Scorpionates: The Coordination Chemistry of Polypyrazolylborate Ligands*; 1st ed.; Imperial College Press: London, 1999.

(7) Huckel, W.; Bretschneider, H. *Chemische Berichte* **1937**, *70*, 2024-2026.

(8) Trofimenko, S. *Journal of the American Chemical Society* **1970**, *92*, 5118-5126.

(9) Bagley, M. J.; Nicholls, D.; Warburton, B. A. *Journal of the Chemical Society A* **1970**, 2694-2697.

(10) Reedijk, J. *Recueil* **1969**, *88*, 1451-1470.

(11) Reedijk, J.; Smit, J. A. *Recueil* **1971**, *90*, 1135-1140.

(12) Astley, T.; Gulbis, J. M.; Hitchman, M. A.; Tiekink, E. R. T. *Journal of the Chemical Society Dalton Transactions* **1993**, 509-515.

(13) Bandoli, G.; Clemento, D. A.; Paolucci, G.; Doretti, L. *Crystal Structure Communications* **1979**, *8*, 965-970.

(14) Churchill, M. R.; Gold, K.; Maw, C. E. *Inorganic Chemistry* **1970**, *9*, 1597-1604.

(15) Nakata, K.; Kawabata, S.; Ichikawa, K. *Acta Crystallographica C* **1995**, *C51*, 1092-1094.

(16) Collison, D.; Helliwell, M.; Jones, V. M.; Mabbs, F. E.; McInnes, E. J. L.; Riedi, P. C.; Smith, G. M.; Pritchard, R. G.; Cross, W. I. *Journal of the Chemical Society Faraday Transactions* **1998**, *94*, 3019-3025.

(17) Hoedt, R. W. M. t.; Driessen, W. L.; Verschoor, G. C. *Acta Crystallographica C* **1983**, *C39*, 71-72.

(18) Lumme, P. O.; Lindell, E.; Mutikainen, I. *Acta Crystallographica C* **1988**, *C44*, 967-970.

(19) Reimann, C. W.; Santoro, A.; Mighell, A. D. *Acta Crystallographica B* **1970**, *B26*, 521-526.

(20) Jesson, J. P. *Journal of Chemical Physics* **1966**, *45*, 1049-1056.

(21) Abragam, A.; Pryce, M. H. L. *Proceedings of the Royal Society A (London)* **1951**, *A206*, 173-191.

(22) Julia, S.; Mazo, J. d.; Avila, L.; Elguero, J. *Organic Preparations and Procedures International* **1984**, *16*, 299-307.

(23) Reger, D. L.; Grattan, T. C.; Brown, K. J.; Little, C. A.; Lamba, J. J. S.; Rheingold, A. L.; Sommer, R. D. *Journal of Organometallic Chemistry* **2000**, *607*, 120-128.

(24) Jesson, J. P.; Trofimenko, S.; Eaton, D. R. *Journal of the American Chemical Society* **1967**, *89*, 3148-3158.

(25) Daugherty, N. A.; Swisher, J. H. *Inorganic Chemistry* **1968**, *7*, 1651-1653.

(26) Krausz, E. *Australian Journal of Chemistry* **1993**, *46*, 1041-1054.

(27) Krausz, E. *Australian Optical Society News* **1998**, *12*, 21-24.

(28) Reedijk, J.; Nieuwenhuijse, B. *Recueil* **1972**, *91*, 533-551.

(29) Wasserman, E.; Snyder, L. C.; Yager, W. A. *Journal of Chemical Physics* **1964**, *41*, 1763-1772.

(30) Anthonisamy, V. S. X.; Padiyan, D. P.; Murugesan, R. *Molecular Physics* **1998**, *94*, 275-281.

(31) Ballhausen, C. J. *Introduction to Ligand Field Theory*; 1st ed.; McGraw-Hill Book Company: New York, 1962.

(32) Figgis, B. N.; Hitchman, M. A. *Ligand Field Theory and Its Applications*; 1st ed.; Wiley-VCH: New York, 2000; Vol. 1.

(33) Bendix, J.; Brorson, M.; Schaeffer, C. E. *Inorganic Chemistry* **1993**, *32*, 2838-2849.

(34) Dubicki, L., private communication.

(35) Keene, F. R.; Tiekink, E. R. T. *Zeitschrift fur Kristallographie* **1994**, *209*, 548-549.

# Chapter 7: Conclusion

This thesis describes work using three different spectroscopic techniques (Raman, electron paramagnetic resonance, and absorption), and two different sample systems (trigonally distorted cobalt and nickel compounds, and self-assembled monoloyers, or SAMs).

A new Raman system was constructed from a triple monochromator and a CCD (chapter 2) and compared to an existing system based on a photomultiplier (PM) tube/photon counter and a double monochromator. The CCD system was found to be superior in terms of speed of spectral acquisition, and signal to noise ratio, while the PM tube system could achieve better resolution.

Dealing first with the SAMs, the aim of this work, described in chapter 3, was characterisation of the AMBRI biosensor using surface Raman spectroscopy. A number of SAM systems were studied; the well-known molecules dodecanethiol and benzyl mercaptan, and DLP (a compound prepared specially for the AMBRI biosensor). All monolayer systems employed a gold substrate. Spectra were measured using a Raman microscope system. Problems were experienced due to high backgrounds, most likely as a result of fluorescence. A series of spectra were obtained and compared with literature examples. The unusual sharp peaks observed by Clark et al and assigned by them as electronic image state transitions were seen for certain excitation conditions. Protocols are available in the literature for removing surface contamination, however many of these are fairly harsh involving either highly corrosive solutions such as piranha solution, or repeated oxidation-reduction cycling. This would appear to severely limit the usefulness of Raman for studying the AMBRI system.

Two groups of trigonally distorted cobalt and nickel complexes were studied by using low temperature absorption spectroscopy of the crystals together with powder EPR.

The absorption spectra of the metal bromate hexahydrates $[Co(H_2O)_6](BrO_3)_2$ and $[Ni(H_2O)_6](BrO_3)_2$ had been previously studied by a number of authors. Due to the absence of detailed crystal structures for these compounds at the time, the role of trigonal splitting

in the spectra was not considered; the site symmetry of the metal ions was assumed to be octahedral. This was despite the existence of a paper describing the EPR of $[Ni(H_2O)_6](BrO_3)_2$, which clearly showed an axial zero-field splitting. The re-measurement of the absorption spectra of these compounds, including the previously unobserved $^3T_{2g}$ peak in the nickel complex, together with the first-time study of the EPR of $[Co(H_2O)_6](BrO_3)_2$ and the modelling of the spectra using the microscopic ligand field model showed conclusively that there is a substantial trigonal field in these complexes. The most obvious piece of experimental evidence is the EPR g-value anisotropy ($g_{\|} = 7.54$, $g_{\perp} = 2.11$). The microscopic ligand field calculations showed a large $v$ trigonal field of around $-985$ cm$^{-1}$ for both complexes, and a much smaller off-diagonal trigonal field $v'$ of around $-14$ cm$^{-1}$.

Raman spectra of the two bromate compounds were measured with the aim of studying the trigonal splitting of the ground states through the electronic Raman transitions expected to be observed for the cobalt compound. Unfortunately, no electronic transitions could be identified in the spectra. The most likely reason is that the electronic Raman peaks are severely broadened (even at 10 K) as a result of short excited state lifetimes. The Raman spectra are presented and discussed in appendices B and C.

The second group of complexes studied was a number of cobalt and nickel pyrazolyl compounds. Spectra were measured for the monodentate pyrazolyl complexes $[M(Pz)_6](NO_3)_2$, and the capped complexes $[M(HBPz_3)_2]$ and $[M(HCPz_3)_2](NO_3)_2$. Again, absorption and EPR spectra were measured, and the results analysed with the help of the microscopic ligand field model. In the case of the monodentate complexes, results from several literature examples were also examined using the microscopic ligand field model.

The differences in the trigonal field strength of the nickel complexes was clearly observable for the $^3T_{1g}(^3F)$ peak in the absorption spectra, with the following ordering: $[Ni(HCPz_3)_2](NO_3)_2 > [Ni(HBPz_3)_2] > [Ni(Pz)_6](NO_3)_2$. The results of the EPR spectra were consistent with these results, the same ordering being observed for the axial zero-field splitting parameters. A temperature dependence was observed for $[Ni(Pz)_6](NO_3)_2$, with an increase in the zero-field splitting factor being observed when the temperature was increased from 10 K to room temperature.

The EPR spectra of the capped cobalt compounds $[Co(HCPz_3)_2](NO_3)_2$ and $[Co(HBPz_3)_2]$ provided further evidence of the pyrazolyl methane compounds having a larger trigonal field than the pyrazolyl borates, with $[Co(HCPz_3)_2](NO_3)_2$ showing a larger disparity in the axial and equatorial g-values than $[Co(HBPz_3)_2]$. The spectra for magnetically dilute powders of these compounds confirmed earlier work, as did the new frozen solution spectra.

The microscopic ligand field calculations for the capped pyrazolyl compounds confirmed that the angle of rotation of the pyrazolyl ligands results in maximisation of the $v$ trigonal field in these compounds. However, it was also shown that the in-plane tilting in these compounds was significant, resulting in a sizeable off-diagonal trigonal field $v'$ (e.g. –848 $cm^{-1}$ for $[Ni(HCPz_3)_2](NO_3)_2$). It was clearly demonstrated in section 6.5.4 that the in-plane tilting of the pyrazolyl ligands was significant even for the monodentate nickel pyrazolyl compounds, and that the angular overlap parameter $e_{\sigma\pi}(||)$ changes sign with the change in tilt between $[Ni(Pz)_6](NO_3)_2$ and $[Ni(HCPz_3)_2](NO_3)_2$).

The Raman spectra of the compounds $[Co(HCPz_3)_2](NO_3)_2$ and $[Zn(HCPz_3)_2](NO_3)_2$ were measured, again with the aim of identifying electronic transitions in the cobalt compound arising from the trigonal splitting of the ground $^4T_{1g}$ state (see the results presented in appendix C). However, as for $[Co(H_2O)_6](BrO_3)_2$, the spectra failed to show any evidence of electronic transitions.

The results presented in this thesis demonstrate a range of different applications for the three spectroscopic techniques employed. The observation of electronic Raman transitions in the cobalt complexes was unfortunately not achieved, despite the existence of many literature examples (see chapter 1).

The study of the pyrazolyl complexes, in particular, has a number of avenues for future exploration; these are discussed in the conclusion section of chapter 6. They include extension of the room temperature absorption spectrum of $[Ni(HBPz_3)_2]$ to the 300-550 nm range to allow measurement of the splitting of the $^3T_{1g}(^3F)$ excited state at room

temperature, measurement of Q-band EPR of both capped nickel compounds at liquid helium temperature, and determination of the crystal structure of at least one of the capped compounds at liquid helium temperature. These last two additional experiments would mean that optical, paramagnetic resonance and structural data would be available for the capped compounds at both room temperature and liquid helium temperature, and would provide a better understanding of temperature dependence of the trigonal ligand fields in these compounds.

# Appendix A: TRIPLE4.BAS, the QuickBasic program written to control the Spex Triplemate

```
'A  custom program (adapted from Spex example programs) to control the
'Spex Model 1877E Triplemate spectrograph
'Declare all subroutines
'Latest modification 15 October 2000
DECLARE SUB WaitWhile (Delay)
DECLARE SUB FlushBuffer ()
DECLARE SUB ReBoot ()
DECLARE SUB MonoChoose (Mono#)
DECLARE SUB FilterInput (Mono#, WLF#, WLS#, GDF#, GDS#)
DECLARE SUB SpectroInput (Mono#, WLF#, WLS#, GDF#, GDS#)
DECLARE SUB Move (Mono#, SPU#, BL#, UL#, LL#, WLF#, WLS#, GDF#, GDS#)
DECLARE SUB MoveRel (Mono#, SPU#, BL#, UL#, LL#, WLF#, WLS#, GDF#,
GDS#)
DECLARE SUB SetSpeed (MNF#, MXF#, RT#)
DECLARE SUB SpeedRead (MNF#, MXF#, RT#)
DECLARE SUB Confirm (NoShow)
DECLARE SUB CloseDown ()
DECLARE SUB HardSet ()
DECLARE SUB MotorBusy ()
DECLARE SUB WaitBefore ()
DECLARE SUB Limstat ()
DECLARE SUB Calibrate (Mono#, WLF#, WLS#)
DECLARE SUB GratingChange (Mono#, GDF#, GDS#)
DECLARE SUB CameraMove ()

PRINT "Welcome to the Sam T-Control (TM) Triplemate program"
'Open the port'
OPEN "com2:4800,N,8,1,RS,DS0" FOR RANDOM AS #2
200
ring = 0
210
```

```
CALL FlushBuffer
PRINT #2, " ";
Delay = .5
CALL WaitWhile(Delay)
IF (LOC(2) > 0) THEN GOTO 220 ELSE GOTO 210
220
ICH$ = INPUT$(1, #2)
PRINT "Character received was ", ICH$
IF ICH$ = "B" OR ICH$ = "b" THEN
GOTO 230
ELSEIF ICH$ = "F" OR ICH$ = "f" THEN
GOTO 250
ELSEIF ICH$ = "*" THEN
GOTO 225
ELSE
END IF
ring = ring + 1: IF ring < 3 THEN GOTO 200 ELSE CALL ReBoot
GOTO 200
225
  CALL FlushBuffer
  PRINT #2, CHR$(247)
  ICH$ = INPUT$(1, #2)
  IF ICH$ = "=" THEN GOTO 230 ELSE GOTO 200
230
  PRINT "Going to main program"
  PRINT #2, "O";
  PRINT #2, "2000"; :
  PRINT #2, CHR$(0);
  WHILE INPUT$(1, #2) <> "*"
  WEND
  PRINT "In main program"
  NoShow = 0
  PRINT #2, "A";
  CALL Confirm(NoShow)
250
```

```
PRINT "Initialise done"
PRINT "RS232 communications established"
SOUND 500, 2: SOUND 1000, 1: SOUND 500, 2
260
CLS
INPUT "What is the current reading on the 'calibrate' display"; WLS#: CLS
INPUT "What is the current reading on the 'filter' display"; WLF#: CLS
PRINT "What is the groove density (in grooves per mm) of the grating"
INPUT "currently in light path of the spectrograph stage"; GDS#: CLS
PRINT "What is the groove density (in grooves per mm) of the gratings"
INPUT "currently in the filter stage"; GDF#: CLS
CALL MonoChoose(Mono#)
IF Mono# = 1 THEN CALL FilterInput(Mono#, WLF#, WLS#, GDF#, GDS#) ELSE
CALL SpectroInput(Mono#, WLF#, WLS#, GDF#, GDS#)
CLS
GOTO 260

SUB Calibrate (Mono#, WLS#, WLF#)
IF Mono# = 0 THEN
INPUT "Enter the reading on the 'calibrate' dial", WLS#
ELSE
INPUT "Enter the reading on the 'filter' dial", WLF#
END IF
END SUB

SUB CameraMove
PRINT "Before proceeding, ensure that the entrance slit viewing camera"
PRINT "is pulled all the way back THEN press any key to continue."
WHILE INKEY$ = ""
SOUND 500, 6
SOUND 1000, 3
SOUND 500, 6
WEND
END SUB
```

```
SUB CloseDown
CLOSE #2
PRINT "Closing program, thank you for visiting, please call again"
END
END SUB

SUB Confirm (NoShow)
ACK$ = INPUT$(1, #2)
IF ACK$ = "o" THEN
IF NoShow <> 1 THEN PRINT "Receive was OK" ELSE
ELSEIF ACK$ = "b" THEN
PRINT "Receive was bad"
PRINT "Character received was "; ASC(ACK$), ACK$
END
END IF
END SUB

SUB FilterInput (Mono#, WLF#, WLS#, GDF#, GDS#)
'Some default values for monochromator parameters
Mono# = 1
SPU# = 50
MNF# = 400
MXF# = 400
RT# = 1000
BL# = 500
UL# = 50000
LL# = 0
30
CLS



PRINT "------------------------------------------------------------"
PRINT "        Spex Triplemate 1877E Filter Options Screen"
PRINT "------------------------------------------------------------"
```

```
PRINT ""
PRINT "Current wavelength setting ="; WLF#; "nm"
PRINT "Grating groove density ="; GDF#; "grooves per millimetre"
PRINT "Actual wavelength passed ="; WLF# * (1200 / GDF#); "nm"
PRINT ""
PRINT "Move filter                    1"
PRINT "Move filter relative           2"
PRINT "Check hardware settings        3"
PRINT "Refresh menu                   4"
PRINT "Change wavelength setting      5"
PRINT "Enter new grating groove density  6"
PRINT "Control spectrograph           7"
PRINT "Quit                          99"
PRINT "                               "
PRINT "                               "
40
INPUT "Enter the number corresponding to your chosen command"; CMDNO#
IF CMDNO# = 99 THEN CALL CloseDown:  ELSE
IF CMDNO# < 1 OR CMDNO# > 7 THEN PRINT "Not an option, please make
another choice.": GOTO 40:  ELSE
IF CMDNO# = 1 THEN CALL Move(Mono#, SPU#, BL#, UL#, LL#, WLF#, WLS#,
GDF#, GDS#): ELSE
IF CMDNO# = 2 THEN CALL MoveRel(Mono#, SPU#, BL#, UL#, LL#, WLF#,
WLS#, GDF#, GDS#): ELSE
IF CMDNO# = 3 THEN CALL HardSet:  ELSE
IF CMDNO# = 4 THEN GOTO 30:  ELSE
IF CMDNO# = 5 THEN CALL Calibrate(Mono#, WLS#, WLF#): ELSE
IF CMDNO# = 6 THEN CALL GratingChange(Mono#, GDF#, GDS#):  ELSE
IF CMDNO# = 7 THEN Mono# = 0: CALL SpectroInput(Mono#, WLF#, WLS#,
GDF#, GDS#)
GOTO 30
END SUB

SUB FlushBuffer
Delay = .5
```

```
CALL WaitWhile(Delay)
WHILE (LOC(2) > 0)
JUNK$ = INPUT$(1, #2): SOUND 2000, 2
WEND
END SUB

SUB GratingChange (Mono#, GDF#, GDS#)
IF Mono# = 0 THEN
PRINT "Currently the groove density of the spectrograph grating "
PRINT "is"; GDS#; "grooves per millimetre."
INPUT "Enter the groove density of the new grating.", GDS#
ELSE
PRINT "Currently the groove density of the filter gratings "
PRINT "is"; GDF#; "grooves per millimetre."
INPUT "Enter the groove density of the new gratings.", GDF#
END IF
END SUB

SUB HardSet
NoShow = 0
PRINT #2, "r";
CALL Confirm(NoShow)
Status$ = INPUT$(1, #2)
IF Status$ = "0" THEN PRINT "System idle"
IF Status$ = "1" THEN PRINT "System busy, a monochromator is stepping"
IF Status$ = "2" THEN PRINT "System busy, controller collecting data"
IF Status$ = "3" THEN PRINT "System busy, controller in DWELL phase"
IF Status$ = "4" THEN PRINT "System busy, controller in DELAY phase"
IF Status$ = "6" THEN PRINT "System busy, controller waiting for trigger"
CALL WaitBefore
END SUB

SUB Limstat
PRINT #2, "K";
NoShow = 1
```

```
CALL Confirm(NoShow)
limit = VAL(INPUT$(1, #2))
PRINT "      "
IF limit > 7 THEN
PRINT "Filter stepper motor has exceeded upper limit"
limit = limit - 8
ELSE PRINT "Filter stepper motor has not exceeded upper limit"
END IF
IF limit > 3 THEN
PRINT "Filter stepper motor has breached lower limit"
limit = limit - 4
ELSE PRINT "Filter stepper motor has not breached lower limit"
END IF
IF limit > 1 THEN
PRINT "Spectrograph stepper motor has exceeded upper limit"
limit = limit - 2
ELSE PRINT "Spectrograph stepper motor has not exceeded upper limit"
END IF
IF limit > 0 THEN
PRINT "Spectrograph stepper motor has breached lower limit"
ELSE PRINT "Spectrograph stepper motor has not breached lower limit"
END IF
PRINT "If any limits have been breached then you'll need to remove the bottom"
PRINT "cover from the appropriate stage of the Triplemate."
PRINT "Check and reset any tripped limit switches (small metal switches at "
PRINT "each end of the brass rods)."
CALL WaitBefore
END SUB

SUB MonoChoose (Mono#)
10
CLS
PRINT "                    "
PRINT "   Do you wish to control the filter stage (f)?"
PRINT "OR Do you wish to control the spectrograph stage (s)?"
```

```
PRINT "OR Do you wish to quit the program (q)?"
INPUT "Enter f, s or q"; monotype$
IF monotype$ = "s" OR monotype$ = "S" THEN
Mono# = 0
ELSEIF monotype$ = "f" OR monotype$ = "F" THEN
Mono# = 1
ELSEIF monotype$ = "q" OR monotype$ = "Q" THEN
CALL CloseDown
ELSE
PRINT "Not an option, please choose again.": GOTO 10
END IF
CLS
END SUB

SUB MotorBusy
3000
PRINT #2, "E";
NoShow = 1
CALL Confirm(NoShow)
Busycheck$ = INPUT$(1, #2)
IF Busycheck$ = "q" THEN
GOTO 3000
ELSEIF Busycheck$ = "z" THEN
END IF
END SUB


SUB Move (Mono#, SPU#, BL#, UL#, LL#, WLF#, WLS#, GDF#, GDS#)
60
IF Mono# = 0 THEN
PRINT "Currently the spectrograph (calibrate) dial is reading"; WLS#; "nm."
AWLS# = WLS# * (1200 / GDS#)
IF GDS# = 1200 THEN PRINT "This is the wavelength of light (in nm) the
spectrograph will pass." ELSE PRINT "This setting will pass light of wavelength";
AWLS#; "nm."
```

```
INPUT "Which wavelength would you like the spectrograph to pass?", WLAIM#
ELSE
CALL CameraMove
PRINT "Currently the filter dial is reading"; WLF#; "nm."
AWLF# = WLF# * (1200 / GDF#)
IF GDF# = 1200 THEN PRINT "This is the wavelength of light the filter stage will
pass." ELSE PRINT "This setting will pass light of wavelength"; AWLF#; "nm."
INPUT "Which wavelength would you like the filter to pass?", WLAIM#
END IF
IF Mono# = 0 THEN
IF WLAIM# * (GDS# / 1200) < LL# / SPU# OR WLAIM# * (GDS# / 1200) > UL# /
SPU# THEN
PRINT "The requested wavelength is outside the limits of the stepper motor."
AUL# = (UL# / SPU#) * (1200 / GDS#)
PRINT "Currently, the available range for the spectrograph stage is"
PRINT "0 to "; AUL#; "nm."
PRINT "Please enter another wavelength or quit the program and turn the"
PRINT "grating turret to a grating with a lower groove density."
GOTO 60
ELSE
END IF
ELSE
IF WLAIM# * (GDF# / 1200) < LL# / SPU# OR WLAIM# * (GDF# / 1200) > UL# /
SPU# THEN
PRINT "The requested wavelength is outside the limits of the stepper motor."
AUL# = (UL# / SPU#) * (1200 / GDF#)
PRINT "Currently, the available range for the filter stage is 0 to "; AUL#; "nm."
PRINT "Please enter another wavelength or quit the program and install gratings"
PRINT "with a lower groove density in the filter stage."
GOTO 60
ELSE
END IF
END IF
IF Mono# = 0 THEN
AWLAIM# = WLAIM# * (GDS# / 1200)
```

```
WL# = WLS#
ELSE
AWLAIM# = WLAIM# * (GDF# / 1200)
WL# = WLF#
END IF
IF AWLAIM# >= WL# THEN
NEWMOVE# = (AWLAIM# - WL#) * SPU#
ELSE
NEWMOVE# = (AWLAIM# - WL#) * SPU# - BL#
END IF
IF Mono# = 0 THEN
WLS# = AWLAIM#
PRINT "Moving spectrograph to target"
ELSE
WLF# = AWLAIM#
PRINT "Moving filter to target"
END IF
PRINT "                "
IF Mono# = 0 THEN
PRINT #2, "F";
PRINT #2, "0,";
PRINT #2, NEWMOVE#
ELSEIF Mono# = 1 THEN
PRINT #2, "F";
PRINT #2, "1,";
PRINT #2, NEWMOVE#
END IF
NoShow = 0
CALL Confirm(NoShow)
CALL MotorBusy
IF NEWMOVE# < 0 THEN
BLM# = BL#
PRINT "Performing a backlash correction."
PRINT "                "
IF Mono# = 0 THEN
```

```
PRINT #2, "F";
PRINT #2, "0,";
PRINT #2, BLM#
ELSEIF Mono# = 1 THEN
PRINT #2, "F";
PRINT #2, "1,";
PRINT #2, BLM#
END IF
NoShow = 0
CALL Confirm(NoShow)
CALL MotorBusy
ELSE
END IF
CALL WaitBefore
END SUB

SUB MoveRel (Mono#, SPU#, BL#, UL#, LL#, WLF#, WLS#, GDF#, GDS#)
INPUT "How far do you want to move the system (in nm)?", WLMOVE#
IF Mono# = 0 THEN
AWLMOVE# = WLMOVE# * (GDS# / 1200)
ELSE
CALL CameraMove
AWLMOVE# = WLMOVE# * (GDF# / 1200)
END IF
IF AWLMOVE# >= 0 THEN
NEWMOVE# = AWLMOVE# * SPU#
ELSE NEWMOVE# = (AWLMOVE# * SPU#) - BL#
END IF
IF Mono# = 0 THEN
PRINT "Moving spectrograph to target."
ELSE PRINT "Moving filter to target."
END IF
PRINT "                "
IF Mono# = 0 THEN
PRINT #2, "F";
```

```
PRINT #2, "0,";
PRINT #2, NEWMOVE#
ELSEIF Mono# = 1 THEN
PRINT #2, "F";
PRINT #2, "1,";
PRINT #2, NEWMOVE#
END IF
NoShow = 0
CALL Confirm(NoShow)
CALL MotorBusy
IF Mono# = 0 THEN
WLS# = WLS# + AWLMOVE#
ELSE WLF# = WLF# + AWLMOVE#
END IF
IF NEWMOVE# < 0 THEN
PRINT "Performing a backlash correction."
PRINT "                    "
IF Mono# = 0 THEN
PRINT #2, "F";
PRINT #2, "0,";
PRINT #2, BL#
ELSEIF Mono# = 1 THEN
PRINT #2, "F";
PRINT #2, "1,";
PRINT #2, BL#
END IF
NoShow = 0
CALL Confirm(NoShow)
CALL MotorBusy
ELSE
END IF
CALL WaitBefore
END SUB

SUB ReBoot
```

```
PRINT #2, CHR$(248);
PRINT #2, CHR$(222);
Delay = .5
CALL WaitWhile(Delay)
END SUB

SUB SetSpeed (MNF#, MXF#, RT#)
INPUT "Enter the desired minimum frequency in Hz."; MiNFReq#
INPUT "Enter the desired maximum frequency in Hz."; MaXFreq#
INPUT "Enter the desired ramp time in milliseconds."; RampTime#
PRINT #2, "B";
PRINT #2, "0,";
PRINT #2, MiNFReq#;
PRINT #2, ",";
PRINT #2, MaXFreq#;
PRINT #2, ",";
PRINT #2, RampTime#
NoShow = 0
CALL Confirm(NoShow)
CALL WaitBefore
END SUB



SUB SpectroInput (Mono#, WLF#, WLS#, GDF#, GDS#)
Mono# = 0
SPU# = 4000
MNF# = 1000
MXF# = 40000
RT# = 2000
BL# = 40000
UL# = 4000000
LL# = 0
20
CLS
```

```
PRINT "------------------------------------------------------------"
PRINT "      Spex Triplemate 1877E Spectrograph Options Screen"
PRINT "------------------------------------------------------------"
PRINT ""
PRINT "Current wavelength setting ="; WLS#; "nm"
PRINT "Grating groove density ="; GDS#; "grooves per millimetre"
PRINT "Actual wavelength passed ="; WLS# * (1200 / GDS#); "nm"
PRINT ""
PRINT "Move spectrograph              1"
PRINT "Move spectrograph relative     2"
PRINT "Set stepping speed             3"
PRINT "Read stepping speed            4"
PRINT "Check hardware settings        5"
PRINT "Refresh menu                   6"
PRINT "Check limit status             7"
PRINT "Change wavelength setting      8"
PRINT "Enter new grating groove density  9"
PRINT "Control filter                10"
PRINT "Quit                          99"
PRINT "                              "
PRINT "                              "
25
INPUT "Enter the number corresponding to your chosen command"; CMDNO#
IF CMDNO# = 99 THEN CALL CloseDown:  ELSE
IF CMDNO# < 1 OR CMDNO# > 10 THEN PRINT "Invalid input, please retry":
GOTO 25:  ELSE
IF CMDNO# = 1 THEN CALL Move(Mono#, SPU#, BL#, UL#, LL#, WLF#, WLS#,
GDF#, GDS#): ELSE
IF CMDNO# = 2 THEN CALL MoveRel(Mono#, SPU#, BL#, UL#, LL#, WLF#,
WLS#, GDF#, GDS#): ELSE
IF CMDNO# = 3 THEN CALL SetSpeed(MNF#, MXF#, RT#):  ELSE
IF CMDNO# = 4 THEN CALL SpeedRead(MNF#, MXF#, RT#):  ELSE
IF CMDNO# = 5 THEN CALL HardSet:  ELSE
IF CMDNO# = 6 THEN GOTO 20:  ELSE
IF CMDNO# = 7 THEN CALL Limstat:  ELSE
```

```
IF CMDNO# = 8 THEN CALL Calibrate(Mono#, WLS#, WLF#): ELSE
IF CMDNO# = 9 THEN CALL GratingChange(Mono#, GDF#, GDS#): ELSE
IF CMDNO# = 10 THEN Mono# = 1: CALL FilterInput(Mono#, WLF#, WLS#, GDF#,
GDS#)
GOTO 20
END SUB

SUB SpeedRead (MNF#, MXF#, RT#)
PRINT #2, "C";
PRINT #2, "0"
NoShow = 0
CALL Confirm(NoShow)
INPUT #2, MiNFReq#, MaXFreq#, RampTime#
PRINT "minimum frequency = ", MiNFReq#
PRINT "maximum frequency = ", MaXFreq#
PRINT "ramp time       = ", RampTime#
CALL WaitBefore
END SUB

SUB WaitBefore
PRINT "Press any key to continue"
WHILE INKEY$ = ""
WEND
END SUB

SUB WaitWhile (Delay)
T0 = TIMER
WHILE ((TIMER - T0) < Delay)
WEND
END SUB
```

# Appendix B: Raman spectroscopy of cobalt and nickel bromates

## B.1 Introduction

This chapter presents the Raman spectral data for the metal bromate hexahydrates. As discussed earlier in the thesis, the aim of measuring the Raman spectra was to locate peaks due to electronic transitions. The transition energies would then have provided information about the trigonal field strength. Unfortunately, no electronic peaks could be positively identified. As a result, the Raman data could not be used to support the discussion on trigonal fields. Therefore, these data have been presented in a separate appendix.

## B.2 Experimental

The compounds $[Co(H_2O)_6](BrO_3)_2$ and $[Ni(H_2O)_6](BrO_3)_2$ were prepared using the method described in section 5.3.1.

Raman spectra of the complexes $[M(H_2O)_6](BrO_3)_2$ and $[M(HCPz_3)_2](NO_3)_2$ (where M = Co, Ni, or Zn) were measured using the laboratory-built (PM tube) Raman spectrometer in the Krausz group, described in detail in chapter 2. The Hamamatsu 943-02 tube was employed for this work, due to its higher sensitivity. Excitation was via various lines of a Spectra Physics krypton ion laser, depending on the colour of the sample being studied.

Spectra were measured for single crystals. Identification of the electronic Raman peaks in the cobalt(II) spectra was attempted by a simple method. This involved direct comparison of the Raman spectra of $[Co(H_2O)_6](BrO_3)_2$ with those of $[Ni(H_2O)_6](BrO_3)_2$. Nickel(II) complexes have an orbitally non-degenerate ground state in octahedral geometry. Octahedral nickel(II) compounds have a spin triplet ground state. This is split by an axial ligand field, however, the splitting is only of the order of 1 $cm^{-1}$, as opposed to the few hundreds of $cm^{-1}$ expected for the low lying excited states of trigonally distorted cobalt(II). Therefore, nickel(II) bromate hexahydrate will have no low-lying electronic excited states

detectable by Raman spectroscopy. Since the two bromate compounds are isostructural, the vibrational Raman spectra are very similar, so electronic Raman bands in the cobalt complexes can in theory be identified by a 'subtraction' method.

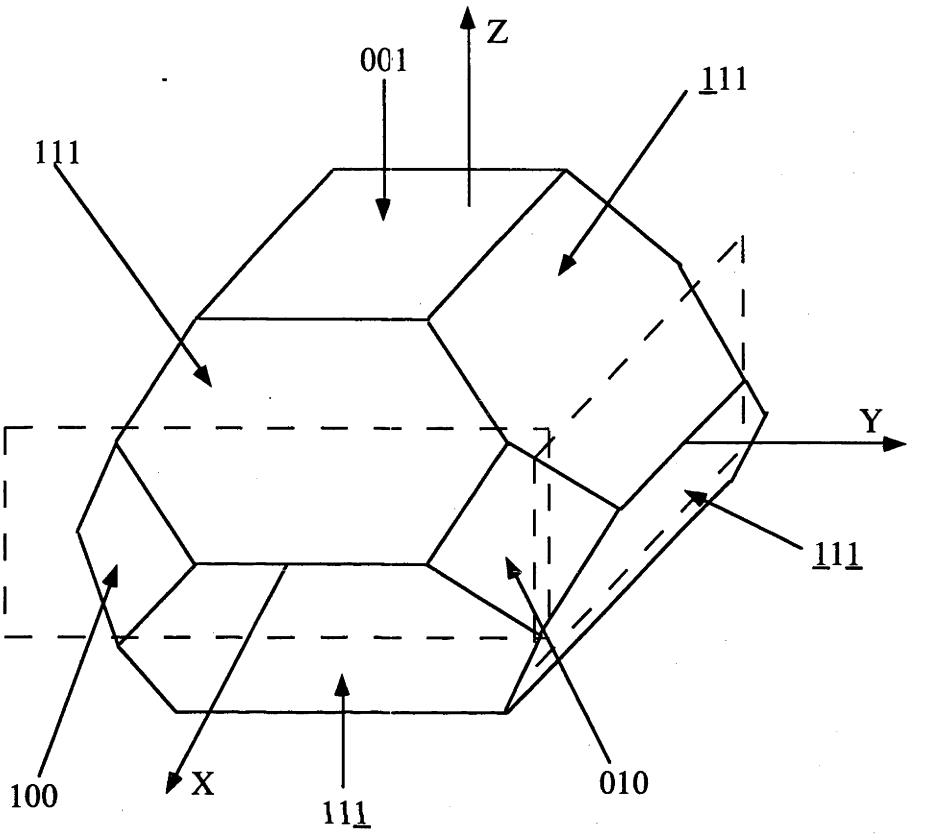


**Figure B.1: The cube-octahedral form of the metal bromate hexahydrate crystals used for polarised Raman measurements. Two mutually perpendicular dodecahedral faces (type 110 and $\underline{1}10$, indicated by the dashed rectangles) were polished perpendicular to a well-developed cubic face.**

Since the bromates have cubic crystal structures, they are optically isotropic. They also have the same space group as the alums ($Pa\bar{3}$). Polarised Raman spectra of the bromates were therefore measured using the same configuration as employed by several authors for Raman spectra of the alums[1-4]. Crystals with the form of an octahedron or cube-octahedron (well-developed 100, 010, 001, 111, $\underline{1}11$, $1\underline{1}1$ and $11\underline{1}$ faces) were selected from those grown from aqueous solution in a refrigerator (figure B.1).

Using 1600 mesh silicon carbide (Wet and Dry) paper, a cubic face (e.g. 001) was polished, along with two perpendicular dodecahedral faces (type 110 and 1$\underline{1}$0). The X, Y and Z directions for the polarised spectra were defined as the perpendiculars to the 110, 1$\underline{1}$0, and 001 faces respectively (figure B.1). In order to expand existing faces, the crystal was mounted via the opposite face to a brass rod, which was in turn held inside a hollow aluminium cylinder by screws. In this way the amount of crystal protuding past the flat face of the aluminium cylinder could be varied and the crystal face could readily be polished until flush with the cylinder face. To create a new face by polishing the crystal was mounted on the edge of a flat aluminium plate (approximate dimensions 60×25×3mm). This plate was then held between two similar parallel plates with the 'crystal' plate mounted at an appropriate angle (e.g. to polish a new cubic face in a crystal mounted via an octahedral face, the angle used was 55°).

The adhesive chosen for all polishing operations was Superglue, since it is readily removed with acetone solvent and the bromate hydrates are all insoluble in acetone. Final polishing was carried out using filter paper and water, then lens tissue and water.

**Table B.1: Experimental parameters used in the Raman spectra of the metal bromates**

| Figure | T (K) | Excitation wavelength (nm) | Polarisation | Time/step (s) | Bandpass ($cm^{-1}$) | Step size ($cm^{-1}$) |
|---|---|---|---|---|---|---|
| B.2 | 9±1 | 568.2 | zz | 2 | 1.6 | 0.25 |
| B.3 | 9±1 | 568.2 | zy | 2 | 1.6 | 0.25 |
| B.4 | 6.5±1.5 | 568.2 | xy | 2 | 1.6 | 0.25 |
| B.5 | 9±1 | 568.2 | zz | 2 | 1.5 | 0.25 |
| B.6 | 9±1 | 568.2 | zy | 2 | 1.5 | 0.25 |
| B.7 | 9±1 | 568.2 | xy | 2 | 1.5 | 0.25 |
| B.8 | 7±1.5 | 530.9 | zz | 2 | 1.8 | 0.25 |
| B.9 | 7±1.5 | 530.9 | zy | 2 | 1.8 | 0.25 |
| B.10 | 7±1.5 | 530.9 | zz | 2 | 1.8 | 0.25 |
| B.11 | 7±1.5 | 530.9 | zy | 2 | 1.8 | 0.25 |

Crystals were mounted in one of two orientations for polarised Raman spectroscopy; either exciting along the X or Y axis and collecting along the Z, or exciting along the X (Y) and collecting along the Y (X). For unpolarised work, crystals were mounted in an arbitrary orientation.

## B.3 Results

Strongly polarised Raman spectra were observed in the region 50-1000 $cm^{-1}$, for both $[Co(H_2O)_6](BrO_3)_2$ and $[Ni(H_2O)_6](BrO_3)_2$. The spectra of the nickel compound were of lower quality due to the higher background. The isostructural nature of the two compounds is clearly reflected in the spectra. As discussed in the experimental section above, the three polarisations shown in the spectra in figures B.2-B.13 below allow observation of all Raman bands in a $Pa\bar{3}$ cubic crystal. Spectral parameters are shown in table B.1 above.

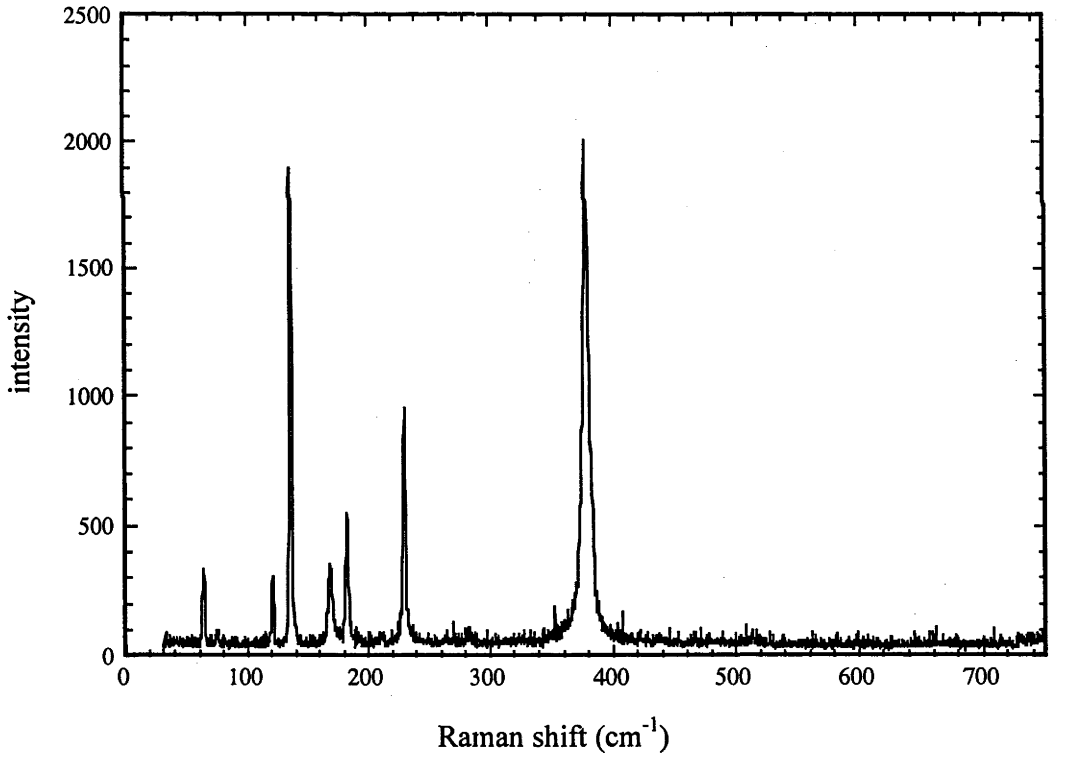


**Figure B.2: Raman spectrum of $[Co(H_2O)_6](BrO_3)_2$ (polarisation zz)**

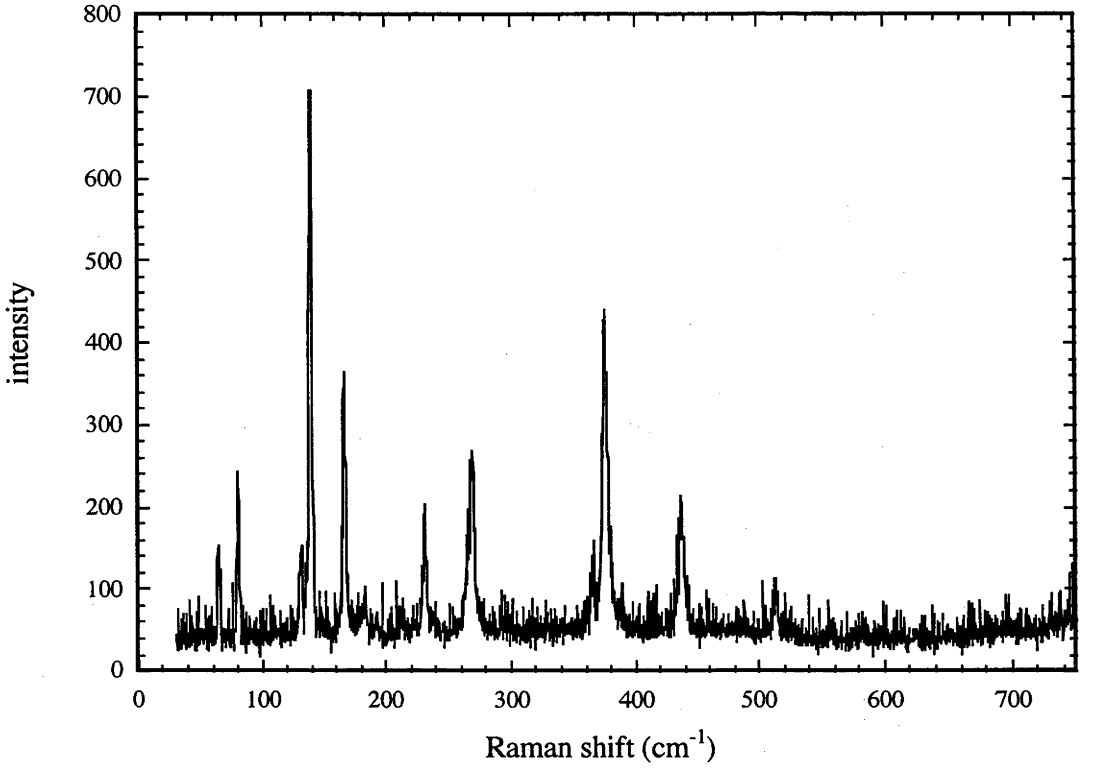


**Figure B.3: Raman spectrum of $[Co(H_2O)_6](BrO_3)_2$ (polarisation zy)**

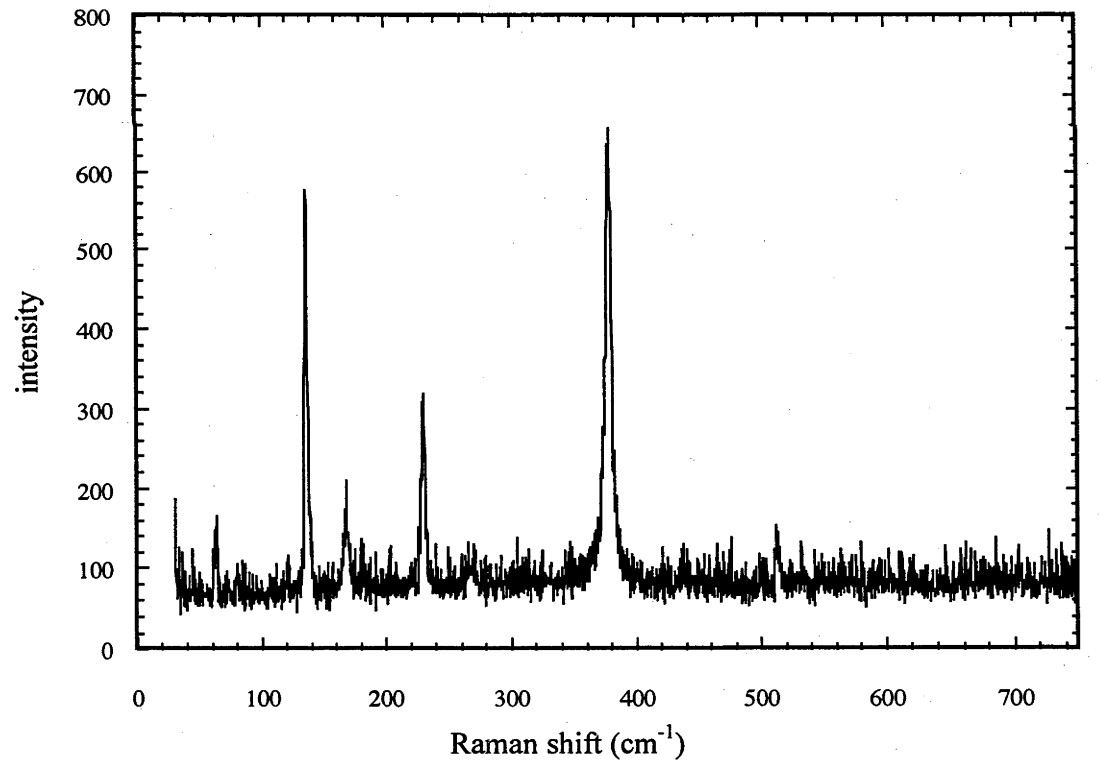


**Figure B.4: Raman spectrum of $[Co(H_2O)_6](BrO_3)_2$ (polarisation xy)**

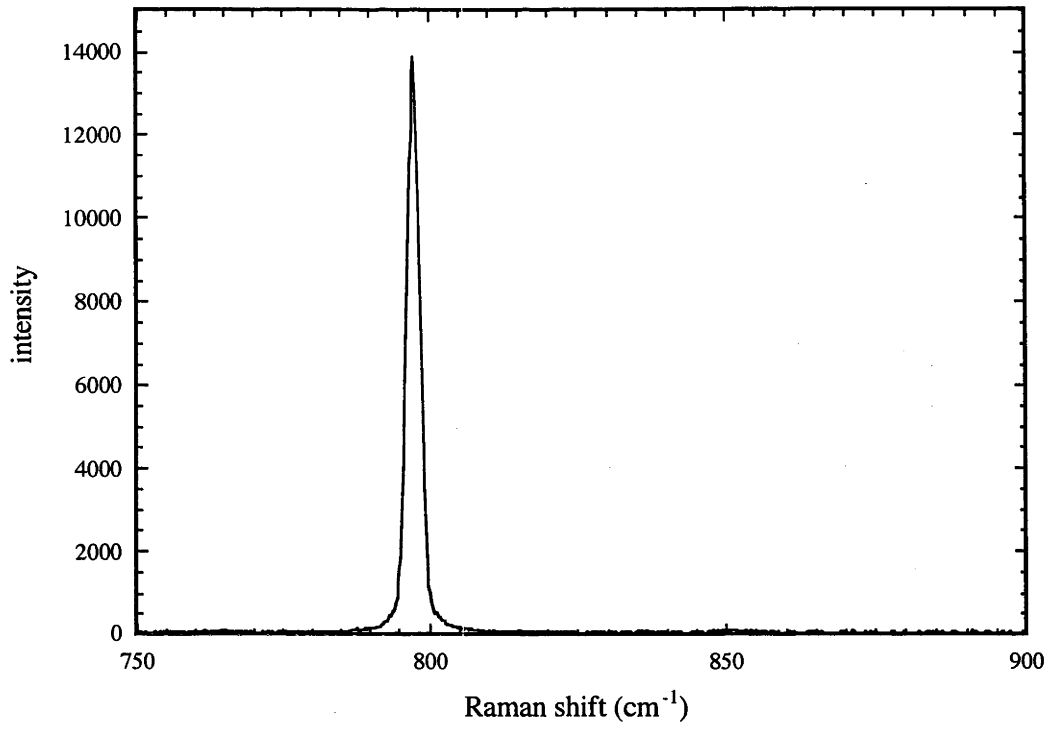


**Figure B.5: Raman spectrum of $[Co(H_2O)_6](BrO_3)_2$ (polarisation zz)**

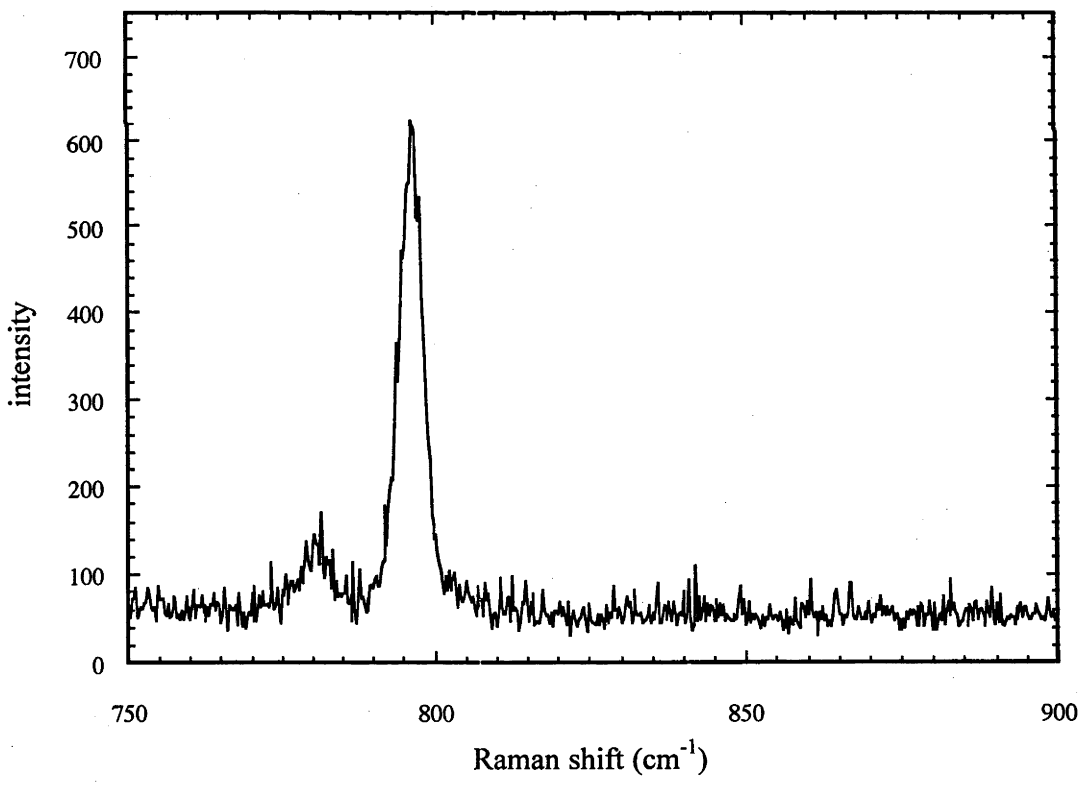


**Figure B.6: Raman spectrum of $[Co(H_2O)_6](BrO_3)_2$ (polarisation zy)**

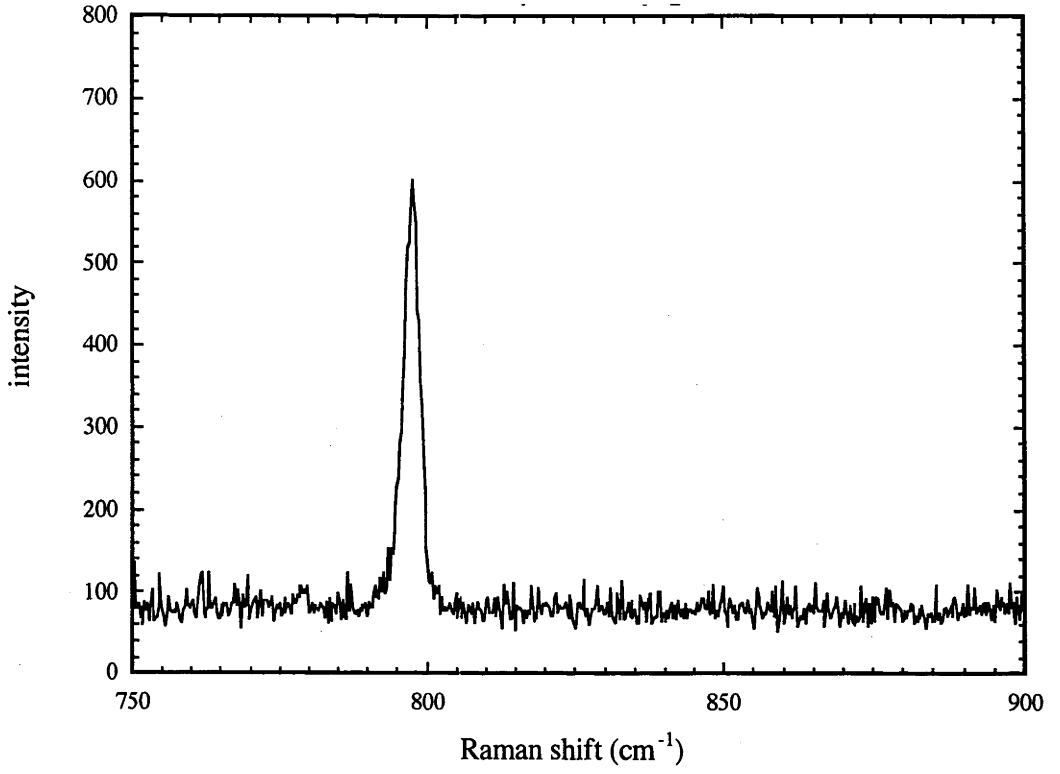


**Figure B.7: Raman spectrum of $[Co(H_2O)_6](BrO_3)_2$ (polarisation xy)**

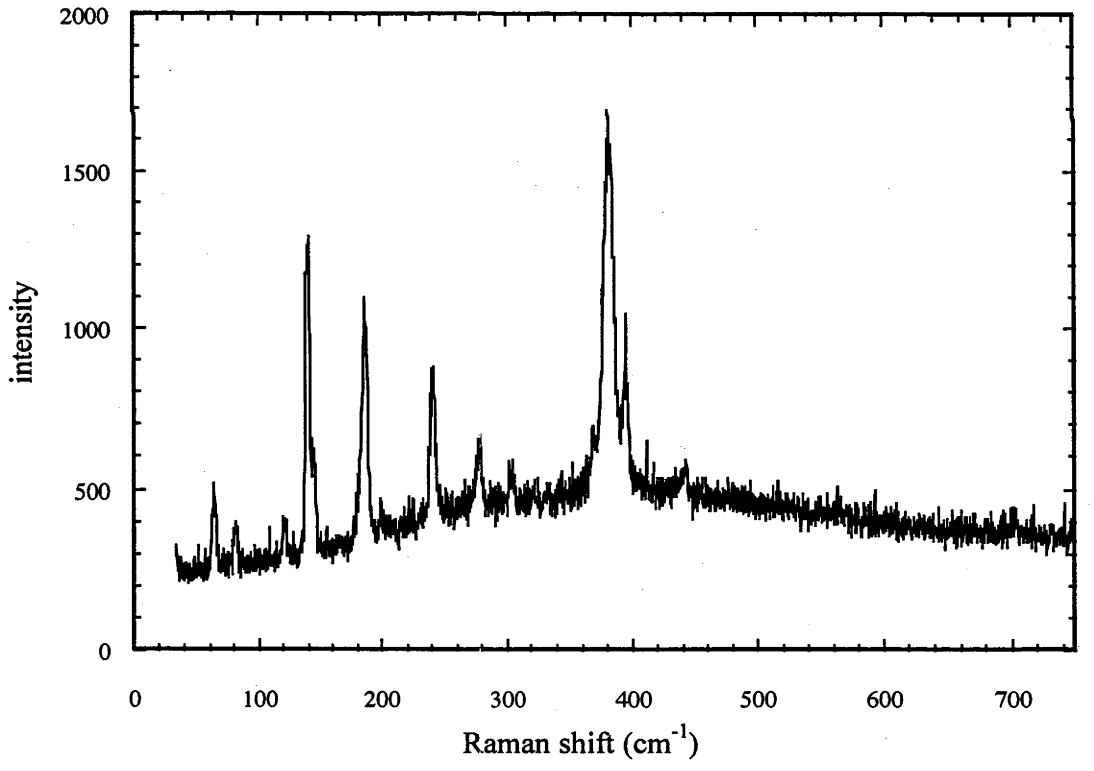


**Figure B.8: Raman spectrum of $[Ni(H_2O)_6](BrO_3)_2$ (polarisation zz)**

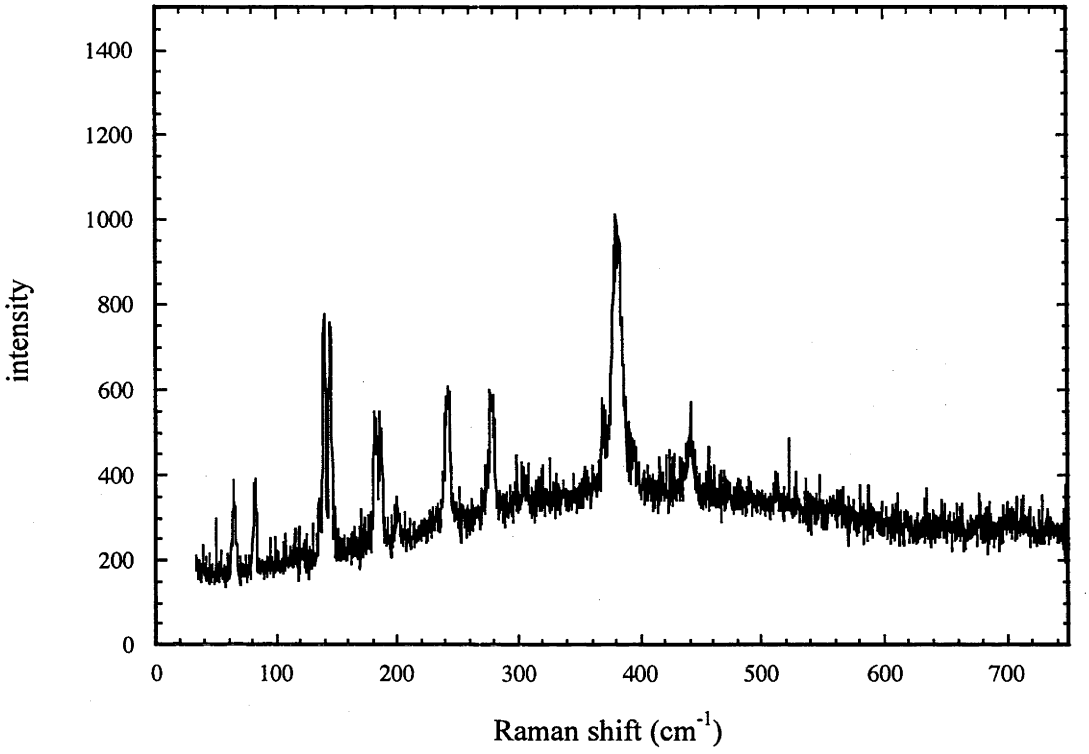


**Figure B.9: Raman spectrum of $[Ni(H_2O)_6](BrO_3)_2$ (polarisation zy)**

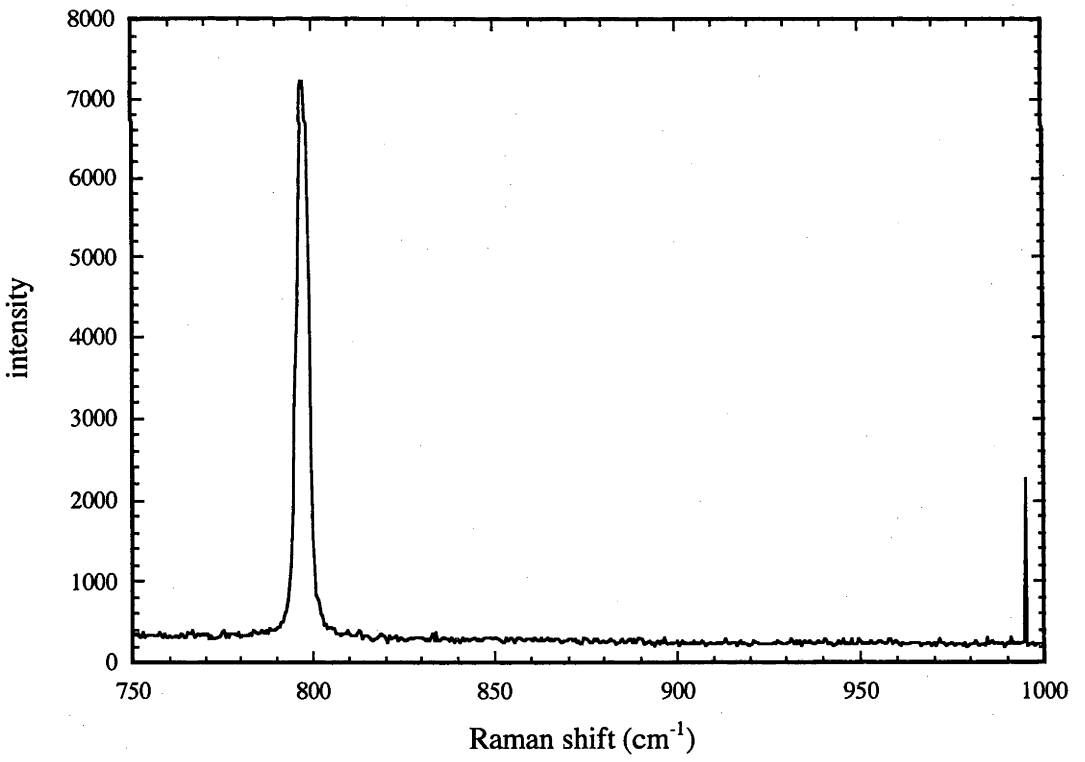


**Figure B.10: Raman spectrum of $[Ni(H_2O)_6](BrO_3)_2$ (polarisation zz)**

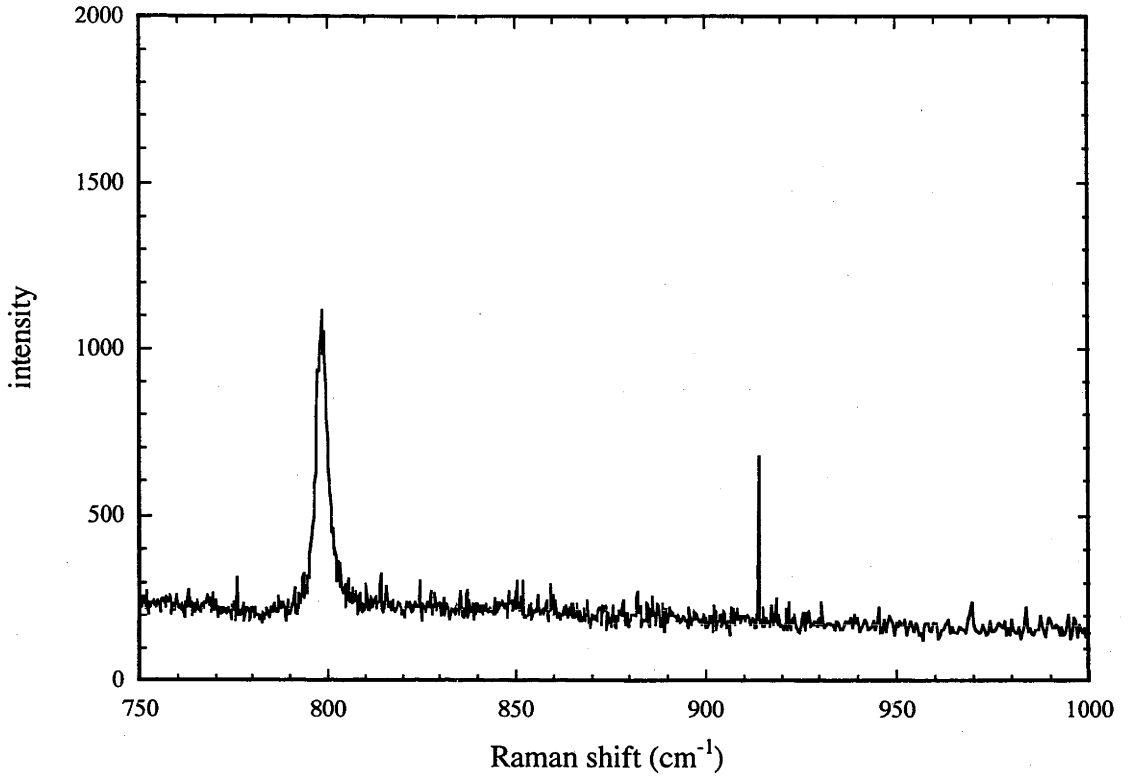


**Figure B.11: Raman spectrum of $[Ni(H_2O)_6](BrO_3)_2$ (polarisation zy)**

The peak positions are tabulated below (table B.2). There are five peaks in the cobalt spectra that cannot be immediately 'matched' to peaks in the nickel spectra (those at 131, 167-168, 513, 780 and 851 $cm^{-1}$). Of these, there appears to be a peak in the $[Ni(H_2O)_6](BrO_3)_2$ zy spectrum (figure B.9) in the region of 513 $cm^{-1}$, however it is indistinct, and can barely be distinguished from the background. The 850 $cm^{-1}$ peak is weak in the cobalt spectra, and any such peak in the nickel spectra could well be hidden as a result of background noise. A similar argument can be made for the 780 $cm^{-1}$ peak. The peaks at 167-168 $cm^{-1}$, which are prominent in all three polarisations of the $[Co(H_2O)_6](BrO_3)_2$ spectra have a very similar width to the surrounding vibrational peaks. Electronic Raman peaks are generally broader than vibrational Raman peaks, as they are affected by inhomogeneous broadening to a much greater degree. Therefore, the 167-168 $cm^{-1}$ peaks cannot be conclusively identified as electronic Raman peaks. A similar argument can be advanced for the 131 $cm^{-1}$ peak, which is only present as a shoulder in the zy spectrum of the cobalt compound (figure B.3). Finally, no peaks can be observed in the 1000-2000 $cm^{-1}$ region of the cobalt spectra (spectra not shown). This is the region where

the peaks arising from transitions to the two Kramers doublets of the $^4A_g$ component of the $^4T_{1g}$ ground state are expected (see table 5.11).

**Table B.2: Experimentally measured Raman frequencies**

| $[Co(H_2O)_6](BrO_3)_2$ | | | $[Ni(H_2O)_6](BrO_3)_2$ | |
|---|---|---|---|---|
| zz | zy | xy | zz | zy |
| 63 | 65 | 63 | 65 | 65 |
| | 80 | | 81 | 83 |
| 121 | | | 121 | |
| | 131 | | | |
| 136 | 139 | 135 | 139 | 139, 145 |
| 168 | 167 | 168 | | |
| 183 | | | 186 | 182, 186 |
| 228 | 230 | 230 | 241 | 242 |
| | 268 | | 277 | 278 |
| 378 | 376 | 377 | 381 | 369, 381 |
| | 436 | | | 440 |
| | 513 | 513 | | |
| | 780 | | | |
| 797 | 796 | 798 | 797 | 798 |
| 851 | | | | |

## B.4 Conclusion

Although polarised Raman spectra were successfully measured for cobalt and nickel bromate, the primary aim of determining the transition energies to the trigonally split components of the $^4T_{1g}$ ground state manifold of Co(II) was not achieved. Electronic Raman transitions could not be identified in the spectra of $[Co(H_2O)_6](BrO_3)_2$. The most likely reason is broadening of the peaks as a result of the short lifetimes of the low-lying electronic excited states.

## B.5 References

(1) Best, S. P.; Armstrong, R. S.; Beattie, J. K. *Journal of the Chemical Society Dalton Transactions* **1982**, 1655-1664.

(2) Best, S. P.; Armstrong, R. S.; Beattie, J. K. *Journal of the Chemical Society, Dalton Transactions* **1992**, 299-304.

(3) Tregenna-Piggott, P. L. W.; Best, S. P. *Inorganic Chemistry* **1996**, *35*, 5730-5736.

(4) Tregenna-Piggott, P. L. W.; Best, S. P.; Guedel, H. U.; Weihe, H.; Wilson, C. C. *Journal of Solid State Chemistry* **1999**, *145*, 460-470.

# Appendix C: Raman spectroscopy of cobalt and zinc pyrazolyl methane complexes

## C.1 Introduction

This appendix presents the Raman spectral data for the metal pyrazolyl methane complexes. As discussed earlier, the aim of measuring the Raman spectra was to locate peaks due to electronic transitions. The transition energies would then have provided information about the trigonal field strength. Unfortunately, no electronic peaks could be positively identified. As a result, the Raman data could not be used to discuss the trigonal fields. Therefore, this data has been presented in a separate appendix.

## C.2 Experimental

The compounds $[Co(HCPz_3)_2](NO_3)_2$ and $[Zn(HCPz_3)_2](NO_3)_2$ were prepared as described in section 6.3.1.

Raman spectra of the complexes $[M(HCPz_3)_2](NO_3)_2$ (where M = Co or Zn) were measured using the laboratory-built (PM tube) Raman spectrometer in the Krausz group, described in detail in chapter 2. The Hamamatsu 943-02 tube was employed for this work, due to its higher sensitivity. Excitation was via various lines of a Spectra Physics krypton ion laser, depending on the colour of the sample being studied. As for the metal bromate hydrates, the idea was to compare the Raman spectra of the zinc compound (which would contain only vibrational peaks) with those from the cobalt compound which in theory will also contain electronic Raman peaks.

Since $[M(HCPz_3)_2](NO_3)_2$ compounds all crystallise in monoclinic space groups, the crystals are optically biaxial. Furthermore, symmetry requirements only dictate that the b crystallographic axis is parallel to one of the axes of the triaxial optical indicatrix. The

other two optical axes can lie in any position in the ac (010) crystallographic plane, not necessarily parallel to either of the a or c crystallographic axes[1]. This means that only crystal faces that are parallel to the b crystal axis will necessarily have extinction directions which are parallel and perpendicular to the crystal edges. It will, as a rule, only be possible to cut two mutually perpendicular faces that have parallel extinction directions for a monoclinic crystal. This contrasts with orthorhombic crystals where it is always possible to cut three mutually perpendicular faces with parallel extinction directions.

**Table C.1: Polarised Raman scattering in monoclinic crystals**

| Geometry | Excitation direction | Scattering direction | Possible for the monoclinic crystal? | Tensor components |
|---|---|---|---|---|
| 90° | x | y | No | zz, zx, yz, yx |
| 90° | x | z | Yes | yy, yx, zy, zx |
| 90° | y | z | No | xx, xy, zx, zy |
| 180° | x | x | Yes | yy, zz, yz |
| 180° | y | y | No | xx, zz, xz |
| 180° | z | z | Yes | xx, yy, xy |

To measure polarised Raman spectra for biaxial crystals (or uniaxial crystals in directions not perpendicular to the c crystallographic axis), it is necessary that the incident and scattered light is polarised along a crystal extinction direction. This requirement, coupled with the restrictions mentioned in the above paragraph mean that it can be difficult to measure Raman spectra for all combinations of incident and scattered light polarisation for monoclinic crystals. This is illustrated in figure C.1 and table C.1.

As can be seen from table C.1, using only 90° geometry Raman measurements for a monoclinic crystal allows determination of the yy, yx, zy and zx components of the Raman tensor. This leaves two of the six components of a symmetric tensor undetermined, the xx and zz components. Using only 180° geometry for monoclinic crystals allows measurement of the xx, yy, zz, yz and xy components, leaving the xz undetermined. If both 90° and 180° measurements are made, then all components can be determined. For

orthorhombic crystals, all six geometries are possible, so all six tensor components can be obtained from either 90° or 180° measurements.

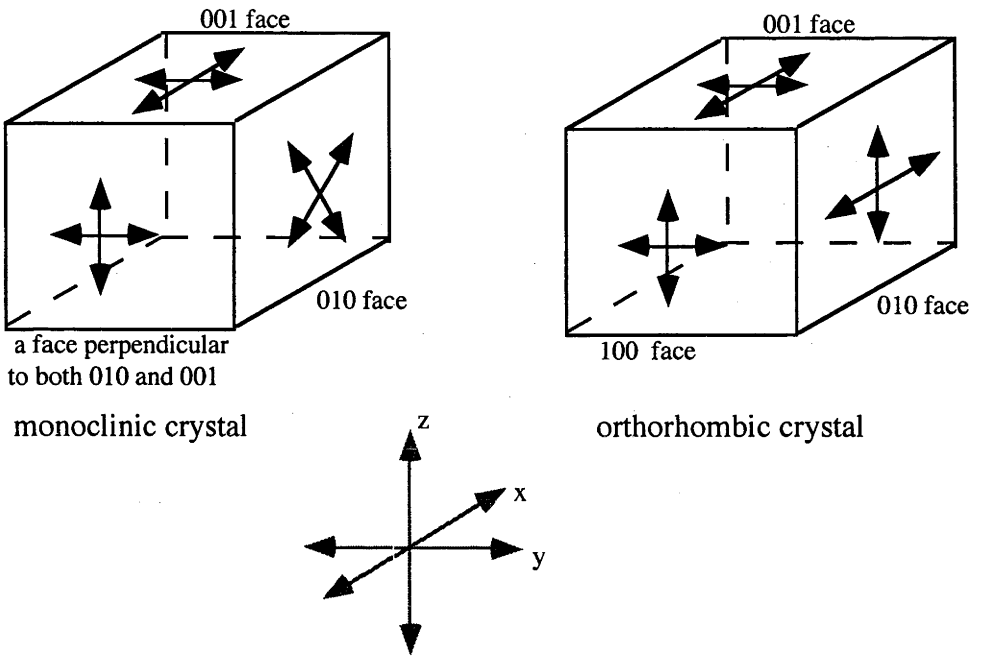


**Figure C.1: Polarised Raman spectroscopy of orthorhombic vs. monoclinic crystals**

Since only a 90° Raman spectrometer was available with the low temperature apparatus necessary for electronic Raman measurements, only limited polarised single crystal work was possible for the $[M(HCPz_3)_2](NO_3)_2$ complexes. A particularly well-developed face is the 10$\underline{1}$, which was used as the collection face in these experiments (see figure C.2). A face was polished perpendicular to the 101 (using the same methods described for the bromates), so that it would also be perpendicular to the 010 face. The excitation and collection faces then have three mutually perpendicular extinction directions, allowing the measurement of polarised Raman spectra with excitation along the y-axis and collection along the x-axis.

The spectra shown were all measured at temperatures of around 7-10 K, using the 568.2 nm line krypton ion laser as the excitation wavelength.

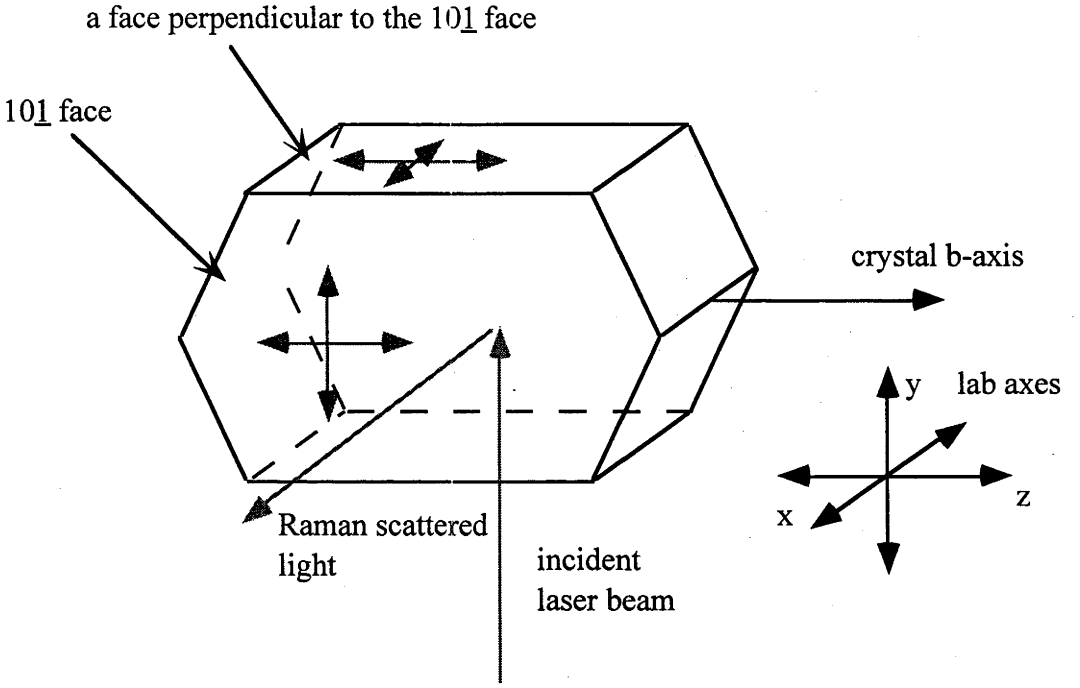


**Figure C.2: Crystal geometry employed for the Raman spectra of $[Co(HCPz_3)_2](NO_3)_2$ and $[Zn(HCPz_3)_2](NO_3)_2$**

## C.3 Results

Measurement of the spectra of these $[M(HCPz_3)_2](NO_3)_2$ compounds has often been hampered by fluorescence swamping the Raman peaks. This has particularly been a problem with the zinc compound where the ligand was prepared by the first synthetic method discussed in section 6.3.1. The problem has been largely remedied since the second synthetic method for the $HCPz_3$ ligand was employed. This synthesis produces much less brown residue, which suggests that the fluorescence was most likely due to such an impurity. Some fluorescence can be seen in the spectra of the cobalt compound. Only the zz polarisation spectra of the two compounds are shown, but peaks from all four polarisations are tabulated.

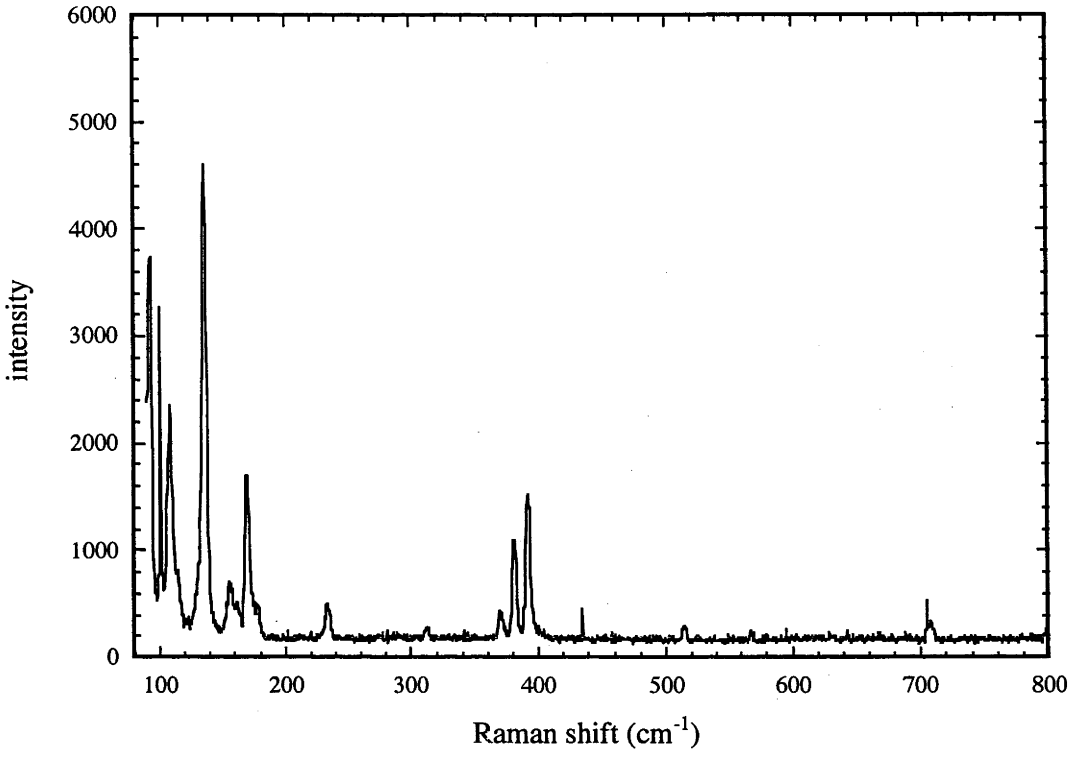


**Figure C.3: Low temperature Raman spectrum of $[Zn(HCPz_3)_2](NO_3)_2$ (zz pol)**

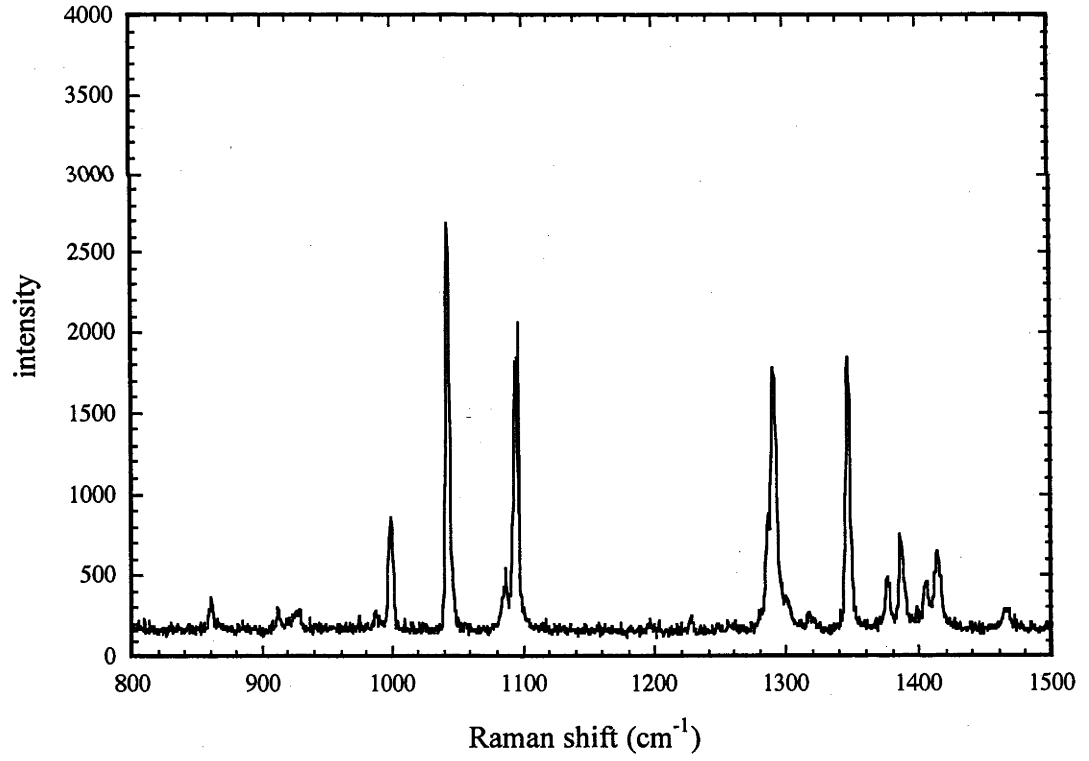


**Figure C.4: Low temperature Raman spectrum of $[Zn(HCPz_3)_2](NO_3)_2$ (zz pol)**

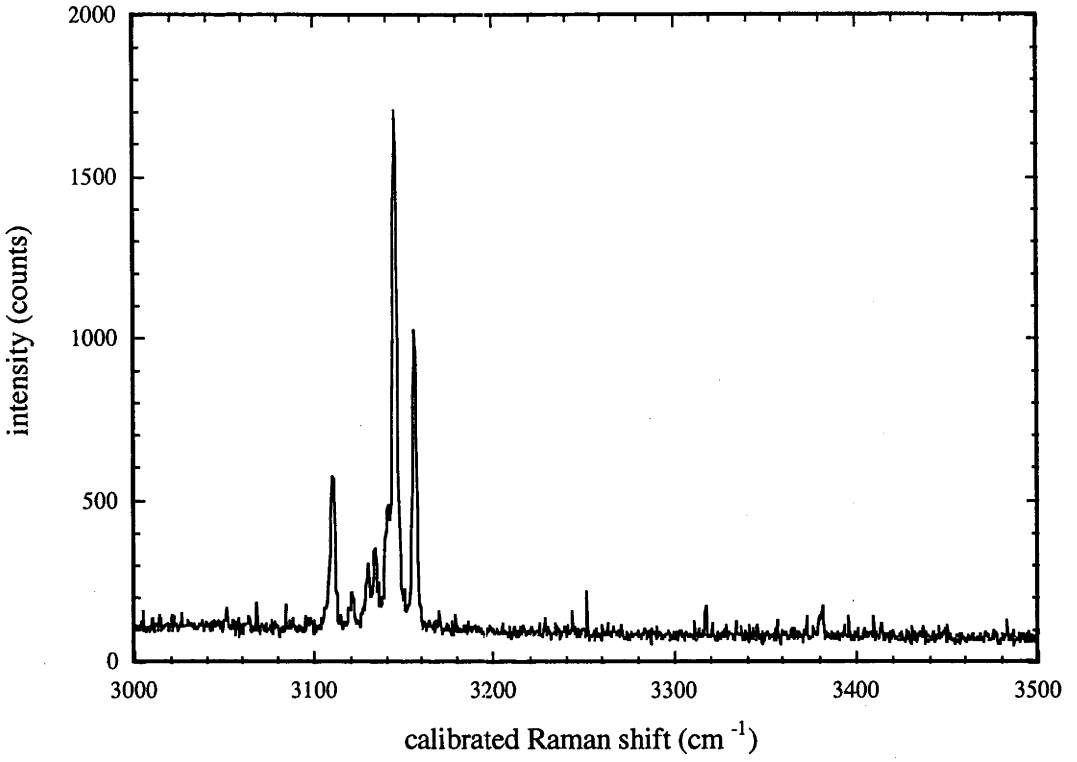


**Figure C.5: Low temperature Raman spectrum of $[Zn(HCPz_3)_2](NO_3)_2$ (zz pol)**

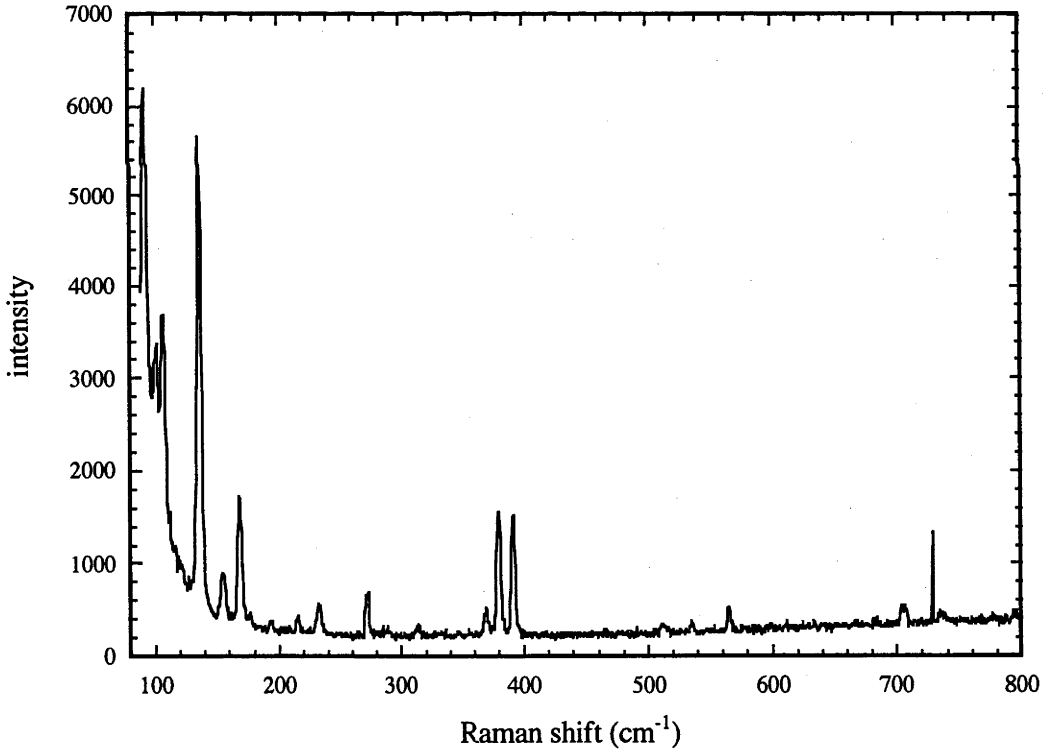


**Figure C.6: Low temperature Raman spectrum of $[Co(HCPz_3)_2](NO_3)_2$ (zz pol)**

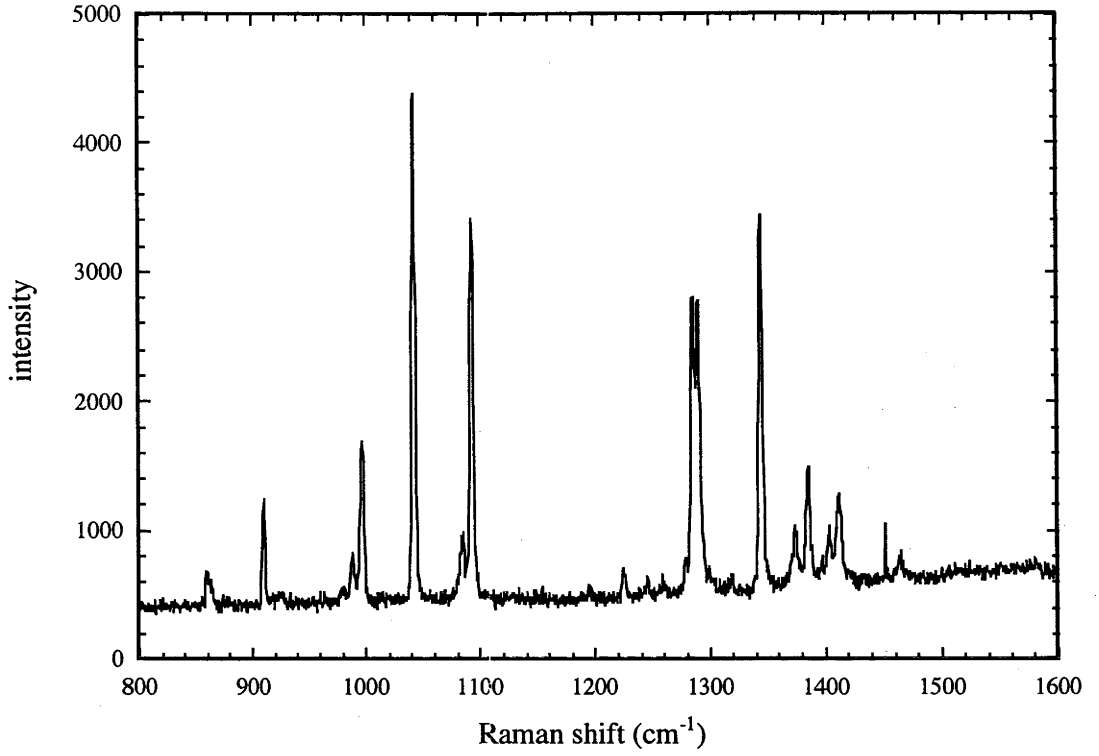


**Figure C.7: Low temperature Raman spectrum of $[Co(HCPz_3)_2](NO_3)_2$ (zz pol)**

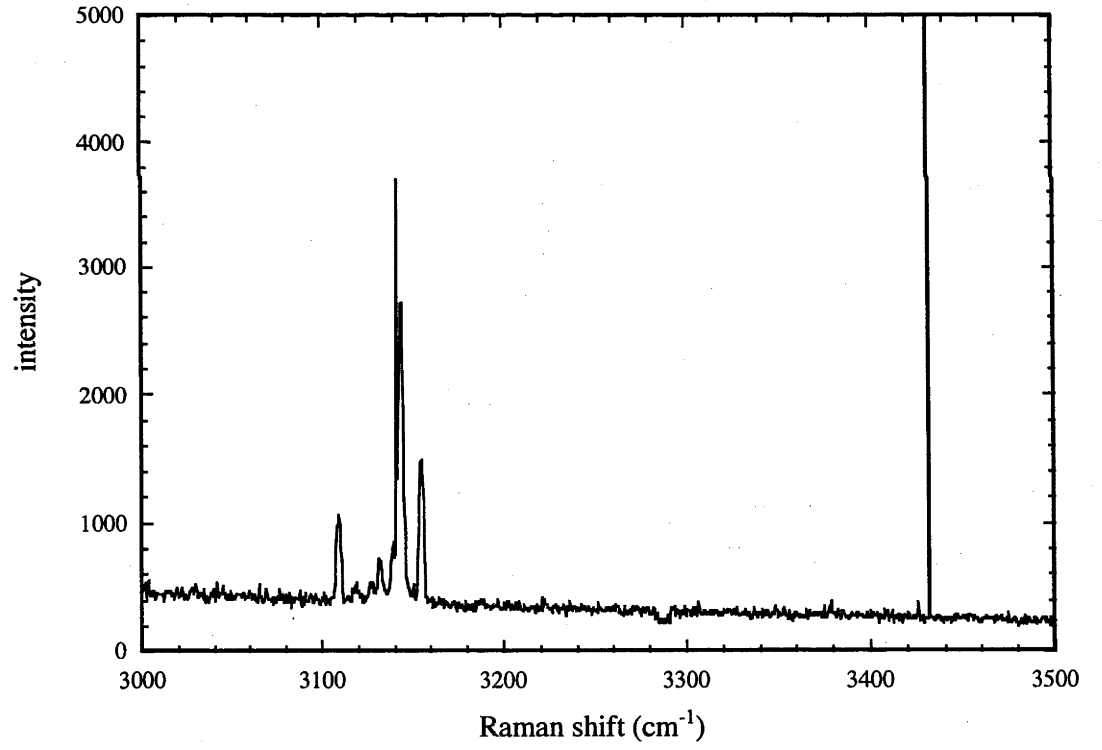


**Figure C.8: Low temperature Raman spectrum of $[Co(HCPz_3)_2](NO_3)_2$ (zz pol)**

## Table C.2: Peak locations in the Raman spectra of $[Zn(HCPz_3)_2](NO_3)_2$

| Raman shift ($cm^{-1}$) | Polarisation | Assignment |
|---|---|---|
| 91.5 | zy, xz | |
| 92 | zz | |
| 97 | zy | |
| 99 | xy | |
| 103 | xz, zy | |
| 106 | xy | |
| 108.5 | zz | |
| 111 | zy | |
| 111.5 | xz | |
| 127.5 | xy | |
| 133.5 | zy, xy | |
| 134.5 | xz | |
| 135.5 | zz | |
| 154 | xy | |
| 156 | zz | |
| 158 | zy | |
| 160 | xz | |
| 166.5 | zy | |
| 167.5 | xy | |
| 169 | xz | |
| 169.5 | zz | |
| 175 | zy | |
| 176 | xz | |
| 230 | zy | |
| 230.5 | xy | |
| 233 | zz | |
| 309.5 | xy | |
| 310 | zy | |
| 312 | xz | |

**Table C.2 (continued)**

| Raman shift ($cm^{-1}$) | Polarisation | Assignment |
|---|---|---|
| 313 | zz | |
| 367 | zy | $Zn(N)_6$ |
| 368 | xy | $Zn(N)_6$ |
| 369.5 | zz | $Zn(N)_6$ |
| 378 | zy | $Zn(N)_6$ |
| 379 | xy | $Zn(N)_6$ |
| 380.5 | zz | $Zn(N)_6$ |
| 389.5 | zy, zz | $Zn(N)_6$ |
| 390 | xy | $Zn(N)_6$ |
| 391.5 | zz | $Zn(N)_6$ |
| 511 | zy | |
| 512.5 | xy | |
| 513 | xz | |
| 514 | zz | |
| 598 | xy | |
| 599 | zy | |
| 612 | zy | pyrazole |
| 616 | xy | pyrazole |
| 657 | zy | pyrazole |
| 658.5 | xy | pyrazole |
| 666 | xy | pyrazole |
| 705 | xy | $\nu_4$ ($NO_3^-$) |
| 705.5 | zy | $\nu_4$ ($NO_3^-$) |
| 706.5 | zz, xz | $\nu_4$ ($NO_3^-$) |
| 786.5 | zy | |
| 795 | zy | |
| 859.5 | xy | |
| 861 | zz | |
| 864 | zy | |

**Table C.2 (continued)**

| Raman shift ($cm^{-1}$) | Polarisation | Assignment |
|---|---|---|
| 874.5 | zy | |
| 883 | xy | |
| 886 | zy | |
| 887.5 | xz | |
| 911 | xy | |
| 912 | zz, zy, xz | |
| 918 | xy | |
| 923.5 | zy | |
| 925 | xz | |
| 928 | xy | |
| 979 | zy | |
| 980.5 | xy | |
| 986.5 | zy | |
| 987.5 | xy | |
| 997 | zy, xy | |
| 998 | xz | |
| 999 | zz | |
| 1041 | zy | $\nu_1$ ($NO_3^-$) |
| 1042 | xz, xy | $\nu_1$ ($NO_3^-$) |
| 1043 | zz | $\nu_1$ ($NO_3^-$) |
| 1049 | zy | |
| 1056 | xz | |
| 1083.5 | xz | pyrazole |
| 1084 | zy | pyrazole |
| 1085 | xy | pyrazole |
| 1086.5 | zz | pyrazole |
| 1091 | xy | pyrazole |
| 1092.5 | zy | pyrazole |
| 1093.5 | xz | pyrazole |

**Table C.2 (continued)**

| Raman shift ($cm^{-1}$) | Polarisation | Assignment |
|---|---|---|
| 1095 | zz | pyrazole |
| 1195 | xy | |
| 1226 | xy | |
| 1245.5 | xy | |
| 1254.5 | xy | |
| 1261 | zy | |
| 1261.5 | xz | |
| 1289 | zy, xz | |
| 1289.5 | xy | |
| 1290.5 | zz | |
| 1294 | zy | |
| 1314 | xy | |
| 1314.5 | xz | |
| 1344.5 | zy | |
| 1346 | xz, xy | |
| 1347 | zz | |
| 1375.5 | xy | |
| 1376.5 | zz | |
| 1384 | zy | $\nu_3$ ($NO_3^-$) |
| 1384.5 | xz | $\nu_3$ ($NO_3^-$) |
| 1385.5 | xy | $\nu_3$ ($NO_3^-$) |
| 1387 | zz | $\nu_3$ ($NO_3^-$) |
| 1398 | xy | |
| 1403.5 | xy | |
| 1405 | zz | |
| 1407 | zy | |
| 1414 | zz, zy | |
| 1414.5 | xz | |
| 1416 | xy | |

**Table C.2 (continued)**

| Raman shift ($cm^{-1}$) | Polarisation | Assignment |
|---|---|---|
| 1516.5 | zy | |
| 1582 | xy | |
| 1735 | xy | plasma |
| 1735.5 | xz | plasma |
| 1811 | xy | |
| 1826.5 | xy | |
| 1933 | zy | |
| 1933.5 | xy | |
| 1952.5 | xy | plasma |
| 1980 | zy, xy | |
| 1980.5 | xz | |
| 2015 | xy | plasma |
| 2022.5 | xz | plasma |
| 2023 | zy | plasma |
| 2023.5 | xy | plasma |
| 2024.5 | zz | plasma |
| 2144.5 | xz | plasma |
| 2146 | xy | plasma |
| 2240 | xz | plasma |
| 2241 | xy | plasma |
| 2242 | zz | plasma |
| 2378.5 | xz | plasma |
| 2458.5 | xz | plasma |
| 2459.5 | xy | plasma |
| 2526.5 | xy | plasma |
| 2534.5 | xz | |
| 2535 | xy | |
| 2539.5 | xy | |
| 2547 | xz | plasma |

**Table C.2 (continued)**

| Raman shift ($cm^{-1}$) | Polarisation | Assignment |
|---|---|---|
| 2548 | xy | plasma |
| 2549 | zz | plasma |
| 2638.5 | xz | |
| 2639 | xy | |
| 2640 | zz | |
| 2814.5 | xz | plasma |
| 2815 | xy | plasma |
| 2815.5 | zz | plasma |
| 2830.5 | xz | plasma |
| 2951.5 | xy | ν (C-H): capping carbon |
| 2952.5 | xz | ν (C-H): capping carbon |
| 3104.5 | xy | ν (C-H): pyrazole |
| 3105 | xz | ν (C-H): pyrazole |
| 3109.5 | xz | ν (C-H): pyrazole |
| 3110 | zy | ν (C-H): pyrazole |
| 3110.5 | zz | ν (C-H): pyrazole |
| 3120 | zy, xy | ν (C-H): pyrazole |
| 3128.5 | zy, xz | ν (C-H): pyrazole |
| 3129 | xy | ν (C-H): pyrazole |
| 3129.5 | zz | ν (C-H): pyrazole |
| 3133 | xy | ν (C-H): pyrazole |
| 3140 | zy, xz, xy | ν (C-H): pyrazole |
| 3141 | zz | ν (C-H): pyrazole |
| 3144.5 | zy, xz, xy | ν (C-H): pyrazole |
| 3155.5 | xz, xy | ν (C-H): pyrazole |
| 3156 | zy | ν (C-H): pyrazole |
| 3156.5 | zz | ν (C-H): pyrazole |

## Table C.3: Peak locations in the Raman spectra of $[Co(HCPz_3)_2](NO_3)_2$

| Raman shift ($cm^{-1}$) | Polarisation | Assignment |
|---|---|---|
| 91 | zy, xz, xy | |
| 91.5 | zz | |
| 99.5 | zy, xy | |
| 100 | zz | |
| 105 | xz | |
| 106 | zz, xy | |
| 109.5 | zy | |
| 118 | xz | |
| 118.5 | zy | |
| 126 | xy | |
| 135 | xy | |
| 135.5 | zz, xz | |
| 136 | zy | |
| 141 | zy | |
| 154 | xy | |
| 154.5 | zz | |
| 158.5 | zy | |
| 160.5 | xz | |
| 167.5 | xy | |
| 168 | zz, zy | |
| 168.5 | xz | |
| 176.5 | zy, xz | |
| 193 | xz, xy | |
| 193.5 | zy, zz | |
| 215.5 | zz | plasma |
| 232 | zz | |
| 271.5 | zz | plasma? |
| 311 | xy | |
| 313.5 | zz, zy | |

**Table C.3 (continued)**

| Raman shift ($cm^{-1}$) | Polarisation | Assignment |
|---|---|---|
| 369.5 | xy | $CoN_6$ |
| 370 | zz | $CoN_6$ |
| 370.5 | zy | $CoN_6$ |
| 378.5 | xz | $CoN_6$ |
| 379.5 | zz, zy, xy | $CoN_6$ |
| 391 | zz, zy, xz, xy | $CoN_6$ |
| 511 | zz, zy, xz, xy | |
| 535 | zz | plasma |
| 565 | zz | plasma |
| 608.5 | xz | |
| 609 | zy | |
| 611.5 | xy | |
| 658 | zy | |
| 666 | xy | |
| 704 | xy | $\nu_4$ ($NO_3^-$) |
| 704.5 | xz | $\nu_4$ ($NO_3^-$) |
| 705.5 | zz | $\nu_4$ ($NO_3^-$) |
| 706 | zy | $\nu_4$ ($NO_3^-$) |
| 735 | xy | |
| 735.5 | zy | |
| 736 | zz, xz | |
| 859 | zz | |
| 863 | zy | |
| 873.5 | zy | |
| 885.5 | xz | |
| 909.5 | xy | |
| 910 | zz | |
| 911.5 | zy | |
| 916.5 | xy | |

**Table C.3 (continued)**

| Raman shift ($cm^{-1}$) | Polarisation | Assignment |
|---|---|---|
| 923.5 | xz, zy | |
| 925.5 | xy | |
| 987.5 | xy | |
| 988.5 | zz | |
| 996.5 | xy, xz | |
| 997 | zz | |
| 1040.5 | zy | $\nu_1$ ($NO_3^-$) |
| 1041 | xy, xz | $\nu_1$ ($NO_3^-$) |
| 1041.5 | zz | $\nu_1$ ($NO_3^-$) |
| 1047 | zy | $\nu_1$ ($NO_3^-$) |
| 1048.5 | xz | $\nu_1$ ($NO_3^-$) |
| 1082.5 | xz | |
| 1083 | xy | |
| 1083.5 | zy | |
| 1084 | zz | |
| 1091.5 | zy, xy | |
| 1092 | xz | |
| 1092.5 | zz | |
| 1224 | zz | |
| 1244 | xy | |
| 1245.5 | zz | |
| 1253.5 | xy | |
| 1259 | zy, xz | |
| 1285 | zz | |
| 1287 | xy | |
| 1288 | xz | |
| 1289.5 | zy, zz | |
| 1315.5 | xz | |
| 1343 | xy | |

**Table C.3 (continued)**

| Raman shift ($cm^{-1}$) | Polarisation | Assignment |
|---|---|---|
| 1343.5 | xz | |
| 1344 | zz, zy | |
| 1373 | xy | |
| 1374 | zz | |
| 1376 | zy | |
| 1383.5 | zy | |
| 1384 | xz, xy | |
| 1385 | zz | |
| 1402.5 | xy | |
| 1403 | zz | |
| 1407.5 | zy | |
| 1411 | xz | |
| 1411.5 | zz | |
| 1413.5 | xy | |
| 1414 | zy | |
| 1464 | zz | |
| 1617 | zz | |
| 1733.5 | zz, xy | plasma |
| 1781 | zz | |
| 1811 | zz | |
| 1825 | zz | |
| 1951 | zz | plasma |
| 1978.5 | xz | |
| 1979 | xy | |
| 1995.5 | xy | plasma |
| 2013 | zz | plasma |
| 2013.5 | xy | plasma |
| 2021.5 | xz | plasma |
| 2022 | zz, xy | plasma |

**Table C.3 (continued)**

| Raman shift ($cm^{-1}$) | Polarisation | Assignment |
|---|---|---|
| 2144 | xy | plasma |
| 2144.5 | zz | plasma |
| 2173 | zz | |
| 2239.5 | zz, xy | plasma |
| 2378 | zz, xy | plasma |
| 2458 | xy | plasma |
| 2525 | xy | plasma |
| 2534 | zz, xy | plasma? |
| 2537.5 | xy | plasma? |
| 2538 | zz | plasma? |
| 2546.5 | zz, xy | plasma |
| 2637.5 | zz | plasma? |
| 2638 | xy | plasma? |
| 2797.5 | xy | |
| 2813.5 | xy | plasma |
| 2814 | zz | plasma |
| 2829.5 | xy | plasma |
| 3028.5 | xy | |
| 3044 | xy | plasma |
| 3078 | xy | |
| 3102 | zy | ν (C-H) pyrazole |
| 3103 | xy | ν (C-H) pyrazole |
| 3108.5 | zy, xy | ν (C-H) pyrazole |
| 3109 | zz | ν (C-H) pyrazole |
| 3109.5 | xz | ν (C-H) pyrazole |
| 3118 | zy, xy | ν (C-H) pyrazole |
| 3126.5 | zy | ν (C-H) pyrazole |
| 3127 | xy, xz | ν (C-H) pyrazole |
| 3131 | zy | ν (C-H) pyrazole |

**Table C.3 (continued)**

| Raman shift ($cm^{-1}$) | Polarisation | Assignment |
|---|---|---|
| 3131.5 | zz, xy, xz | ν (C-H) pyrazole |
| 3139 | xy | ν (C-H) pyrazole |
| 3139.5 | xz | ν (C-H) pyrazole |
| 3143 | zy | ν (C-H) pyrazole |
| 3143.5 | zz, xy, xz | ν (C-H) pyrazole |
| 3154.5 | zz | ν (C-H) pyrazole |
| 3155 | zy, xz, xy | ν (C-H) pyrazole |

Literature sources of frequencies/energies:

Pyrazole[2]

Laser plasma lines[3]

Nitrate, metal-ligand modes[4]

## C.4 Discussion

Vibrational peaks arising from the $HCPz_3$ ligand, the metal-nitrogen bonds, and the nitrate anion can all be identified in the spectra of $[Zn(HCPz_3)_2](NO_3)_2$ and $[Co(HCPz_3)_2](NO_3)_2$. A number of laser plasma lines can also be observed. A large amount of splitting is observed due to the lifting of degeneracy as a result of the low symmetry environments. For example, around seven peaks are observed in the region 3100-3160 $cm^{-1}$ (pyrazole ring C-H stretches) compared with the three observed for pyrazole aqueous solution.

The totally symmetric stretch of the $NO_3^-$ ion is observed between 1040 and 1050 $cm^{-1}$. It is an intense peak and was often used for optimising the spectrum. The asymmetric stretch frequency of the nitrate ion can also be observed at ca. 1385 $cm^{-1}$, while the less intense $\nu_4$ asymmetric bend mode is seen at 705 $cm^{-1}$. The fourth band ($\nu_2$), the 'umbrella opening' bend mode is Raman inactive.

The majority of peaks are due to internal modes of the ligands which is not surprising as each $HCPz_3$ molecule contains 26 atoms and as a result possesses 72 internal modes. As

mentioned above, a number of peaks can be seen above 3100 $cm^{-1}$, arising from stretching of pyrazole ring C-H bonds. A weak peak at around 2950 $cm^{-1}$ is probably the C-H stretch peak of the capping carbon[5]. Other peaks can be identified with the help of reference data for pyrazole itself[2]. The peaks due to the pyrazolyl ring itself mostly lie between 1000 and 1500 $cm^{-1}$, with a few lying between 600 and 1000 $cm^{-1}$.

$[Co(HCPz_3)_2](NO_3)_2$ is isomorphic with the zinc complex. The molecular geometries (bond lengths and angles) are very similar, and zinc and cobalt have similar atomic masses. This means that their vibrational spectra should be almost identical, and any peaks appearing in the cobalt spectrum which do not appear in the zinc spectrum can be assigned to electronic Raman transitions. Unfortunately, the spectra present a veritable forest of peaks, due to the number of atoms, and low symmetry of the structure. As discussed previously in appendix C, electronic Raman peaks are generally broader than vibrational peaks. No obvious candidates for electronic Raman peaks can be identified in the spectra. In particular, no electronic Raman peaks were observed in the 2000-3000 $cm^{-1}$ region (not shown). The peaks resulting from transitions to the two Kramers doublets of the $^4A_{2g}$ trigonally-split component of the $^4T_{1g}$ ground state are expected to lie in this region (see table 6.13).

## C.5 References


(1) Wahlstrom, E. E. *Optical Crystallography*; 5 ed.; John Wiley and Sons:, 1979.

(2) Billes, F.; Endredi, H.; Jalsovszky, G. *Journal of Molecular Structure* **1999**, *465*, 157-172.

(3) Julien, C.; Hirlimann, C. *Journal of Raman Spectroscopy* **1980**, *9*, 62-66.

(4) Nakamoto, K. *Infrared and Raman Spectra of Inorganic and Coordination Compounds*; 5th ed.; John Wiley and Sons Inc: New York, 1997.

(5) Julia, S.; Mazo, J. d.; Avila, L.; Elguero, J. *Organic Preparations and Procedures International* **1984**, *16*, 299-307.